



ISAS - INTERNATIONAL SCHOOL FOR ADVANCED STUDIES

Numerical Relativistic Hydrodynamics: New Ideas and Applications

Thesis submitted for the degree of—
“Doctor Philosophiæ”

CANDIDATE

Olindo Zanotti

SUPERVISORS

Dr. Luciano Rezzolla
Prof. John C. Miller

October 2002



SCUOLA INTERNAZIONALE SUPERIORE DI STUDI AVANZATI
INTERNATIONAL SCHOOL FOR ADVANCED STUDIES

Numerical Relativistic Hydrodynamics: New Ideas and Applications

Thesis submitted for the degree of
“Doctor Philosophiæ”

CANDIDATE

Olindo Zanotti

SUPERVISORS

Dr. Luciano Rezzolla
Prof. John C. Miller

October 2002

“Dans les jours d’affliction, la science des choses extérieures ne pourra pas me consoler de l’ignorance de la morale; mais la science de cette-ci me consolera toujours de l’ignorance du monde estérieur.”

B. Pascal

Contents

1	Overview	1
2	Numerical Relativistic Hydrodynamics	5
1	Introduction	5
2	Historical Overview	6
3	Introduction to Hyperbolic Partial Differential Equations	7
3.1	Conservation Laws	8
3.2	Characteristic Equations	8
4	Linear and Nonlinear behavior	10
4.1	Nonlinearities and Shock Formation	11
5	The Riemann Problem	12
5.1	Mathematical Definition	12
5.2	Physical Definition	13
6	Godunov Type Methods	14
6.1	Integral Form of Conservation Laws	14
7	Exact and Approximate Riemann Solvers	17
7.1	Exact Riemann Solver in Special Relativistic Hydrodynamics	18
7.2	Approximate Riemann Solvers	20
7.3	Approximate State Riemann Solvers	20
7.4	Approximate Flux Riemann Solvers	21
8	High Resolution Shock Capturing Methods	23
8.1	Total Variation Diminishing Methods	24
8.2	Reconstruction Procedures	25
9	The Conservation Form of the Relativistic Hydrodynamics Equations	26

9.1	Eigenstructure of the Equations	28
9.2	Structure of a HRSC numerical code	30
3	A New Exact Riemann Solver in Special Relativistic Hydrodynamics	33
1	Introduction	33
2	General Presentation of the Method	33
2.1	Limiting Relative Velocities	36
3	One-dimensional Flows	37
3.1	$1 \mathcal{S}_{\leftarrow} 3 \mathcal{C} 3' \mathcal{S}_{\rightarrow} 2$: Two Shock Waves	38
3.2	$1 \mathcal{R}_{\leftarrow} 3 \mathcal{C} 3' \mathcal{S}_{\rightarrow} 2$: One Shock and One Rarefaction Wave	39
3.3	$1 \mathcal{R}_{\leftarrow} 3 \mathcal{C} 3' \mathcal{R}_{\rightarrow} 2$: Two Rarefaction Waves	40
4	Multi-dimensional Flows	42
4.1	Jumps Across a Shock Wave	43
4.2	Jumps Across a Rarefaction Wave	44
4.3	$1 \mathcal{S}_{\leftarrow} 3 \mathcal{C} 3' \mathcal{S}_{\rightarrow} 2$: Two Shock Waves	46
4.4	$1 \mathcal{R}_{\leftarrow} 3 \mathcal{C} 3' \mathcal{S}_{\rightarrow} 2$: One Shock and One Rarefaction Wave	47
4.5	$1 \mathcal{R}_{\leftarrow} 3 \mathcal{C} 3' \mathcal{R}_{\rightarrow} 2$: Two Rarefaction Waves	48
5	Numerical Implementation	49
4	New Relativistic Effects in the Dynamics of Non-linear Hydrodynamical Waves	53
1	Introduction	53
2	Preliminary Discussion	53
3	The New Effect: Changing the Wave-pattern	54
5	Quasi-Periodic Accretion and Gravitational Wave Emission from oscillating “Toroidal Neutron Stars”	63
1	Introduction	63
2	Analytic solutions for stationary configurations	65
3	Mathematical Framework	68
3.1	Hydrodynamic equations	68
3.2	Spacetime Evolution	70
3.3	Numerical Approach	71

4	Initial Data	72
4.1	Introducing a Perturbation	73
5	Numerical Results	75
5.1	Dynamical Spacetime: the run-away Instability	75
5.2	Fixed Spacetime: Quasi-Periodic Oscillations	78
6	Gravitational wave emission	88
6.1	Detectability	92
6	Axisymmetric Oscillations of Vertically Integrated Discs	97
1	Introduction	97
2	Local approach in the Newtonian case	99
2.1	Basic assumptions	99
2.2	Governing Equations	100
2.3	Perturbed Equation	100
3	General Relativistic Discs	103
3.1	Assumptions and Governing Equations	103
3.2	Local Analysis	105
3.3	Global Analysis	107
4	Constant angular momentum discs	110
4.1	Perturbation equations	110
4.2	Results	110
5	Non-constant angular momentum discs	113
5.1	Equilibrium model	113
5.2	Results	114
7	Dissipative Hydrodynamics	121
1	Introduction	121
2	Do we need Rational Extended Thermodynamics in Astrophysics?	124
2.1	Thermal Relaxation in Gravitational Collapse	126
3	Dissipative Fluids	127
4	Classical Irreversible Thermodynamics	129
5	Extended Thermodynamics	130

6	Divergence Type Theories	132
6.1	The Connection With Kinetic Theory	132
6.2	The Non-degenerate Relativistic gas	134
6.3	Extended Thermodynamics of moments	136
7	Discussion	136
8	Magnetic Field Decay in Neutron Stars	139
1	Introduction	139
2	The Structure of the Star	141
3	Evolution of the Internal Magnetic Field	143
3.1	The Relativistic Induction Equations	143
3.2	Strategy of the Numerical Solution	146
3.3	The Initial Value Problem	147
3.4	Boundary Conditions	149
4	Numerical Results	151
9	Conclusions	157
A	Monotonicity of the relative velocity as function of p_*	161
1	One-dimensional Flows	161
2	Multi-dimensional flows	163
B	Newtonian limits of $(\tilde{v}_{12})_{2S}$, $(\tilde{v}_{12})_{SR}$, $(\tilde{v}_{12})_{2R}$	166
C	A closed form solution in the case of Two Rarefaction Waves	168
D	The numerical solution of the induction equations	171
E	Implementing surface boundary conditions	173
F	The stress formula	175
	Bibliography	177

Publications

The third chapter is based on two works submitted to *J. Fluid. Mech.*, the first of which has already been published in *J. Fluid. Mech.*, 2001, Vol. 449, 395. The fourth chapter has been published in *Phys. Rev. Letter*, 2002, Vol. 89, Issue 11.

The content of the fifth chapter is widely based on a paper recently submitted to *MNRAS*. Finally, the eighth chapter has been published in *MNRAS*, 2002, Vol. 331, 376.

Acknowledgments

Ci sono i ringraziamenti dal tono ufficiale, quelli che in genere si presentano in queste occasioni, e i ringraziamenti con un taglio decisamente piu' personale, che rifuggono le espressioni formali ma che allo stesso tempo non si addicono ad alcun tipo di pubblicita'. Vorrei tentare una via di mezzo, saltando tutta quella parte in cui, partendo dai propri supervisori, per passare agli amici, poi i collaboratori e infine i famigliari, si esprime la propria gratitudine nei confronti di quanti hanno in varia maniera reso possibile il compimento di un'opera. Non che non provi un sentimento di gratitudine. Anzi, so bene che avrei combinato molto poco senza tutto quello che da ognuno ho ricevuto. Ma talvolta accade che un'enfasi eccessiva nel sottolineare un debito di riconoscenza, che nel mio caso certamente esiste, si traduca in un'autocelebrazione del proprio lavoro.

La scienza oggi si fa in gruppo, oppure non si fa; pertanto, piu' che soffermarmi con parole di ringraziamento nei confronti di singole persone e dei molteplici privilegi di cui ho goduto, preferisco riabbracciare nella sua totalita' il gruppo di Astrofisica della SISSA, con il quale in questi anni ho vissuto momenti entusiasmanti. Che poi parole decisamente speciali vadano riservate a Luciano Rezzolla, John Miller e Shin'chirou Yoshida, questo e' fuori discussione. Così' come il sostegno di tutti gli amici di stanza 10, 9, 101 e 103 ai quali va il mio sentimento di amicizia. Ma mi accorgo di scivolare inesorabilmente verso quello stereotipo di ringraziamenti da cui volevo prendere le mosse. Percio' lascio da parte almeno i famigliari, con i quali me la vedro' personalmente...

There are mainly two types of acknowledgments, those that traditionally fall into the serious category and those that are much more personal aimed at family and friends, which have nothing to do with the previous ones because of their highly confidential content. That is why I will try to find the best compromise between them. I will deliberately leave out the list of supervisors, colleagues, friends and relatives who, in different ways, have made this project possible. I am afraid that this might sound ungrateful, but the opposite is correct. Therefore, I would like to express my gratitude to those who have helped and supported me throughout these years and given me the opportunity to achieve my ambitious plans. Nevertheless, to put too much emphasis on my feelings of gratitude and recognition (which in my case are sincerely true!) would be perceived as an overwhelming exaggeration of my efforts.

Science, today, means teamwork research. No-one would manage to get through it all alone and this is the reason why I would like to address my gratitude to the Astrophysics group of SISSA as a whole, instead of saying a few words of thanks to every single member of the group. My final words of thanks are especially to Luciano Rezzolla, John Miller e Shin'chirou Yoshida and also to my dear friends and colleagues from room 10, 9, 101 and 103. Thank you for the great support, not only scientific but also moral, and for your kindness! Finally, since I am getting away from the path I was supposed to follow, in order to fulfill my promise, I will leave out my relatives, who I will thank separately...

Chapter 1

Overview

It has often been said that our Universe is like a laboratory where very important physical phenomena can be studied which could never be repeated on Earth. Unfortunately, astrophysicists cannot prepare their own experiments as the other physicists do in their laboratories. This represents a serious limitation which prevents astrophysics from being also an experimental science. The occurrence of an astrophysical event, in fact, is obviously neither arbitrarily repeatable nor checkable, and therefore it lacks the two minimum requirements for a physical phenomenon to be called an experiment in the Galilean sense. On the basis of these considerations some philosophers of science have cast doubts on the scientific status of astrophysics as a whole! Leaving aside all of the objections that could be made to this statement, it is interesting to note that since numerical simulations have become a common tool in astrophysics, a new kind of “laboratory” has become available. Of course its epistemological status is quite different from that of the usual laboratory: after all, numerical simulations describe the evolution of physical systems according to some law which is known *a priori*. However, they can provide a fundamental link between our present theories and the physical systems under investigation, filling the gap between the theory and the experimental activity. In most of the cases, for example, astrophysic processes involve extreme conditions which are absolutely inaccessible to the experiments in the laboratory, and one has to rely on extrapolations of the known physics into different regimes. Moreover, the timescales of the processes involved are often much longer than the human life and what can be observed astronomically is in many cases just a particular short phase of a long lasting phenomena. Finally, and remarkably, highly non linear processes take place in a wide variety of astrophysical systems which can only be handled by adopting sophisticated numerical techniques. In these circumstances, in fact, the theoretical model adopted, which is supposed to provide a good description of the physical system under investigation, has some *predictive power* which can only be tested by mean of simulations where the non-linear evolution equations are solved exploring a large parameter space. For all of these reasons, a *numerical experiment* offers the extraordinary means of unveiling fundamental physical aspects that the mere knowledge of the theory, no matter how deep it is, could never reveal.

This is particularly true for numerical relativistic hydrodynamics¹, whose applications to

¹Unless stated otherwise, with the term “relativistic” we will refer to both special and general relativity.

astrophysics are nowadays numerous, allowing for a quantitative description of a large variety of astrophysical phenomena. A significant portion of this Thesis (Chapter 2 to Chapter 4) is directly devoted to this field of research.

Chapter 2 serves as an introductory chapter where High Resolution Shock Capturing (HRSC) methods are presented and the most important ingredients for their developments are discussed. Particular attention is focused on the presentation of the Riemann problem², which is the subject of the following two chapters.

In Chapter 3, in fact, we concentrate on the exact solution of the Riemann problem in special relativistic hydrodynamics by proposing a new procedure which focusses on the relativistic invariant relative velocity between the two unperturbed initial states of the fluid. This new approach, which is valid for both one-dimensional and multi-dimensional flows, allows extraction of some important information contained in the initial data, that traditional approaches were not able to reveal. In particular, we have shown that, given a Riemann problem with assigned initial conditions, it is possible to determine in advance both the nature of the nonlinear waves that will be produced after the removal of the initial discontinuity and the bracketing interval of the unknown pressure in the region that forms behind the wave fronts. These new ideas can be successfully implemented in the construction of an efficient numerical algorithm. Although in modern hydrodynamical codes using HRSC methods the solution of the Riemann problem is usually obtained in approximate ways (through the so called Approximate Riemann solvers), is yet very important for improving an Exact Riemann Solver. In a typical flow, in fact, the overwhelming majority of local Riemann problems are in regions of smooth flows, and approximate Riemann solvers give satisfactory results. When large gradients occur, however, approximate Riemann solvers can be very inaccurate, causing the numerical method to fail. Under these conditions, one might think of a hybrid scheme, where an approximate Riemann solver is used in regions of smooth flows, while adopting the exact solver in the presence of large gradients. The method proposed here could be particularly suitable within such an “adaptive” approach. It should also be stressed that special relativistic Riemann solvers can be exploited in general relativistic hydrodynamics by means of a local change of coordinates.

Chapter 4 shows a further advantage of the new method presented in Chapter 3. New hydrodynamical effects, in fact, emerge in a special relativistic Riemann problem when velocities tangential to the initial discontinuity surface are present. In particular, a smooth transition from one wave-pattern to another can be produced by varying the initial tangential velocities while otherwise maintaining the initial states unmodified. These special relativistic effects are produced by the coupling through the relativistic Lorentz factors, do not have a Newtonian counterpart and naturally emerge when solving the Riemann problem with the method presented in Chapter 3.

Chapter 5 represents the part of this Thesis where many of the sophisticated numerical techniques for the solution of general relativistic hydrodynamics equations find a concrete

²The Riemann problem consists in following the decay of a discontinuity between two regions with different uniform initial states.

application. We have in fact performed axisymmetric simulations of constant angular momentum tori orbiting a Schwarzschild black hole. It is well known that in a system consisting of a black hole surrounded by a torus, the fluid flows in an effective potential, whose structure resembles that of a close binary. There are three fundamental circumstances making these objects astrophysically relevant. Firstly, as became apparent from the very beginning, they could develop a dynamical instability, called the “runaway” instability, which could have important astrophysical consequences in connections with γ -ray bursts models. The occurrence of this instability has been the subject of several numerical simulations over the years. Overall, a final conclusion on its occurrence is still premature, because different effects such as the self gravity of the torus, rotation of the black hole, and the dynamical response of the background metric have not yet been included in a comprehensive manner. The second important reason for being interested in tori around black holes is that they are likely to be significant sources of gravitational waves, a fact which has been somewhat underestimated. Finally, thick discs around black holes may develop internal oscillations under various kinds of external perturbations, a fact which is attracting the interest of both theoreticians and observers, given the large existing phenomenology of periodic and quasi periodic X -ray emitters. Our attention in this Chapter has been oriented towards each of these three issues. In particular, by introducing suitable perturbations, we have shown that these systems either become unstable to the run-away instability or exhibit a strikingly regular oscillatory behavior resulting in a quasi-periodic variation of the mass accretion rate as well as of the density distribution. Despite being axisymmetric, the perturbed discs experience large variations of the rest-mass distribution hence emitting considerable amounts of gravitational radiation. The strength of the gravitational waves emitted is of the same order of magnitude of that expected in stellar-core collapse making these new sources of gravitational waves potentially detectable.

Chapter 6 is a natural follow up of the previous one, in the sense that it presents an interpretation of the oscillations detected numerically. Oscillations are ubiquitous phenomena in physical systems and accretion discs are not exceptions. However, these oscillations have been mostly studied in thin accretion discs, either Newtonian or relativistic. Our approach, based on a perturbative analysis for computing the fundamental frequencies of oscillations in a “vertically integrated system”, is a first attempt towards a fully two-dimensional detailed study and strongly supports the idea that the oscillations appearing in our numerical simulations are, in fact, acoustic modes.

Chapter 7 is a short review of relativistic Extended Thermodynamics, a fascinating field of research which we started studying recently. As it is well known, the Navier-Stokes theory of dissipative fluids introduces a parabolic nature into the equations and thus predicts infinite signal speeds. Naturally, this feature is unsatisfactory in relativistic hydrodynamics and pushed for the formulation of alternative theories, ultimately leading to extended thermodynamics. The latter is better described as a hierarchy of theories with an increasing number of fields as the gradients and the rates of thermodynamic processes become steeper and faster. We summarize the basic concepts of this new formulation, emphasizing its importance in

specific astrophysical contexts, from both theoretical and computational points of view.

Chapter 8, which is the last one of the Thesis, deviates from the main course taken so far, and focusses on a very hot topic in astrophysics, namely the influence of strongly curved spacetimes on the properties of electromagnetic fields in rotating neutron stars. After presenting the physical aspects of the problems, we have solved numerically the general relativistic induction equations in the interior background spacetime of a slowly rotating magnetized neutron star. The analytic form of these equations shows that corrections due both to the spacetime curvature and to the dragging of inertial frames are present. By means of a number of calculations we investigate the evolution of the magnetic field with different rates of stellar rotation, different inclination angles between the magnetic moment and the rotation axis, as well as different values of the electrical conductivity.

Notation

The common conventions adopted through the Thesis are the following. A space-like signature $(-, +, +, +)$ is used. Greek indices are taken to run from 0 to 3 and Latin indices from 1 to 3. Partial derivatives are either indicated with a comma or with the standard “ ∂ ” notation. The system of units adopted, on the other hand, is specified at the beginning of each Chapter, whenever necessary.

Chapter 2

Numerical Relativistic Hydrodynamics

1 Introduction

The Euler equations are a nonlinear hyperbolic system of equations that follow from the Navier-Stokes equations when both viscosity and heat conduction are neglected. One of the most remarkable features of these equations is that, at least in the case of compressible fluids and in the classical fluid description, they admit discontinuities, even if the initial data are smooth. We recall here that the concept of *discontinuity* is a natural consequence of the hydrodynamical description, according to which the quantities characterizing the fluid are averaged over a *fluid element*, whose linear size is smaller than the typical macroscopic size of the system, but which is larger than the collisional mean free path of the particles. From a microscopical point of view, the relevant physical quantities across these discontinuities are certainly continuous, although they might experience large variations¹ which make them appear as “discontinuities” on a macroscopic scale.

From a computational point of view the appearance of discontinuities represents a formidable obstacle for any numerical method. In traditional *finite difference methods*, the differential of a function u at a point \bar{x} is approximated by using only values of u at a finite number of points near \bar{x} . However, a finite-difference approximation to a derivative is not satisfactory in the presence of discontinuities, which are usually reproduced with strong smearing or with very pronounced oscillations in their vicinity.

Fortunately, the mathematical structure of the hyperbolic equations can be successfully exploited in order to develop numerical methods that are very efficient in resolving these discontinuities. In this Chapter we will present the main ideas of this approach, which collects a large family of techniques going under the name of High Resolution Shock Capturing (HRSC) methods. Several authors have contributed to the development of this field of research in the last few decades, bringing it now into a rather mature stage. As a result, the number of numerical techniques has grown considerably and there are often a lot of

¹In general, we classify discontinuity surfaces as *contact discontinuities* and *shock fronts*. The former are characterized by the fact that there is no fluid flow across them, while the opposite is true for the latter.

different numerical methods to choose from when solving a numerical problem. It is not our intention to give a systematic presentation of all the computational methods for the solution of hyperbolic equations. Rather, we will restrict ourselves to a short selection of fundamental ideas, putting more emphasis on those techniques which will be further discussed in this Thesis.

Before doing this, however, it is worth giving a short historical perspective, which will be presented in the following Section.

2 Historical Overview

One of the first general relativistic hydrodynamical codes was the one dimensional Lagrangian code of May & White (1996) that allowed the first numerical modelling of a collapse leading to black hole formation. As is well known, the Lagrangian formulation prevents the occurrence of numerical diffusion of momentum during the simulations. However, this advantage is largely lost when considering multidimensional problems, since the comoving grid of the Lagrangian coordinates is easily distorted in the presence of shear or vortex flows, thus requiring complicated *rezoning* of the grid. This difficulty was the main motivation for the development of Eulerian codes, the first of which was that of Wilson (1972), followed by Centrella & Wilson (1984) and Hawley *et al.* (1984). All of these codes share the same technique for handling the appearance of shock waves. Namely, a wavelength-dependent artificial viscosity term is introduced in the stress energy tensor in exactly the same way as a physical bulk viscosity, and has the property of spreading the shock over several grid zones, sacrificing resolution. The main motivation for introducing numerical dissipation was that the continuity and the Euler equations were not written in such a way to preserve the *conservation form* of the original hyperbolic system, and the solution across discontinuities had to be stabilized. In spite of these limitations, this approach has been widely adopted to simulate flows in relativistic stellar collapse, accretion onto compact objects, and cosmology. A fundamental step forward in the simulation of relativistic flows was obtained with the introduction of High Resolution Shock Capturing (HRSC) methods (Martí *et al.*, 1991; Marquina *et al.*, 1992), which are based on a new approach taking full advantage of the hyperbolic and conservative formulation of the hydrodynamics equations. In particular, the resulting numerical schemes, which avoid completely the introduction of artificial viscosity terms, combine the following ingredients: the conservative formulation of the hydrodynamics equations, the knowledge of the *characteristic fields* of the system, the application of Godunov methods (Godunov, 1959) based on the hyperbolic formulation, the introduction of Riemann Solvers, either exact or approximate, and the introduction of particular procedures for increasing accuracy without producing nonphysical oscillations. The two most striking features of relativistic flows are the presence of large Lorentz factors and of strong shock waves. As a result, the competition which naturally started between artificial viscosity methods and HRSC methods has been played by comparing the relative performances in dealing with these kind of intrinsic difficulties. Norman & Winkler (1986), for example,

showed that numerical schemes using artificial viscosity are not able to model relativistic flows with Lorentz factors larger than 2. Over the years, moreover, the performances of HRSC methods have been extensively tested (see Ibañez & Martí, 1999 for a review) showing that they allow for second order (or higher) accuracy of the solution in smooth regions of the flow, while producing very small smearing of strong discontinuities.

3 Introduction to Hyperbolic Partial Differential Equations

The set of first order partial differential equations considered in the present Chapter is of the type

$$\frac{\partial u_i}{\partial t} + \sum_{j=1}^m a_{ij} \frac{\partial u_j}{\partial x} + b_i = 0, \quad (2.1)$$

with $i = 1, \dots, m$. This is clearly a system of m equations in m unknowns u_i , which in general depend both on space² x and on time t . It is sometimes useful to write the system (2.1) in matrix notation as

$$\mathbf{U}_{,t} + \mathbf{A}\mathbf{U}_{,x} + \mathbf{B} = 0, \quad (2.2)$$

where

$$\mathbf{U} \equiv \begin{bmatrix} u_1 \\ u_2 \\ \vdots \\ u_m \end{bmatrix}, \quad \mathbf{B} \equiv \begin{bmatrix} b_1 \\ b_2 \\ \vdots \\ b_m \end{bmatrix}, \quad \mathbf{A} \equiv \begin{bmatrix} a_{11} & a_{12} & \cdots & a_{1m} \\ a_{21} & a_{22} & \cdots & a_{2m} \\ \vdots & \vdots & \ddots & \vdots \\ a_{m1} & a_{m2} & \cdots & a_{mm} \end{bmatrix}.$$

The system is said to be *linear with constant coefficients* if all of the elements of the matrix \mathbf{A} and of the vector \mathbf{B} are constant. If instead $a_{ij} = a_{ij}(x, t)$ and $b_j = b_j(x, t)$ the system is said to be *linear with variable coefficients*. If the matrix \mathbf{A} of the coefficients is a function of the vector \mathbf{U} , the system is then said to be *quasi-linear*³, whereas the system is said to be *homogeneous* if $\mathbf{B} = 0$. Finally, we recall that the system (2.2) is said to be *hyperbolic* if the matrix \mathbf{A} is diagonalizable with a set of real eigenvalues $\lambda_1, \dots, \lambda_m$ and a corresponding set of m linearly independent right eigenvectors $\mathbf{K}^{(1)}, \dots, \mathbf{K}^{(m)}$ such that

$$\mathbf{A}\mathbf{K}^{(i)} = \lambda_i \mathbf{K}^{(i)}. \quad (2.3)$$

A peculiar feature of hyperbolic systems is that they typically describe physical processes involving wave motion or advective transport, and indeed, as will become clear in the rest of the Chapter, the condition of reality for the eigenvalues is associated with the existence of propagating waves.

²In the following we will refer to the one dimensional case, although all the results can be generalized to the full three dimensional case.

³Note that, despite the name, quasi-linear systems are in general systems of nonlinear equations, such as the Euler equations.

3.1 Conservation Laws

A system of partial differential equations is said to be in *conservative form* if it can be written as

$$\mathbf{U}_{,t} + \mathbf{F}(\mathbf{U})_{,x} = 0 , \quad (2.4)$$

where \mathbf{U} is then called the vector of *conserved quantities* and $\mathbf{F} = \mathbf{F}(\mathbf{U})$ is the vector of *fluxes*. The main property of equation (2.4) is that the knowledge of the state-vector $\mathbf{U}(x, t)$ at a given point x at time t allows to determine the rate of flow, or flux, of each state variable at (x, t) . Conservation laws of the form given by (2.4) can also be written as a quasi-linear form

$$\mathbf{U}_{,t} + \mathbf{A}(\mathbf{U})\mathbf{U}_{,x} = 0 , \quad (2.5)$$

where $\mathbf{A}(\mathbf{U}) \equiv \partial \mathbf{F} / \partial \mathbf{U}$ is the Jacobian of the flux vector $\mathbf{F}(\mathbf{U})$. The use of a conservation form of the equations is particularly important when dealing with problems admitting shocks or other discontinuities in the solution. A non-conservative method, i.e. a method in which the equations are not written in a conservative form, might give a numerical solution which looks reasonable but is incorrect. A well known example is provided by Burger's equation, i.e. the momentum equation of an isothermal gas in which pressure gradients are neglected, and whose non-conservative representation fails dramatically in providing the correct shock speed if the initial conditions contain a discontinuity (see LeVeque 1992). Moreover, since the hydrodynamical equations follow from the physical principle of conservation of mass and energy-momentum, the most obvious choice for the set of variables u_j to be used is that of the conserved quantities. As proved by Hou & Le Floch (1994), non conservative schemes do not converge to the correct solution if a shock wave is present in the flow, whereas, as Lax & Wendroff (1960) showed in a classical paper, conservative numerical methods, if convergent, do converge to the *weak solution* of the problem (see the box below for the definition of weak solution).

3.2 Characteristic Equations

The simplest example of a hyperbolic equation in conservation form is given by the scalar linear advection equation

$$\partial_t u + \lambda \partial_x u = 0 , \quad (2.6)$$

with generic initial conditions given by

$$u(x, 0) = u_0(x) . \quad (2.7)$$

Here the Jacobian and the eigenvalue of the system coincide and are given by the constant λ , which is called the “characteristic speed”.

Definition of Weak Solution:

It should be noted that a discontinuous function of class C^0 clearly does not satisfy the partial differential equation (2.4) in the classical sense, since the derivatives are not defined at the discontinuities. For this reason, another integral formulation can be adopted in order to rewrite a differential equation in a form admitting non smooth “solutions”. The basic idea consists in multiplying the PDE by a smooth test function ϕ , and integrating it by parts to move derivatives off the function \mathbf{U} onto the test function. For instance, if we multiply $\mathbf{U}_t + \mathbf{F}_x = 0$ by a continuously differentiable function $\phi(x, t)$ of compact support and we then integrate over space and time we get

$$\int_0^\infty \int_{-\infty}^{+\infty} [\phi \mathbf{U}_t + \phi \mathbf{F}_x] dx dt = 0. \quad (2.8)$$

Integration by parts leads to

$$\int_0^\infty \int_{-\infty}^{+\infty} [\phi_t \mathbf{U} + \phi_x \mathbf{F}] dx dt = - \int_{-\infty}^{+\infty} \phi(x, 0) \mathbf{U}(x, 0) dx, \quad (2.9)$$

where the property that ϕ has compact support, and therefore vanishes at infinity, has been used. As a result, a function \mathbf{U} is called a *weak solution* of the conservation law if it satisfies equation (2.9) for all functions ϕ , as described above. In practice, all the solutions involving discontinuities in the physical quantities are weak solutions. Note also that weak solutions to a problem are often not unique, and a criterion is needed in order to identify which one is physically correct. In most of the cases the choice is made according to the *entropy condition*. Namely, a discontinuity is physically realistic only if the entropy of the fluid increases as the fluid crosses the discontinuity.

Although very simple, this equation represents the prototype of all hyperbolic equations and it offers the opportunity for introducing the concept of *characteristics*, or *characteristic curves*. These may be defined as curves $x = x(t)$ in the (x, t) plane along which a partial differential equation becomes an ordinary differential equation (ODE). The rate of change of u along $x = x(t)$ is in fact

$$\frac{du}{dt} = \frac{\partial u}{\partial t} + \frac{dx}{dt} \frac{\partial u}{\partial x}, \quad (2.10)$$

and if $x = x(t)$ satisfies:

$$\frac{dx}{dt} = \lambda, \quad (2.11)$$

then equation (2.6) ensures that (2.10) is identically zero, or, in other words, that u is constant along the curve $x = x(t)$ with slope λ in the (x, t) plane. As a result, if u is given an initial value according to (2.7), then the solution along the whole characteristic curve $x(t) = x_0 + \lambda t$ crossing the initial point x_0 on the x -axis (see Fig 2.1) is

$$u(x, t) = u_0(x_0) = u_0(x - \lambda t). \quad (2.12)$$

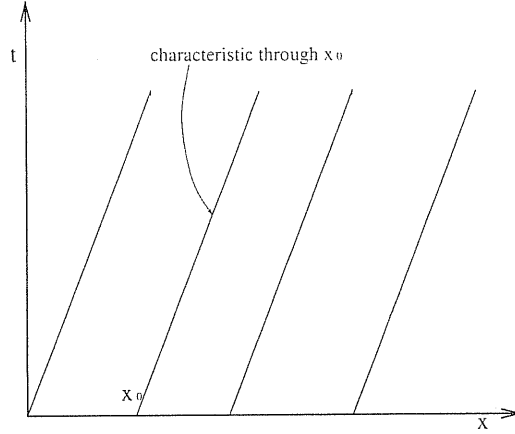


Figure 2.1: Characteristics for the linear advection equation with positive characteristic speed λ .

Therefore, given initial data $u_0(x)$, the linear advection equation simply translates this data with velocity λ to the right or to the left, according to whether $\lambda > 0$ or $\lambda < 0$, respectively. For more complicated systems of equations, such as the Euler equations, it is possible to associate a set of characteristic lines to each eigenvalue of the Jacobian matrix \mathbf{A} , and these determine the worldlines of small disturbances propagating in the fluid.

4 Linear and Nonlinear behavior

Since in many cases the integration of a nonlinear hyperbolic system is obtained by first approximating it with a suitable linear system, we will first consider how these systems are usually treated. In the previous Section we presented the simplest PDE of hyperbolic type: a linear advection equation with constant wave propagation speed. We can now extend our analysis to a set of m hyperbolic PDEs of the form (2.2), where the coefficients of the matrix \mathbf{A} are still constant and where we further assume that $\mathbf{B} = 0$. The hyperbolicity of the system guarantees that the matrix \mathbf{A} is diagonalizable as

$$\mathbf{\Lambda} = \mathbf{K}^{-1}\mathbf{A}\mathbf{K}, \quad (2.13)$$

where

$$\mathbf{\Lambda} = \begin{bmatrix} \lambda_1 & 0 & \cdots & 0 \\ 0 & \lambda_2 & \cdots & 0 \\ \vdots & \vdots & \ddots & \vdots \\ 0 & 0 & 0 & \lambda_m \end{bmatrix}$$

is the diagonal matrix of eigenvalues λ_i and \mathbf{K} is the matrix whose columns are the right eigenvectors of the matrix \mathbf{A} . If we now introduce the *characteristic variables* defined as

$$\mathbf{W} = \mathbf{K}^{-1}\mathbf{U}, \quad (2.14)$$

the system

$$\mathbf{U}_{,t} + \mathbf{A}(\mathbf{U})\mathbf{U}_{,x} = 0 \quad (2.15)$$

can be rewritten as

$$\mathbf{W}_{,t} + \mathbf{\Lambda}\mathbf{W}_{,x} = 0. \quad (2.16)$$

This is called the *canonical form* of system (2.15) and it consists of m decoupled independent linear advection equations, each of which, as discussed in the previous Section, has solution

$$w_i(x, t) = w_i^{(0)}(x - \lambda_i t, 0), \quad (2.17)$$

where the $w_i^{(0)}$'s denote the initial values corresponding to the initial data of the vector \mathbf{U} . Once the canonical form of the system has been solved, the solution of the original system is immediately recovered by inverting equation (2.14) as $\mathbf{U} = \mathbf{K}\mathbf{W}$. It should be noted that w_i is the coefficient of the vector $\mathbf{K}^{(i)}$ in an eigenvector expansion of \mathbf{U} , that is to say

$$\mathbf{U}(x, t) = \sum_{i=1}^m w_i(x, t)\mathbf{K}^{(i)}. \quad (2.18)$$

Combining this last expression with the solutions (2.17) of the decoupled scalar equations yields

$$\mathbf{U}(x, t) = \sum_{i=1}^m w_i^{(0)}(x - \lambda_i t)\mathbf{K}^{(i)}. \quad (2.19)$$

Equation (2.19) reveals two important properties of linear hyperbolic systems. The first and more obvious one is that the knowledge of the *eigenstructure*, i.e. of the eigenvalues and of the eigenvectors, makes the solution of a linear system straightforward. The second one is that the solution can be written as the superposition of m waves, each propagating undistorted with a speed given by the corresponding eigenvalue.

4.1 Nonlinearities and Shock Formation

The two most distinctive features of nonlinear hyperbolic equations are the “*wave steepening*” and the “*shock formation*”. This can be simply illustrated by considering the inviscid Burger’s scalar equation

$$u_{,t} + uu_{,x} = 0, \quad (2.20)$$

where the vector of fluxes has only one component $F = \frac{1}{2}u^2$. At small times, the solution can still be constructed in terms of characteristic curves. These are straight lines, but no longer parallel, unless the solution is the trivial one (i.e. $u_{,x} = 0$). The characteristic speed, in fact, is now in general a function of the solution itself, $\lambda(u) = df/du$, and this

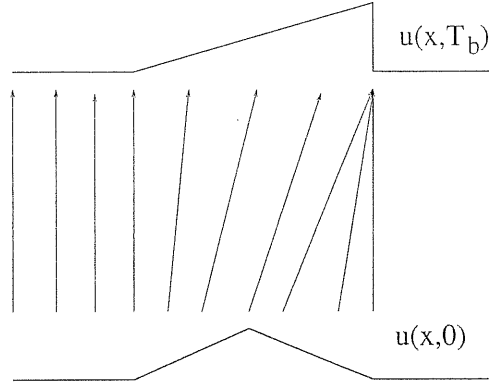


Figure 2.2: Shock formation in Burger's equation. Characteristics intersect at time $t = T_b$.

produces distortions in the initial profile as time evolves. Higher values of u , in fact, will propagate faster than lower values, with expansive and compressive regions forming. The wave steepening mechanism will eventually produce a “folding over” of the solution profile with the characteristic curves intersecting at a certain time. As a result, the solution can be found by following the characteristics only for times shorter than a precise breaking time T_b (see Figure 2.2), after which the waves “break” and a shock might form (see Whitham 1974). It is important to underline that in the evolution of inviscid compressible flows wave steepening and shock formation are very common situations.

5 The Riemann Problem

The appearance of discontinuities poses the problem of how to treat them numerically in a consistent way and without losing accuracy. In the following we will first define the Riemann problem mathematically for a general set of hyperbolic equations and then illustrate it for the particular case of the Euler equations. In Section 6, where Godunov's scheme is introduced, we will show how the solution of the Riemann problem is included as a crucial building block in a numerical scheme, while in Section 7 we will consider some existing Riemann solvers.

5.1 Mathematical Definition

From a mathematical point of view, the Riemann problem for a general $m \times m$ nonlinear hyperbolic system like (2.2) is an initial value problem with initial conditions given by

$$\mathbf{U}(x, 0) = \begin{cases} \mathbf{U}_L & \text{if } x < 0, \\ \mathbf{U}_R & \text{if } x > 0, \end{cases}$$

where \mathbf{U}_L and \mathbf{U}_R are two constant values. Depending on the particular set of hyperbolic equations considered, different wave structures emerge in the solution. For instance, if the equations are simply given by the linear advection equation (2.6), then we expect the initial profile to propagate rigidly. In particular, the initial discontinuity at $x = 0$ will propagate a distance $d = \lambda t$, and the characteristic curve $x = \lambda t$ will separate those characteristic curves to the left, on which the solution is the constant value \mathbf{U}_L , from those curves to the right, on which the solution is \mathbf{U}_R . As a result, the solution of the Riemann problem for the linear advection equation can be written as

$$\mathbf{U}(x, t) = \mathbf{U}_0(x - \lambda t) = \begin{cases} \mathbf{U}_L & \text{if } x - \lambda t < 0 \\ \mathbf{U}_R & \text{if } x - \lambda t > 0. \end{cases}$$

On the other hand, in the case of nonlinear equations, such as the Euler equations, the solution of the Riemann problem may contain rarefaction waves as well as discontinuities. The main properties of the Riemann problem under these circumstances will be discussed in the following section.

5.2 Physical Definition

Consider a fluid, initially divided by a membrane into two sections. The fluid has different values of uniform velocity, pressure and density on the two sides of the membrane. At a certain time the membrane is removed and the system starts evolving. The problem of describing this evolution was addressed by Riemann more than a hundred years ago and became the prototype of the initial value problem for nonlinear hyperbolic systems of partial differential equations with discontinuous initial conditions. The conclusion reached by Riemann in Newtonian hydrodynamics is that the one-dimensional flow that develops when the barrier separating the initial “left” (L) and “right” (R) states is removed, will allow for four different and distinct solutions. All of the solutions are composed of nonlinear waves, in the form of either shock waves or rarefaction waves, that propagate in opposite directions and join the two unperturbed left and right states. Schematically, the fluid solution for any $t > 0$ can therefore be represented as (Martí & Müller 1994)

$$L \mathcal{W}_{\leftarrow} L_* \mathcal{C} R_* \mathcal{W}_{\rightarrow} R, \quad (2.21)$$

where \mathcal{W} denotes a shock or a rarefaction wave that propagates towards the left (\leftarrow) or the right (\rightarrow) with respect to the initial discontinuity, while L_* and R_* are the new hydrodynamic states that form behind the two waves propagating in opposite directions. These waves are separated by a contact discontinuity \mathcal{C} and therefore have the same values of the pressure and velocity, but different values of the density. As a result, three different “wave-patterns” can be produced as listed below

(i) *two shock waves*, one moving towards the initial left state, and the other towards the initial right state: $LS_{\leftarrow} L_* \mathcal{C} R_* S_{\rightarrow} R$.

(ii) *one shock wave and one rarefaction wave*, the shock moving towards the initial right state, and the rarefaction towards the initial left state (or viceversa): $L\mathcal{R}_{\leftarrow}L_*CR_*S_{\rightarrow}R$.

(iii) *two rarefaction waves*, one moving towards the initial left state, and the other towards the initial right state⁴: $L\mathcal{R}_{\leftarrow}L_*CR_*\mathcal{R}_{\rightarrow}R$.

The Riemann problem is said to be solved when the velocity, pressure and density in the new states L_* and R_* have been computed, as well as the positions of the waves separating the four states. In Section 7 we will consider different approaches to the solution.

6 Godunov Type Methods

The solution of the Riemann problem attracted a wider interest when it was realized that its numerical solution could be implemented as building blocks in the construction of numerical methods for the accurate solution of the hydrodynamical equations. In such methods, which are usually referred to as Godunov-type finite difference methods after the fundamental work of Godunov (1959), the computational domain is discretized and each interface between two adjacent grid-zones is used to construct the initial left and right states of a “local Riemann problem” (see Martí & Müller, 1999; Ibañez & Martí, 1999 for recent reviews). In the present Section we will present the basic features of this procedure.

6.1 Integral Form of Conservation Laws

Conservation laws may be expressed in differential form, as done in Section 2.1, and in integral form. The major advantage of the integral form rests on the fact that the governing equations are naturally derived in terms of integral relations (see LeVeque, 1998). Consider a one-dimensional time dependent system described by the Euler equations. We can define a “control volume” in the $x - t$ plane as $V \equiv [x_1, x_2] \times [t_1, t_2]$. The integral form of the conservative equations (2.4) on this domain can be written as

$$\frac{d}{dt} \int_{x_1}^{x_2} \mathbf{U}(x, t) = \mathbf{F}(\mathbf{U}(x_1, t)) - \mathbf{F}(\mathbf{U}(x_2, t)) . \quad (2.22)$$

If we now integrate it in time between t_1 and t_2 , with $t_1 < t_2$ we get

$$\int_{x_1}^{x_2} \mathbf{U}(x, t_2) = \int_{x_1}^{x_2} \mathbf{U}(x, t_1) + \int_{t_1}^{t_2} \mathbf{F}(\mathbf{U}(x_1, t)) dt - \int_{t_1}^{t_2} \mathbf{F}(\mathbf{U}(x_2, t)) dt , \quad (2.23)$$

which represents our integral form of the equations. In order to solve them numerically, the spatial domain is discretized into N computing cells $I_i = [x_{i-1/2}, x_{i+1/2}]$ of size $\Delta x = x_{i+1/2} - x_{i-1/2}$, with $i = 1, \dots, N$. In Godunov’s method the evolution from the time t^n to the time $t^{n+1} = t^n + \Delta t$ is obtained by first assuming a *piece-wise* constant distribution of

⁴A special case of this wave pattern is produced when the two rarefaction waves leave a vacuum region behind them.

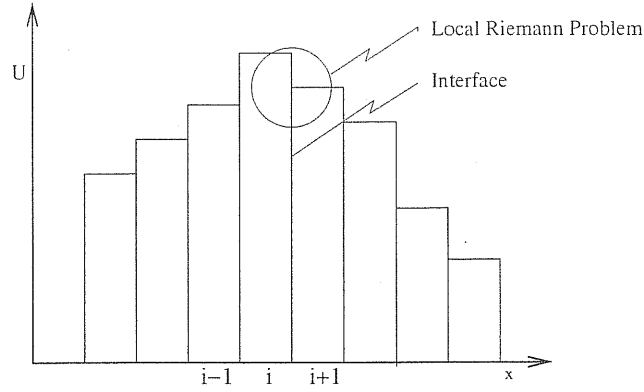


Figure 2.3: Schematic representation of a piece-wise constant distribution of a general quantity U giving rise to a sequence of local Riemann problems at the interface between adjacent cells.

the data over the spatial grid, according to the following averaging (see also Figure 2.3)

$$U_i^n \equiv \frac{1}{\Delta x} \int_{x_{i-1/2}}^{x_{i+1/2}} U(x, t^n) dx. \quad (2.24)$$

Of course, by doing so, part of the knowledge of the original initial data $U(x, t^n)$ inside the cell is lost, and to increase the accuracy a number of reconstruction procedures have been developed (see discussion in Section 8.2). If we now apply the integral conservation form (2.23) to the control volume with $x_1 = x_{i-1/2}$, $x_2 = x_{i+1/2}$, $t_1 = t^n$, $t_2 = t^{n+1}$, we obtain

$$\int_{x_{i-1/2}}^{x_{i+1/2}} U(x, t^{n+1}) dx = \int_{x_{i-1/2}}^{x_{i+1/2}} U(x, t^n) dx + \int_{t^n}^{t^{n+1}} F(U(x_{i-1/2}, t)) dt - \int_{t^n}^{t^{n+1}} F(U(x_{i+1/2}, t)) dt. \quad (2.25)$$

Dividing all terms of (2.25) by Δx and recalling the definition (2.24) we obtain the Godunov scheme as

$$U_i^{n+1} = U_i^n + \frac{\Delta t}{\Delta x} (F_{i-1/2} - F_{i+1/2}), \quad (2.26)$$

where we have defined

$$F_{i\pm 1/2} \equiv \frac{1}{\Delta t} \int_{t^n}^{t^{n+1}} F[U(x_{i\pm 1/2}, t)] dt. \quad (2.27)$$

A relevant comment about the scheme (2.26) is that no approximation has been introduced yet in its derivation. One should in fact distinguish between the mathematical formulation

of the method, which assumes the knowledge of the analytic functions $\mathbf{U}(x, t)$ and $\mathbf{F}(x, t)$, from its numerical application, which requires an interpretation of the terms entering (2.26) before a numerical scheme is effectively built. In particular, the correct interpretation is suggested by the fact that the scheme (2.26) takes into account quantities that are averaged over the grid cells of the numerical grid. From a computational point of view, we can only suppose to be dealing with approximations to these averages (i.e. the piece-wise constant distributed quantities (2.24)), which for simplicity we shall still denote as \mathbf{U}_i^n . Different numerical algorithms can then be devised from (2.26) according to the method used to calculate the fluxes at each interface, $\mathbf{F}_{i-1/2}$ and $\mathbf{F}_{i+1/2}$. If these fluxes are calculated by solving the sequence of local Riemann problems generated at the edges of two adjacent zones (see Figure 2.3) and by adopting as left and right states the same piece wise constant distribution of data given by (2.24), then the resulting method is called *Godunov's first-order upwind method*. Solving the local Riemann problem provides either the term $\mathbf{U}(x_{i\pm 1/2}, t)$ to be used in (2.27), or the $\mathbf{F}[\mathbf{U}(x_{i\pm 1/2}, t)]$ term itself (see Section 7).

Another important remark about the scheme (2.26) is that the time step Δt must satisfy a Courant-Friedrich-Lewy type condition (Courant *et al.* 1928)

$$\Delta t \leq \frac{\Delta x}{|v_{\max}^n|}, \quad (2.28)$$

where v_{\max}^n denotes the maximum wave velocity⁵ present through the computational domain at time t^n .

It should be emphasized that the originality of Godunov's idea consists on the way an upwind method is obtained for a general nonlinear system of equations. Upwind methods, we recall, are characterized by the fact that the spatial differencing is performed using grid points on the side from which information flows. If we think of the advection equation as modelling the advection of a concentration profile in a fluid stream, then this is exactly the upwind direction. For a linear system of equations, upwind methods can only be used if all the eigenvalues of the matrix \mathbf{A} have the same sign. If the eigenvalues have mixed signs, an alternative procedure is often adopted aimed at identifying the direction of propagation of information on the numerical grid. According to this procedure, the flux \mathbf{F} is decomposed in two parts, \mathbf{F}^+ and \mathbf{F}^- , in such a way that the corresponding Jacobian matrices $\mathbf{A}^+ = \partial \mathbf{F}^+ / \partial \mathbf{U}$ and $\mathbf{A}^- = \partial \mathbf{F}^- / \partial \mathbf{U}$ contain just the positive and negative eigenvalues, respectively, of the original matrix \mathbf{A} . The upwind character of the resulting numerical methods, called Flux Vector Splitting methods (FVS), is thus guaranteed. However, for nonlinear systems of equations the matrix of eigenvectors is not constant, and this same approach does not apply directly. Godunov succeeded in obtaining an upwind method in which the local characteristic

⁵Note that in a Riemann problem both shock waves and rarefaction waves are produced, so one has to look for the fastest wave at each time step. In multidimensional problems, when this procedure might become unsuitable, a common alternative is to select v_{\max}^n as $v_{\max}^n = \max(|v_i^n| + a_i^n)$, where v_i^n is the flow velocity and a_i^n is the sound speed.

structure is not provided by diagonalizing the Jacobian matrix, but rather by solving a Riemann problem forward in time. The solutions of Riemann problems, in fact, provide the necessary information about the characteristic structure, and lead to conservative methods, since they are themselves solution of the conservation laws.

Finally, it should be recalled that the Godunov scheme (2.26) with the piece wise constant distribution of the data is just first order accurate in time and space. This can be better appreciated if we apply the scheme (2.26) to the linear advection equation (2.6) with the flux given by $\mathbf{F} = \lambda \mathbf{U}$. In this case, as explained in Section 5.1, the solution of each local Riemann problem at the generic cell interface $x_{i+1/2}$ is given by \mathbf{U}_i^n , if $\lambda < 0$, and by \mathbf{U}_{i+1}^n , if $\lambda > 0$. Therefore, the resulting scheme is given by

$$\mathbf{U}_i^{n+1} = \mathbf{U}_i^n - c(\mathbf{U}_i^n - \mathbf{U}_{i-1}^n), \quad \text{if } \lambda > 0, \quad (2.29)$$

and

$$\mathbf{U}_i^{n+1} = \mathbf{U}_i^n - c(\mathbf{U}_{i+1}^n - \mathbf{U}_i^n), \quad \text{if } \lambda < 0, \quad (2.30)$$

where $c = \lambda \Delta t / \Delta x$ is the *Courant factor*. The schemes (2.29) and (2.30) are nothing but the *first order upwind* method first introduced by Courant *et al.* (1952). The spatial accuracy of the first order Godunov's method presented here can be improved by adopting some kind of reconstruction procedure, as discussed in Section 8.2, while the time accuracy can be increased by combining the method outlined above with a conservative Runge-Kutta scheme (see, for instance, Aloy *et al.*, 1999).

7 Exact and Approximate Riemann Solvers

Godunov's method, and its higher order modifications, require the solution of the Riemann problem at every cell boundary and on each time level. According to the notation of Section 5.2, this amounts to calculating the solution in the regions L_* and R_* , as well as the wave speeds necessary for deriving the complete wave structure of the solution.

The solution of the general Riemann problem cannot be given in a closed analytic form, even for one dimensional Newtonian flows. What can be done is to find the answer numerically to any required accuracy, and in this sense the Riemann problem is said to have been solved *exactly*, even though the actual solution is not analytical. In Newtonian hydrodynamics, the exact solution of the one dimensional Riemann problem was found by Courant & Friedrichs (1948). In special relativistic hydrodynamics the *shock tube problem*, which is basically a particular case of the Riemann problem given by the case (ii) mentioned in Section 5.2, was first considered by K. Thompson (1986), while the general solution of the one dimensional Riemann problem was first obtained by Martí & Müller (1994). Interestingly, it is also possible to take advantage of the local flatness of a curved spacetime in order to exploit this special relativistic Riemann solver in general relativistic hydrodynamics (see Pons *et al.*, 1998).

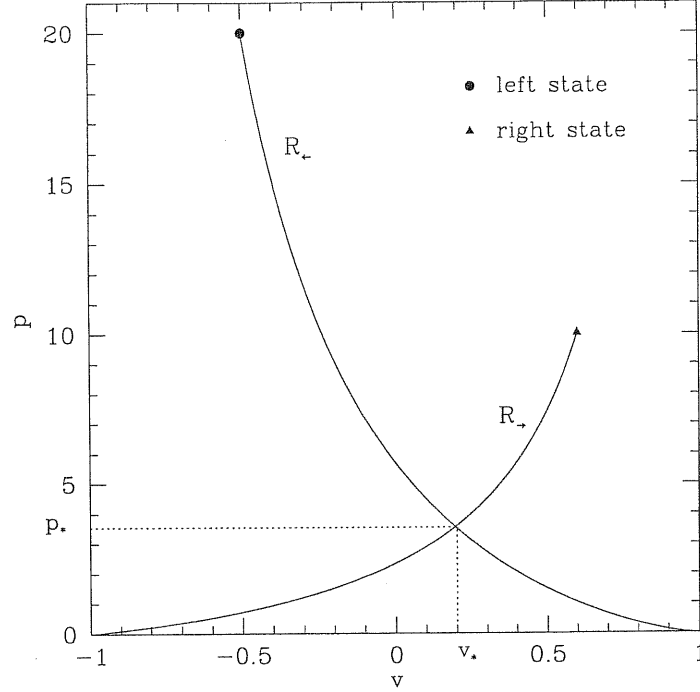


Figure 2.4: Solution of the Riemann problem in the (v, p) plane with initial conditions given by $p_L = 20$, $\rho_L = 10$, $v_L = -0.5$, $p_R = 10$, $\rho_R = 1$, $v_R = 0.6$ for an polytropic gas with adiabatic index $\gamma = 5/3$. The solution for this set of initial conditions consists of two rarefaction waves, propagating towards the left, \mathcal{R}_{\leftarrow} , and towards the right, $\mathcal{R}_{\rightarrow}$. The intersection of the two curves identifies the pressure and velocity in the unknown region.

Since in Chapter 3 we will propose a new idea for the exact solution of the Riemann problem in special relativistic hydrodynamics, we will briefly concentrate here on the procedure adopted by Martí & Müller (1994), so as to make the comparison more apparent later on.

7.1 Exact Riemann Solver in Special Relativistic Hydrodynamics

The fundamental physical principle exploited in the exact solution of the Riemann problem, both in Newtonian and in special relativistic hydrodynamics, is the continuity of pressure and velocity across the contact discontinuity separating the two regions L_* and R_* . The velocity $v_{L_*} = v_{R_*}$ in the unknown region is then written as a function of the pressure $p_{L_*} = p_{R_*}$ in the same region. This is done by connecting the unknown state forming between the two nonlinear waves to the initial left and right states. The connection is done separately for the wave propagating to the left and to the right and it is obtained by exploiting the condition of self similar flow if the propagating wave is a rarefaction wave, and the Rankine-Hugoniot relations across shocks if the propagating wave is a shock wave. The numerical solution of the Riemann problem consists then of finding the root $p_* = p_{L_*} = p_{R_*}$ of the nonlinear equation

$$v_{L_*}(p_*) - v_{R_*}(p_*) = 0, \quad (2.31)$$

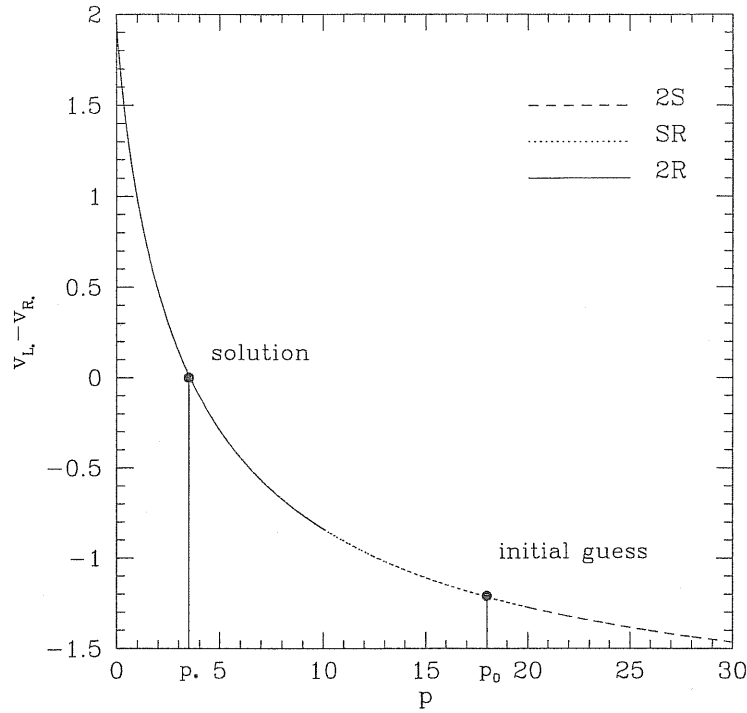


Figure 2.5: $v_{L*}(p_*) - v_{R*}(p_*)$ as a function of the pressure. The curve is given by the smooth joining of three different branches, corresponding to the three possible wave patterns. Here $2S$, SR and $2R$ indicate a two shock, a shock-rarefaction and a two rarefaction wave-pattern, respectively. The initial conditions are the same as those in Fig 2.4 and the unknown pressure p_* falls in the branch corresponding to two rarefaction waves propagating in both directions. The smoothness of the function guarantees the convergence to the correct p_* even if the initial guess p_0 belongs to the wrong branch.

which is obtained numerically by an iterative root finding procedure. Figure 2.4 shows the solution of (2.31) in the (v, p) plane for a particular set of initial conditions. In the figure the two initial states have been denoted with filled dots of different shape, and they are connected to the unknown state through rarefaction waves propagating to the left and to the right. The intersection of the two curves identifies the solution of the Riemann problem in this particular case. For general initial conditions such as those appearing in the local Riemann problems of a numerical code, the nature of the waves connecting the initial states to the unknown state is not known a priori, and the resulting wave pattern is discovered only at the end of the solution procedure. Once the pressure p_* has been computed, in fact, we can deduce the nature of the nonlinear waves produced by performing the following simple check

$$\begin{aligned}
 (i) \quad & p_* > \max(p_L, p_R) : \quad LS_{\leftarrow} L_* CR_* S_{\rightarrow} R, \\
 (ii) \quad & \min(p_L, p_R) < p_* < \max(p_L, p_R) : \quad LR_{\leftarrow} L_* CR_* S_{\rightarrow} R, \\
 (iii) \quad & p_* < \min(p_L, p_R) : \quad LR_{\leftarrow} L_* CR_* R_{\rightarrow} R.
 \end{aligned} \tag{2.32}$$

Note that the solution of the Riemann problem may consists of a single wave, and this corresponds to the case when $p_* = p_L$, or $p_* = p_R$. The reason why it is possible to solve

(2.31) without knowing what is the analytic form of $v_{L*}(p_*)$ and $v_{R*}(p_*)$ (i.e. not knowing the wave pattern that will be produced) is clear by looking at Figure 2.5, where we have plotted $v_{L*}(p_*) - v_{R*}(p_*)$ as a function of the unknown pressure p_* . This function, whose root will provide us with the solution, is given by the continuous joining of three branches, corresponding to the three possible wave patterns. Remarkably, it can be shown that it is a function of class C^1 . Therefore, even if we start from an initial guess p_0 , corresponding to the filled dot in Figure 2.5, which belongs to the wrong branch, i.e. assuming a wrong wave pattern, a standard root finding algorithm will converge to the correct solution p_* thanks to the smoothness of the function $v_{L*}(p_*) - v_{R*}(p_*)$. This is the way in which this exact Riemann solver is usually implemented in a numerical code. In the next Chapter we will propose an alternative approach.

7.2 Approximate Riemann Solvers

The exact solution of the Riemann problem is available in both Newtonian and relativistic hydrodynamics, but, due to its high computational cost, a large number of *approximate Riemann Solvers* have been proposed that are computationally less expensive and yet give results that are equally satisfactory.

Approximate Riemann solvers can be divided in *approximate State* Riemann Solvers, where an approximation is given to the state $\mathbf{U}(x_{i\pm 1/2}, t)$ which is then used to evaluate the corresponding flux by (2.27), and in *approximate Flux* Riemann Solvers, where an approximation is given to the flux directly, thus avoiding the computation of the state $\mathbf{U}(x_{i\pm 1/2}, t)$ at each zone edge. For this reason, approximate State Riemann Solvers, such as the Marquina method discussed below, are not strictly considered as Riemann solvers, and are referred to as *flux formulae*. In the following we will briefly summarize some of the most important Riemann solvers used in computational hydrodynamics, focusing just on the main ideas on which they are based.

7.3 Approximate State Riemann Solvers

“Two-Rarefaction” Riemann Solver

Finding the wave pattern in a Riemann problem is part of the solution procedure, but if one assumes a priori that both nonlinear waves are rarefactions, then the solution can be obtained analytically (see Toro (1997) for the Newtonian case and Appendix C for the relativistic case). The resulting method is very accurate for flow conditions near vacuum, when rarefaction waves give indeed the best approximation to the problem.

“All-Shock” Riemann Solver

In analogy with the previous solver, it is possible to ignore the occurrence of rarefaction waves and assume that both nonlinear waves are shock waves. This represents a good approximation in a wide range of flow conditions, particularly when dealing with more complicated

equations of state than the usual polytropic one (see Colella, 1982). However, this approach is typically inadequate in the case of a transonic rarefaction, yielding a numerical solution which does not satisfy the entropy condition.

7.4 Approximate Flux Riemann Solvers

The HLLE Solver

In the Riemann solver given by Harten, Lax and van Leer (1983) and later improved byinfeldt (1988) the regions L_* and R_* are approximated by a single state bounded by two waves moving in opposite directions

$$\mathbf{U} = \begin{cases} \mathbf{U}_L & \text{if } x/t < \xi_{\min}, \\ \mathbf{U}^{HLL} & \text{if } \xi_{\min} < x/t < \xi_{\max}, \\ \mathbf{U}_R & \text{if } x/t > \xi_{\max}, \end{cases}$$

where ξ_{\min} and ξ_{\max} are the smallest and the largest of the signal speeds arising from the solution of the Riemann problem⁶. The resulting numerical flux to be used in the Godunov scheme is given by

$$\mathbf{F}^{HLL} = \frac{\xi_{\max} \mathbf{F}(\mathbf{U}_L) - \xi_{\min} \mathbf{F}(\mathbf{U}_R) + \xi_{\min} \xi_{\max} (\mathbf{U}_R - \mathbf{U}_L)}{\xi_{\max} - \xi_{\min}}. \quad (2.33)$$

This Riemann solver, which is very simple in its original form, performs well at critical sonic rarefactions but produces excessive smearing at contact discontinuities due to the fact that middle waves are ignored in the solution. Furthermore, it needs to be implemented with an algorithm for the calculation of the wave speeds ξ_{\min} and ξ_{\max} .

The Roe Solver

The idea behind Roe's Riemann solver (Roe, 1981) is to determine an approximate solution by solving a constant coefficient linear system, instead of the original nonlinear one, after which the solution of the Riemann problem can be obtained⁷ exploiting the properties of linear systems, as illustrated in Section 4. The Jacobian matrix \mathbf{A} is replaced by a constant coefficient matrix $\tilde{\mathbf{A}}(\mathbf{U}_L, \mathbf{U}_R)$ so as to satisfy the following conditions

1. $\tilde{\mathbf{A}}$ is still diagonalizable with real eigenvalues
2. $\tilde{\mathbf{A}}(\mathbf{U}_L, \mathbf{U}_R) \cdot (\mathbf{U}_R - \mathbf{U}_L) = \mathbf{F}(\mathbf{U}_R) - \mathbf{F}(\mathbf{U}_L)$
3. $\tilde{\mathbf{A}}(\mathbf{U}, \mathbf{U}) = \mathbf{A}(\mathbf{U})$

⁶The simplest choice is to take the smallest and the largest among the eigenvalues of the Jacobian matrix $\partial \mathbf{F} / \partial \mathbf{U}$ evaluated at some intermediate state.

⁷In this sense Roe's Riemann solver can also be considered an Approximate State Riemann solver, as long as it allows the computation of the state vector \mathbf{U} .

Condition (1) guarantees that the modified system is still hyperbolic and solvable. Condition (2) is required for the special case in which the initial states are connected by a single shock wave or a contact discontinuity. In this case, in fact, the Rankine Hugoniot condition must be satisfied

$$\mathbf{F}(\mathbf{U}_R) - \mathbf{F}(\mathbf{U}_L) = s(\mathbf{U}_R - \mathbf{U}_L) \quad (2.34)$$

with s being the velocity of propagation of the discontinuity. In these circumstances, condition (2) guarantees that $(\mathbf{U}_R - \mathbf{U}_L)$ is an eigenvector of $\tilde{\mathbf{A}}$ with eigenvalue s , and so also the approximate solution consists of a single jump. Finally, condition (3) ensures consistency with the conservation laws. The Roe flux at each zone edge is then calculated as

$$\mathbf{F}_{i+1/2}^{\text{Roe}} = \frac{1}{2} \left[\mathbf{F}(\mathbf{U}_L) + \mathbf{F}(\mathbf{U}_R) - \sum_{i=1}^m \tilde{\omega}_i \tilde{\lambda}_i \tilde{\mathbf{K}}^{(i)} \right], \quad (2.35)$$

where $\tilde{\mathbf{K}}^{(i)}$ and $\tilde{\lambda}_i$ are the right eigenvectors and the eigenvalues of the approximating matrix $\tilde{\mathbf{A}}$, respectively. The quantities $\tilde{\omega}_i$ represent the jumps of the characteristic variables across each characteristic field and are obtained from

$$\mathbf{U}_R - \mathbf{U}_L = \sum_{i=1}^m \tilde{\omega}_i \tilde{\mathbf{K}}^{(i)}. \quad (2.36)$$

In all modern application of Roe's method, however, the computation of the constant matrix $\tilde{\mathbf{A}}$ is avoided, and one seeks to evaluate directly averages of the quantities $\tilde{\mathbf{K}}^{(i)}$, $\tilde{\lambda}_i$ and $\tilde{\omega}_i$. Roe's method has been widely used by the astrophysics community (see Font *et al.* 1994; Eulderink & Mellema 1994, for an application to relativistic jets; Banyuls *et al.* 1997 for simulation of accretion onto compact objects) and, making no assumption on the equation of state, can be adopted in a large variety of different physical conditions.

The Marquina Solver

Marquina's flux formula obtained by Donat & Marquina (1996) aims at removing a fundamental disadvantage of Roe's solver. This is due to the fact that the solution to linear systems like the one considered by Roe's method does not admit rarefaction waves and this can lead to numerical approximations of discontinuities violating the entropy condition. The new flux formula obtained by Donat & Marquina has a flux splitting structure, and leads to an upwind scheme. One first defines the left eigenvector $\mathbf{L}(\mathbf{U}_{L,R})$ and the right eigenvector $\mathbf{R}(\mathbf{U}_{L,R})$ and evaluates the eigenvalues $\lambda(\mathbf{U}_{L,R})$ of the Jacobian matrix $\partial\mathbf{F}/\partial\mathbf{U}$ computed at the left and right states. Then, the characteristic variables and fluxes are calculated as

$$\mathbf{W}_{L,R} = \mathbf{L}(\mathbf{U}_{L,R}) \cdot \mathbf{U}_{L,R}, \quad (2.37)$$

and

$$\phi_{L,R} = \mathbf{L}(\mathbf{U}_{L,R}) \cdot \mathbf{F}(\mathbf{U}_{L,R}), \quad (2.38)$$

respectively. Finally, one chooses the correct sided characteristic flux if the eigenvalues $\lambda_i(\mathbf{U}_L)$ and $\lambda_i(\mathbf{U}_R)$ have the same sign, and switches to the entropy satisfying Lax-Friedrichs scheme⁸ if they change sign. The resulting Marquina's flux formula is ultimately given by

$$\mathbf{F}_{i+1/2}^m = \sum_{i=1}^m [\phi_+^i \mathbf{R}^i(\mathbf{U}_L) + \phi_-^i \mathbf{R}^i(\mathbf{U}_R)], \quad (2.39)$$

where the choice on the fluxes ϕ_\pm^i depends on the criterion specified above (see Donat & Marquina 1996 for the details). This formula is often used together with Runge-Kutta time stepping and with cell reconstruction procedures (see Section 8.2) in order to achieve higher order accuracy both in time and in space. It has been successfully adopted in many astrophysical contexts, including simulation of relativistic jets (Martí *et al.*, 1995; Martí *et al.*, 1997), long-term dynamics of relativistic stars (Font *et al.*, 2002), simulation of the runaway instability in thick discs (Font & Daigne, 2002), etc.

In the dynamical simulations presented in Chapter 5 of this Thesis we have adopted Marquina's flux formula.

8 High Resolution Shock Capturing Methods

A large effort has been spent in recent years in developing a numerical method able to satisfy the following requirements

- at least second order accuracy on smooth parts of the solution,
- sharp resolution of discontinuities without large smearing,
- absence of spurious oscillations everywhere in the solution,
- converge to the “true” solution as the grid is refined.

Irrespective of the Riemann solver adopted, the original Godunov method is only first order accurate on smooth solutions and gives poor approximations to shock waves and other discontinuities. However, if we wanted to modify the first order Godunov method in order to obtain a higher order numerical scheme we would encounter a fundamental difficulty. Namely, all higher order linear schemes produce nonphysical oscillations in the vicinity of large gradients. If we define a *monotone* linear scheme of the form $u_i^{n+1} = H(u_{i-l}^n, \dots, u_{i+r}^n)$, where H is a linear operator, as a scheme for which $\partial H / \partial u_k^n \geq 0$ for all k , then only monotone linear schemes do not suffer from oscillations. Unfortunately, as proved by Godunov (1959), monotone schemes are at most first order accurate. As a result, higher order linear

⁸The first order Lax-Friedrichs scheme can be written as $u_i^{n+1} = \frac{1}{2}(1+c)u_{i-1}^n + \frac{1}{2}(1-c)u_{i+1}^n$, c being the Courant factor.

schemes and absence of oscillations are two incompatible requirements, forcing the use of nonlinear numerical methods. To summarize: HRSC methods result from the combination of Godunov type methods, which take advantage of the conservation form of the equations, and of numerical techniques aimed at obtaining second order (or higher) accuracy in smooth parts of the solution without producing oscillations.

8.1 Total Variation Diminishing Methods

The concept of spurious oscillations in the solution can be made more quantitative by the notion of the *total variation* of the solution. The total variation of a grid function Q at time level t^n is defined as

$$TV(Q^n) \equiv \sum_{i=-\infty}^{+\infty} |Q_i^n - Q_{i-1}^n|, \quad (2.40)$$

and is used to “measure” the oscillations appearing in a numerical solution. The requirement to have a scheme that is both second (or higher) order accurate and does not produce spurious oscillations is that the total variation should not be increasing in time, so that the total variation at any time is uniformly bounded by the total variation of the initial data. In other words, a numerical method is said to be *total variation diminishing* (TVD) if, for any set of data Q^n , the values Q^{n+1} computed by the method satisfy

$$TV(Q^{n+1}) \leq TV(Q^n). \quad (2.41)$$

TVD schemes are intimately linked to the more traditional Artificial Viscosity methods (see Richtmyer & Morton, 1967), where viscous terms were introduced explicitly in the scheme in order to eliminate or at least control the appearance of the oscillations. In modern TVD methods, on the contrary, artificial viscosity is inherent to the scheme itself in a rather sophisticated way. TVD methods do not generally extend beyond second order accuracy. To construct third (and higher) order methods one must drop condition (2.41) and allow for an increase of the total variation which is proportional to some power of the typical step size. The resulting methods are called Essentially Non-Oscillatory (ENO) (see Toro, 1997).

A large variety of TVD methods have been developed in computational hydrodynamics over the years. Some of them, like the *Flux Limiter Methods* and the *Slope Limiter Methods* are particular types of Approximate Flux Riemann solvers. Some others, like the so called MUSCL method, are based on the idea of producing a better representation of the solution than the simple piece-wise constant provided by (2.24) and paying attention to how the data behaves at the zone edges of each cell. Since this second approach is the one that we also adopted in the numerical simulations of accretion discs presented in Chapter 5, we will briefly present it in the following section, while addressing the reader to the books of LeVeque (1998) and Toro (1997) for a complete description of the flux limiter and slope limiter methods.

8.2 Reconstruction Procedures

Due to the discrete numerical representation, any information about the behavior of the quantities inside the numerical cell is lost. In order to recover in part this information and improve the spatial accuracy of a numerical code based on Riemann solvers, different spatial reconstruction procedures have been developed. The common goal is to interpolate the profiles of the various thermodynamical quantities within each cell, thus providing a better estimate for the calculation of the left and of the right state of the Riemann problem to be solved at the interface between two adjacent cells.

Van Leer (1979) was the first to introduce the idea of modifying the piece-wise constant data (2.24) as a first step in achieving higher order spatial accuracy. This approach has been generically called Monotone Upstream-centered Scheme for Conservation Laws (MUSCL). Since then, many other reconstruction procedures have been developed, such as the piece-wise parabolic method (PPM) of Colella & Woodward (1984), or, more recently, the piece-wise hyperbolic (PHM) method of Marquina (1994), where the interpolation is obtained by using hyperbolae instead of parabolae⁹.

Because of its great popularity, in the following we will quickly present the PPM method, which has been adopted in a variety of numerical codes. An important extension of this method to one dimensional relativistic hydrodynamics can be found in Martí & Müller (1996).

The Piecewise Parabolic Method

Consider the initial averaged values of the general quantity u between $x_{i-1/2}$ and $x_{i+1/2}$ over a general non-uniform spatial grid

$$u_i^n = \frac{1}{\Delta x_i} \int_{x_{i-1/2}}^{x_{i+1/2}} u(x, t^n) dx, \quad (2.42)$$

where $\Delta x_i = x_{i+1/2} - x_{i-1/2}$. The basic idea of the PPM is to build an interpolating parabola $\Phi(\xi)$ inside each zone

$$\Phi(\xi) = a\xi^2 + b\xi + c, \quad (2.43)$$

where $\xi = (x - x_{i-1/2})/\Delta x_i$, $x \in [x_{i-1/2}, x_{i+1/2}]$, satisfying the condition

$$u_i^n = \int_0^1 \Phi(\xi) d\xi. \quad (2.44)$$

An additional constraint is that no new extrema appear in the interpolating function Φ which do not already appear in the u_i^n 's. Since determining a parabola requires the calculation of the three unknown coefficients a, b, c , and one condition for their calculation is obtained

⁹In this method some growth of the total variation is allowed for preventing degeneration to first order accuracy at extreme points (see Osher & Chakravarty, 1984).

from (2.44), we still have the freedom to choose the values $u_{L,i}$ and $u_{R,i}$ of the interpolating parabola at the left and right edge of the i -th numerical cell. The common procedure is to interpolate a value $u_{i+1/2}^n$, i.e. an approximation of the value of u at $x_{i+1/2}$, subject to the constraint that $u_{i+1/2}$ does not fall outside the range between the two adjacent values u_i^n and u_{i+1}^n . This can be achieved by performing a polynomial Lagrangian interpolation on the values of the indefinite integral of u , $U(x) = \int^x u(x', t^n) dx'$, whose value at zone edges is known by definition

$$U(x_{i+1/2}) = \sum_{k \leq i} u_k^n \Delta x_k. \quad (2.45)$$

As a result, the value of u at the edge of the numerical cell can be calculated by differentiating (2.45), and, in case of a uniform spatial grid, this is given by

$$\begin{aligned} u_{i+1/2}^n &= \left. \frac{dU}{dx} \right|_{x_{i+1/2}} \\ &= \frac{7}{12}(u_i^n + u_{i+1}^n) - \frac{1}{12}(u_{i+2}^n + u_{i-1}^n). \end{aligned} \quad (2.46)$$

In the smooth parts of the solution, away from the extrema, $u_{i+1/2}^n = u_{R,i} = u_{L,i+1}$, so that the interpolation function is continuous at $x_{i+1/2}$. The values $u_{R,i}$ and $u_{L,i+1}$ are further modified to guarantee the monotonicity of the function $\Phi(\xi)$ within each numerical cell. It is this step which introduces the discontinuities at the zone edges, thus generating the initial left and right states of the local Riemann problem to be solved in the implementation of a Godunov-type method. Monotonicity is an essential requirement for these interpolating algorithms, since it avoids the production of spurious oscillations typical of higher order schemes (Ibañez & Martí, 1999).

Further technical details regarding the monotonicity part of the algorithm and the way in which spurious postshock oscillations can be avoided near strong shocks can be found in Martí & Müller (1996).

9 The Conservation Form of the Relativistic Hydrodynamics Equations

Considerable progress in the application of HRSC methods to relativistic hydrodynamics was achieved in 1991 (Martí *et al.*, 1991), when the relativistic Euler equations were recast as a hyperbolic system of conservation laws. In particular, the Jacobian matrix of the system was obtained explicitly in terms of suitable *conserved variables*. As a result, this formulation allows the spectral decomposition of the system and, therefore, the application of all of those Godunov type methods involving approximate Riemann solvers where this information is

required.

It is very interesting to consider this procedure in the general case of a curved background space-time. In this case (see Banyuls *et al.*, 1997), the local conservation of baryon number and of energy momentum can be written as

$$\nabla \cdot \mathbf{J} = 0 \quad (2.47)$$

and

$$\nabla \cdot \mathbf{T} = 0, \quad (2.48)$$

respectively, where $\nabla \cdot$ stands for the covariant derivative. If $\{\partial_t, \partial_i\}$ define the basis vectors “adapted” to the coordinates, the *current of rest-mass*, \mathbf{J} , and the *energy-momentum tensor*, \mathbf{T} , for a perfect fluid of four-velocity u^μ can be written as

$$J^\mu = \rho u^\mu, \quad (2.49)$$

and

$$T^{\mu\nu} = \rho h u^\mu u^\nu + p g^{\mu\nu}, \quad (2.50)$$

respectively, where ρ is the rest-mass density, p the pressure, h the specific enthalpy, and $g_{\mu\nu}$ the metric components. The usual thermodynamic expressions relating e and p to the specific enthalpy h and to the specific internal energy ϵ of the fluid are

$$e = \rho(1 + \epsilon), \quad (2.51)$$

$$h = 1 + \epsilon + \frac{p}{\rho}. \quad (2.52)$$

An equation of state $p = p(\rho, \epsilon)$ closes the system. For computational purposes, it is also very useful to adopt a 3+1 decomposition of the metric¹⁰, according to which the space time is assumed to admit a slicing by hypersurfaces Σ_t ($t = \text{const.}$). The coordinate basis vector ∂_t is therefore decomposed into normal and parallel components relative to the slicing,

$$\partial_t = \alpha \mathbf{n} + \beta, \quad (2.53)$$

where \mathbf{n} is a unit timelike vector field normal to the hypersurface Σ_t ($\mathbf{n} \cdot \partial_i = 0$), whereas the vector $\beta = \beta^i \partial_i$, called the *shift*, is tangent to it. The function α , called the *lapse*, measures how time is advancing between different slices. In this representation, the metric can be rewritten as

$$ds^2 = -(\alpha^2 - \beta_i \beta^i) dt^2 + 2\beta_i dx^i dt + \gamma_{ij} dx^i dx^j. \quad (2.54)$$

The advantage of this representation is that all measurements can be referred to an Eulerian observer \mathbf{n} at rest in the slice Σ_t . For instance, the components of the three velocity of the

¹⁰The idea was originally due to Arnowitt, Deser & Misner, 1962.

fluid measured by \mathbf{n} are given by

$$v^i = \frac{u^i}{\alpha u^t} + \frac{\beta^i}{\alpha}, \quad (2.55)$$

where $W \equiv -(\mathbf{u} \cdot \mathbf{n}) = \alpha u^t$ is the Lorentz factor, satisfying $W = (1 - v^2)^{-1/2}$, with $v^2 = \gamma_{ij}v^iv^j$. The next step is to introduce suitable “*conserved*” variables allowing for a conservative formulation of the general relativistic hydrodynamic equations. These are not the ordinary fluid, or “*primitive*”, variables $\mathbf{w} = (\rho, v_i, \epsilon)$, but rather the quantities $\mathbf{U}(\mathbf{w}) = (D, S_j, \tau)$, with

$$\begin{aligned} D &= \rho W, \\ S_j &= \rho h W^2 v_j, \\ \tau &= \rho h W^2 - p - D. \end{aligned} \quad (2.56)$$

Here D , S_j and E are the rest mass density, the momentum in the j -direction and the total energy density, respectively, as measured by the Eulerian observer. As a result, the fundamental system in quasi-conservation form reads

$$\frac{1}{\sqrt{-g}} \left(\frac{\partial \sqrt{\gamma} \mathbf{U}(\mathbf{w})}{\partial x^0} + \frac{\partial \sqrt{-g} \mathbf{F}^i(\mathbf{w})}{\partial x^i} \right) = \mathbf{s}(\mathbf{w}), \quad (2.57)$$

where $g \equiv \det(g_{\mu\nu})$ and $\sqrt{-g} = \alpha \sqrt{\gamma}$ ($\gamma \equiv \det(\gamma_{ij})$). The fluxes $\mathbf{F}^i(\mathbf{w})$ and the source terms $\mathbf{s}(\mathbf{w})$ in (2.57) take the explicit form

$$\mathbf{F}^i(\mathbf{w}) = \left(D \left(v^i - \frac{\beta^i}{\alpha} \right), S_j \left(v^i - \frac{\beta^i}{\alpha} \right) + p \delta_j^i, \tau \left(v^i - \frac{\beta^i}{\alpha} \right) + p v^i \right), \quad (2.58)$$

and

$$\mathbf{s}(\mathbf{w}) = \left(0, T^{\mu\nu} \left(\frac{\partial g_{\nu j}}{\partial x^\mu} - \Gamma_{\nu\mu}^\delta g_{\delta j} \right), \alpha \left(T^{\mu 0} \frac{\partial \ln \alpha}{\partial x^\mu} - T^{\mu\nu} \Gamma_{\nu\mu}^0 \right) \right), \quad (2.59)$$

respectively, where the $\Gamma_{\beta}^{\mu\nu}$'s are the Christoffel symbols of the given metric. Note that the presence of the source terms $\mathbf{s}(\mathbf{w})$ does not prevent the application of conservative methods, since the sources do not include gradients of the conserved variables and are just related to the curvature of the metric. In case of a Minkowski spacetime equations (2.57) assume a strict conservation form (see Font *et al.* 1994 for a specific analysis of the flat spacetime).

9.1 Eigenstructure of the Equations

As we have shown in the previous Sections, the characteristic decomposition of the Jacobian matrix of a nonlinear system such as (2.57) is a key ingredient in the construction of a Godunov type numerical method using Riemann solvers. The source terms due to gravity

in (2.57) do not represent a problem from a computational point of view as long as they do not contain any differential operator acting on the conserved quantities, a fact which would break the hyperbolic nature of the system.

There are three 5×5 Jacobian matrices \mathbf{A}^i associated with system (2.57), one for each spatial dimension. They are defined as

$$\mathbf{A}^i = \alpha \frac{\partial \mathbf{F}^i}{\partial \mathbf{U}}, \quad i = 1, 2, 3. \quad (2.60)$$

The eigenvalues and the right eigenvectors of \mathbf{A}^x , for instance, are given by

$$\lambda_0 = \alpha v^x - \beta^x \quad (2.61)$$

$$\lambda_{\pm} = \frac{\alpha}{1 - v^2 c_s^2} \left\{ v^x (1 - c_s^2) \pm c_s \sqrt{(1 - v^2) [\gamma^{xx} (1 - v^2 c_s^2) - v^x v^x (1 - c_s^2)]} \right\} - \beta^x, \quad (2.62)$$

and

$$\mathbf{r}_{\pm} = \begin{bmatrix} 1 \\ hW \left(v_x - \frac{v^x - \Lambda_{\pm}^x}{\gamma^{xx} - v^x \Lambda_{\pm}^x} \right) \\ hW v_y \\ hW v_z \\ \frac{hW (\gamma^{xx} - v^x v^x)}{\gamma^{xx} - v^x \Lambda_{\pm}^x} - 1 \end{bmatrix}, \quad \mathbf{r}_{0,1} = \begin{bmatrix} \frac{\mathcal{K}}{hW} \\ v_x \\ v_y \\ v_z \\ 1 - \frac{\mathcal{K}}{hW} \end{bmatrix}$$

$$\mathbf{r}_{0,2} = \begin{bmatrix} W v_y \\ h (\gamma_{xy} + 2W^2 v_x v_y) \\ h (\gamma_{yy} + 2W^2 v_y v_y) \\ h (\gamma_{zy} + 2W^2 v_z v_y) \\ W v_y (2hW - 1) \end{bmatrix}, \quad \mathbf{r}_{0,3} = \begin{bmatrix} W v_z \\ h (\gamma_{xz} + 2W^2 v_x v_z) \\ h (\gamma_{yz} + 2W^2 v_y v_z) \\ h (\gamma_{zz} + 2W^2 v_z v_z) \\ W v_z (2hW - 1) \end{bmatrix}$$

respectively, where $\Lambda_{\pm}^i \equiv \tilde{\lambda}_{\pm} + \tilde{\beta}^i$ and $\tilde{\lambda} \equiv \lambda/\alpha$. The eigenvectors \mathbf{r}_{\pm} are associated with the eigenvalues λ_{\pm} defining the acoustic waves of the system, while the remaining eigenvectors are associated with the triple degenerate eigenvalue λ_0 , which defines the material waves.

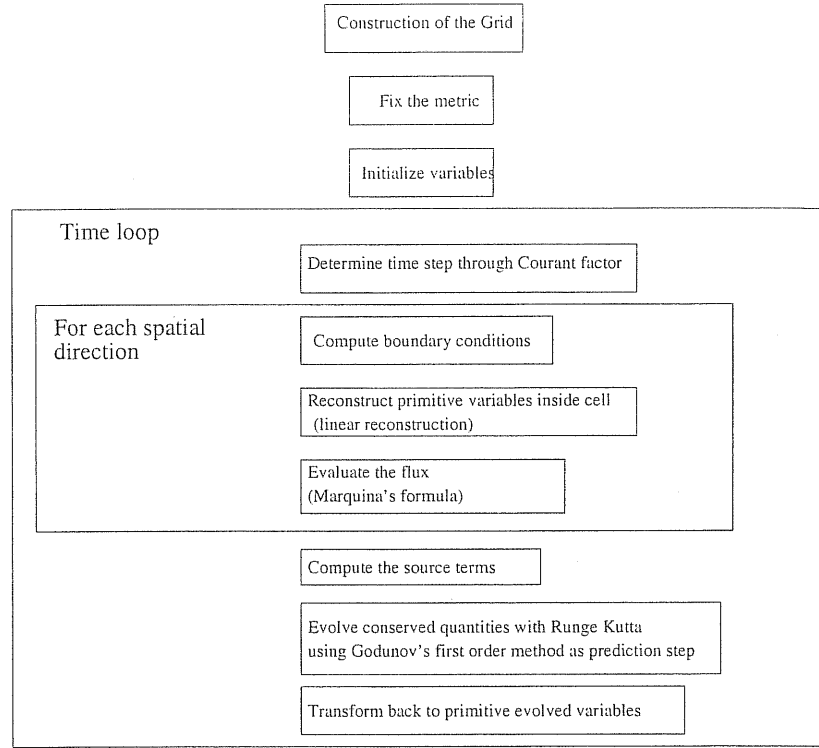


Figure 2.6: Flow chart of the hydrodynamical code used in Chapter 5.

9.2 Structure of a HRSC numerical code

In Chapter 5 a numerical code using HRSC methods and originally developed by Font & Ibañez (1998), has been implemented for the study of quasi-periodic accretion and gravitational wave emission from accretion discs around Schwarzschild black holes. We conclude this Chapter on numerical methods by showing in Figure 2.6 the flow chart of the code implemented there. Note that the expressions (2.56) relating the conserved variables to the primitive ones cannot be inverted analytically. This means that at each time step an iterative method is needed for recovering the primitive variables pressure, density and velocity. This represents a rather time consuming procedure, and particular attention is needed for its optimization. For an ideal gas equation of state $p = \rho\epsilon(\gamma - 1)$ the method has been extensively described by Martí *et al.* (1991), Aloy *et al.* (1999). For an adiabatic evolution of an ideal gas obeying a polytropic equation of state $p = \kappa\rho^\gamma$, like the one considered in Chapter 5, the variable τ in (2.56) does not need to be evolved, and the recovering of the physical variables is performed by expressing the norm $S^2 = (\rho h)^2 W^4 v^2$ of S_i as a function

of the Lorentz factor only

$$\begin{aligned}
 S^2 &= \left(\frac{D}{W}\right)^2 \left[1 + \frac{\gamma}{\gamma-1} \kappa \rho^{\gamma-1}\right]^2 W^4 v^2 \\
 &= D^2 \left[1 + \frac{\gamma}{\gamma-1} \kappa \left(\frac{D}{W}\right)^{\gamma-1}\right]^2 (W^2 - 1).
 \end{aligned} \tag{2.63}$$

Once the Lorentz factor has been calculated, the other primitive variables are recovered by $\rho = D/W$, $h = 1 + \frac{\gamma}{\gamma-1} \kappa \rho^{\gamma-1}$ and $v_i = S_i / \rho h W^2$.

Chapter 3

A New Exact Riemann Solver in Special Relativistic Hydrodynamics

1 Introduction

The solution of the general Riemann problem in special relativistic hydrodynamics, first obtained by Martí & Müller (1994) after the special case of the shock tube problem had already been solved by Thompson K. (1986), exploits two properties of the Riemann problem. The first one is that both pressure and velocity are continuous across the contact discontinuity, and the second one is that the velocity in the intermediate states forming behind the two non-linear waves can be written explicitly as a function of pressure. Alternatively, the solution of the Riemann problem can be obtained exploiting the relativistic invariant expression for the relative velocity between the unperturbed left and right states. This chapter is devoted to the presentation of this exact Riemann solver which is particularly suitable for implementation in a numerical scheme. After a general introduction, given in Section 2, the new method will be first applied to the case of one dimensional flows in Section 3, and then generalized to flows with nonzero component of the velocity tangentially to the contact discontinuity in Section 4. In Chapter 4 we will show how the new approach is also useful for revealing new physical aspects that have remained hidden for a long time.

2 General Presentation of the Method

In a flat spacetime consider a perfect fluid described by the stress-energy tensor

$$T^{\mu\nu} \equiv (e + p)u^\mu u^\nu + p\eta^{\mu\nu} = \rho h u^\mu u^\nu + p\eta^{\mu\nu} , \quad (3.1)$$

where $\eta^{\mu\nu} = \text{diag}(-1, 1, 1, 1)$ and e , p , ρ , and h are the proper energy density, the isotropic pressure, the proper rest mass density, and the specific enthalpy, respectively. Assume moreover that the fluid obeys a polytropic equation of state

$$p = k(s)\rho^\gamma = (\gamma - 1)\rho\epsilon , \quad (3.2)$$

where ρ is the proper rest mass density, γ is the adiabatic index, and $k(s)$ is the polytropic constant, dependent only on the specific entropy s . For such an equation of state, the relations (2.51) and (2.52) given in Chapter 2 take the form

$$e = \rho(1 + \epsilon) = \rho + \frac{p}{\gamma - 1} , \quad (3.3)$$

$$h = 1 + \epsilon + \frac{p}{\rho} = 1 + \frac{p}{\rho} \left(\frac{\gamma}{\gamma - 1} \right) . \quad (3.4)$$

Further assume the fluid to consist of an initial “left” state (indicated with an index 1) and an initial “right” state (indicated with an index 2), each having prescribed and different values of uniform pressure, rest mass density and velocity. The two discontinuous states are initially separated by a planar surface Σ_0 placed at a constant value of the x coordinate so that the unit space-like 4-vector n_0^μ normal to this surface at $t = 0$ has components $n_0^\mu \equiv (0, 1, 0, 0)^1$. Notice that, in contrast with Newtonian hydrodynamics, in special relativity this surface Σ_0 is of constant time only for the set of inertial frames connected by a boost in the direction normal to the initial discontinuity or by spatial rotations. In a different set of inertial frames, in fact, a hypersurface of constant time consisting of a single initial discontinuity separating two constant states will not exist. Rather, the “initial states” will be more complex and reflect the rich structure of the solution of the Riemann problem.

Because we are in general considering a multidimensional flow, the fluid 4-velocity on either side of the initial discontinuity is allowed to have components in spatial directions orthogonal to n_0^μ , i.e.

$$u^\mu \equiv W(1, v^x, v^y, v^z) , \quad (3.5)$$

where $W^2 = (1 - v^2)^{-1}$ is the square of the Lorentz factor and $v^2 \equiv v^i v_i = (v^x)^2 + (v^y)^2 + (v^z)^2$ is the norm of the 3-velocity. The hydrodynamical properties of the initial left and right states are described by the “state-vectors”

$$\mathbf{Q}_{1,2} = \begin{pmatrix} p \\ \rho \\ v^x \\ v^t \end{pmatrix}_{1,2} ,$$

where we have indicated with $v^t \equiv [(v^y)^2 + (v^z)^2]^{1/2}$ the *tangential* component of the three velocity, satisfying the obvious relativistic constraint that $(v^t)^2 + (v^x)^2 \leq 1$. Hereafter, we will refer to v^x as the *normal* velocity.

The fluid states \mathbf{Q}_1 and \mathbf{Q}_2 represent the initial conditions of a multidimensional “Riemann problem” whose solution consists of determining the flow that develops when the system is allowed to relax² (see Section 5.2 of Chapter 2).

¹More precisely, the unit normal to the hypersurface Σ_0 is defined as the one-form mapping each vector tangent to the surface into zero.

²Note that both the rest mass density and the tangential velocities can be discontinuous across the contact

The new approach that we introduce here focuses on $(v_{12}^x)_0$, the relativistic invariant expression for the relative velocity between the two unperturbed initial states. By construction, this quantity measures the relativistic jump of the fluid velocity normal to the discontinuity surface. The solution of the relativistic Riemann problem is then found after the pressure in the region between the two nonlinear waves, p_* , is calculated as the root of the nonlinear equation

$$v_{12}^x(p_*) - (v_{12}^x)_0 = 0, \quad (3.6)$$

where $v_{12}^x(p_*)$ has a functional form that is *different* for each of the *three* possible wave-patterns that might result from the decay of the initial discontinuity. The key aspect of the new approach is that the wave-pattern produced can be entirely predicted in terms of the initial data $Q_{1,2}$. This represents an important advantage since it allows to deduce in advance which set of equations to use for the solution of the exact Riemann problem and the interval bracketing the root of (3.6).

The validity of the approach discussed here is in the mathematical proof that the function $v_{12}^x = v_{12}^x(p_*)$ is monotonically increasing with p_* and it is composed of three branches corresponding to the three possible wave-patterns (see Fig. 3.1). Furthermore, the three different

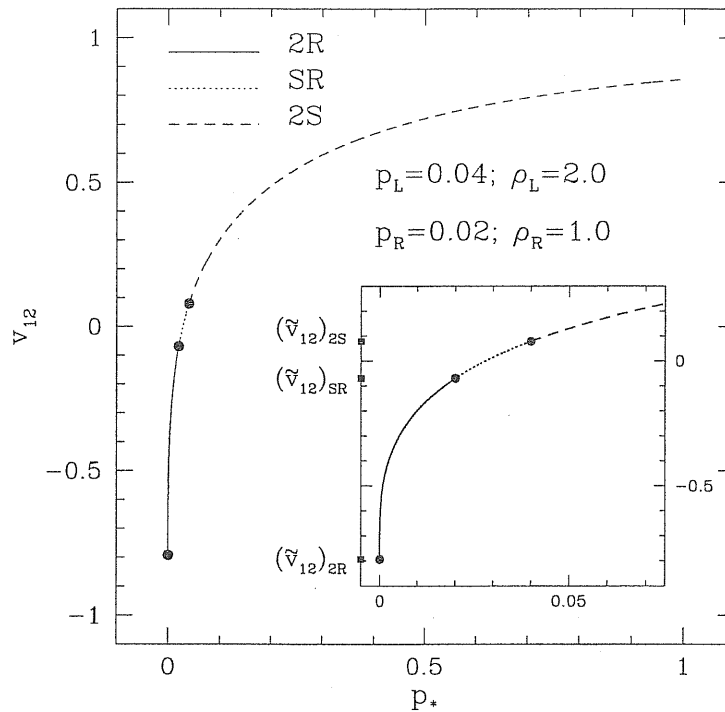


Figure 3.1: Relative velocity between the two initial states 1 and 2 as a function of the pressure at the contact discontinuity in a Riemann problem with zero tangential velocities. Note that the curve shown is given by the continuous joining of three different curves describing the relative velocity corresponding respectively to two shocks (dashed line), one shock and one rarefaction wave (dotted line), and two rarefaction waves (continuous line). The joining of the curves is indicated with filled dots. The small inset on the right shows a magnification for a smaller range of p_* and we have indicated with filled squares the limiting values for the relative velocities $(\tilde{v}_{12})_{2S}$, $(\tilde{v}_{12})_{SR}$, $(\tilde{v}_{12})_{2R}$.

discontinuity \mathcal{C} .

branches always join smoothly through specific values of $v_{12}^x(p_*)$, denoted respectively as³ $(\tilde{v}_{12}^x)_{2S}$, $(\tilde{v}_{12}^x)_{SR}$, $(\tilde{v}_{12}^x)_{2R}$. In view of these properties, it is possible to compare $(v_{12}^x)_0$ with the relevant limiting values $(\tilde{v}_{12}^x)_{2S}$, $(\tilde{v}_{12}^x)_{SR}$, $(\tilde{v}_{12}^x)_{2R}$ constructed from the initial conditions and determine, prior to the solution of equation (3.6), both the wave-pattern that will be produced and the functional form of $v_{12}^x(p_*)$ to be used. Before entering the details of our analysis, however, it is worth showing how relative velocities can be calculated in different reference frames.

2.1 Limiting Relative Velocities

The expression for the relative normal-velocity between the two initial states of the Riemann problem represents the building block in our approach and, to simplify our notation, hereafter we will refer to the different flow regions using the following mapping

$$LW_{\leftarrow} L_* CR_* W_{\rightarrow} R \quad \Longleftrightarrow \quad 1 \mathcal{W}_{\leftarrow} 3 \mathcal{C} 3' \mathcal{W}_{\rightarrow} 2, \quad (3.7)$$

so that, for instance, $p_* = p_3 = p_{3'}$.

While the values of v_{12}^x are relativistic invariants under a Lorentz boost in the x -direction, there exists a reference frame which is better suited to evaluate this quantity. In the reference frame of the contact discontinuity, in fact, the normal velocities behind the nonlinear waves are, by definition, zero (i.e. $v_{3,C}^x = 0 = v_{3',C}^x$) and the relative velocities across the nonlinear waves measured in this reference frame will be

$$(v_{13}^x)_{,C} \equiv \frac{v_{1,C}^x - v_{3,C}^x}{1 - (v_{1,C}^x)(v_{3,C}^x)} = v_{1,C}^x, \quad (3.8)$$

$$(v_{23'}^x)_{,C} \equiv \frac{v_{2,C}^x - v_{3',C}^x}{1 - (v_{2,C}^x)(v_{3',C}^x)} = v_{2,C}^x. \quad (3.9)$$

Because of their invariance, the normal velocity jumps across the nonlinear waves measured in the Eulerian frame can be expressed as

$$(v_{13}^x) = \frac{v_1^x - v_3^x}{1 - v_1^x v_3^x} = (v_{13}^x)_{,C} = v_{1,C}^x, \quad (3.10)$$

$$(v_{23'}^x) = \frac{v_2^x - v_{3'}^x}{1 - v_2^x v_{3'}^x} = (v_{23'}^x)_{,C} = v_{2,C}^x. \quad (3.11)$$

As a result, the relative normal-velocity between the two initial states can be written as

$$v_{12}^x = (v_{12}^x)_{,C} = \frac{v_{1,C}^x - v_{2,C}^x}{1 - (v_{1,C}^x)(v_{2,C}^x)}. \quad (3.12)$$

³Here $2S$, SR and $2R$ indicate a two shock, a shock-rarefaction and a two rarefaction wave-pattern, respectively.

As mentioned before, the basic operation in our approach consists of calculating the relative normal-velocity across the two initial states and comparing it with the limiting relative velocities for each of the three possible wave-patterns. In practice, this amounts to calculating equation (3.12) making use of expressions (3.10) and (3.11). In the following two sections we will apply our procedure to the case when the flow is one-dimensional and multi-dimensional. In doing so we will adopt the convention by which $p_1 > p_2$, with the x -axis normal to the discontinuity surface being positively oriented from 1 to 2.

3 One-dimensional Flows

As a first application of our method we will consider the case when there are no tangential velocities. The solution of the Riemann problem consists of three different wave patterns, each being composed of two nonlinear waves moving in opposite directions and separated by a region where a contact discontinuity is present. In the case of a shock in a one-dimensional flow, the relativistic expression for the relative velocities ahead of (a) and behind (b) the shock can be easily obtained in a reference frame comoving with the shock front, and takes the form (Taub 1978)

$$v_{ab} \equiv \frac{v_a - v_b}{1 - v_a v_b} = \sqrt{\frac{(p_b - p_a)(e_b - e_a)}{(e_a + p_b)(e_b + p_a)}}. \quad (3.13)$$

In the case of a rarefaction wave, on the other hand, it is more convenient to use the Eulerian frame in which the initial states are measured. In such a frame, the flow velocity at the back of a rarefaction wave can be expressed as a function of pressure at the back of the wave as

$$v_b = \frac{(1 + v_a)A_{\pm}(p_b) - (1 - v_a)}{(1 + v_a)A_{\pm}(p_b) + (1 - v_a)}. \quad (3.14)$$

The quantity $A_{\pm}(p)$ in (3.14) is defined as (Martí & Müller 1994)

$$A_{\pm}(p) \equiv \left\{ \left[\frac{(\gamma - 1)^{1/2} - c_s(p)}{(\gamma - 1)^{1/2} + c_s(p)} \right] \left[\frac{(\gamma - 1)^{1/2} + c_s(p_a)}{(\gamma - 1)^{1/2} - c_s(p_a)} \right] \right\}^{\pm 2/(\gamma - 1)^{1/2}}, \quad (3.15)$$

with the \pm signs corresponding to rarefaction waves propagating to the left (\mathcal{R}_{\leftarrow}) and to the right ($\mathcal{R}_{\rightarrow}$) of the contact discontinuity, respectively. The quantity $c_s(p)$ in (3.15) is the local sound speed which, for a polytropic equation of state, can be written as

$$c_s = \sqrt{\frac{\gamma(\gamma - 1)p}{(\gamma - 1)\rho + \gamma p}}. \quad (3.16)$$

We can now use expression (3.14) to write an invariant expression for the relative velocity across a rarefaction wave (i.e. the relative velocity of the fluid ahead of the rarefaction wave

and behind the tail of the rarefaction wave) as

$$v_{ab} = \frac{1 - A_{\pm}(p_b)}{1 + A_{\pm}(p_b)} . \quad (3.17)$$

Equations (3.13) and (3.17) can now be used in (3.10)-(3.11) to obtain $v_{1,C}^x$ and $v_{2,C}^x$, after which the calculation of the relative normal-velocity between the two initial states will be straightforward [cf. eq. (3.12)].

In the following three sub-sections we will apply the procedure outlined above to derive the relative velocity between the left and right states for the three different wave patterns that might be formed in a one-dimensional Riemann problem.

3.1 $1 \mathcal{S}_{\leftarrow} 3 \mathcal{C} 3' \mathcal{S}_{\rightarrow} 2$: Two Shock Waves

We start by considering the wave pattern produced by two shocks propagating in opposite directions (see Fig. 3.2). This situation is characterized by a value of the pressure downstream of the shocks which is larger than the pressures in the unperturbed states, i.e. $p_3 > p_1 > p_2$. By simply applying equation (3.13) to the shock front propagating toward the left and evaluating it in the reference frame of the contact discontinuity, we can write the velocity ahead of the left propagating shock as

$$v_{1,C}^x = \sqrt{\frac{(p_3 - p_1)(e_3 - e_1)}{(e_1 + p_3)(e_3 + p_1)}} . \quad (3.18)$$

Similarly, we can apply equation (3.13) to the shock front moving towards the right and evaluate it in the frame comoving with the contact discontinuity to obtain that the velocity ahead of the right propagating shock is

$$v_{2,C}^x = -\sqrt{\frac{(p_3 - p_2)(e_{3'} - e_2)}{(e_2 + p_3)(e_{3'} + p_2)}} . \quad (3.19)$$

Equations (3.18) and (3.19) can now be used to derive the relativistic expression for the relative velocity of the flow ahead of the two shocks $(v_{12}^x)_{2S}$ through (3.12). As proved in Appendix A, the expression for the relative velocity between the unperturbed states is a monotonic function of p_3 for all possible wave patterns. In particular, for the present choice of initial data, this expression is a monotonically increasing function of p_3 . As a result, the value of $(v_{12}^x)_{2S}$ can be used to build a criterion for the occurrence of two shocks propagating in opposite directions. In fact, since p_1 is the smallest value that p_3 can take, two shocks will form if

$$v_{12}^x > (\tilde{v}_{12}^x)_{2S} \equiv \sqrt{\frac{(p_1 - p_2)(\hat{e} - e_2)}{(\hat{e} + p_2)(e_2 + p_1)}} , \quad (3.20)$$

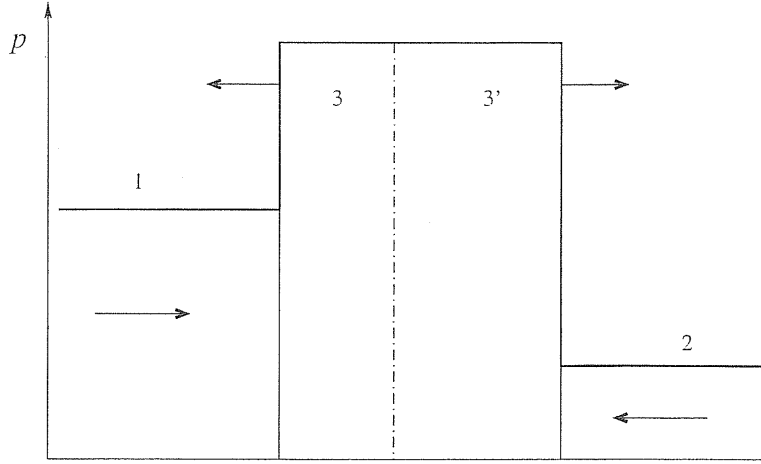


Figure 3.2: Schematic wave pattern in the pressure for the decay of a discontinuity generating two shock waves propagating in opposite directions. The vertical solid lines show the position of the shock fronts while the dot-dashed vertical line shows the position of the contact discontinuity. The different arrows show the gas flow and the directions of propagation of the different fronts.

where

$$\hat{e} = \hat{h}\hat{\rho} - p_1 = \hat{h} \frac{\gamma p_1}{(\gamma - 1)(\hat{h} - 1)} - p_1, \quad (3.21)$$

and \hat{h} is the only positive root of the Taub adiabat (Taub 1978, Martí & Müller 1994)

$$\left[1 + \frac{(\gamma - 1)(p_2 - p_3)}{\gamma p_3} \right] \hat{h}^2 - \frac{(\gamma - 1)(p_2 - p_3)}{\gamma p_3} \hat{h} + \frac{h_2(p_2 - p_3)}{\rho_2} - h_2^2 = 0. \quad (3.22)$$

when $p_3 \rightarrow p_1$. Simple calculations reported in Appendix B show that the Newtonian limit of $(\tilde{v}_{12}^x)_{2S}$ corresponds to the expression derived by Landau and Lifshitz (1987).

3.2 1 \mathcal{R}_{\leftarrow} 3 \mathcal{C} 3' $\mathcal{S}_{\rightarrow}$ 2: One Shock and One Rarefaction Wave

We next consider the wave pattern produced by one shock front propagating towards the right and one rarefaction wave propagating in the opposite direction (see Fig. 3.3). This situation is therefore characterized by $p_1 > p_3 > p_2$.

Evaluating expression (3.17) in the reference frame comoving with the contact discontinuity, we can evaluate the flow velocity ahead of the rarefaction wave to be

$$v_{1,C}^x = \frac{1 - A_+(p_3)}{1 + A_+(p_3)}, \quad (3.23)$$

where

$$A_+(p_3) \equiv \left\{ \left[\frac{(\gamma - 1)^{1/2} - c_s(p_3)}{(\gamma - 1)^{1/2} + c_s(p_3)} \right] \left[\frac{(\gamma - 1)^{1/2} + c_s(p_1)}{(\gamma - 1)^{1/2} - c_s(p_1)} \right] \right\}^{2/(\gamma - 1)^{1/2}}. \quad (3.24)$$

The flow velocity ahead of the shock front can be derived as in Section 3.1 and is given

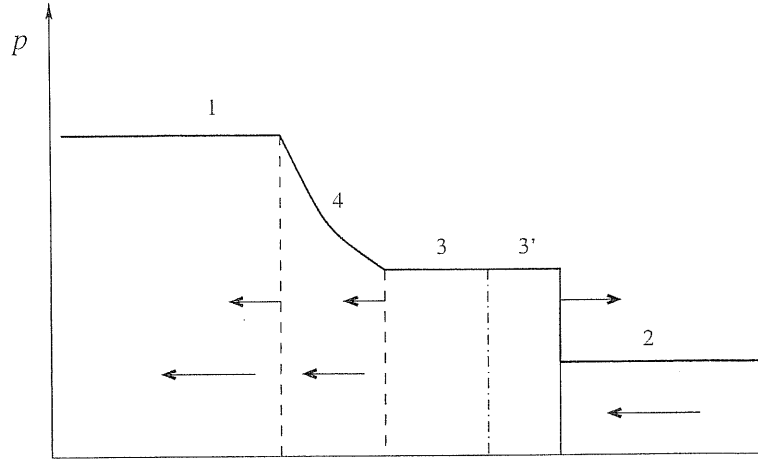


Figure 3.3: Schematic wave pattern in the pressure for the decay of the discontinuity into a shock wave propagating towards the right and a rarefaction wave propagating in the opposite direction. The vertical lines show the discontinuities formed (continuous for the shock front; dashed for the head and the tail of the rarefaction wave; dot-dashed for the contact discontinuity) while the arrows show their direction of propagation and that of the gas flow.

by equation (3.19). When combined with expression (3.23), it can be used to derive the relativistic expression for the relative velocity of the fluids ahead of the shock and ahead of the rarefaction wave $(v_{12}^x)_{SR}$. As for $(v_{12}^x)_{2S}$, it can be shown that $(v_{12}^x)_{SR}$ is a monotonically increasing function of p_3 (see Fig. 3.1 and Appendix A for an analytic proof). Exploiting now the knowledge that for this wave pattern the pressure in the region between the two waves must satisfy $p_2 < p_3 < p_1$, we can establish that the criterion on the relative velocity for having one shock and one rarefaction wave is

$$(\tilde{v}_{12}^x)_{SR} = \frac{1 - A_+(p_3)}{1 + A_+(p_3)} \Big|_{p_3=p_2} < v_{12}^x \leq \sqrt{\frac{(p_1 - p_2)(\hat{e} - e_2)}{(e_2 + p_1)(\hat{e} + p_2)}} = (\tilde{v}_{12}^x)_{2S} . \quad (3.25)$$

Note that the upper limit of (3.25) coincides with $(\tilde{v}_{12})_{2S}$, which is the lower limit for the occurrence of 2 shock waves (3.20) and whose Newtonian limit coincides with the equivalent one found by Landau and Lifshitz (1987) (see Appendix B). Note also that in the limit, $p_3 \rightarrow p_2$, regions 1 and 2 are connected by a single rarefaction wave. In this case the sound speed can be computed using $p_3 = p_2$ but with $\rho_3 = \rho_1(p_2/p_1)^{1/\gamma}$. Finally, note that this is the only wave pattern in which v_1 and v_2 have the same sign and it therefore includes the classical *shock-tube problem*, where $v_1 = v_2 = 0$.

3.3 $1 \mathcal{R}_\leftarrow 3 \mathcal{C} 3' \mathcal{R}_\rightarrow 2$: Two Rarefaction Waves

We now consider the wave pattern produced by two rarefaction waves propagating in opposite directions (see Fig. 3.4). This situation is characterized by $p_1 > p_2 > p_3$ and when the waves are sufficiently strong it might lead to a vacuum region ($\rho_3 = 0$) behind the rarefaction waves.

Following again the same procedure discussed in the previous Section, we can determine

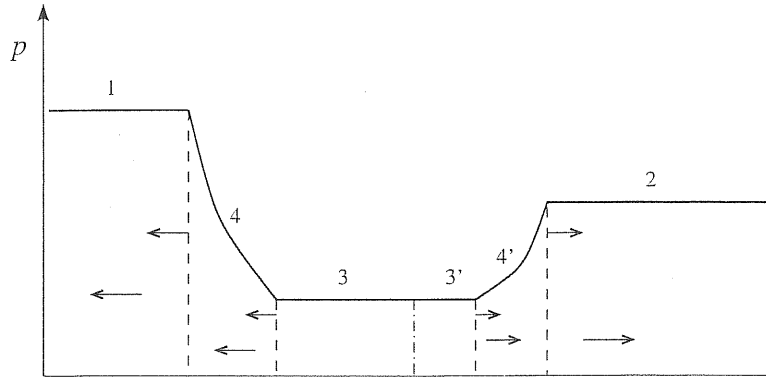


Figure 3.4: Schematic wave pattern in the pressure for the decay of the discontinuity into two rarefaction waves propagating in opposite directions. The vertical lines show the discontinuities formed (dashed for the head and the tail of the rarefaction waves; dot-dashed for the contact discontinuity) while the arrows show their direction of propagation and that of the gas flow. Note that the region downstream of the two rarefaction waves has a density $\rho_3 > 0$.

the values of the fluid velocities ahead of the two rarefaction waves as, respectively,

$$v_{1,C}^x = -\frac{A_+(p_3) - 1}{A_+(p_3) + 1}, \quad (3.26)$$

$$v_{2,C}^x = \frac{1 - A_-(p_{3'})}{1 + A_-(p_{3'})}, \quad (3.27)$$

where

$$A_-(p_{3'}) \equiv \left\{ \left[\frac{(\gamma - 1)^{1/2} - c_s(p_{3'})}{(\gamma - 1)^{1/2} + c_s(p_{3'})} \right] \left[\frac{(\gamma - 1)^{1/2} + c_s(p_2)}{(\gamma - 1)^{1/2} - c_s(p_2)} \right] \right\}^{-2/(\gamma - 1)^{1/2}}. \quad (3.28)$$

We have indicated with $c_s(p_{3'})$ the sound speed in the region $3'$, which differs from the one in region 3 because of the jump in the densities ρ_3 and $\rho_{3'}$. The relative velocity built using (3.26) and (3.27) is then

$$(v_{12}^x)_{2R} = -\frac{A_+(p_3) - A_-(p_{3'})}{A_+(p_3) + A_-(p_{3'})}. \quad (3.29)$$

As for the relative velocities of the previous wave patterns, it can be shown that $(v_{12})_{2R}$, is a monotonically increasing function of p_3 (see Fig. 3.1 and Appendix A for an analytic proof) so that the criterion for the occurrence of two rarefaction waves can be expressed as

$$(v_{12}^x)_{2R}|_{p_3=0} < v_{12}^x \leq (v_{12}^x)_{2R}|_{p_3=p_2} = (\tilde{v}_{12}^x)_{SR}, \quad (3.30)$$

where $A_-(p_3 = p_2) = 1$ and therefore the upper limit for (3.30) coincides with the lower limit for (3.25).

The condition (3.30) can also be expressed in a more useful form as

$$-\frac{S_1 - S_2}{S_1 + S_2} < v_{12}^x \leq -\frac{1 - A_+(p_2)}{1 + A_+(p_2)}, \quad (3.31)$$

where, the constants S_1 and S_2 are shorthand for

$$S_1 \equiv \left[\frac{(\gamma - 1)^{1/2} + c_s(p_1)}{(\gamma - 1)^{1/2} - c_s(p_1)} \right]^{2/(\gamma-1)^{1/2}} \quad (3.32)$$

$$S_2 \equiv \left[\frac{(\gamma - 1)^{1/2} + c_s(p_2)}{(\gamma - 1)^{1/2} - c_s(p_2)} \right]^{-2/(\gamma-1)^{1/2}} \quad (3.33)$$

An important property of equation (3.29) is that it can be inverted analytically. This involves rewriting it in terms of a quartic equation in the unknown sound speed in the region L_* (see Appendix C for the explicit form of the equation). Once the relevant real root of this equation has been calculated analytically, the value of the pressure p_* can be found through a simple algebraic expression. In this case, therefore, the solution of the exact relativistic Riemann problem can be found in an analytic closed form.

We conclude the analysis of the different wave patterns with a comment on the case of two rarefaction waves propagating in opposite directions and leaving behind them a region with zero density and pressure. This situation occurs when the fluids in the regions 1 and 2 are moving sufficiently fast in opposite directions. This is the case whenever the relative velocity between the two states ahead of the rarefaction waves is less than or equal to the lower limit for $(v_{12}^x)_{2R}$, i.e.

$$v_{12}^x \leq (\tilde{v}_{12}^x)_{2R} \equiv -\frac{S_1 - S_2}{S_1 + S_2}. \quad (3.34)$$

Also in this case, taking the Newtonian limit of $(\tilde{v}_{12}^x)_{2R}$ we obtain the corresponding expression derived by Landau and Lifshitz (1987) (see Appendix B). Finally, note that when a vacuum is produced, v_{12}^x is no longer dependent on p_3 and this branch of the curve cannot be plotted in Fig 3.1.

4 Multi-dimensional Flows

The extension of the approach presented in the previous section to the case when tangential velocities are present is straightforward and equation (3.6) applies unmodified. The major changes introduced by the presence of tangential velocities are restricted to the expressions for the limiting values of the relative velocity $(\tilde{v}_{12}^x)_{2S}$, $(\tilde{v}_{12}^x)_{SR}$, $(\tilde{v}_{12}^x)_{2R}$. However, there are two further complications. The first one concerns shock waves, and it rests on the fact that calculating jump conditions in the rest frame of the shock front is now not particularly advantageous. In this case, in fact, the velocity jump across the shock cannot be expressed

as an algebraic relation among the thermodynamic quantities across the shock. Rather, the ratio of the velocities ahead and behind the shock front needs to be found as root of a nonlinear equation. Analytic solutions to this equation can be found only in the *weak-shock* limit or for an ultrarelativistic equation of state (see Koenigl 1980 for a discussion). The practical consequence is that it is not possible to derive a simple expression analogous to equation (3.13). The second complication concerns rarefaction waves, namely that there are not closed form solutions for them if tangential velocities are present. For these reasons, in the following two subsections we will show how shock and rarefaction waves can be handled in the usual Eulerian frame.

4.1 Jumps Across a Shock Wave

Following Pons *et al* (2000), we use the Rankine-Hugoniot conditions in the fixed Eulerian reference frame. In particular, adopting the standard notation in which the difference of a quantity evaluated behind (subscript b) and ahead (subscript a) of the wave is denoted as $[[F]] \equiv F_a - F_b$ (Anile 1989), these conditions can be expressed as

$$[[v^x]] = -\frac{J}{W_s}[[1/D]] , \quad (3.35)$$

$$[[p]] = \frac{J}{W_s}[[S^x/D]] , \quad (3.36)$$

$$[[S^y/D]] = 0 = [[S^z/D]] , \quad (3.37)$$

$$[[v^x p]] = \frac{J}{W_s}[[\tau/D]] . \quad (3.38)$$

In expressions (3.35), (3.36) and (3.38), J represents the mass flux across the shock

$$J \equiv W_s D_a (V_s - v_a^x) = W_s D_b (V_s - v_b^x) , \quad (3.39)$$

and $W_s \equiv (1 - V_s^2)^{-1/2}$ is the Lorentz factor of the shock velocity V_s , with the latter being

$$V_s^\pm = \frac{\rho_a^2 W_a^2 v_a^x \pm |J| \sqrt{J^2 + \rho_a^2 W_a^2 [1 - (v_a^x)^2]}}{\rho_a^2 W_a^2 + J^2} , \quad (3.40)$$

and with the \pm signs referring to a shock wave propagating to the right or to the left, respectively. We can now exploit equations (3.35)–(3.38) to express the normal velocity of the fluid on the back of the shock front in terms of the pressure as

$$v_b^x = \frac{h_a W_a v_a^x + W_s (p_b - p_a)/J}{h_a W_a + (p_b - p_a)[W_s v_a^x/J + 1/(\rho_a W_a)]} . \quad (3.41)$$

Besides giving the jump in the normal velocity across a shock wave, expression (3.41) states that the two regions of the flow across the shock wave are effectively coupled through a Lorentz factor which, we recall, is built also in terms of the tangential velocities. This is a purely relativistic feature and an important difference from Newtonian hydrodynamics, in which the solution of the Riemann problem does not depend on the tangential component of the flow. An important consequence introduced by this coupling will be discussed in detail in Chapter 4. For the moment it is interesting to notice that expression (3.37) implies that the ratio v^y/v^z remains unchanged through shocks, so that the tangential velocity 3-vector does not rotate but can change its norm. This property, which applies also across rarefaction waves, represents a major difference from the behaviour of the tangential 3-velocity vector across Newtonian nonlinear waves, which does not rotate, nor changes its norm: $[[v^y]] = 0 = [[v^z]]$.

The square of the mass flux across the wave can be expressed as

$$J^2 = -\frac{[[p]]}{[[h/\rho]]} , \quad (3.42)$$

where the ratio h/ρ in the shocked region can be calculated through the Taub adiabat (Taub, 1948)

$$[[h^2]] = \left(\frac{h_a}{\rho_a} + \frac{h_b}{\rho_b} \right) [[p]] . \quad (3.43)$$

In a general case, the mass flux can be obtained as a function of just one thermodynamic variable (p_*) after using the EOS and the physical ($h \geq 1$) solution of the nonlinear equation (3.43). In the case of an ideal fluid EOS, like the one considered here, this can be done explicitly because (3.42) and (3.43) take respectively the simple form

$$J^2 = -\frac{\gamma}{\gamma - 1} \frac{[[p]]}{[[h(h - 1)/p]]} , \quad (3.44)$$

and

$$\left[1 + \frac{(\gamma - 1)(p_a - p_b)}{\gamma p_b} \right] h_b^2 - \frac{(\gamma - 1)(p_a - p_b)}{\gamma p_b} h_b + \frac{h_a(p_a - p_b)}{\rho_a} - h_a^2 = 0 . \quad (3.45)$$

4.2 Jumps Across a Rarefaction Wave

When considering a rarefaction wave it is convenient to introduce the self-similar variable $\xi \equiv x/t$ in terms of which similarity solutions to the hydrodynamical equations can be found. An explicit expression for ξ can be obtained by requiring that non-trivial similarity solutions for the rarefaction wave exist. This then yields (see Pons *et al* 2000 for details)

$$\xi = \frac{v^x(1 - c_s^2) \pm c_s \sqrt{(1 - v^2)[1 - v^2 c_s^2 - (v^x)^2(1 - c_s^2)]}}{1 - v^2 c_s^2} , \quad (3.46)$$

where here too the \pm signs correspond to rarefaction waves propagating to right or to the left, respectively. In the case of a perfect fluid, the isentropic character of the flow allows to calculate the velocity on the back of the wave as a solution of an ordinary differential equation

$$\frac{dv^x}{dp} = \frac{1}{\rho h W^2} \frac{(1 - \xi v^x)}{(\xi - v^x)} , \quad (3.47)$$

In principle, to calculate the normal fluid velocity at the tail of the rarefaction wave one should solve the ordinary differential equation (3.47), which might be very expensive numerically. To overcome this, it is convenient to make use of constraints such as those in expressions (??) (which remain valid also across a rarefaction wave) and express equation (3.47) in a different way. Defining $\mathcal{A} \equiv h_a W_a v_a^t = h_b W_b v_b^t$, the tangential velocity along a rarefaction wave can be expressed as

$$(v^t)^2 = \mathcal{A}^2 \left[\frac{1 - (v^x)^2}{h^2 + \mathcal{A}^2} \right] . \quad (3.48)$$

This allows us to eliminate the dependence on v^t from equation (3.46). From the definition of the Lorentz factor and equation (3.48) it is straightforward to obtain

$$W^2 = \frac{h^2 + \mathcal{A}^2}{h^2(1 - (v^x)^2)} , \quad (3.49)$$

and after some algebra one can arrive at

$$\frac{(1 - \xi v^x)}{(\xi - v^x)} = \pm \frac{\sqrt{h^2 + \mathcal{A}^2(1 - c_s^2)}}{h c_s} \quad (3.50)$$

Using this results, equation (3.47) can be written as follows

$$\frac{dv^x}{1 - (v^x)^2} = \pm \frac{\sqrt{h^2 + \mathcal{A}^2(1 - c_s^2)}}{(h^2 + \mathcal{A}^2)} \frac{dp}{\rho c_s} . \quad (3.51)$$

Note that in this way we have isolated the thermodynamical quantities on the right hand side of (3.51) and the kinematical ones on the left hand side, which can then be integrated analytically. For some particular cases (for example when the sound speed is constant), the right hand side too is integrable but for a generic EOS a numerical integration is necessary. The velocity at the tail of the rarefaction wave can then be obtained directly as

$$v_b^x = \tanh \mathcal{B} , \quad (3.52)$$

where

$$\mathcal{B} \equiv \frac{1}{2} \log \left(\frac{1 + v_a^x}{1 - v_a^x} \right) \pm \int_{p_a}^{p^*} \frac{\sqrt{h^2 + \mathcal{A}^2(1 - c_s^2)}}{(h^2 + \mathcal{A}^2)} \frac{dp}{\rho c_s} \quad (3.53)$$

Here, $h = h(p, s)$, $\rho = \rho(p, s)$, and $c_s = c_s(p, s)$, and the isentropic character of rarefaction waves allows to fix $s = s_a$. Despite its complicated look, the integrand is a smooth, monotonic function of p , and a Gaussian quadrature with only 10-20 points has proved to be more accurate and efficient than a third order Runge-Kutta integrator requiring hundreds of function evaluations to solve (3.47).

In the following, analogously to what done for the one-dimensional case, we will apply our procedure to derive the relative velocity between the left and right states for the three different wave patterns that might be formed.

4.3 1 \mathcal{S}_\leftarrow 3 \mathcal{C} 3' \mathcal{S}_\rightarrow 2: Two Shock Waves

We first consider a wave-pattern in which two shock waves propagate in opposite directions. In this case, the general expression for the relative normal-velocities between the two initial states $(v_{12}^x)_{2S}$ can be calculated from (3.12) with the velocities behind the shock waves v_3^x and $v_{3'}^x$ being determined through the jump condition (3.41). Because p_1 is the smallest value that the pressure at the contact discontinuity p_3 can take, the limiting value for the two shock waves branch $(\tilde{v}_{12}^x)_{2S}$ can be expressed as

$$(\tilde{v}_{12}^x)_{2S} = \lim_{p_3 \rightarrow p_1} (v_{12}^x)_{2S} . \quad (3.54)$$

Evaluating the limit (3.54) basically involves calculating the limits of $v_{1,C}^x$ and $v_{2,C}^x$ for p_3 tending to p_1 . Both these limits are straightforward to calculate and are

$$\lim_{p_3 \rightarrow p_1} v_{1,C}^x = 0 , \quad (3.55)$$

$$\lim_{p_3 \rightarrow p_1} v_{2,C}^x = \frac{v_2^x - \bar{v}_{3'}^x}{1 - v_2^x \bar{v}_{3'}^x} , \quad (3.56)$$

where $\bar{v}_{3'}^x$ is simply the value of v_3^x for $p_3 = p_1$, i.e.

$$\bar{v}_{3'}^x \equiv \lim_{p_3 \rightarrow p_1} v_{3'}^x . \quad (3.57)$$

Using now the limits (3.55)–(3.56) and some lengthy but straightforward algebra, the explicit analytic expression for the limiting value of the two shock waves branch can be calculated as

$$(\tilde{v}_{12}^x)_{2S} = - \lim_{p_3 \rightarrow p_1} v_{2,C}^x = \frac{(p_1 - p_2)(1 - v_2^x \bar{V}_s)}{(\bar{V}_s - v_2^x) \{ h_2 \rho_2 (W_2)^2 [1 - (v_2^x)^2] + p_1 - p_2 \}} . \quad (3.58)$$

Here \bar{V}_s is the velocity of the shock wave propagating towards the right in the limit of $p_3 \rightarrow p_1$ and an explicit expression for it can be found in the box below in the case of an ideal fluid. Expression (3.58) will be discussed further in Section 3 but it is sufficient to point out here that the threshold value $(\tilde{v}_{12}^x)_{2S}$ does not depend on the initial velocity in the state 1, v_1^x .

Detail: an explicit expression for \bar{V}_s .

We provide here an explicit expression of the velocity of the shock wave propagating towards the right in the limit of $p_3 \rightarrow p_1$ and when the fluid is ideal. This quantity, which is necessary to calculate the limiting relative velocity $(\tilde{v}_{12}^x)_{2S}$ in equation (3.58), can be easily computed as [cf. eq. (3.40)]

$$\bar{V}_s = \frac{\rho_2^2 W_2^2 v_2^x + |J_{23'}| \sqrt{J_{23'}^2 + \rho_2^2 W_2^2 [1 - (v_2^x)^2]}}{\rho_2^2 W_2^2 + J_{23'}^2}, \quad (3.59)$$

where the mass flux $J_{23'}$ is given by [cf. eq. (3.44)]

$$J_{23'}^2 = - \left(\frac{\gamma}{\gamma - 1} \right) \frac{p_1 - p_2}{h_{3'}(h_{3'} - 1)/p_1 - h_2(h_2 - 1)/p_2}, \quad (3.60)$$

and where, finally, $h_{3'}$ is the positive root of the Taub adiabat (3.45) in the limit of $p_3 \rightarrow p_1$, i.e.

$$h_{3'} = \frac{(\sqrt{\mathcal{D}} - 1)(\gamma - 1)(p_1 - p_2)}{2[(\gamma - 1)p_2 + p_1]}. \quad (3.61)$$

The quantity \mathcal{D} in the root (3.61) is just a shorthand for

$$\mathcal{D} = 1 - 4\gamma p_1 \frac{(\gamma - 1)p_2 + p_1}{(\gamma - 1)^2(p_1 - p_2)^2} \left[\frac{h_2(p_2 - p_1)}{\rho_2} - h_2^2 \right]. \quad (3.62)$$

4.4 $1 \mathcal{R}_{\leftarrow} 3 \mathcal{C} 3' \mathcal{S}_{\rightarrow} 2$: One Shock and One Rarefaction Wave

We next consider the wave-pattern consisting of a rarefaction wave propagating towards the left and of a shock wave propagating towards the right. Also in this case, $(v_{12}^x)_{SR}$ can be calculated from (3.12) with $v_{3'}^x$ being determined through the jump condition (3.41) and v_3^x from the numerical integration of equation (3.47) in the range $[p_1, p_3]$. Because p_2 is now the lowest pressure in the unknown region behind the two nonlinear waves, the limiting value for the one shock and one rarefaction waves branch $(\tilde{v}_{12}^x)_{SR}$ can be expressed as

$$(\tilde{v}_{12}^x)_{SR} = \lim_{p_3 \rightarrow p_2} (v_{12}^x)_{SR}. \quad (3.63)$$

In the limit $p_3 \rightarrow p_2$, the right-propagating shock is suppressed, $v_{3'}^x \rightarrow v_2^x$ so that

$$\lim_{p_3 \rightarrow p_2} v_{2,C}^x = 0, \quad (3.64)$$

and

$$(\tilde{v}_{12}^x)_{SR} = \lim_{p_3 \rightarrow p_2} v_{1,C}^x. \quad (3.65)$$

Defining now

$$\mathcal{B}_1 \equiv \frac{1}{2} \log \left(\frac{1 + v_1^x}{1 - v_1^x} \right), \quad (3.66)$$

and using (3.52), it is readily obtained that

$$(\tilde{v}_{12}^x)_{SR} = \lim_{p_3 \rightarrow p_2} \tanh(\mathcal{B}_1 - \mathcal{B}) = \tanh \left(\int_{p_1}^{p_2} \frac{\sqrt{h^2 + \mathcal{A}_1^2(1 - c_s^2)}}{(h^2 + \mathcal{A}_1^2)\rho c_s} dp \right), \quad (3.67)$$

where the above integral can be evaluated numerically. A better look at the integral shows that only quantities in the left state are involved (through the constant $\mathcal{A}_1 \equiv h_1 W_1 v_1^t$) and that $(\tilde{v}_{12}^x)_{SR}$ does not depend on the initial velocity in the state 2, v_2^x . This property has an important consequence that will be discussed in the following Chapter.

4.5 1 \mathcal{R}_\leftarrow 3 \mathcal{C} 3' \mathcal{R}_\rightarrow 2: Two Rarefaction Waves

When the wave-pattern consists of two rarefaction waves propagating in opposite directions, $(v_{12}^x)_{2R}$ can be calculated from (3.12) with the velocities behind the waves being calculated using (3.52) and (3.53). Since the lowest value of the pressure behind the tails of the rarefaction waves is zero, the limiting value for the two rarefaction waves branch $(\tilde{v}_{12}^x)_{2R}$ is given by

$$(\tilde{v}_{12}^x)_{2R} = \lim_{p_3 \rightarrow 0} (v_{12}^x)_{2R}. \quad (3.68)$$

Proceeding as in previous subsection, we can now express $(\tilde{v}_{12}^x)_{2R}$ as

$$(\tilde{v}_{12}^x)_{2R} = \frac{\bar{v}_{1,C}^x - \bar{v}_{2,C}^x}{1 - (\bar{v}_{1,C}^x)(\bar{v}_{2,C}^x)}, \quad (3.69)$$

where

$$\bar{v}_{1,C}^x = \tanh \left(\int_{p_1}^0 \frac{\sqrt{h^2 + \mathcal{A}_1^2(1 - c_s^2)}}{(h^2 + \mathcal{A}_1^2)\rho c_s} dp \right), \quad (3.70)$$

$$\bar{v}_{2,C}^x = \tanh \left(\int_0^{p_2} \frac{\sqrt{h^2 + \mathcal{A}_2^2(1 - c_s^2)}}{(h^2 + \mathcal{A}_2^2)\rho c_s} dp \right), \quad (3.71)$$

and where $\mathcal{A}_2 \equiv h_2 W_2 v_2^t$. While the determination of $(\tilde{v}_{12}^x)_{2R}$ requires the numerical calculation of the integrals (3.70) and (3.71), it has very little practical importance as it marks the transition to a wave-pattern with two rarefaction waves separated by vacuum; this is a very rare physical configuration which cannot be handled by a generic numerical code.

Note that in computing (3.69), both the left state quantities and the right ones are involved and, as a result, $(\tilde{v}_{12}^x)_{2R}$ will depend on both v_1^x and v_2^x . Fig. 3.5 shows the functional behaviour of $v_{12}^x = v_{12}^x(p_3)$ and how this behaviour is changed by the presence of nonzero tangential velocities. The initial conditions are those of a modified Sod's problem (Sod, 1978) in which $p_1 = 1.0$, $\rho_1 = 1.0$, $v_1^x = 0.0$, $p_2 = 0.1$, $\rho_2 = 0.125$, $v_2^x = 0.0$, and $\gamma = 5/3$.

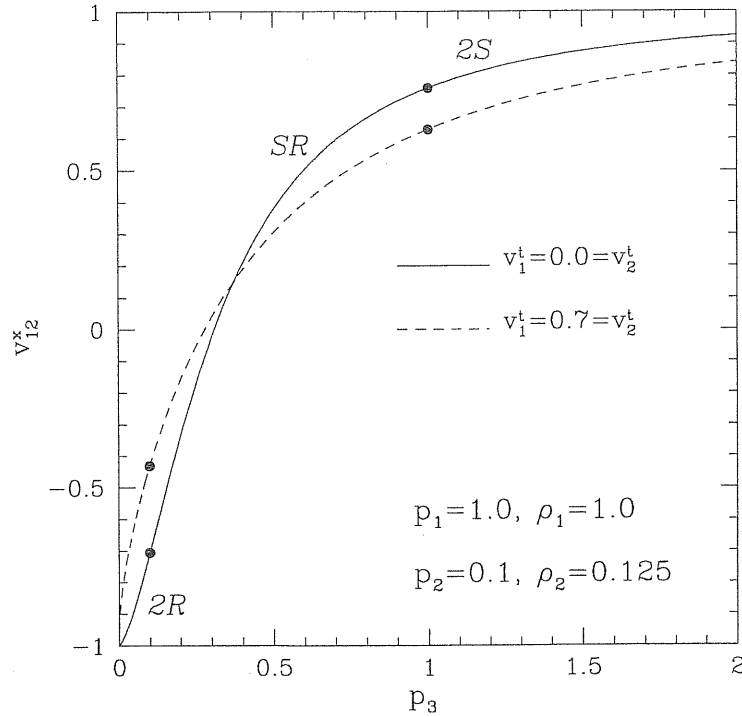


Figure 3.5: Relative normal-velocity between the two initial states as a function of the pressure at the contact discontinuity. Each curves is the continuous joining (marked by the solid dots) of three different curves corresponding respectively to two shock waves (2S), one shock and one rarefaction wave (SR), and two rarefaction waves (2R). The solid line refers to the case of zero tangential velocities, while the dashed line to the case in which $v_1^t = 0.7 = v_2^t$. The initial state vectors are those of Sod's problem.

Each of the two curves shown is effectively the composition of three different ones (joined at the solid dots) corresponding to wave-patterns consisting of two shock waves (2S), one shock and one rarefaction wave (SR), and two rarefaction waves (2R). While the solid curve refers to initial conditions with zero tangential velocities, the dashed one is produced when nonzero tangential velocities, $v_1^t = 0.7 = v_2^t$, are considered. Note that also in this latter case, the three branches are monotonically increasing with p_3 (a fundamental property whose mathematical proof can be found in Appendix A) but are all altered by the presence of nonzero tangential velocities.

5 Numerical Implementation

As shown, the core of an exact Riemann solver, both in Newtonian and relativistic hydrodynamics, is based on the numerical computation of the pressure in the regions L_* and R_* that form behind the waves. The key property exploited when performing the numerical calculation is that the velocity in such regions can be expressed as a monotonic function of the pressure i.e. $v_{L_*}^x = v_{L_*}^x(p_{L_*})$, and $v_{R_*}^x = v_{R_*}^x(p_{R_*})$. Since there is no jump across a contact discontinuity in either the velocity or in the pressure, the numerical solution of the

Riemann problem consists then of finding the root $p_* = p_{L_*} = p_{R_*}$ of the nonlinear equation

$$v_{L_*}^x(p_*) - v_{R_*}^x(p_*) = 0, \quad (3.72)$$

where $v_{L_*}^x, v_{R_*}^x$ have different functional forms according to the different wave patterns produced (see Section 7.1 of Chapter 2). This method has two obvious disadvantages: (1) it cannot determine, using the initial conditions, the wave pattern produced and thus which of the functional forms to use for $v_{L_*}^x, v_{R_*}^x$; (2) it cannot provide a straightforward bracketing interval for the root. In practice, however, these difficulties are effectively balanced by efficient algorithms based on a sequence of trial and error attempts that rapidly bracket the root and determine the correct equation to solve (see, for instance, Martí, & Müller 1999 and the algorithm presented therein).

The exact Riemann solver which we have presented differs from the one discussed above mostly because it avoids the disadvantages (1) and (2). In fact, as shown in the previous Sections, by comparing the relative velocity between the initial left and right states $(v_{12}^x)_0$ with the relevant limiting values constructed from the initial conditions $(\tilde{v}_{12}^x)_{2S}, (\tilde{v}_{12}^x)_{SR}, (\tilde{v}_{12}^x)_{2R}$, we can determine both the wave pattern which will be produced and the correct bracketing range in the pressure. Once this information has been obtained, the Riemann problem can be solved either through the solution of equation (3.72) or, equivalently, by looking for the value of the pressure p_* which would produce a relative velocity $(v_{12}^x)_0$. This latter approach, involves then the solution of the nonlinear equation (3.6), where $v_{12}^x(p_*)$ is given by the expressions for $(v_{12}^x)_{2S}$, or $(v_{12}^x)_{SR}$, or $(v_{12}^x)_{2R}$ derived in Sections 3.1–3.3 for the one-dimensional case and in Sections 4.3–4.5 for the multi-dimensional case.

Besides providing direct information about the wave pattern produced, about the correct equation to solve and the relevant bracketing interval, our approach is also very simple to implement numerically. In practice, the basic steps for the solution of the Riemann problem can be summarized as follows:

1. Evaluate from the initial conditions the three limiting relative velocities $(\tilde{v}_{12}^x)_{2S}, (\tilde{v}_{12}^x)_{SR}, (\tilde{v}_{12}^x)_{2R}$.
2. Determine the wave pattern and the functional form of $v_{12}^x(p_*)$ by comparing $(v_{12}^x)_0$ with the limiting values calculated in (1) and according to the scheme below

$$\begin{aligned}
(v_{12}^x)_0 > (\tilde{v}_{12}^x)_{2S} : & \quad LS_{\leftarrow} L_* CR_* S_{\rightarrow} R, & \quad v_{12}^x(p_*) = (v_{12}^x)_{2S} \\
(\tilde{v}_{12}^x)_{SR} < (v_{12}^x)_0 \leq (\tilde{v}_{12}^x)_{2S} : & \quad LR_{\leftarrow} L_* CR_* S_{\rightarrow} R, & \quad v_{12}^x(p_*) = (v_{12}^x)_{SR} \\
(\tilde{v}_{12}^x)_{2R} < (v_{12}^x)_0 \leq (\tilde{v}_{12}^x)_{SR} : & \quad LR_{\leftarrow} L_* CR_* \mathcal{R}_{\rightarrow} R, & \quad v_{12}^x(p_*) = (v_{12}^x)_{2R} \\
(v_{12}^x)_0 \leq (\tilde{v}_{12}^x)_{2R} : & \quad LR_{\leftarrow} L_* CR_* \mathcal{R}_{\rightarrow} R \text{ with vacuum,} & \quad -
\end{aligned}
\tag{3.73}$$

3. According to the wave pattern found, determine the extremes p_{max} and p_{min} of the pressure interval bracketing p_* . Within our conventions this is equivalent to setting⁴

	$LS_{\leftarrow} L_* CR_* S_{\rightarrow} R$	$LR_{\leftarrow} L_* CR_* S_{\rightarrow} R$	$LR_{\leftarrow} L_* CR_* \mathcal{R}_{\rightarrow} R$
p_{min}	$\max(p_1, p_2)$	$\min(p_1, p_2)$	0
p_{max}	∞	$\max(p_1, p_2)$	$\min(p_1, p_2)$

4. Solve equation (3.6) and determine p_* .
5. Complete the solution of the Riemann problem by computing the remaining variables of the intermediate states L_* and R_* .

We have implemented our algorithm for an exact Riemann solver and have tested it for a range of classical test Riemann problems. We have also compared the performance of our algorithm with the “standard” approach presented by Martí & Müller 1999 and have found a systematic reduction in the computational costs for the same level of accuracy in the solution. The quantitative efficiency improvement depends on the type of problem under consideration. In the case of a generic hydrodynamical problem (in which very simple Riemann problems are solved), our approach brackets the solution very closely and this produces substantial computational improvements of up to 30%. More systematic tests in three-dimensional relativistic hydrodynamics codes and also in comparison to some approximate Riemann solvers are still in progress.

There is a final advantage of the new method presented here, namely that it allows for the discovery of new relativistic effects arising in a Riemann problem with non zero tangential velocities. This will be the subject of Chapter 4.

⁴Note that in practice, the upper limit for the pressure in the case of two shocks is found by starting from a reasonable value above p_{min} , which is incremented until the solution is effectively bracketed.

Chapter 4

New Relativistic Effects in the Dynamics of Non-linear Hydrodynamical Waves

1 Introduction

An important aspect of the new approach that has been presented in the previous Chapter for the solution of the Riemann problem is that it naturally points out a relativistic effect that takes place whenever the relative velocity normal to the initial surface of discontinuity is nonzero. When this is the case, in fact, the tangential velocities can affect the solution of the Riemann problem and cause a transition from one wave-pattern to another one. More specifically, by varying the tangential velocities on either side of the initial discontinuity while keeping the remaining state vectors unchanged, the nonlinear waves involved in the solution of the Riemann problem can change from rarefaction waves to shock waves and vice-versa.

2 Preliminary Discussion

The extension of the one-dimensional Riemann problem to fluid velocities for which special relativistic expressions are needed, has been performed by Thompson K. (1986) for the “shock-tube” problem and by Martí & Müller (1994) for the general problem. Besides the obvious additional complications introduced by special relativity, the *one-dimensional* Riemann problem in relativistic hydrodynamics *does not* show qualitative differences from its Newtonian counterpart.

In the previous Chapter it was shown that new insight on the Riemann problem is offered by considering the key quantity $v_{12}^x = v_{12}^x(p_3)$, the relative velocity between the two unperturbed left and right states. It is useful to remind that in Newtonian hydrodynamics a multidimensional Riemann problem does not depend on the values of the tangential velocities in the two initial states. Rather, different wave-patterns can be produced only after a suitable change in either the normal velocity, the rest-mass density or the pressure. This is essentially due to the fact that tangential velocities are not changed across Newtonian nonlinear waves, neither

in the modulus, nor in the orientation. In relativistic hydrodynamics, on the other hand, this is not the case and is at the origin of the effects discussed here.

3 The New Effect: Changing the Wave-pattern

Let us restrict our attention to a situation in which the tangential velocity of only one of the two initial states is varied. This is simpler than the general case as it basically represents a one-dimensional cross-section of the three-dimensional parameter space, but it maintains all of the relevant properties. The two panels of Fig. 4.1 show the relative normal-velocity for the same initial conditions of Fig. 3.5 where either v_1^t or v_2^t is varied while all the other quantities of the initial state vectors are left unchanged. Different line types mark the different branches (joined at the filled dots) describing the relative velocity corresponding to two shock waves (2S, dashed line), one shock and one rarefaction wave (SR, dotted line), and two rarefaction waves (2R, continuous line), respectively. Both panels of Fig. 4.1 indicate that when tangential velocities are present the relative normal-velocity¹ is a function of p_3 but also of v_1^t and v_2^t .

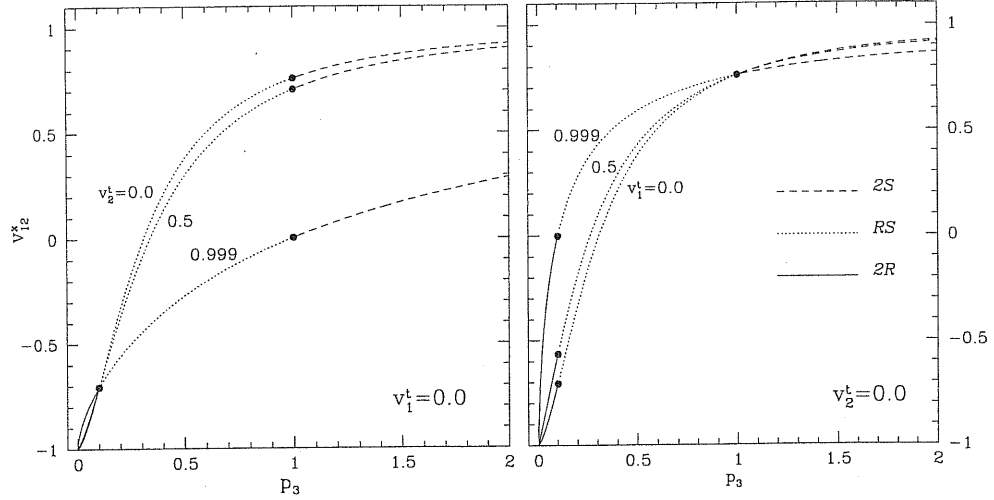


Figure 4.1: The same as in Fig. 3.5 but here the different line types mark the different branches corresponding to two shock waves (dashed line), one shock and one rarefaction wave (dotted line), and two rarefaction waves (continuous line), respectively. The two panels show how the functional behaviour is modified when only one of the initial tangential velocities is varied (v_2^t for the left panel and v_1^t for the right one) while all the other components of the initial state vectors are left unchanged.

Consider, for instance, the case in which the normal velocities are chosen to be $v_1^x = 0.5$, $v_2^x = 0.0$, and there are no tangential velocities. In this case, $(v_{12}^x)_0 = 0.5$ and the left panel of Fig. 4.1 shows that the solution to the Riemann problem falls in the *SR* branch, hence producing a wave-pattern consisting of a shock and a rarefaction wave moving in opposite directions. This is shown in more detail in the left panel of Fig. 4.2 where the different

¹For the of initial conditions chosen in Fig. 4.1 the position of $(\tilde{v}_{12})_{2R}$ is very close to the limit -1 .

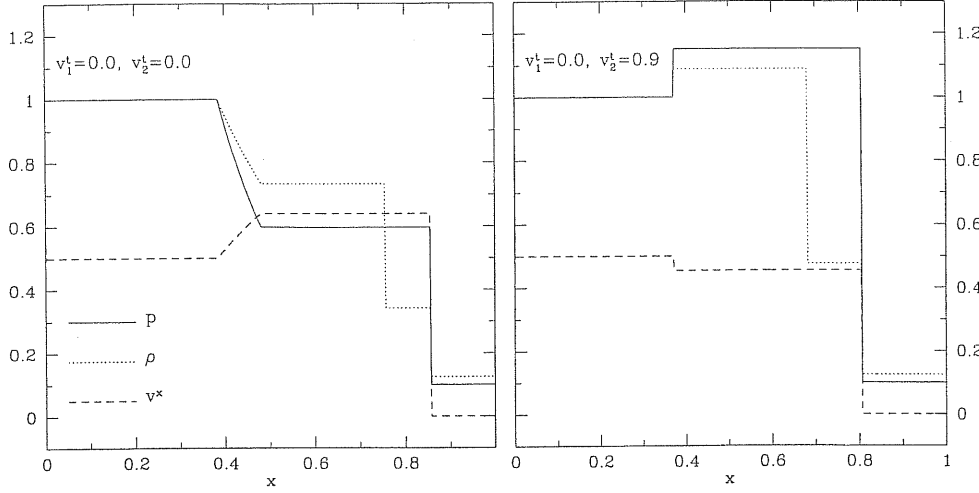


Figure 4.2: Transition from a *SR* wave-pattern to a *2S* one. The left and right panels show the exact solution of the Riemann problem corresponding to models (a) and (e) in Table 4.1, respectively. The initial state vectors are identical except for the values of v_2^t . Solid, dotted and dashed profiles refer to pressure, rest-mass density and normal velocity, respectively.

types of line show the solution of the Riemann problem at a time $t > 0$ for the pressure, the rest-mass density and the velocity.

However, if we now maintain the *same* initial conditions but allow for nonzero tangential velocities in state 2, the left panel of Fig. 4.1 also shows that the solution to the Riemann problem can fall in the *2S* branch, hence producing a wave-pattern consisting of two shock waves moving in opposite directions. This is shown in the right panel of Fig. 4.2 which illustrates the solution of the same Riemann problem but with initial tangential velocities $v_1^t = 0.0$ and $v_2^t = 0.9$. Note that except for the tangential velocities, the solutions in Figs. 4.2 have the same initial state-vectors but different intermediate ones (i.e. p_3 , ρ_3 , ρ_3' , and v_3^x). The Riemann problem shown in Fig. 4.2 is only one possible example but shows that a change in the tangential velocities can produce a *smooth transition from one wave-pattern to another while maintaining the initial states unmodified*. Furthermore, because the coupling among the different states is produced by the Lorentz factors, the effect is not sensitive on the sign chosen for the tangential velocity. The transition from one wave-pattern to the other is better illustrated in Fig. 4.3 where we have collected in a three-dimensional plot a sequence of solutions for the pressure in which v_2^t is gradually increased from 0 to 0.9. Note that when $v_2^t = 0$, the *SR* wave-pattern is well defined and the pressure at the contact discontinuity is intermediate between p_1 and p_2 . Note also that as v_2^t is increased, the wave-pattern gradually changes, p_3 increases up until it becomes larger than p_1 , signalling the transition to a *2S* wave-pattern.

Interestingly, the transition does not need to always produce a solution consisting of two shock waves. Suppose, in fact, that the normal velocities are now chosen to be $v_1^x = 0.0$, $v_2^x = 0.5$. We can repeat the considerations made above and start by examining the wave-pattern produced when there are zero tangential velocities. In this new setup, $(v_{12}^x)_0 = -0.5$ and the

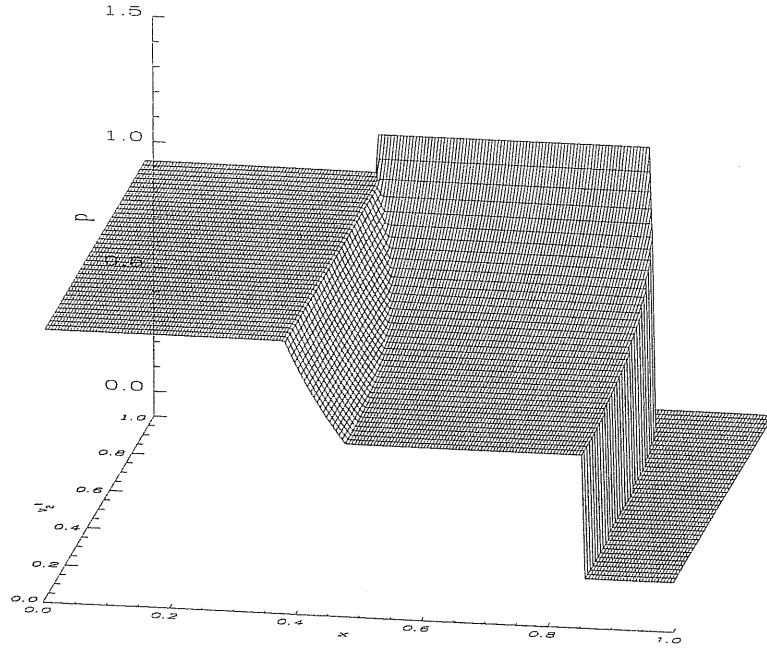


Figure 4.3: Sequence of solutions for the pressure in Sod's problem. The initial tangential velocity v_2^t is gradually increased from 0 to 0.9. The first and last solution of this sequence are also plotted in Fig. 4.2

right panel of Fig. 4.1 shows that the solution to the Riemann problem still falls in the SR branch (cf. dashed line), with the corresponding solution at a time $t > 0$ being presented in the left panel of Fig. 4.4 (Note that the wave-patterns in Fig. 4.2 and 4.4 both consist of a shock and a rarefaction wave, but have alternating initial normal velocities.).

When nonzero tangential velocities are now considered in state 1, the right panel of Fig. 4.1 shows that $(v_{12}^x)_0$ can fall in the $2R$ branch, hence producing a wave-pattern consisting of two rarefaction waves moving in opposite directions. The solution to this Riemann problem is shown in right panel of Fig. 4.4 where we have chosen initial tangential velocities $v_1^t = 0.999$ and $v_2^t = 0.0$. In this case too, it should be noted that, except for the tangential velocities, the solutions in the two panels of Fig. 4.4 have the same initial state-vectors but different intermediate ones.

In analogy with Fig. 4.3, we have collected in Fig. 4.5 a sequence of solutions for the pressure in which v_1^t is gradually increased from 0 to 0.999. Here too, when $v_2^t = 0$, the SR wave-pattern is well defined and the pressure at the contact discontinuity is intermediate between p_1 and p_2 . However, as v_1^t is increased, the wave-pattern gradually changes, p_3 decreases until it becomes smaller than p_2 , signalling the transition to a $2R$ wave-pattern. Note that while this happens, the region of the flow covered by the rarefaction wave becomes progressively smaller.

In Table 4.1 we have summarized a few of the solutions shown in Figs. 4.3 and 4.5, presenting numerical values for all of the relevant quantities in the Riemann problem when different combinations of the tangential velocities are used.

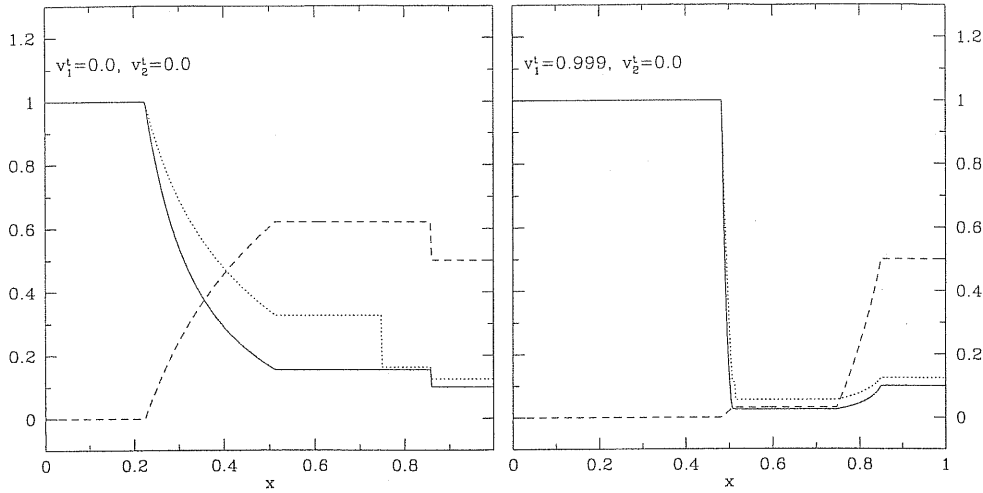


Figure 4.4: The same as in Fig. 4.2 but for models (h) and (n) in Table 4.1. Also in this case the initial state vectors are identical except for the values of v_1^t . Note that in the right panel the left-propagating rarefaction wave covers a very small region of the flow and is closely followed by the contact discontinuity.

To gain a better insight in these effects it can be instructive to consider how the velocities at which the various nonlinear waves propagate in the unperturbed media change when the tangential velocities v_1^t and v_2^t are varied separately. This information is contained in Fig. 4.6 in which different curves show the behaviour of the head and tail of a left-propagating rarefaction wave (i.e. ξ_{tl}^- , ξ_{hd}^-), of the head and tail of a right-propagating rarefaction wave (i.e. ξ_{tl}^+ , ξ_{hd}^+), and of a left or a right-propagating shock wave (i.e. V_s^- , V_s^+). The left panel of Fig. 4.6, in particular, shows the transition from a SR to a $2S$ wave-pattern with the dotted line marking the value of v_2^t at which this occurs. Similarly, the right panel shows the transition from a SR to a $2R$ wave-pattern and the dotted line is again used to mark the value of v_1^t distinguishing the two regions of the parameter space. A number of interesting features can be noted and some of these were pointed out also by Pons *et al* (2000). Firstly, the speed of the head of a rarefaction wave propagating towards a region of constant tangential velocity is constant, or, stated it differently, ξ_{hd}^- does not depend² on v_2^t . Secondly, the velocity of the waves converges to zero if they propagate in regions with increasingly large tangential velocities. Thirdly, the values of v^t at which the speeds of the head and tail of the rarefaction wave coincide, mark the transition from one wave-pattern to another and are indicated with vertical dotted lines in Fig. 4.6.

As mentioned before, the appearance of these new relativistic effects is related to the behaviour of the function $v_{12}^x = v_{12}^x(p_3)$ for different values of the initial tangential velocities and in particular to how the three branches composing the curve change under variation of $v_{1,2}^t$. As a result, the occurrence of these effects can be recast into the study of the depen-

²The reason is actually trivial, because ξ_{hd}^- propagates with the characteristic speed of the left sound wave of the left state.

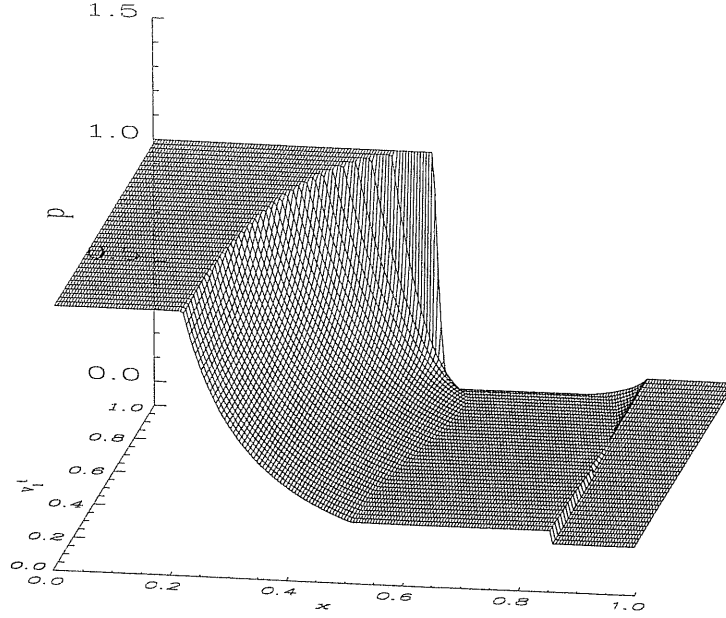


Figure 4.5: The same as in Fig. 4.3 but here the initial tangential velocity v_1^t is gradually increased from 0 to 0.999. The first and last solution of this sequence are also plotted in Fig. 4.4.

dence of $(\tilde{v}_{12}^x)_{2S}$, $(\tilde{v}_{12}^x)_{SR}$ and $(\tilde{v}_{12}^x)_{2R}$ on the tangential velocities. Using expressions (3.58), (3.67), and (3.69), this dependence can be summarized as follows

$$(\tilde{v}_{12}^x)_{2S} = (\tilde{v}_{12}^x)_{2S}(v_2^t), \quad (4.1)$$

$$(\tilde{v}_{12}^x)_{SR} = (\tilde{v}_{12}^x)_{SR}(v_1^t), \quad (4.2)$$

$$(\tilde{v}_{12}^x)_{2R} = (\tilde{v}_{12}^x)_{2R}(v_1^t, v_2^t), \quad (4.3)$$

and can be best studied by considering the limits of $(\tilde{v}_{12}^x)_{2S}$, $(\tilde{v}_{12}^x)_{SR}$ and $(\tilde{v}_{12}^x)_{2R}$ when $W_{1,2} \rightarrow \infty$. In the case of a $2S$ wave-pattern, expression (3.58) simply indicates that

$$\lim_{W_2 \rightarrow \infty} (\tilde{v}_{12}^x)_{2S} = 0. \quad (4.4)$$

This result is also shown in the left panel of Fig. 4.1, where the right solid dot converges to zero as $W_2 \rightarrow \infty$, while the left one does not vary. The limit (4.4) can also be used to deduce that for any $(v_{12}^x)_0 > 0$, there exists a value \bar{W}_2 of W_2 such that

$$(v_{12}^x)_0 > (\tilde{v}_{12}^x)_{2S} \quad \text{for } W_2 > \bar{W}_2. \quad (4.5)$$

A direct consequence of (4.5) is that given a Riemann problem having initial state vectors with positive relative normal-velocity and producing a SR wave-pattern, it is always possible to transform it into a $2S$ wave-pattern by increasing the value of the initial tangential velocity in the state of initial lower pressure.

In the case of a SR wave-pattern we refer to (3.67) to notice that in the limit of $W_1 \rightarrow \infty$

Model	v_1^x	v_2^x	v_1^t	v_2^t	p_*	v_*^x	ρ_3	$\rho_{3'}$	w-p
(a)	0.5	0.0	0.0	0.000	0.597	0.640	0.734	0.342	SR
(b)	0.5	0.0	0.0	0.300	0.621	0.631	0.751	0.349	SR
(c)	0.5	0.0	0.0	0.500	0.673	0.611	0.788	0.364	SR
(d)	0.5	0.0	0.0	0.700	0.787	0.570	0.866	0.394	SR
(e)	0.5	0.0	0.0	0.900	1.150	0.455	1.088	0.474	2S
(f)	0.5	0.0	0.0	0.990	2.199	0.212	1.593	0.647	2S
(g)	0.5	0.0	0.0	0.999	3.011	0.078	1.905	0.750	2S
(h)	0.0	0.5	0.000	0.0	0.154	0.620	0.326	0.162	SR
(i)	0.0	0.5	0.300	0.0	0.139	0.594	0.306	0.152	SR
(j)	0.0	0.5	0.500	0.0	0.115	0.542	0.274	0.136	SR
(k)	0.0	0.5	0.700	0.0	0.085	0.450	0.228	0.113	2R
(l)	0.0	0.5	0.900	0.0	0.051	0.280	0.168	0.084	2R
(m)	0.0	0.5	0.990	0.0	0.031	0.095	0.123	0.061	2R
(n)	0.0	0.5	0.999	0.0	0.026	0.031	0.110	0.052	2R

Table 4.1: Solution of the modified Sod's problem at $t = 0.4$. All models refer to an ideal EOS with $\gamma = 5/3$ and share the same values of pressure and rest-mass density: $p_1 = 1.0$, $\rho_1 = 1.0$, $p_2 = 0.1$, $\rho_2 = 0.125$. The only differences present in the problems considered are in the normal relative velocity and in the tangential velocities. These quantities are reported in the first three columns, while the remaining ones show a few relevant quantities of the solution in the newly formed region as well as the wave pattern produced.

the integrand vanishes ($C \rightarrow \infty$) and therefore:

$$\lim_{W_1 \rightarrow \infty} (\tilde{v}_{12}^x)_{SR} = 0. \quad (4.6)$$

As for the previous one, the limit (4.6) can be deduced from the right panel of Fig. 4.1, where the left solid dot converges to zero as $W_1 \rightarrow \infty$, while the right one does not vary. Also in this case the limit (4.6) can be used to conclude that for any $(v_{12}^x)_0 < 0$, there exists a value \bar{W}_1 of W_1 such that

$$(v_{12}^x)_0 < (\tilde{v}_{12}^x)_{SR} \quad \text{for } W_1 > \bar{W}_1, \quad (4.7)$$

and therefore causing an initial *SR* wave-pattern solution to become a *2R* one as a consequence of an increased tangential velocity in the state of initial higher pressure³.

Overall, expressions (4.4) and (4.6) indicate that for tangential velocities assuming increasingly larger values, the *SR* branch of the v_{12}^x curve spans a progressively smaller interval of relative normal-velocities. When the tangential velocities reach their asymptotic values, the *SR* branch reduces to a point. In practice, therefore, the main effect introduced by relativistic tangential velocities in a Riemann problem is that of “disfavoring” (in a statistical sense) the occurrence of a wave-pattern consisting of a shock and a rarefaction wave.

³Note that it is not possible to provide analytic expressions for \bar{W}_2 nor for \bar{W}_1 .

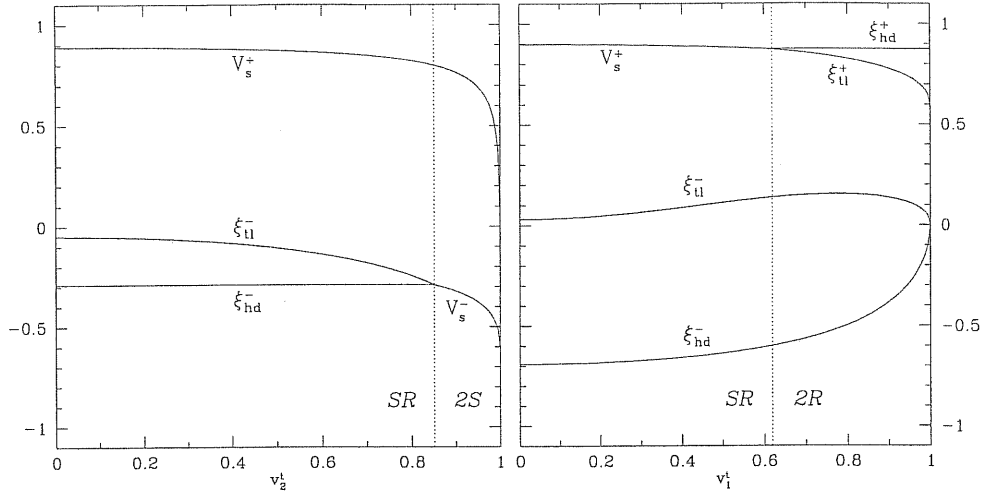


Figure 4.6: Velocities of the various nonlinear waves when the tangential velocities v_1^t and v_2^t are varied separately. The initial conditions are those of Sod's problem and the different curves refer to the head and tail of a left-propagating rarefaction wave (i.e. ξ_{1l}^- , ξ_{hd}^-), to the head and tail of a right-propagating rarefaction wave (i.e. ξ_{1l}^+ , ξ_{hd}^+), and to a left or a right-propagating shock wave (i.e. V_s^- , V_s^+).

For completeness we also report the limit of the relative normal-velocity marking the branch of two rarefaction waves separated by vacuum. In this case, the limit is taken for both W_1 and W_2 tending to infinity, and using (3.70)-(3.71) yields

$$\lim_{W_{1,2} \rightarrow \infty} (\tilde{v}_{12}^x)_{2R} = 0. \quad (4.8)$$

Because the effects discussed here have a purely special relativistic origin they might conflict with our physical intuition, especially when the latter is based on the knowledge of the Riemann problem in Newtonian hydrodynamics. However, the behaviour reported here is typical of those special relativistic phenomena involving Lorentz factors including also tangential velocities. A useful example in this respect is offered by the relativistic transverse-Doppler effect, in which the wavelength of a photon received from a source moving at relativistic speeds changes also if the source has a velocity component orthogonal to the direction of emission of the photon (Rindler, 1980). In this case too, a Lorentz factor including the transverse velocity is responsible for the effect.

It should be pointed out that there exists a set of initial conditions for which these new relativistic effects cannot occur. These initial conditions are those in which $v_1^x = v_2^x$ as in the classic “shock-tube” problem, where $v_1^x = 0 = v_2^x$. In this case, in fact, $(v_{12}^x)_0 = 0$ and, because of the limits (4.4) and (4.6), the solution of the Riemann problem will be given by a wave-pattern consisting of a shock and a rarefaction wave, independently of the values of the tangential velocities.

The effects that have been shown in this Chapter have a purely relativistic nature, do not have a Newtonian counterpart and could be relevant in several astrophysical scenarios, such

as those involving relativistic jets or γ -ray bursts, in which nonlinear hydrodynamical waves with large Lorentz factors and complex multidimensional flows are expected (Blandford 2002, Meszaros 2002).

Chapter 5

Quasi-Periodic Accretion and Gravitational Wave Emission from oscillating “Toroidal Neutron Stars”

1 Introduction

The theory of non-geodesic, perfect fluid, relativistic tori orbiting a black hole has a long history dating back to fundamental works made in the late 60s and 70s (Boyer 1965; Abramowicz 1974; Fishbone 1976; Abramowicz 1978; Kozłowski 1978). One of the most important results obtained in this series of investigations was the discovery that stationary barytropic configurations exist in which the matter is contained within “constant-pressure” equipotential surfaces. Under rather generic conditions, these surfaces can then possess a sharp cusp on the equatorial plane. The existence of this cusp does not depend on the choice of the specific angular momentum distribution and introduces important dynamical differences with respect to the standard model of thin accretion discs proposed by Shakura & Sunyaev (1973) and then extended to general relativity by Novikov & Thorne (1973).

The first important difference is that the cusp at the inner edge of the disc can behave as an effective L_1 Lagrange point (although this is really a circle), providing a simple way in which accretion can take place even in the absence of a shear viscosity in the fluid. The second important difference is that for a disc filling its outermost equipotential surface (the equivalent of its Roche lobe) the mass loss through the cusp could possibly lead to a “run-away” instability (Abramowicz *et al.* 1983). The basic mechanism at work in this instability is rather simple. Any amount of matter accreted through the cusp onto the black hole would change the mass of the latter thus affecting the equipotential surfaces and the location of the cusp. If, as a result of the increased mass of the black hole, the cusp would move to *smaller* radial positions, the new configuration would be of equilibrium and no further accretion would follow. If, on the other hand, the cusp would move to *larger* radial positions, the new configuration would *not* be of equilibrium and new matter (which was previously in

equilibrium) would be forced to accrete onto the black hole which, in turn, would increase its mass. This process clearly triggers a run-away mechanism in which more and more mass is accreted onto the hole, evacuating the whole disc on a timescale between 10 ms and 1 s. Besides being a catastrophic event, the run-away instability has also attracted attention in connection with models of γ -ray bursts. In these models, in fact, the central engine is assumed to be a disc of high density matter orbiting a stellar mass black hole, with intense electromagnetic emission processes lasting for a few seconds at least, as deduced from observations (see Ruffert & Janka 1999, 2001 for a recent review on this). While many of the investigations of the run-away instability have concentrated on the stability properties of stationary disc models (both in Newtonian gravity and in General Relativity), a time-dependent and fully relativistic study of the run-away stability has been presented only recently (Font & Daigne 2002a). Through a number of different hydrodynamical simulations the authors were able to show that, at least for constant specific angular momentum tori slightly overflowing their Roche lobes, the runaway instability does takes place and for a wide range of ratios between the mass of the disc and that of the black hole.

It should be noted, however, that while the instability seems a robust feature of the dynamics of constant specific angular momentum tori, its existence has been severely questioned under generic initial conditions. Different works, in fact, have shown that a more detailed modelling of the initial configurations can either suppress or favour the instability.

Taking into account the self-gravity of the torus seems to favour it (Masuda & Erigichi 1997). The inclusion of rotation of the black hole, on the other hand, has a general stabilizing effect (Wilson 1984; Abramowicz *et al.*). The same applies for tori with non-constant angular momentum distributions, as shown first by Daigne & Mochkovitch (1997) using stationary models and by Masuda *et al.* (1998) with SPH time-dependent simulations with a pseudo-Newtonian potential. We note that very recently Font & Daigne (2002b) have extended their relativistic simulations to the case of non self-gravitating tori with *non-constant* angular momentum, finding that the runaway instability can be suppressed already with a slowly increasing specific angular momentum distribution. A summary of the different results obtained with the different approximations made so far can be found in Table I of Font & Daigne 2002a.

The first aim of our research is to establish how sensitive the onset of the instability is on the choice of constant specific angular momentum configurations that are initially overflowing their Roche lobe. As it will become apparent in the rest of the Chapter, one of the peculiarities of the tori that we have considered in our simulations is that they have very high rest-mass densities, in some cases almost reaching nuclear matter density. A second and most important aim of our work is to investigate the dynamical response of these relativistic tori to perturbations. Our interest for this has a simple justification: because of their toroidal topology, these objects have intrinsically high mass quadrupoles and if the latter are induced to change rapidly as a consequence of perturbations, large amounts of gravitational waves could be produced.

Both of the aspect mentioned above justify in part our choice of terminology. Over the years, in fact, different authors have referred to these disc models in a number of different ways, starting from the original suggestion of Abramowicz *et al.* (1978) of “toroidal stars” to the more recent and common denomination of “accretion tori”, or “thick discs”. Hereafter, however, we will refer to these specific objects as tori but also as “*toroidal neutron stars*”. There are three reasons for this unconventional choice. Firstly, these objects have equilibrium configurations with (small) finite sizes that are pressure supported and not accreting. In this sense, they are very different and should not be confused with standard accretion discs that are in principle infinitely extended, are generically thin because not pressure supported and are, of course, accreting. Secondly, these objects have rest-mass densities much larger than the ones usually associated with standard accretion discs. Thirdly, while possessing a toroidal topology these objects effectively behave as the more familiar neutron stars, most notably in their response to perturbations.

While this analogy is attractive, important differences exist between toroidal and ordinary neutron stars, the most important being that toroidal neutron stars are generically unstable while spherical neutron stars are generically stable. More of these differences will appear in the following Sections. As a final remark we note that the idea of toroidal neutron stars might appear less bizarre when considering a neutron star as a fluid object whose equilibrium is mainly determined by the balance of gravitational forces, pressure gradients and centrifugal forces. In this framework then, the familiar neutron stars with spherical topology are those configurations in which the contributions coming from the centrifugal force are much smaller than the ones due to pressure gradients and gravitational forces. On the other hand, when the contributions of the pressure gradients are smaller than the ones due to the centrifugal and gravitational forces, a toroidal topology is inevitable and a toroidal neutron star then becomes an obvious generalization (see Ansorg *et al.* (2002) for a recent summary of the research on uniformly rotating axisymmetric fluid configurations).

The system of units used in this Chapter results from setting $G = c = 1$. The unit of length is chosen to be the gravitational radius of the black hole, $r_g \equiv GM/c^2$, where M is the mass of the black hole.

2 Analytic solutions for stationary configurations

In what follows we recall the basic properties of stationary disc configurations in a curved spacetime and the interested reader will find a more detailed discussion in Font & Daigne (2002a). The considerations made here will be useful only for the construction of the background initial disc model which we will then perturb as detailed in Section 4.

Consider a perfect fluid with four-velocity \mathbf{u} and described by the usual stress-energy tensor

$$T^{\mu\nu} \equiv (e + p)u^\mu u^\nu + pg^{\mu\nu} = \rho h u^\mu u^\nu + pg^{\mu\nu} , \quad (5.1)$$

where $g^{\mu\nu}$ are the coefficients of the metric which we choose to be those of a Schwarzschild

black hole in spherical coordinates (t, r, θ, ϕ) . The thermodynamics quantities e , p , ρ , and $h = (e + p)/\rho$ have the same meaning as in (2.50) of Chapter 2. In the following we will model the fluid as ideal with a polytropic equation of state (EOS) $p = \kappa \rho^\gamma = \rho \epsilon (\gamma - 1)$, where $\epsilon = e/\rho - 1$ is the specific internal energy and γ is the adiabatic index. Also, for simplicity we will consider the fluid not be magnetized. This may represent a crude approximation given that the toroidal neutron star will probably be created by material originally magnetized and that very large magnetic fields can be easily produced when rapid shearing motions are present in highly conducting magnetized fluids (Spruit 1999, Rezzolla *et al.* 2000).

The fluid is assumed to be in circular non-geodesic motion with four-velocity $u^\alpha = (u^t, 0, 0, u^\phi) = u^t(1, 0, 0, \Omega)$, where $\Omega = \Omega(r, \theta) \equiv u^\phi/u^t$ is the coordinate angular velocity as observed from infinity. If we indicate with ℓ the specific angular momentum (i.e. the angular momentum per unit energy) $\ell \equiv -u_\phi/u_t^1$, the orbital velocity can then be written in term of the angular momentum and of the metric functions only, $\Omega = -\ell(g_{tt}/g_{\phi\phi})$.

From the normalization condition for the four-velocity vector, $u^\alpha u_\alpha = -1$, we derive both the total specific energy of the fluid element, u_t and the redshift factor, u^t as

$$(u_t)^2 = -\frac{g_{\phi\phi}g_{tt}}{g_{\phi\phi} + \ell^2 g_{tt}}, \quad (u^t)^2 = -\frac{1}{g_{tt} + \Omega^2 g_{\phi\phi}}. \quad (5.2)$$

Under these assumptions, the equations of motion for the fluid can be generically written as $h^i{}_\nu \nabla_\mu T^{\mu\nu} = 0$ where $h_{\mu\nu} \equiv g_{\mu\nu} + u_\mu u_\nu$ is the projector tensor orthogonal to \mathbf{u} and ∇ the covariant derivative in the Schwarzschild spacetime. Enforcing the conditions of hydrostatic equilibrium and of axisymmetry simplifies the above equations considerably. Furthermore, if the contributions coming from the self-gravity of the disc are neglected, the relativistic hydrodynamics equations then reduce to Bernoulli-type equations

$$\frac{\nabla_i p}{e + p} = -\nabla_i \ln(u_t) + \frac{\Omega \nabla_i \ell}{1 - \Omega \ell}. \quad (5.3)$$

The simplest solution to equations (5.3) is the one with $\ell = \text{const.}$, since in this case the equipotential surfaces can be computed directly through the metric coefficients and the value of the specific angular momentum. Note that for any value of (r, θ) , the potential can either be positive (indicating equipotential surfaces that are open) or negative (indicating equipotential surfaces that are closed). The special case $W = 0$ refers then to that equipotential surface which is closed at infinity. Note also that the equipotential surfaces contain local extrema and in the equatorial plane these mark two very important points. There, in fact, $\nabla_i W = 0 = \nabla_i p$ and an orbiting fluid element would not experience any net acceleration,

¹Note that this is not the only definition for the specific angular momentum used in the literature. Often, in fact, the specific angular momentum is defined as $\ell' \equiv u_\phi$ because this is a constant of geodesic (i.e. zero-pressure) motion in axially symmetric spacetimes. When the pressure is non-zero, on the other hand, $h u_\phi$ is a constant of motion, while ℓ' is not. For axially symmetric, stationary spacetimes $\ell \equiv -u_\phi/u_t$ is constant for both geodesic and perfect fluid motion.

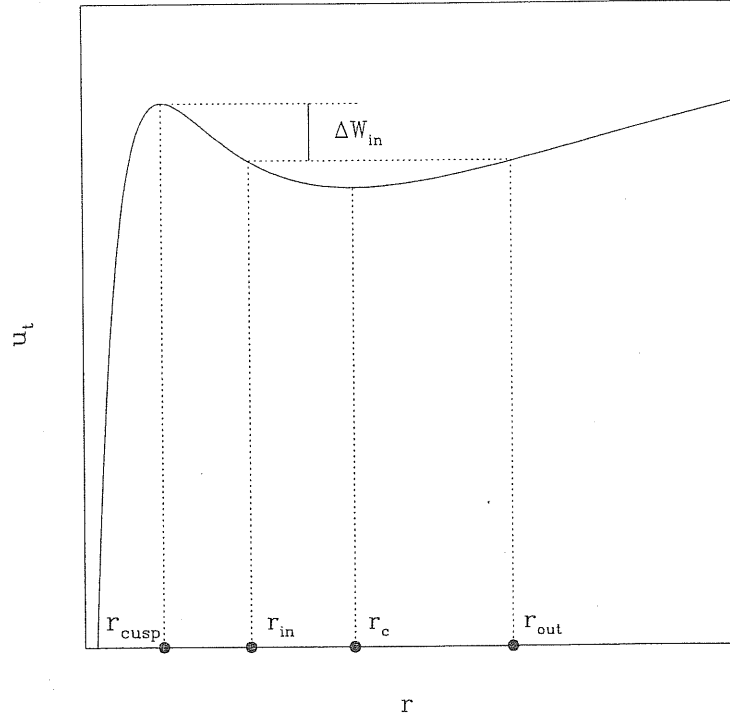


Figure 5.1: Total specific energy of the fluid element on the equatorial plane. The two extrema mark the position of the keplerian points, namely the cusp, r_{cusp} , and the centre, r_c of the disc. The inner edge r_{in} can be chosen anywhere between r_{cusp} and r_c . The energy gap ΔW_{in} is used to fix r_{in} . See the text for further discussion.

with the centrifugal pull balancing the gravitational force exactly. These points correspond to the (radial) positions of the cusp r_{cusp} , and of the “centre” of the disc r_c (see Figure 5.1). Because at these radial positions the specific angular momentum must be that of a Keplerian geodesic circular orbit

$$\ell^2 = \ell_K^2 = \frac{Mr^3}{(r - 2M)^2}, \quad (5.4)$$

equation (5.4) can effectively be used to calculate the position of both the centre and the cusp.

In the case of a marginally stable disc it is straightforward to show that the position of the cusp is located between the marginally bound circular orbit r_b and the marginally stable circular orbit r_{ms} of a point-like particle orbiting the black hole (Abramowicz *et al.* 1978). Note that the position of the inner edge of the disc r_{in} and the position of the r_{cusp} need not coincide and indeed r_{in} can be chosen to be anywhere between the cusp and the centre of this disc. Once made, however, the choice for r_{in} also determines the position of the outer edge of the disc on the equatorial plane through the constraint that both points belong to the same equipotential surface, i.e. $W(r_{\text{out}}, \pi/2) = W(r_{\text{in}}, \pi/2)$ (see Fig. 5.1).

A particularly attractive feature of tori with constant specific angular momentum is that once the background spacetime and the value of the specific angular momentum have been fixed, the angular velocity $\Omega = \Omega(r, \theta)$ is fully determined and if a polytropic EOS is used, the

Bernuolli equations (5.3) can then be integrated analytically to yield the rest-mass density (and pressure) distribution inside the disc as

$$\rho(r, \theta) = \left\{ \frac{\gamma - 1}{\kappa \gamma} [\exp(W_{\text{in}} - W) - 1] \right\}^{1/(\gamma-1)}, \quad (5.5)$$

where $W_{\text{in}} \equiv W(r_{\text{in}}, \pi/2)$ and r_{in} has been conveniently chosen. Once the rest-mass distribution (5.5) is known, the total rest-mass of the disc can be easily calculated as

$$M_{\text{t},*} = \int \rho \sqrt{-g} u^0 d^3x, \quad (5.6)$$

while the total mass-energy in the toroidal neutron star is computed as

$$M_{\text{t}} = \int (T_r^r + T_\phi^\phi + T_\theta^\theta - T_t^t) \sqrt{-g} d^3x, \quad (5.7)$$

where $d^3x = dr d\theta d\phi$ is the coordinate volume element. For simplicity, hereafter, we will refer to the mass-energy of the toroidal neutron star as the “mass” of the toroidal neutron star. Depending on the value of ℓ chosen and in particular on how this compares with the specific angular momenta corresponding to orbits that are marginally bound $\ell_{\text{mb}} = 4$ or that are marginally stable $\ell_{\text{ms}} = 3\sqrt{3/2}$, different configurations can be built. A detailed classifications of the disc models can be found in the literature (Abramowicz *et al.* 1978, Font & Daigne 2002a), but we here simply recall that if $\ell_{\text{ms}} < \ell < \ell_{\text{mb}}$ there will be an equipotential surface closed at a finite radius and possessing a cusp. As a result, a stationary toroidal neutron star of finite extents can be built and this will represent our fiducial, background initial toroidal neutron star.

3 Mathematical Framework

3.1 Hydrodynamic equations

The conservative formulation of the equations of general relativistic hydrodynamics was given in Chapter 2 [cf. Eq. (2.57)], and we rewrite it here in a slightly different form

$$\frac{\partial \mathbf{U}(\mathbf{w})}{\partial t} + \frac{\partial [\alpha \mathbf{F}^r(\mathbf{w})]}{\partial r} + \frac{\partial [\alpha \mathbf{F}^\theta(\mathbf{w})]}{\partial \theta} = \mathbf{S}(\mathbf{w}), \quad (5.8)$$

where $\alpha = \sqrt{-g_{00}}$ is the lapse function of the Schwarzschild metric and where $\mathbf{U}(\mathbf{w}) = (D, S_r, S_\theta, S_\phi, \tau)$ is the state-vector of the conserved variables to be evolved. The other vectors \mathbf{F}^i , \mathbf{S} appearing in (5.8) represent the of fluxes and sources, as usual. The relation between the conserved and primitive variables in the vector $\mathbf{w} = (\rho, v_i, \epsilon)$ are given by (2.56), which, we recall, cannot be inverted analytically.

Note that the covariant components of the three-velocity are defined in terms of the spatial 3-metric γ_{ij} to be $v_i = \gamma_{ij}v^j$, where $v^i = u^i/\alpha u^t$ [cf. Eq. (2.55)] (note that although in axisymmetry, we evolve also the azimuthal component of the equations of motion, so that the index j in equations (2.56) takes the values $j = r, \theta, \phi$). More specifically, the only non-zero component of the three-velocity of a fluid element in orbital non-keplerian motion around the black hole is given by

$$v^\varphi = \frac{u^t \Omega}{\sqrt{1 + g_{\varphi\varphi}(u^t)^2 \Omega^2}} , \quad (5.9)$$

which correctly reduces to $\alpha^{-1}\Omega_K$ in the keplerian limit of $\Omega^2 = \Omega_K^2 = 1/r^3$. The Lorentz factor W measured by a local static observer and appearing in equations (2.56) is renamed here as Γ , to avoid confusion with the potential. The explicit expressions for the components of the flux vectors \mathbf{F}^i and of the source vector \mathbf{S} are given by

$$\mathbf{F}^r(\mathbf{w}) = (Dv^r, S_r v^r + p, S_\theta v^r, S_\phi v^r, (\tau + p)v^r) , \quad (5.10)$$

$$\mathbf{F}^\theta(\mathbf{w}) = (Dv^\theta, S_r v^\theta, S_\theta v^\theta + p, S_\phi v^\theta, (\tau + p)v^\theta) , \quad (5.11)$$

$$\mathbf{S}(\mathbf{w}) = (S_1, S_2, S_3, S_4, S_5) , \quad (5.12)$$

respectively, where

$$S_1 = D(\mathcal{A}v^r - \mathcal{B}v^\theta) , \quad (5.13)$$

$$S_2 = -\frac{M}{\alpha^2 r^2}(\tau + D) - \alpha \cot \theta S_r v^\theta + \frac{\alpha}{r}(S_\theta v^\theta + S_\phi v^\phi - 2S_r v^r) , \quad (5.14)$$

$$S_3 = S_\theta(\mathcal{A}v^r - \mathcal{B}v^\theta) + \alpha r^2 S^\phi v^\phi \sin \theta \cos \theta , \quad (5.15)$$

$$S_4 = S_\phi(\mathcal{A}v^r - \mathcal{B}v^\theta) , \quad (5.16)$$

$$S_5 = -\frac{2\alpha}{r}S^r - S^\theta \mathcal{B} - S_1 , \quad (5.17)$$

and

$$\mathcal{A} = \frac{M}{\alpha r^2} - \frac{2\alpha}{r} , \quad (5.18)$$

$$\mathcal{B} = \alpha \cot \theta . \quad (5.19)$$

3.2 Spacetime Evolution

The general relativistic hydrodynamics equations we solve assume that the fluid moves in a curved spacetime (provided by the Schwarzschild solution) that is static. On the other hand, the onset and development of the run-away instability depends crucially on the response of the fluid to variations of the spacetime and in particular of its longitudinal part. To follow this in a self-consistent manner would require the solution of the Einstein field equations together with those of relativistic hydrodynamics. However, this is a much harder problem computationally and “full” numerical relativity codes evolving black hole spacetimes with perfect fluid matter (either in two or three spatial dimensions) are being developed only recently (Brandt *et al.* 2000; Shibata & Uryū 2000, Shibata *et al.* 2000, Font *et al.* 2002). Furthermore, the level of grid resolution and the need to evolve these configurations for timescales that are much larger than the dynamical one, may still be too taxing for full numerical relativity codes.

To avoid the solution of the full Einstein equations and yet simulate the onset and development of the instability we have followed the approach first proposed in Font & Daigne 2002a. Most notably, we calculate at each timestep the accretion rate at the innermost radial point of the grid as

$$\dot{m}(r_{\text{in}}) = -2\pi \int_0^\pi \sqrt{-g} Dv^r d\theta \Big|_{r_{\text{in}}} , \quad (5.20)$$

where $\sqrt{-g} = r^2 \sin \theta$ and thus determine the amount of matter that would be accreted onto the black hole as

$$M^{n+1} = M^n + \Delta t \dot{m}^n(r_{\text{in}}) , \quad (5.21)$$

where, the upper indices refer to a given time-level. Once the new mass of the black hole has been computed, the relevant metric functions are instantaneously updated as

$$g_{\mu\nu}(r, M^n) \longrightarrow \tilde{g}_{\mu\nu}(r, M^{n+1}) , \quad (5.22)$$

so that $\tilde{g}_{\mu\nu}$ will describe the new spacetime over which the hydrodynamical equations will be solved. We note that to be consistent the transfer of angular momentum from the torus to the black hole should also be taken into account. While we have not considered this here, the interested reader will find the details on a procedure to account for the angular momentum transfer onto the black hole in Font & Daigne (2002b). Our approach for the spacetime evolution is clearly an approximation and it masks important features such as transfer of angular momentum from the toroidal neutron star to the black hole or the response of the latter to the accreted mass and the consequent emission of gravitational radiation. Nevertheless, this approximation is often very good especially when the toroidal neutron star is not very massive and the rest-mass accretion rates are therefore small. In these cases, then, the fractional variation of the black hole mass between two adjacent time-levels is minute and treating the spacetime evolution as a discrete sequence of stationary spacetimes represents a very good approximation.

3.3 Numerical Approach

The numerical code used in our computations is based on a code that has been extensively described in Font & Ibañez 1998 (see also Font & Daigne (2002a)). This code performs the numerical integration of system (5.8) using High Resolution Shock Capturing schemes as discussed in Chapter 2. In particular, the time evolution of the discretized data from a time-level n to the subsequent one $n + 1$ is performed according to

$$\begin{aligned} \mathbf{U}_{i,j}^{n+1} = \mathbf{U}_{i,j}^n & - \frac{\Delta t}{\Delta r} \left(\hat{\mathbf{F}}_{i+1/2,j}^r - \hat{\mathbf{F}}_{i-1/2,j}^r \right) \\ & - \frac{\Delta t}{\Delta \theta} \left(\hat{\mathbf{F}}_{i,j+1/2}^\theta - \hat{\mathbf{F}}_{i,j-1/2}^\theta \right) \\ & + \Delta t \mathbf{S}_{i,j} , \end{aligned} \quad (5.23)$$

where the subscripts i, j refer to spatial (r, θ) grid points, so that $\mathbf{U}_{i,j}^n \equiv \mathbf{U}(r_i, \theta_j, t^n)$. The intercell numerical fluxes, $\hat{\mathbf{F}}_{i\pm 1/2,j}^r$ and $\hat{\mathbf{F}}_{i,j\pm 1/2}^\theta$, are computed using Marquina's approximate Riemann solver (Donat & Marquina, 1996). A piecewise-linear cell reconstruction procedure provides second-order accuracy in space, while the same order in time is obtained with a conservative two-step second-order Runge-Kutta scheme applied in the above time update. Our computational grid consists of $N_r \times N_\theta$ zones in the radial and angular direction, respectively, covering a computational domain extending from $r_{\min} = 2.1$ to $r_{\max} = 30$ and from 0 to π . We have used numerical grids with different number of grid-points and found that the truncation error is reduced to reasonable values when $N_r = 250$ and $N_\theta = 84$. All of the results presented in the following Section have been computed with this number of grid-points. The radial grid is logarithmically spaced in term of a tortoise coordinate $r_* = r + 2M \ln(r/2M - 1)$, with the maximum radial resolution at the innermost grid being $\Delta r = 6 \times 10^{-4}$. As in Font & Daigne (2002a), we tend to use a finer angular grid in the region that are usually within the disc and a much coarser one for the regions outside the disc. A grid-point belongs to the external surface of the initial unperturbed disc when $u_t(r, \theta) = u_{t,\text{in}} = u_t(r_{\text{in}}, \pi/2)$. This equation defines the meridional section of the surface as a closed polar curve \mathcal{C} of equation

$$\sin \theta = \left[\frac{u_{t,\text{in}}^2 \ell^2 (1 - 2M/r)}{r^2 (u_{t,\text{in}}^2 - 1 + 2M/r)} \right]^{1/2} . \quad (5.24)$$

The angular extension θ_m of the unperturbed disc can then be computed by searching for the local extrema of the curve \mathcal{C} . As a result of this, in most of our simulations 75% of the angular grid points were uniformly distributed in the range $[\theta_m, \pi - \theta_m]$, while the remaining points cover the outside region.

As far as the boundary conditions are concerned, we have adopted the following procedure. In the radial direction the primitive variables ρ , v_r , v_θ and v_ϕ have been extrapolated linearly at the inner boundary r_{in} (the rest mass density is however assumed to have zero gradient there). At the outer boundary r_{max} all the variables have been frozen to their constant initial values. On the other hand, reflection boundary conditions have been adopted at both poles ($\theta = 0, \pi$). Finally, the numerical grid outside the toroidal neutron star is filled with a low density atmosphere, in such away to avoid vacuum regions while not affecting the dynamics of the simulations (see Font & Daigne, 2002a).

4 Initial Data

Simulating a dynamical instability with a numerical code inevitably brings up the problem of suitable initial conditions. A natural choice would be that of a configuration that is in equilibrium, where the latter is not a stable one. In this case, then, any perturbation would move the configuration away from the equilibrium and induce the instability on a finite timescale. While we see this happen regularly in Nature, it is rather difficult to simulate numerically and the major obstacle in this respect is given by need of performing such simulations on the rather short timescales that can be afforded computationally. Fortunately, however, there are ways of by-passing this limitation and these generally consist of choosing an initial configuration which is, although only very slightly, already out of equilibrium. Controlling the deviation away from the equilibrium state in some parametrized form, the timescale for the development of the instability can then be reduced to values that are compatible with the computational ones.

An approach of this type has been used in the past also to simulate the run-away instability, where a measure of deviation away from the unstable equilibrium can be made in terms of the potential difference $\Delta W_{\text{in}} > 0$ at the inner edge of the disc. This quantity, defined as $\Delta W_{\text{in}} \equiv W_{\text{in}} - W_{\text{cusp}}$ (see Fig. 5.1), accounts for the potential jump on the equatorial plane between the inner edge of the disc and the cusp (Igumenshev & Beloborodov (1997)). By simply varying the value of ΔW_{in} , it is then possible to select a configuration corresponding to a disc inside its Roche lobe and for which no mass transfer is possible (i.e. $\Delta W_{\text{in}} < 0$), or a disc overflowing its Roche lobe and therefore accreting (i.e. $\Delta W_{\text{in}} > 0$). The case limiting the two classes of solutions, (i.e. $\Delta W_{\text{in}} = 0$) refers to a configuration that is just marginally stable to the run-away instability, which will therefore develop over an infinite timescale².

All of the models considered by Font & Daigne (2002a), for instance, have been constructed with potential differences $\Delta W_{\text{in}} > 0$, so that the outermost potential surface is not closed at the cusp but reaches the black hole. After truncating the disc at $r = r_{\text{cusp}}$, the simulations were then carried out by evolving the set of equations discussed in Section 3.1. With this choice, a non negligible volume fraction of the initial fluid configuration (i.e. all the one residing outside the Roche lobe) is out of equilibrium. Of course, this is not the only way of

²Note that this condition is also equivalent to setting $r_{\text{in}} = r_{\text{cusp}}$.

Model	M_t/M	κ cgs	ℓ	r_{in}	r_{out}	r_{cusp}	r_{centre}	t_{orb} ms	ρ_{centre} cgs	$\langle \rho \rangle$ cgs
(a)	1.	4.46×10^{13}	3.8000	4.576	15.889	4.576	8.352	1.86	1.14×10^{14}	9.32×10^{11}
(b)	0.5	5.62×10^{13}	3.8000	4.576	15.889	4.576	8.352	1.86	5.74×10^{13}	4.67×10^{11}
(c)	0.1	0.96×10^{14}	3.8000	4.576	15.889	4.576	8.352	1.86	1.14×10^{13}	9.35×10^{10}
(d)	0.05	1.21×10^{14}	3.8000	4.576	15.889	4.576	8.352	1.86	5.74×10^{12}	4.67×10^{10}
(e)	0.1	7.0×10^{13}	3.7845	4.646	14.367	4.646	8.165	1.80	1.60×10^{13}	1.12×10^{11}
(f)	0.1	1.0×10^{14}	3.8022	4.566	16.122	4.566	8.378	1.87	1.10×10^{13}	9.89×10^{10}
(g)	0.1	2.0×10^{14}	3.8425	4.410	21.472	4.410	8.839	2.03	4.96×10^{12}	7.22×10^{10}
(h)	0.1	3.5×10^{14}	3.8800	4.290	29.539	4.290	9.246	2.17	2.41×10^{12}	5.10×10^{10}

Table 5.1: Definition of the models. From left to right the columns report: the name of the model, the mass ratio M_t/M , the polytropic constant κ , the specific angular momentum ℓ (normalized to M), the inner and outer radii of the toroidal neutron star r_{in} and r_{out} , the radial position of cusp r_{cusp} , the radial position of the centre r_{centre} (all radii are in units of the gravitational radius r_g), and the orbital period at the center of the disc t_{orb} , expressed in milliseconds. All of the models share the same mass for the black hole, $M = 2.5M_{\odot}$ and adiabatic index $\gamma = 4/3$.

triggering the instability and in the calculations by Masuda & eriguchi (1997), for example, the size of the disc was expanded by a small amount past the Roche lobe so as to set the configuration out of equilibrium and to trigger the conditions for the occurrence of the run-away instability. While it has been argued that the occurrence of the instability is not much affected by the choice of the initial model (Masuda & Eriguchi 1997) we have here followed a different approach to the problem of initial condition for the run-away instability as discussed below.

4.1 Introducing a Perturbation

Firstly, all of the models we have considered have a potential barrier $\Delta W_{\text{in}} \leq 0$. As a result, these represent configurations that are either marginally stable (i.e. $\Delta W_{\text{in}} = 0$) or even *stable* (i.e. $\Delta W_{\text{in}} < 0$) with respect to the runaway instability. However, because these configurations cannot develop the instability on a finite timescale, we have introduced parametrized perturbations that would induce a small outflow through the cusp. More specifically, we have modified the stationary equilibrium configuration discussed in Section 2 with a small radial velocity which we have expressed in terms of the radial inflow velocity characterizing a relativistic spherically symmetric accretion flow onto a Schwarzschild black hole (the Michel solution, Michel 1972). Using η to parametrize the strength of the perturbation, we have specified the radial (covariant) component of the three-velocity as

$$v_r = \eta(v_r)_{\text{Michel}} \quad (5.25)$$

We regard this choice of initial data as a more realistic one for at least two reasons. Firstly, in this way only the a small region of the fluid configuration, (i.e. the one located near the cusp) is out of equilibrium. Secondly and more importantly, an initial configuration of this type is much closer to the one that might be produced in nature. We recall, in fact, that tori of the type considered here are expected to form in a number of different events such as the collapse of supermassive neutron stars (Vietri & Stella, 1998), or the iron-core collapse

of a massive stars (Macfayden & Woosley, 1999). Other scenarios for the genesis of these objects involve the coalescence of a binary system, either consisting of two neutron stars (especially if they have unequal masses) or consisting of a black hole and of a neutron star which is then disrupted by the intense tidal field (Lee & Kluzniak, 1999a,b; Lee, 2000). In all of these catastrophic events, the newly formed torus will be initially highly perturbed and is expected to maintain also a radial velocity in addition to the orbital one. In recent Newtonian simulations performed by Ruffert & Janka (1999) the torus resulting from the dynamical merging of two neutron stars was observed to oscillate and accrete onto the newly formed black hole. The average inflow velocity in the central region of the newly formed torus was measured to be $\sim 3 \times 10^{-3}$, whereas at very small distances from the black hole the fluid was infalling much more rapidly. To be consistent with the estimates provided by Ruffert & Janka (1999), we have chosen the parameter η in the range $[0.001, 0.06]$, corresponding to an average inward radial velocity in the range $[0.0002, 0.04]$, respectively. However, simulations with values as small as $\eta = 0$ and as large as $\eta = 0.17$ have also been performed, but these have not introduced qualitatively new features. It should also be noted that because the orbital velocities are at least one order of magnitude larger than the radial ones induced through the perturbations, the contribution of the latter to the kinetic energy budget is rather small even when large values of η are considered.

An aspect of our initial models worth underlining is that while in principle $\dot{m} = 0$ when $\Delta W_{\text{in}} = 0$, the accretion rate induced at the cusp can be made arbitrarily small after a suitable choice of the mass of the disc and of the strength of perturbation. This represents an important possibility because in the case of very small rest-mass accretion rates, the variations in the spacetime metric can be neglected and we can therefore investigate the response of the toroidal neutron stars in the absence of metric variations. This, in turn, allows for long-term evolutions and we will refer to this regime as to the one with a “fixed” spacetime to distinguish it from the “dynamical” regime, in which the accretion rate is not negligible and metric functions need to be updated as in (5.22).

With the choice of initial conditions discussed above, we have evolved a large number of models covering only in part a large parameter space. The properties of the different models simulated are summarised in Table 5.1 where we have reported the ratio between the mass of the toroidal star and the black hole, the polytropic constant, the specific angular momentum, as well as the inner and outer radii. Each of the models in Table 5.1 has been simulated for at least four different values of the parameter η , either on a fixed or dynamical spacetime or in both. Two quantities we have kept fixed in all of the simulations and these are the adiabatic index, taken to be that of degenerate relativistic electron gas $\gamma = 4/3$, and the initial black hole mass, that we have chosen to be $M = 2.5M_{\odot}$ for comparison with the results of Font & Daigne (2002a).

5 Numerical Results

In what follows we will discuss in detail the dynamics of the perturbed toroidal neutron stars summarised in Table 5.1. In particular, we will first report the results about the run-away instability and subsequently will discuss the long-term dynamics of the toroidal neutron stars in response to perturbations.

5.1 Dynamical Spacetime: the run-away Instability

Because the code implemented here is similar but distinct from the one used by Font & Daigne (2002a), we have first tested it against the results published there. More precisely, we have considered out-of-equilibrium initial conditions ($\Delta W_{\text{in}} > 0$) and evolved this configuration using the set of equations (5.8) and the metric update (5.22). The results obtained confirm (with differences less than one percent) what found by Font & Daigne (2002a), indicating that with this choice of initial conditions, and after an initial relaxation, the instability develops rapidly on timescales that are progressively smaller as the mass ratio and the initial potential jump ΔW_{in} are increased. The occurrence of the instability is signaled by the exponential growth of the rest-mass accretion rate which rapidly reaches super-Eddington values. It should be noted that while the simulated mass fluxes are many orders of magnitude larger than the Eddington limit (this is $\sim 1.2 \times 10^{-16} \text{ M}_{\odot}/\text{s}$ for the black hole considered here), these mass fluxes are also the ones required to account for the large energetic release observed in γ -ray bursts.

After this validating test, we have investigated the onset and development of the run-away instability using the initial conditions discussed in Section 4. Shown in Figure 5.2 is the evolution of the rest-mass accretion rate for model (a) (see Table 5.1) and with three different values of initial velocity perturbation, η . The time is expressed in terms of the orbital period $t_{\text{orb}} = 2\pi/\Omega_{\text{centre}}$ of the centre of the toroidal neutron star and is reported in Table 5.1 for the different models considered. Note that the minimum rest-mass accretion rate in Figure 5.2 is never zero but of the order $\sim 0.02\text{M}_{\odot}/\text{s}$, even initially. This is just the cumulative result of a small truncation error which is always producing a tiny and constant in time mass overflow at the cusp, coupled to the use of very high density matter which then amplifies the accretion rate.

The behaviour of the mass flux reported in Figure 5.2 incorporates two important features. Firstly, it shows that the run-away instability does occur also with this choice of initial data and that the growth-rate is smaller for larger initial velocity perturbations (i.e. larger values of η). As mentioned in the Introduction of this Chapter, this is a rather important point confirming that Roche lobe-overflowing is not a necessary condition for the development of the instability and that the latter is inevitable, at least in constant specific angular momentum tori whose self-gravity is not considered. The small inset of Figure 5.2, offers a more detailed view of the simulation with $\eta = 0.06$ on a logarithmic scale for the time and should be considered as the dynamical evolution that more than any other resembles the one

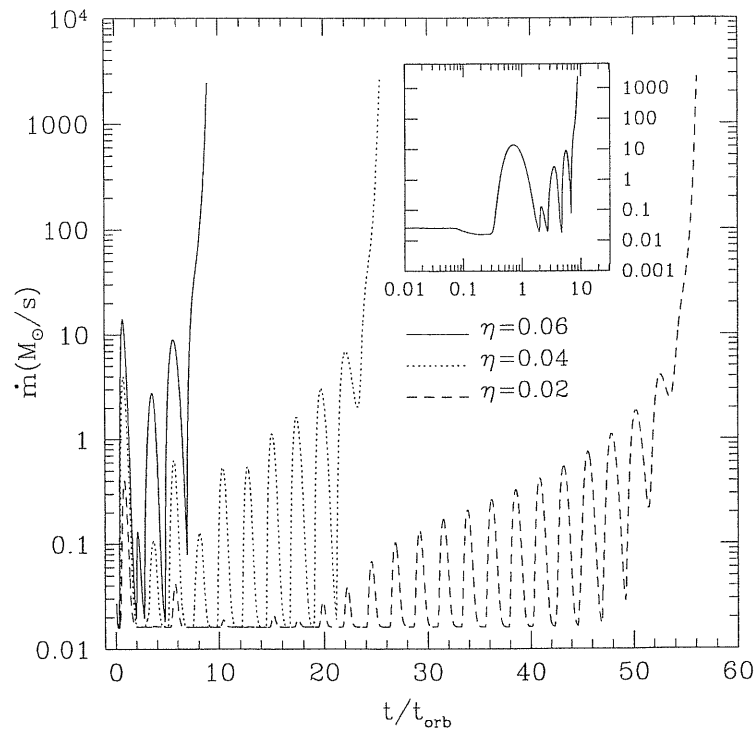


Figure 5.2: Evolution of the rest-mass accretion rate for model (a) and for different values of η when the spacetime is allowed to vary. The time is expressed in terms of the timescale for the centre of the toroidal neutron star to perform an orbit. The small inset focuses on the case in which $\eta = 0.06$, showing the results on a logarithmic scale.

observed for Roche lobe overflowing tori by Font & Daigne (2002a).

The behaviour observed in Figure 5.2 for the onset of the instability with different values of the perturbation velocity has a rather simple interpretation. In fact, In order to trigger the instability a certain fractional change in the mass of the black hole (and therefore in the spacetime curvature) needs to be reached. If the initial strength of the perturbation is large, a considerable amount of matter will be accreted onto the black hole already during the first oscillation in the accretion rate and the instability is therefore able to develop very rapidly. If, on the other hand, the strength perturbation is small, much less mass will be accreted during each oscillation and more oscillations will be needed to produce the fractional change in the black hole mass that will accelerate the development of the instability. In this latter case, the instability will develop on larger timescales which do not scale linearly with η .

A second novel and remarkable feature to notice in Figure 5.2 is that, after the system has relaxed from the initial conditions (i.e. at about $t/t_{\text{orb}} \simeq 2$) the secular growth in the rest-mass accretion rate is accompanied by an oscillatory behaviour with increasing amplitude. These oscillations are less regular in the case of the high amplitude perturbation (i.e. $\eta = 0.06$) but are much more regular as the strength of the perturbation is gradually reduced. It is also interesting to notice that when very low amplitude perturbations are used, the amount of accreted matter is so small that new features can be revealed. In the case of the simulation for $\eta = 0.02$ in Figure 5.2, for instance, it is possible to distinguish at

least three different stages. Most notably, an *initial* stage for $t/t_{\text{orb}} \lesssim 18$, during which the rest-mass accretion rate is very small and does not manifest a regular oscillatory behaviour. Despite the apparent quiescence, and as it will become clearer in the following Section, during this stage the toroidal neutron star is not at all static and other hydrodynamical quantities manifest a different behaviour. This stage is then followed by an *intermediate* stage for $18 \lesssim t/t_{\text{orb}} \lesssim 45$, during which the rest-mass accretion rate shows the secular growth already observed for higher amplitudes perturbations. Note that while this happens, the toroidal neutron star enters in phases during which no accretion is present (i.e. the accretion rate reaches the minimum possible values). Eventually, a third *final* stage sets in for $t/t_{\text{orb}} \gtrsim 45$, during which the instability starts to develop more clearly. This can be deduced from the fact that during this phase the accretion rate does not reach the floor as it did in the previous intermediate stage and the oscillations have progressively smaller amplitude while the accretion rate grows exponentially.

It worth pointing out that each of these oscillations deposits a considerable amount of matter onto the black hole which, before reaching the event horizon, is likely to lose part of its potential binding energy by emitting electromagnetic radiation. In view of this, it is plausible to expect that the quasi-periodic accretion measured during our simulations could also be observed in the form of a quasi-periodic X-ray luminosity, as it is indeed the case in the quasi-periodic oscillations (QPO's) observed in the X-ray luminosity of Low Mass X-ray Binaries (LMXB's) (van der Klis, 2000). While the connection between the two phenomenologies is very suggestive, it should be remarked that the discs which are thought to be behind the quasi-periodic X-ray luminosity in LMXB's have much smaller rest-mass densities and more detailed calculations need to be made before a conclusion on the connection between the two phenomenologies can be drawn.

All of the calculations shown in Figure 5.2 terminate when the accretion rate has reached a maximum value of $\sim 3 \times 10^3 M_{\odot}/\text{s}$ and the rest-mass of the disc has become only a few percent of the initial one (cf. Figure 5.4). During these very final stages of the instability the calculations are made very difficult by the exponential changes in the hydrodynamical quantities and Courant factors as small as 0.01 are needed to prevent the code from crashing. Soon after the accretion rate has reached its maximum, it drops rapidly to very small values as a result of the almost complete disappearance of the disc (this final part of the evolution is not reported in Figure 5.2).

As mentioned above, the growth-time for the instability depends on the efficiency of the mass accretion process and on the reaching of a certain fractional change in the black hole mass. How rapidly this change is achieved depends both the strength of the initial velocity perturbation (as shown in Figure 5.2) but also on the density of the accreted matter. To confirm this, we have performed simulations for the same initial perturbation but with different mass ratios. The results of these simulations are summarized in Figure 5.3 which shows the behaviour of the rest-mass accretion rate for models (b) and (c) in Table 5.1, which have the same properties of model (a) of Figure 5.2, but have been constructed using larger values

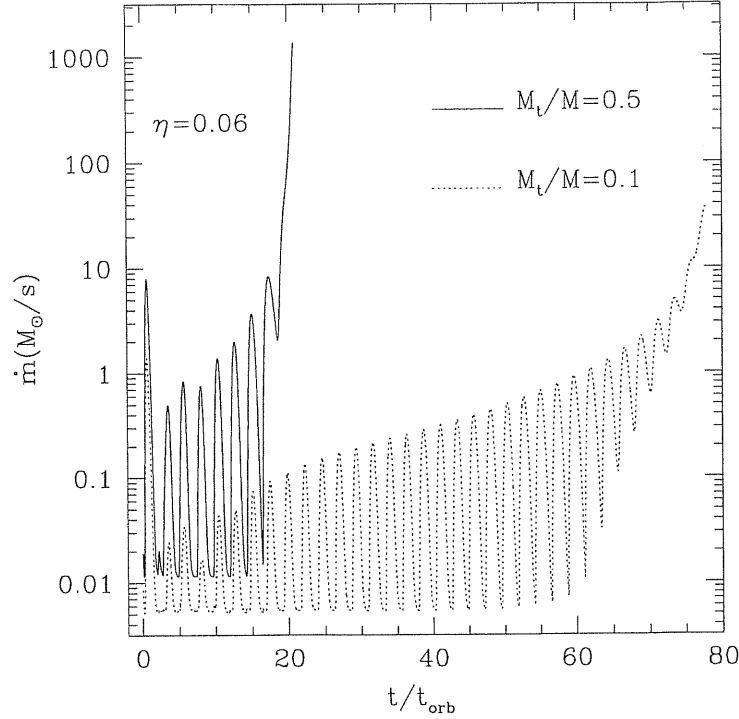


Figure 5.3: Rest-mass accretion rate for three different mass ratios in a dynamical spacetime evolution. The solid and dotted lines correspond to models (b) and (c), respectively, after a perturbation with $\eta = 0.06$.

of the polytropic constant κ [cf. equation (5.5)]. As expected, lower density toroidal neutron stars have proportionally smaller accretion rates (note that the floors are also different) and proportionally longer timescales for the onset and development of the instability. Two interesting aspects of Figure 5.3 need to be pointed out. Firstly, the timescale for the instability to set in has an almost linear dependence on the mass ratio M_t/M . This is a rather important detail as it reveals that what could be considered as a “realistic” toroidal neutron star, i.e. one with $M_t/M \simeq 0.1$ and with a level of perturbations of the order $\eta \simeq 0.02$, has a lifetime of roughly 1 s. (cf. also with Figure 5.2). Secondly, when the mass accretion rate is generically low, the amount of matter accreted can be very small even over several tens of dynamical timescales. When this is the case, and as mentioned in Section 4.1, the spacetime can be held fixed and the overall calculations simplified. More importantly, this provides the possibility of distinguishing the dynamical response of the toroidal neutron star to perturbations from the development of the stability. We will exploit this possibility in the following Section which focuses on the investigation of the oscillation properties of toroidal neutron stars.

5.2 Fixed Spacetime: Quasi-Periodic Oscillations

The dynamical response of the toroidal neutron star to perturbations provides information about the basic properties of this object in a strong gravitational field. While the details of

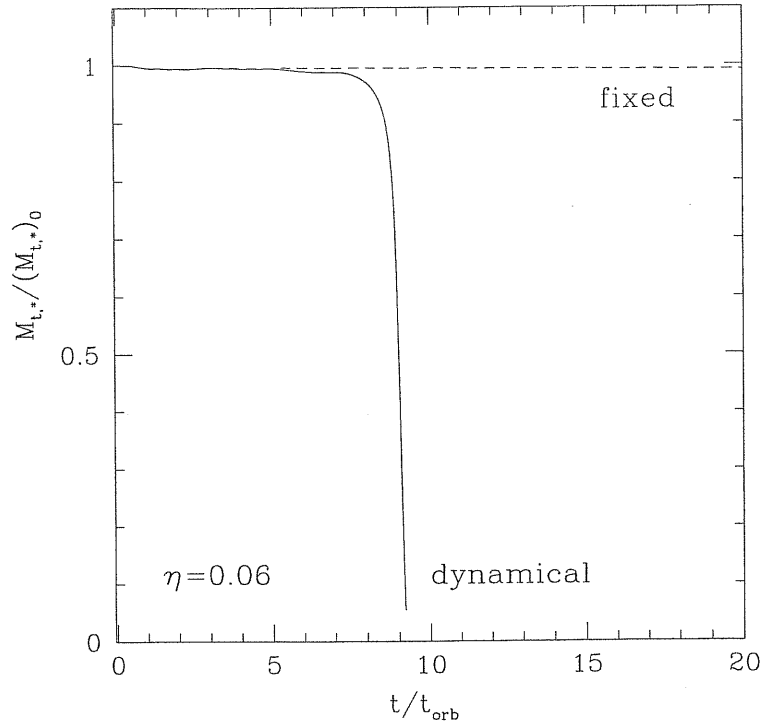


Figure 5.4: Evolution of the rest-mass of the toroidal neutron star (normalized to its initial value) in a dynamical (continuous line) and in a fixed (dashed line) spacetime simulation. The calculations refer to model (a) with an initial perturbation $\eta = 0.06$.

these properties depend on the details of the gravitational field the torus is experiencing, we expect some features to be generic and therefore to be present also in those circumstances in which the runaway instability is suppressed. To prevent the runaway instability from hiding the quasi-periodic response of the torus to perturbations, we have simply suppressed the instability by maintaining the spacetime fixed.

The most apparent consequence of this choice is that the disc is no longer dramatically accreted onto the black hole but remains at almost constant rest-mass for extremely long times. This is shown in Figure 5.4 where we present the evolution of the rest-mass of the disc (normalized to its initial value) in the two different cases of a dynamical and of a fixed background spacetime. The dotted line, in particular, refers to the model shown in Figure 5.2 with the same line type. Note that when the instability is fully developed and the calculations are interrupted, the toroidal neutron star has almost completely disappeared into the black hole, the residual mass being just $\sim 4\%$ of the initial one. Note also the the rest-mass in evolution with fixed spacetime is not exactly constant but shows a secular decay as a result of the small amounts of matter that are quasi-periodically accreted onto the black hole (cf. Figure 5.5).

Figure 5.5 is the equivalent of Figure 5.2, but shows the quasi-periodic accretion rate during the first 30 orbital periods for a simulation in which the spacetime is being held fixed. It is apparent that the both the dynamical and the fixed spacetime evolutions have a qualitatively similar behaviour: after the toroidal neutron star has relaxed at $t/t_{\text{orb}} \simeq 2$, it starts accreting

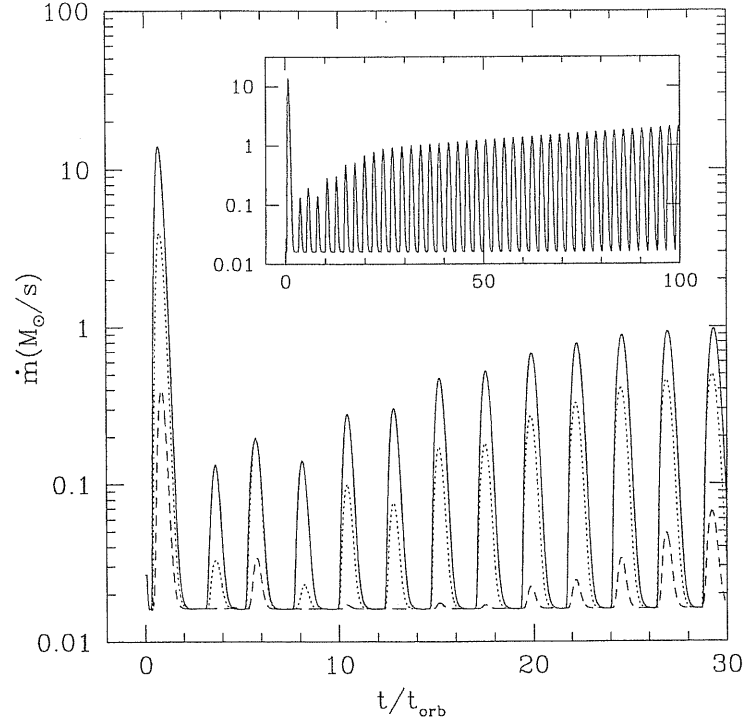


Figure 5.5: Rest-mass accretion rate in a fixed spacetime evolution. The solid, dotted and dashed lines correspond to $\eta = 0.006, 0.04, 0.02$, respectively.

matter onto the black hole at quasi-periodic intervals which do not depend on the strength of the perturbation. On the other hand, the amplitude of the mass accretion rate does depend on the value of η , producing larger amounts of accreted matter with increasingly larger values of η . (Note that when $\eta = 0.02$, the mass accretion rate seems to drop to an almost constant value for $6 \lesssim t/t_{\text{orb}} \lesssim 15$. This is just the consequence of the logarithmic scale used and, as shown in Figure 5.6, it is indeed possible to observe a periodicity also during this time interval.).

The periodicity at which this happens is remarkable if one considers that these curves are the result of numerical calculations in which each period requires several thousands of iterations. In addition to this, the periodic behaviour does not seem to be altered even when observed over 100 orbital timescales as shown in the inset of Figure 5.5, although some new secular features appear. Most notably, it is quite evident that the mass accretion rate oscillates around values that are increasingly larger. This is due to the fact that as the accretion proceeds, matter of increasingly larger rest-mass density reaches the cusp (the low-density, outer regions of the toroidal neutron star have already been accreted) and this will therefore produce a small secular growth in the amplitude of the mass flux.

The mass accretion rate is not the only quantity showing a periodic behaviour and indeed all of the fluid variables can be shown to oscillate periodically. In Figure 5.6 we have reported the time evolution, over 30 orbital periods, of the central rest-mass density of the toroidal neutron star normalized to its initial value. The small inset shows the evolution of the same

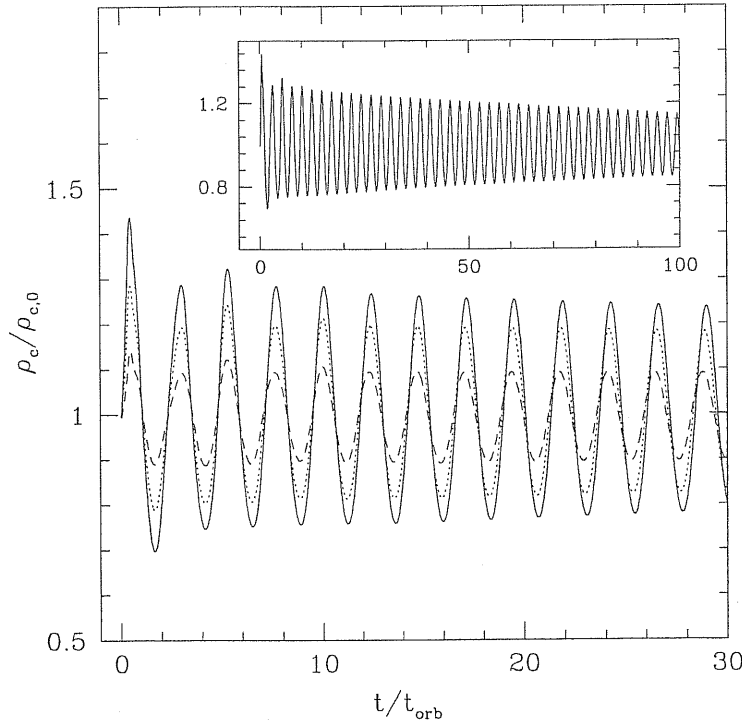


Figure 5.6: Evolution of the central rest-mass density normalized to its initial value. As in Figure 5.5, The solid, dotted and dashed lines correspond to $\eta = 0.006, 0.04, 0.02$, respectively.

quantity but for a much longer timescale and offers a direct evidence of the regularity of the oscillation. The inset should be contrasted with the evolution of the rest-mass density in a simulation with a dynamical spacetime. In that case, in fact, the oscillations in the rest-mass density do not remain (roughly) constant but grow exponentially as the runaway instability develops.

The periodic behaviour presented in Figure 5.6 is due to the fact that, as a result of the initial perturbation, the toroidal neutron star has acquired a linear momentum in the radial direction pushing it towards the black hole. When this happens, the pressure gradients become stronger to counteract the steeper gravitational potential experienced as the disc moves inward, thus increasing the central density and eventually pushing the disc back to its original position. This is illustrated more in detail in the different panels of Figure 5.7, which show the rest-mass distribution at different times during the oscillation.

More precisely, the sequence in Figure 5.7 shows that once the unperturbed toroidal neutron star [whose initial rest-mass density distribution is shown in the panel (a) of Figure 5.7] is subject to a radial velocity perturbation, it will then start moving towards the black hole [see panel (b)]. The existence of a potential barrier at $r \simeq 4.5$, however, causes a compression of the matter that is approaching the black hole [see panel (c)], giving rise to the first peak in the central density visible in Figure 5.6 at $t/t_{\text{orb}} \simeq 0.45$. Because the initial configuration is just marginally stable, a small fraction of the matter in the disc will be pushed over the maximum of the potential barrier and generate the first maximum in the rest-mass accretion

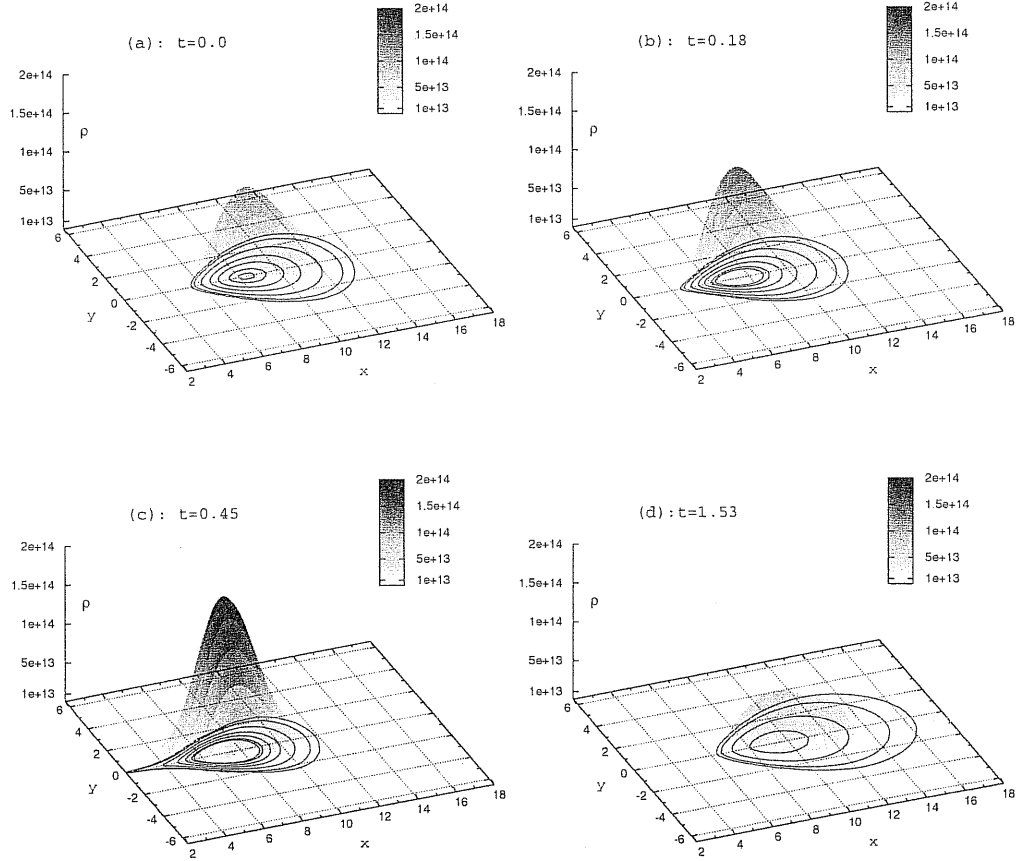


Figure 5.7: Rest-mass distributions of a perturbed toroidal neutron star at different times. The sequence illustrates the periodic behaviour during the first cycle of an oscillation excited with $\eta = 0.06$. The iso-density contours plotted on the (x, y) planes of the different panels can be used to trace the motion of the matter and are the same for all of the panels (in particular they refer to $\rho = 5.0 \times 10^{12}, 1. \times 10^{13}, 2.5 \times 10^{13}, 5.0 \times 10^{13}, 7.5 \times 10^{13}, 1.0 \times 10^{14}$, and 1.11×10^{14} , respectively). The times are expressed in terms of the orbital timescale, while the spatial coordinates are in terms of the gravitational radius.

rated reported in Figure 5.5. The presence of a net mass flux onto the black hole can directly be appreciated through iso-density contours shown in the (x, y) planes of Figure 5.7. Most notably, the lower density contours of panel (c) are closed on the event horizon and signal therefore a thin channel of accreting matter that is linking the toroidal neutron with the black hole (Note that because of this correlation between the rest-mass density and the accretion rate, the peaks in Figure 5.6 are slightly advanced in time with respect to the corresponding peaks in Figure 5.5.). As the compression increases, the pressure gradients become sufficiently strong to produce a restoring force on the toroidal neutron star which is then pushed back, away from the black hole. The restoring effect is so efficient that the disc overshoots the original position [panel (a)] and moves outwards to larger radii [panel (d)]. When this happens, the central density decreases and the mass accretion rate drops to its floor value; both of these effects are reflected in the first minima of Figures 5.5 and 5.6.

The dynamics of this process can also be followed by monitoring the total energy of a fluid element at the edge of the disc, $(u_t)_{\text{cusp}}$. If, at a given time, this quantity becomes larger than the potential barrier at the cusp, W_{cusp} , the corresponding fluid element will have sufficient kinetic energy to overcome the barrier but not sufficient angular momentum to sustain an orbital motion at the smaller radius at which it has been displaced. As a result, it will be forced to fall into the black hole, producing, after its free-fall time, a peak in the mass accretion rate.

Once triggered, the behaviour described above will repeat itself with great regularity and minimal numerical dissipation up until the numerical simulation is stopped or the toroidal neutron star has been entirely accreted by the black hole (cf. the small insets of Figures 5.5 and 5.6). During these oscillations, the pressure gradients act as restoring forces during the periodic transformation of the excess kinetic energy (transferred with the initial velocity perturbation) into potential gravitational energy and viceversa. As we shall comment later on, this is a first clue about the nature of these pulsations.

A final comment should be made about initial models consisting of initially stable toroidal neutron stars and that are therefore fully contained in barotropic surfaces smaller than their Roche lobe. Also for these models we have performed a number of simulations investigating their behaviour for different initial perturbations as well as for different initial masses. Overall, the behaviour observed with this initial data is qualitatively similar to the one already discussed for marginally stable discs, i.e. these models also develop the runaway instability or show a quasi-periodic behaviour depending on whether the spacetime evolution is taken into account or not.

The most significant difference introduced by these models is that smaller rest-mass accretion rates are generally produced for the same initial perturbation. This is clearly due to the fact that in stable models a large potential barrier is present at the cusp and is therefore increasingly more difficult for a fluid element to reach the black hole as a result of the initial perturbation.

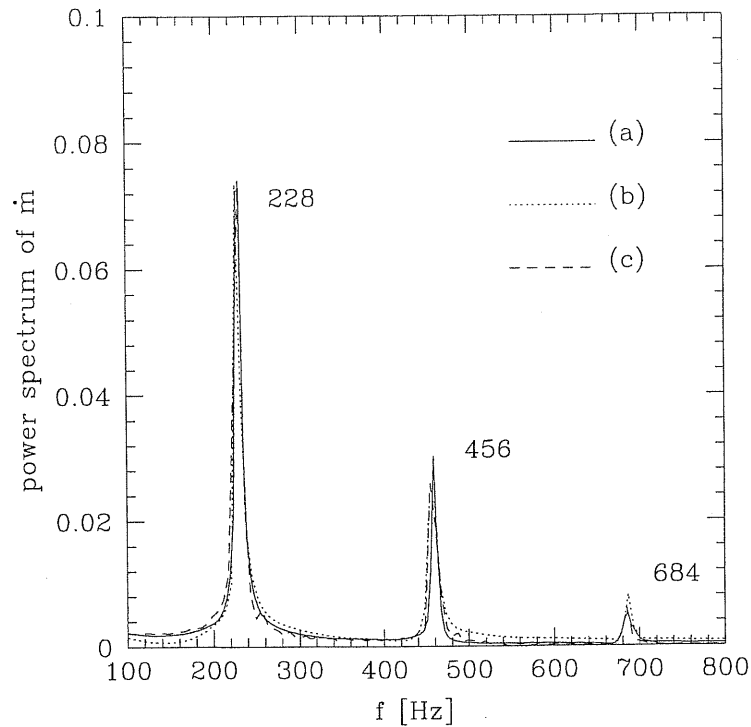


Figure 5.8: Power spectrum of the accretion rate for the models (a), (b), (c) and (d). The values on the vertical axis have been suitably normalized to match the power in the fundamental frequency and arbitrary units have been used.

Fourier Analysis

We have so far commented on the “quasi-periodic” behaviour of the hydrodynamical variables in response to the initial perturbation but we have not yet discussed how *periodic* is “quasi-periodic”. To this scope, we have calculated the Fourier transforms of the relevant fluid quantities for a number of different models. As a good representative case, we have reported in Figure 5.8 the power spectrum of the rest-mass accretion for models (a), (b) and (c) of Table 5.1. The Fourier transform has been calculated with data obtained with $\eta = 0.06$ and computed over a time interval going up to $t/t_{\text{orb}} \simeq 100$. Note that larger values of η produce correspondingly higher peaks, but the data in Figure 5.8 has been suitably normalized to match the power in the fundamental peak.

There are two important features of Figure 5.8 that need to be pointed out. The first one is that all of the three power spectra shown consist of a fundamental frequency f_0 (228 Hz for the models considered in Figure 5.8) and a series of overtones (at 456 and 684 Hz, respectively) in a ratio which can be determined to be $1 : 2 : 3 \dots$ and to an accuracy of a few percent (note that higher overtones have been measured, though with much lower power than the one found in the first three peaks.). Indeed, the presence of at least three peaks can be detected also in the power spectra of basically all of the fluid variables as well as in the overall displacement of the toroidal neutron star during the oscillations. It should also be noted that the power spectra of some fluid variables, such as that of the L_2 norm of the rest-

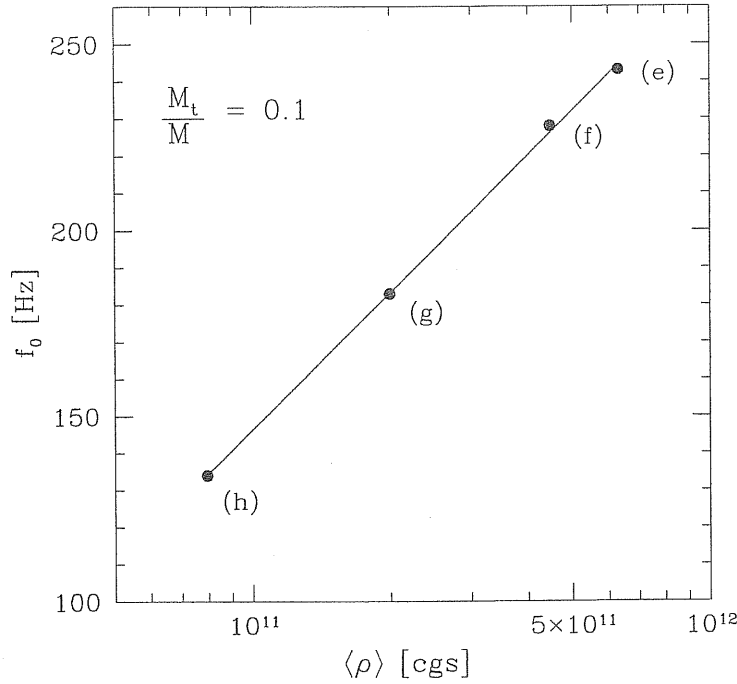


Figure 5.9: Dependence of the fundamental frequency f_0 on the average density in a sequence of models having the same mass ratios.

mass density, seem to show peaks with much lower power also at intermediate frequencies, and in particular at frequencies that are in a ratio $2 : 3 : 4 : 5 : \dots$ with respect to the fundamental one. Because the energy of these peaks is very close to the background noise, it is not yet clear whether these modes correspond to physical modes or are due to numerical errors. The second important feature is that the peaks in the power spectra have all the same frequencies, with differences below 0.1%. All of these properties are clearly suggesting that the quasi-periodic response observed is the consequence of some fundamental mode of oscillation of toroidal neutron stars and that, as for isolated neutron stars, it is probably independent even of the presence of a central black hole.

An important clue on the nature of these modes can be deduced if one considers that all of the models reported in Figure 5.8 refer to toroidal neutron stars with fixed spatial dimensions and specific angular momentum, but with varying mass (cf. Table 5.1). This has basically been obtained by suitably rescaling the polytropic constant in the EOS. However, another common property that these models share is that they all have the same initial average sound speed. This can be deduced if one bears in mind that for the fluid configurations considered here, the local sound speed can be calculated as $c_s = \sqrt{\gamma(\gamma - 1)p/[(\gamma - 1)\rho + \gamma p]}$, but this is effectively a constant for models with an initial density distribution given by equation (5.5). As a result, it is not surprising that the peaks coincide in all of the models if the oscillations discussed so far should be associated to the *p-modes* (or acoustic modes) of toroidal neutron star. Proving that the periodic oscillations observed in our simulations can

be interpreted as p -modes and validating the presence of modes at intermediate frequencies is something that needs a detailed perturbative analysis and will be discussed in Chapter 6 under certain simplifying assumptions. For the moment, let us just make the conjecture that these oscillations represent the vibrational modes of relativistic toroidal neutron stars having time-varying pressure gradients as the restoring force.

Since the peaks in the power spectra seem to depend on the average sound speed, the dependence of the fundamental frequency on the properties of the toroidal neutron star needs to be investigated along sequences different from the one considered in Figure 5.8. As an example, we have reported in Figure 5.9 the fundamental frequency f_0 as a function of the average rest-mass density inside the disc. The data refer to the evolution of models (e)–(h) that, we recall, have different dimensions, specific angular momenta and polytropic constants, but all have the same mass ratio M_t/M (cf. Table 5.1). An evident correlation exists between the fundamental frequency and the logarithm of the average rest-mass density, and a fit to the data has shown this correlation to be (cf. straight line in Figure 5.9)

$$f_0 = (122.55 \log \langle \rho \rangle - 1201.67) \text{ Hz} , \quad (5.26)$$

where $\langle \rho \rangle$ is expressed in cgs units. This expression is important as it indicates that a systematic study of these oscillations is possible for different initial models of toroidal neutron stars. Furthermore, it represents a first step towards a relativistic disc-seismology analysis for massive and vertically extended discs in General Relativity, in analogy to the one extensively developed for geometrically thin discs (Rodríguez *et al.* 2002; Kato 2001; Silbergleit *et al.* 2001).

Linear and Nonlinear Regimes

All of the quasi-periodic behaviour discussed so far is the consequence of the finite size perturbations that have been introduced in the initial configuration. It is also clear that there will be a *linear* regime in which the response of the toroidal neutron star will be linearly proportional to the perturbation introduced and a *nonlinear* regime when this will cease to be true. It comes then natural to investigate what is the strength of the perturbation which marks the transition between the two regimes and this is shown in Figure 5.2 where we have reported the averaged maximum rest-mass density measured during the oscillations and normalized to the central one in the toroidal neutron star.

A rapid look at Figure 5.2, in fact, reveals the presence of both the linear and nonlinear regimes with the first one being shown magnified in the inset, where the solid line shows the very good linear fit to the data. The transition between the two regimes seems to occur for $\eta \simeq 0.05$, with the nonlinear regime producing maximum amplitudes that are $\sim 35\%$ larger than the initial one. A careful analysis of the behaviour of the fluid variables shows that for perturbations with strength $\eta \gtrsim 0.05$, some of the kinetic energy which is confined to the lower order modes in the linear regime, tends to be transferred also to higher order modes (As remarked above, while in Figure 5.8 we have reported only the

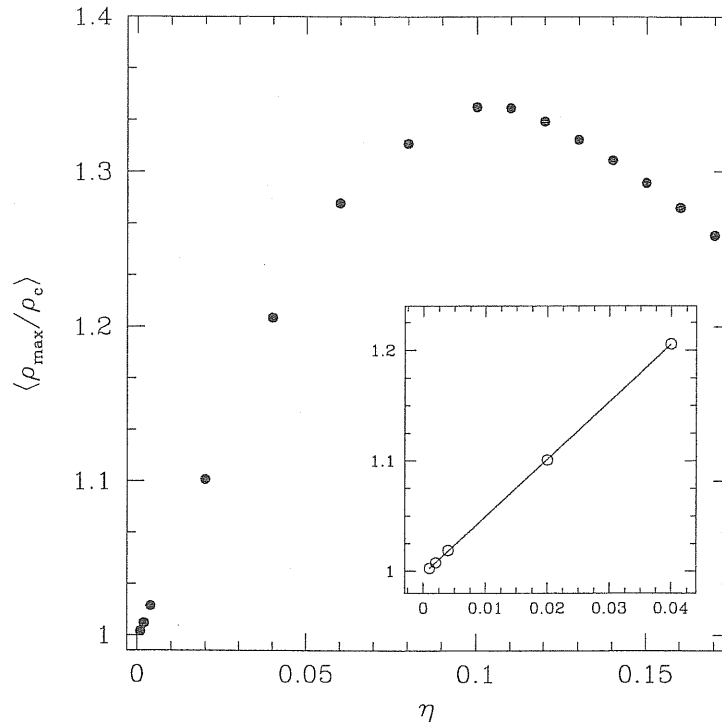


Figure 5.10: Averaged maximum rest-mass density measured during the oscillations and normalized to the central one in the toroidal neutron star. The small inset shows a magnification of the behaviour in the linear regime and the solid line shows a linear fit to the data. The data refers to model (a) and has been averaged over 10 orbital timescales.

first three peaks, the power spectrum shows the presence of higher order overtones, with up to the seventh one being clearly visible). The nonlinear coupling among different modes and the excitation of higher order overtones is often encountered in Nature where it serves to redistribute the excess kinetic energy before the production of shocks. In practice, the nonlinear coupling deprives of energy the fundamental mode (which is the one basically represented in Figure 5.2) and is therefore responsible for the decay of $\langle \rho_{\max}/\rho_c \rangle$ for $\eta \gtrsim 0.1$. Interestingly, when analysed in terms of the power spectra, this effect shows a very distinctive behaviour. As the nonlinear mode-mode coupling becomes effective, the amount of power in the fundamental mode becomes increasingly smaller as the strength of the perturbation is increased. At the same time, the conservation of energy transfers powers to the overtones, with the first ones reaching amplitudes comparable to the fundamental one and with the high order ones becoming more and more distinct from the background.

Determining the transition to the nonlinear regime represents an important result because it sets an approximate upper limit on the amplitude of the oscillations and, as will be discussed in the following Section, will be particularly relevant when discussing the emission of gravitational waves. It should also be noted that in the parameter range for η in which we have performed our calculations (i.e. $\eta \in [0.001, 0.1]$) the peak frequencies in the power spectra have not shown to depend on the values used for η , while, of course, their amplitude does. This is of course consistent with them being fundamental frequencies (and overtones)

but we also expect that as the perturbation amplitude enters in a fully nonlinear regime, other modes will probably be excited and appear in the power spectra.

A final comment should be made on the minimum value of the perturbation parameter η which is sufficient to produce the quasi-periodic behaviour described in the previous Section. On the basis of the continuum equations one expects that this minimum value is strictly larger than zero. However, we have performed simulations of marginally stable disc configurations with $\eta = 0$ and observed much of the phenomenology described above even if at rather minute amplitudes and with a larger numerical noise. This result, which has been encountered also in other accurate simulations of relativistic stars (Font *et al.* 2002), is not surprising and is simply indicating that in the absence of finite size perturbations, even the small truncation error introduced in the construction of the initial configuration is sufficient to excite the pulsations in these modes of vibration.

6 Gravitational wave emission

Despite our analysis has been restricted to axisymmetry, two simple considerations suggest that strong quasi-periodic gravitational waves should be expected together with the quasi-periodic accretion. The first of these considerations is that these oscillating tori undergo large and rapid variations of their mass quadrupole moment which, we recall, can be calculated as

$$I \equiv \int \rho \left(\frac{3}{2} z^2 - \frac{1}{2} \right) r^4 dr dz , \quad (5.27)$$

where $z \equiv \cos \theta$. It is therefore reasonable to expect that gravitational waves, with a strain proportional to the second time derivative of Eq. (5.27), should be produced during such oscillations³. The second consideration is suggested by expression (5.27), which shows that a configuration with toroidal topology and in which the rest-mass density has a maximum away from the origin will naturally have a large mass quadrupole simply because of the product ρr^4 in the integrand of this equation. This should be contrasted with what happens for stars with spherical topology and which have instead the largest densities at the centre. Both of these arguments justify the intense gravitational radiation and the large signal-to-noise ratio we have calculated using the Newtonian quadrupole approximation. Before discussing this in detail, however, it is useful to remind that since we are not solving the Einstein field equations, we are unable to account for that part of the gravitational radiation that is emitted by the black hole itself as a result of the quasi-periodic mass accretion. For the same reason we cannot estimate the amount of gravitational radiation that will be captured by the black hole and will not reach null infinity. Work is now in progress to calculate also this part of the radiative field using an approach in which the fluid evolution is used as a “source” for a perturbative form of the Einstein equations.

The presence of an azimuthal Killing vector has two important consequences. Firstly, the

³It is worth underlying that a deviation from axisymmetry is only a sufficient condition for the emission of gravitational waves and not, as sometimes stated (Mineshige *et al.* 2002), a necessary condition.

gravitational waves produced by these axisymmetric oscillating tori will carry away energy but not angular momentum, which is a conserved quantity in this spacetime. This is to be contrasted with the gravitational wave emission from non-axisymmetric perturbations in a massive torus orbiting a black hole, whose strength has been estimated in recent papers (van Putten 2001a,b; Mineshige *et al* 2002). Secondly, the gravitational waves produced will have a single polarization state (i.e. the “plus” one in our coordinate system, Kochanek *et al.* 1990), so that the transverse traceless gravitational field is completely determined in terms of its only nonzero transverse and traceless (TT) independent components, $h_{\theta\theta}^{TT} = -h_{\phi\phi}^{TT}$ (Zwerger & Müller, 1997). Adopting then Newtonian quadrupole approximation, we can calculate the gravitational waveform $h^{TT}(t)$ observed at a distance R from the source in terms of the quadrupole wave amplitude A_{20}^{E2} (see also Zwerger & Müller 1997)

$$h^{TT}(t) = F_+ \left(\frac{1}{8} \sqrt{\frac{15}{\pi}} \right) \frac{A_{20}^{E2}(t - R)}{R}, \quad (5.28)$$

where $F_+ = F_+(R, \theta, \phi)$ is the detector’s beam pattern function and depends on the orientation of the source with respect to the observer. As customary in these calculations, we will assume it to be optimal, i.e. $F_+ = 1$. The wave amplitude A_{20}^{E2} in Eq. (5.28) is simply the second time derivative of the mass quadrupole moment and can effectively be calculated without taking time derivatives, which are instead replaced by spatial derivatives after exploiting the continuity and the Euler equations (Finn, 1989; Blanchet *et al.* 1990; Rezzolla *et al.* 1999) to give

$$\begin{aligned} A_{20}^{E2} \equiv \frac{d^2 I}{dt^2} &= k \int \rho \left[v_r v^r (3z^2 - 1) + v_\theta v^\theta (2 - 3z^2) - v_\phi v^\phi \right. \\ &\quad \left. - 6z \sqrt{(v^r v_r)(v_\theta v^\theta)(1 - z^2)} - r \frac{\partial \Phi}{\partial r} (3z^2 - 1) \right. \\ &\quad \left. + 3z \frac{\partial \Phi}{\partial \theta} \sqrt{1 - z^2} \right] r^2 dr dz, \end{aligned} \quad (5.29)$$

where $k = 16\pi^{3/2}/\sqrt{15}$, and Φ is the gravitational potential. Since Eq. (5.29) is intrinsically Newtonian, it brings up two subtle issues when evaluated within a relativistic context. These basically have to do with the definition of the radial coordinate and with the definition of the gravitational potential appearing in Eq. (5.29). We have here opted for a pragmatical approach and treated r as the Schwarzschild radial coordinate and computed the gravitational potential in terms of the radial metric function as $\Phi = (1 - g_{rr})/2$, which is correct to the first Post-Newtonian (PN) order.

To validate the correct implementation of the integral in Eq. (5.29), we have considered a stationary torus in stable equilibrium, (i.e. $\Delta W_{\text{in}} < 0$) and without any perturbation besides

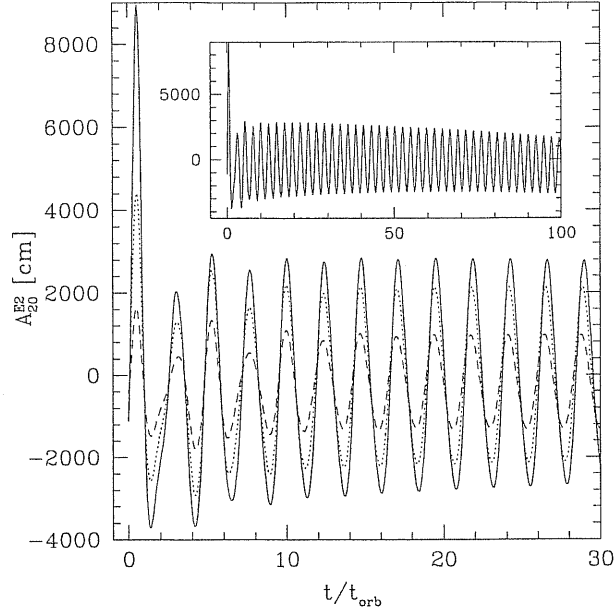


Figure 5.11: Time evolution of the second time derivative of the mass quadrupole, computed for model (a). The solid, dotted and dashed lines correspond to $\eta = 0.06, 0.04, 0.02$, respectively. The inset corresponds to the case $\eta = 0.06$ and spans 100 orbital timescales.

the one introduced by the truncation error (i.e. $\eta = 0$). Under these circumstances, no gravitational radiation can be produced and the terms in the square brackets of Eq. (5.29) should therefore compose to give zero identically. When computed numerically, we have found that the sum of these terms is effectively very small and of the order $\sim 10^{-2}$. This small residual in the integrand is due to approximations mentioned above (i.e. the use of the Schwarzschild radial coordinate and the first PN approximation to the gravitational potential) and should be interpreted, in practice, as a consequence of the fact that our tori are highly relativistic objects, whose equilibrium is not exactly given by the balancing of the Newtonian terms in the square brackets. Because of this residual, however, the wave amplitude A_{20}^{E2} will not average to zero over an oscillation but will have a net offset. We account for this by removing the overall residual in the evaluation of the wave amplitude (see also Dimmelmeier et al. 2002 for the discussion of an analogous technique).

Figure 5.11 shows the time evolution of the wave amplitude A_{20}^{E2} computed for model (a) via the expression (5.29). The different line types refer to $\eta = 0.06, 0.04$ and 0.02 , respectively. The computed gravitational waveform exhibits the same periodic behaviour discussed in the previous Sections for several fluid variables and shows oscillations that are in phase with the ones observed in the rest-mass density (cf. Figure 5.6). Furthermore, and as one would expect, the wave amplitude scales with the strength of the initial perturbation. Note that in the case of a simulation with a dynamical spacetime (not shown in Figure 5.11), the gravitational waveform does not maintain a constant in time amplitude but, as the runaway instability develops, the variations in A_{20}^{E2} become increasingly large, with an exponential

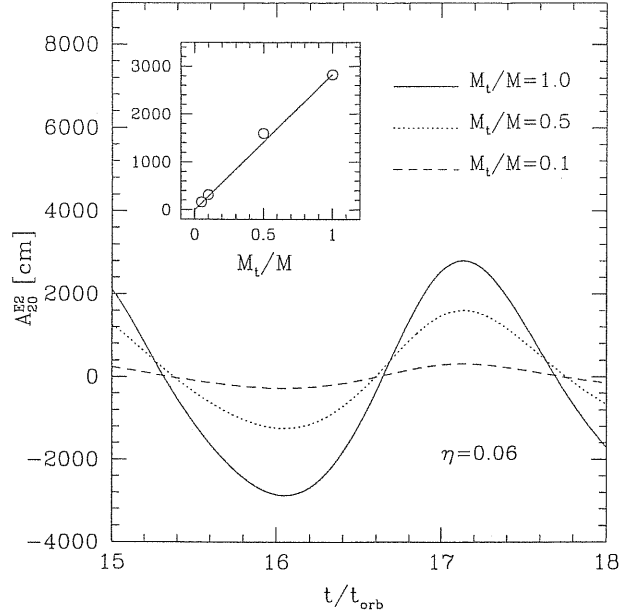


Figure 5.12: Dependence of the wave amplitude A_{20}^{E2} on the mass of the torus. The solid, dotted and dashed lines correspond to models (a), (b) and (c), respectively. The data refers to an initial perturbation of strength $\eta = 0.06$ and the inset shows a linear fit (solid straight line) of the data, including the one for model (d).

growth rate that matches the one observed in the density evolution.

Since the mass quadrupole and its second time derivative are linear in the rest-mass density [cf. Eq. (5.29)] and the latter exhibits a quasi-periodic behaviour upon perturbations, it is natural to expect the same linear dependence to be present also in terms of the mass ratio M_t/M . To verify this we have computed A_{20}^{E2} with an initial perturbation $\eta = 0.06$ for models (a), (b), and (c) that, we recall, differ only for their mass M_t . The results of this analysis are reported in Fig. 5.12 which shows the behaviour of A_{20}^{E2} over one representative period of oscillation and for the four models. As expected, the scaling of the amplitude is linear with M_t/M and this is more clearly shown in the inset where the wave amplitude [including the data for model (d)] is fitted linearly with M_t/M .

Using Eq. (5.28), it is possible to derive a phenomenological expression for the gravitational waveform that could be expected as a result of the oscillations induced in the toroidal neutron star. Restricting our analysis to the linear regime for which a simpler scaling is possible, we can express the transverse traceless gravitational wave amplitude for a source in the Galaxy in terms of the relevant parameters in our problem

$$h^{TT} \simeq 2.2 \times 10^{-21} \left(\frac{\eta}{0.04} \right) \left(\frac{M_t}{0.1 M_{2.5}} \right) \left(\frac{10 \text{ Kpc}}{R} \right), \quad (5.30)$$

where we have defined $M_{2.5} \equiv M/(2.5 M_{\odot})$.

Overall, expression (5.30) shows that, already in the linear regime for the perturbations, a non-negligible gravitational wave amplitude can be produced by an oscillating toroidal

neutron star orbiting around a black hole. This amplitude is indeed comparable with the average gravitational wave amplitude computed in the case of core collapse in a supernova explosion (Zwerger & Müller, 1997; Dimmelmeier *et al.* 2002) and can become stronger for larger perturbations or masses in the torus.

Of course, the large wave amplitudes suggested by expression (5.30) are referred to a galactic source and would become three orders of magnitude smaller for a source located at the edge of the Virgo cluster (i.e. at about 20 Mpc). What is important to bear in mind from expression (5.30) is that oscillating toroidal neutron stars can be sources of gravitational waves *as strong or stronger* than a core collapse and that could occur with *comparable* event rates⁴. This notion then serves as a useful normalization for estimating their relevance. It should also be noted, however, that a strong gravitational wave signal is just a necessary condition for the detectability of the gravitational wave emission from toroidal neutron stars and that additional conditions, such as a sufficiently high event rate or a good matching with the sensitivities of the detectors, need to be met. In the following Section we will discuss these issues in more detail and evaluate the detectability of these potential new sources of gravitational waves.

6.1 Detectability

To assess the detectability of toroidal neutron stars as sources of gravitational radiation we have computed the *characteristic* gravitational wave frequency and amplitude, as well as the corresponding signal-to-noise ratio for the interferometric detectors that will soon be operative. More specifically we have first computed the gravitational waveform in the frequency domain as the Fourier transform of the traceless transverse waveform in the time domain

$$\tilde{h}(f) \equiv \int_{-\infty}^{\infty} e^{2\pi i f t} h^{TT}(t) dt, \quad (5.31)$$

where $h^{TT}(t)$ is calculated according to Eq. (5.28) and where we have considered the gravitational wave amplitude computed over a *fixed* spacetime only. (Hereafter we will indicate $h^{TT}(t)$ simply as $h(t)$.) While in principle the integral in Eq. (5.31) is over an infinite time interval, in practice $h(t)$ is nonzero only over a finite interval τ_{life} . If the initial model chosen for the toroidal neutron star is not a stable one, this time interval is simply set by the timescale over which the runaway instability develops. If, on the other hand, the initial model is stable, the timescale over which a gravitational wave signal is produced can be considerably longer and is basically set by the time over which the star is able to survive, for instance, against non-axisymmetric instabilities. Hereafter, as a representative timescale for our “realistic” toroidal neutron star model we will assume $\tau_{\text{life}} \simeq 0.2$ s, while longer/shorter timescales will be assumed for models with smaller/larger initial perturbations (cf. Table 5.2).

⁴Of course not all of the collapsing iron cores will produce a black hole surrounded by a massive torus. On the other hand, and as discussed in Section 4.1, there is a multiplicity of scenarios in which toroidal neutron stars could be produced.

Table 5.2: Characteristic properties for the detection of the gravitational wave signal emitted by a toroidal neutron star. The first two columns show the mass of toroidal neutron star normalized to the black hole one, as well as the strength of the initial perturbation η . The following nine columns report the characteristic frequency, the characteristic wave strain and the signal-to-noise ratio computed for the three detectors LIGO I, LIGO II and EURO, assuming a galactic distance for a source detected by LIGO I, and an extragalactic distance for a source detected by LIGO II and EURO. The last column reports the characteristic lifetime for the existence of toroidal neutron stars that are unstable to the runaway instability.

M_t/M	η	f_c (Hz)		f_c (Hz)		f_c (Hz)	h_c		h_c		h_c	S/N		S/N		τ_{life} (s)
		LIGO I (10 Kpc)	LIGO I (20 Mpc)	LIGO II (20 Mpc)	LIGO II (20 Mpc)		LIGO I (10Kpc)	LIGO II (20 Mpc)	LIGO I (10 Kpc)	LIGO II (20 Mpc)						
0.50	0.06	234	230	230	230	319	5.2×10^{-20}	2.6×10^{-23}	2.4×10^{-23}	98.4	0.4	7.8	0.08			
0.50	0.04	227	223	223	223	243	4.3×10^{-20}	2.1×10^{-23}	2.1×10^{-23}	84.4	0.4	6.4	0.12			
0.50	0.02	230	229	229	229	238	2.7×10^{-20}	1.3×10^{-23}	1.3×10^{-23}	51.8	0.2	4.0	0.16			
0.25	0.06	231	228	228	228	248	2.9×10^{-20}	1.4×10^{-23}	1.4×10^{-23}	55.3	0.2	4.3	0.12			
0.25	0.04	227	224	224	224	239	2.4×10^{-20}	1.2×10^{-23}	1.2×10^{-23}	47.4	0.2	3.6	0.16			
0.25	0.02	229	228	228	228	234	1.4×10^{-20}	7.2×10^{-24}	7.2×10^{-24}	28.2	0.1	2.1	0.19			
0.10	0.06	230	226	226	226	250	1.2×10^{-20}	6.0×10^{-24}	6.0×10^{-24}	23.2	0.1	1.8	0.14			
0.10	0.04	229	227	227	227	239	1.0×10^{-20}	5.1×10^{-24}	5.0×10^{-24}	19.9	0.1	1.5	0.18			
0.10	0.02	228	227	227	227	234	6.1×10^{-21}	3.0×10^{-24}	3.0×10^{-24}	11.9	<0.1	0.9	0.20			

Given a detector whose response has a power spectral density $S_h(f)$, it is then useful to calculate *characteristic frequency* of the signal (Thorne, 1987)

$$f_c \equiv \left[\int_0^\infty \frac{\langle |\tilde{h}(f)|^2 \rangle}{S_h(f)} f df \right] \left[\int_0^\infty \frac{\langle |\tilde{h}(f)|^2 \rangle}{S_h(f)} df \right]^{-1} . \quad (5.32)$$

where $\langle |\tilde{h}(f)|^2 \rangle$ denotes an average over randomly distributed angles, that we have simply approximated as $\langle |\tilde{h}(f)|^2 \rangle \simeq |\tilde{h}(f)|^2$. The characteristic frequency provides a representative measure of where, in frequency, most of the signal is concentrated and is therefore relevant when the gravitational wave signal has a rather broad spectrum in frequency, as is the case in a gravitational core collapse. In the case of an oscillating toroidal neutron star, on the other hand, the signal is basically emitted at the fundamental frequency of oscillation (cf. Table 5.2), increasing the detectability.

Once the characteristic frequency is known, it can be used to determine the *characteristic amplitude* as

$$h_c \equiv \left[3 \int_0^\infty \frac{S_h(f_c)}{S_h(f)} \langle |\tilde{h}(f)|^2 \rangle f df \right]^{1/2} . \quad (5.33)$$

It worth remarking that when the characteristic frequency fits well in the minima of the sensitivity curves, the weight $S_h(f_c)/S_h(f)$ in the integral of (5.33) can significantly increase h_c when compared to h^{TT} . This is indeed what happens for the toroidal neutron stars considered here (cf. Table 5.2).

A direct comparison of characteristic amplitude with the root-mean-square *strain noise* of the detector

$$h_{\text{rms}} = \sqrt{f S_h(f)} , \quad (5.34)$$

finally determines the signal-to-noise ratio at the characteristic frequency as

$$\frac{S}{N} = \frac{h_c}{h_{\text{rms}}(f_c)} . \quad (5.35)$$

In Figure 5.13 we show the characteristic wave amplitude for sources located at a distance of $R = 10$ Kpc and $R = 20$ Mpc, as computed for two different values of the toroidal neutron star mass. These amplitudes have been computed for the expected strain noise of LIGO I and LIGO II, but the strain curves of VIRGO (that is similar in this frequency range, (Damour *et al.* 2001) and of EURO (Winkler, 2001) have also been reported for comparison. Interestingly, with small initial perturbations ($\eta = 0.04$) and mass ratios ($M_t/M = 0.1$), the computed characteristic amplitudes can be above the sensitivity curves of LIGO I for sources within 10 Kpc and above the sensitivity curve of EURO for sources within 20 Mpc. Both results suggest that a toroidal neutron stars oscillating in the Virgo cluster could be detectable by the present and planned interferometric detectors. Summarized in Table 5.2

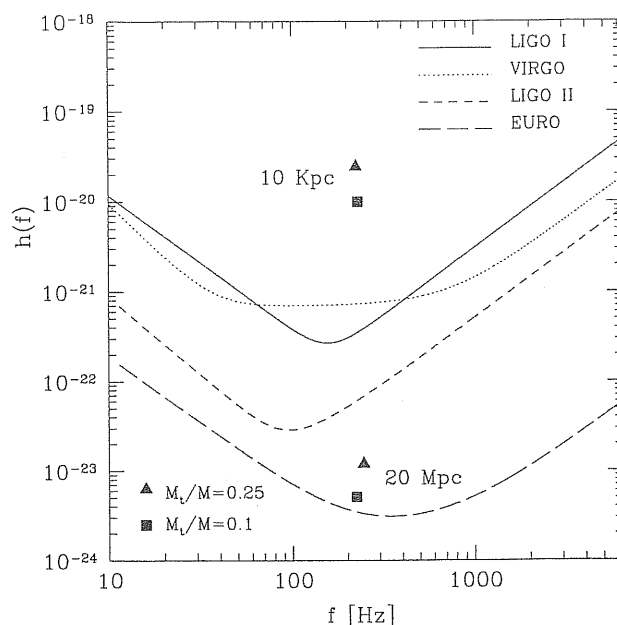


Figure 5.13: Characteristic wave amplitudes for a perturbed toroidal neutron star with $\eta = 0.04$. These amplitudes have been computed using the strain noise estimated for LIGO I for a source located at a distance of 10 Kpc and for LIGO II for a source at a distance of 20 Mpc. The numbers can also be effectively compared with the sensitivity curves of VIRGO and EURO that are similar in this frequency range. Different points refer to different mass ratios, with triangles indicating $M_t/M = 0.25$ and squares $M_t/M = 0.1$.

are the basic properties of the gravitational wave signal emitted by a toroidal neutron star. Most notably, we report: the characteristic frequency, the characteristic wave strain and the signal-to-noise ratios as computed for LIGO I, LIGO II and EURO, as well as the timescale over which the signal has been computed. All of these quantities refer to models with different initial perturbations and located at either 10 Kpc (for LIGO I) or 20 Mpc (for LIGO II and EURO).

The values for the signal-to-noise ratios reported in Table 5.2 are already interesting, but could become larger in at least three different ways. Firstly, and as remarked above, the signal strength computed does not include the exponential growth in the gravitational waveform that would accompany the runaway instability and that would provide an important contribution to the overall characteristic amplitude, as it is the case in binary mergers. As an illustrative example, consider that if the last 10 ms (i.e. roughly the last 5 oscillations) before the disappearance of an unstable torus at 10 Kpc with $M_t/M = 0.1$ and an initial perturbation with $\eta = 0.02$ were taken into account, they would yield a final $S/N \simeq 90$. This is to be contrasted with the corresponding $S/N = 11.9$, obtained when the oscillations are considered on a fixed spacetime (cf. Table 5.2). Secondly, we here have assumed the lifetime of the tori to be limited by the runaway instability to avoid the uncertainties related to the very existence of the instability when the specific angular momentum is not constant. On the other hand, a toroidal neutron star oscillating for a timescale longer than the one assumed in Table 5.2 will have a proportionally stronger signal even when the exponentially

growing phase is neglected. Again, as an example, it is useful to consider that the model yielding $S/N = 11.9$ over 0.2 s would produce a $S/N = 16.3$ if $\tau_{\text{life}} = 0.4$ s. Thirdly, an oscillating toroidal neutron star stable to the runaway instability would probably be subject to viscous or magnetic driven non-axisymmetric instabilities on timescales longer than the ones discussed here. Once the non-axisymmetric deformations are fully developed the torus would then have a mass quadrupole with much larger time variations, losing amounts of energy (and angular momentum) in gravitational waves larger than the ones computed here. The final point to be addressed is the rate at which the emission of gravitational waves from toroidal neutron stars could be detected. Although a realistic estimate of this rate is very difficult since very little is still known about the formation of toroidal neutron stars, it is reasonable to expect that these objects will be produced in a significant fraction of the events leading to core collapse in supernova explosions, binary neutron star mergers and tidal disruption of neutron stars orbiting a black hole. Because in a volume comprising the Virgo cluster all of these sources are among the most promising ones, overall our results indicate that toroidal neutron stars could potentially be new sources of gravitational radiation and certainly suggest a more accurate analysis.

More extended discussions will be provided in the Conclusions of the Thesis.

Chapter 6

Axisymmetric Oscillations of Vertically Integrated Discs

1 Introduction

Oscillations and waves in accretion discs have been much less studied than those in stars. This is partially due to the fact that both the existence and the importance of discs as fundamental astrophysical objects were recognized much later than stars. Nowadays, however, periodic and quasi-periodic variations are currently observed in different classes of astrophysical objects containing accretion discs. In black hole candidates, for instance, quasi-periodic oscillations (QPOs) in the *X*-ray band were first found in LMC X-1 (Ebisawa *et al.*, 1989), and later on in a large number of different analogous sources¹. Moreover, after the launching of the Rossi X-ray Timing Explorer (RXTE), a new class of sources was discovered, namely kiloHertz quasi-periodic oscillations². There are of course a number of parameters of the central compact object that can be expected to influence the *X*-ray variability. In case of black holes candidates, for instance, observational differences can be mostly due to the mass and to the spin rate of the black hole. However, the flow dynamics and therefore the emerging radiation will be also strongly affected by the accretion rate and by the magnitude and orientation of the specific angular momentum of the accreting matter. Although many different models have been proposed for the interpretation of the large phenomenology that is now available, there seems not to be a widely accepted mechanism for most of the observed sources (see van der Klis, 2000 for a review; Lewin *et al.*, 1995).

As in stars, oscillatory motions are in general the consequence of restoring forces responding to perturbations and these offer a way for classifying oscillations. In particular, in non rotating hydrodynamical systems, without magnetic fields, the main restoring forces are due to pressure gradients and to the stratification of entropy and/or chemical composition. The first ones give rise to *acoustic waves*, while the second one is responsible for the *internal gravity waves*. The presence of rotation is responsible for additional modes of oscillations

¹Reviews of some of the observed QPOs features in black-hole candidates can be found in Novak (1995) and Tanaka & Lewin (1995).

²The first two sources in which kHz QPOs were detected were 4U 1728-34 and Sco X-1 (Van der Klis 1996).

appearing in a physical system. In stars, for instance, the Coriolis force due to rotation produces the so called r -modes. Moreover, a general linear perturbation in a star can be written as the sum of quasi-normal modes characterized by the indices (l, m) of the spherical harmonics Y_l^m . A further effect of rotation on these modes is to remove the degeneracy that exists in the index m , thus splitting a non rotating mode of index l into $2l + 1$ different modes (Stergioulas, 1998).

In accretion discs, on the other hand, the major restoring force against gravitational attraction is the centrifugal force, which is responsible for the appearance of so called *inertial oscillations* tightly related to the orbital motion of the disc. A second peculiar restoring force in accretion discs is the vertical gravitational field, which causes *corrugation waves*. If a portion of the disc plane is perturbed in the vertical direction, in fact, the vertical component of the gravitational field will produce a harmonic oscillation across the equatorial plane with oscillation frequency equal to the orbital frequency (see Kato, Fukue & Mineshige, 1998, for a complete overview on classification of disc oscillations). Referring to the fundamental frequency, disc oscillations can be roughly classified as

- Modes of higher frequency; also called inertial-acoustic waves, or *p-modes*.
- Modes of lower frequency; also called inertial gravity waves, or *g-modes*.
- Corrugation waves, with no nodes in the vertical direction.

It should be emphasized that this terminology can be somewhat confusing, since it does not match the convention adopted for stellar oscillations, where the naming of the gravity mode is used for denoting “internal gravity waves”.

Two complementary approaches have been followed for studying the perturbations of equilibrium models of geometrically thin accretion discs. The first one is a local approach, and it has been extensively used to investigate the propagation of waves with the inclusion of many different physical effects, such as buoyancy, atmospheres and magnetic fields (see, among the others, Lubow & Ogilvie, 1998). Being local, these approaches derive dispersion relations, where the frequency of the perturbation is expressed as a function of a given radial coordinate and as the combination of different contributions (Kato, 2001). The second approach is a global one and it is based on the fact that, under suitable conditions, Eulerian perturbations to all physical quantities can be expressed through a single function satisfying a second order partial differential equation, which is then solved as an eigenvalue problem, the eigenvalue being the frequency of oscillation (see Ipser & Lindblom, 1992; Silbergleit *et al.*, 2001; Novak & Wagoner, 1991).

In the previous Chapter we have shown that global modes of oscillation might be excited in non Keplerian discs as a response to a given perturbation in the initial velocity field. We have also argued that the restoring forces responsible for this behaviour appear to be pressure gradients. In this Chapter we present a perturbative analysis of axisymmetric relativistic discs in the Cowling approximation. Since the discs we are considering are non Keplerian

and geometrically thick, a full two-dimensional treatment would be required, to accomplish for the coupling of the oscillations in the radial direction with those in the vertical one (Kato, 2001). However, we will consider a simpler system where the vertical structure of the disc is accounted for by integrating each quantity along the direction perpendicular to the equatorial plane of the disc. In our analysis we will follow both the local and the global approach. The first one will allow us to derive the local dispersion relation obeyed by the oscillations in relativistic non Keplerian discs, while the global approach will provide us the eigenfrequencies of the system resulting from the solution of an eigenvalue problem. In the height of the results obtained with this perturbative analysis, the dynamical behaviour discussed in Chapter 5 will find a consistent explanation.

The system of units chosen in this Chapter is given by setting $G = c = M_{\odot} = 1$.

2 Local approach in the Newtonian case

In this Section we first present the derivation of the dispersion relation in the Newtonian case. This is a useful exercise to clarify the concept of local analysis and introduce the most important assumptions which will remain valid in our extension to the general relativistic case, to be considered with more details in Section 3. Moreover, a comparison between the physical properties of Newtonian and relativistic oscillations clarifies the differences among the two regimes and is very useful for understanding the basic concepts of *diskoseismology*.

2.1 Basic assumptions

We here neglect the perturbations in the gravitational potential (this is referred to as the Cowling approximation, Cowling 1941), and consider fluid configurations that are not self-gravitating.

We first introduce a cylindrical coordinate system, (ϖ, φ, z) , whose origin is at the center of the central object, the z axis being taken in the direction of the disc rotation. Physical quantities like density and pressure are integrated in the direction vertical to the disc and the dependence of these quantities on the vertical coordinate is therefore neglected. As a consequence of this assumption, the equation of state is defined as a relation between integrated quantities

$$P = \mathcal{K} \Sigma^{\Gamma}, \quad (6.1)$$

where we have defined the vertically integrated pressure, P , and the vertically integrated surface density, Σ , as

$$P \equiv \int_{-H}^H p dz, \quad (6.2)$$

and

$$\Sigma \equiv \int_{-H}^H \rho dz, \quad (6.3)$$

respectively³, H being the local thickness of the disc. Note that equation (6.1) mimics a polytropic equation of state, with the constants \mathcal{K} and Γ playing the role of the polytropic constant and of the adiabatic index, respectively. However, this analogy should be taken with care, since the equation of state (6.1) does not represent a vertically integrated equation of state (unless the adiabatic index γ appearing in $p = \kappa\rho^\gamma$ is equal to unity).

The unperturbed fluid is supposed to be in circular non Keplerian motion with angular velocity Ω , and we will define the averaged components of velocity in the ϖ and in the φ directions as

$$U \equiv \frac{1}{2H} \int_{-H}^H v^\varpi dz, \quad (6.4)$$

and

$$W \equiv \frac{1}{2H} \int_{-H}^H v^\varphi dz, \quad (6.5)$$

respectively⁴. Furthermore, as another approximation of our approach, the component of the fluid normal to the equatorial plane will be neglected.

2.2 Governing Equations

Since the motion in the vertical direction is neglected, the basic hydrodynamical equations reduce to (see Shu 1992 for a general analysis)

$$\partial_t \Sigma + \partial_\varpi(\Sigma U) + \frac{1}{\varpi} \Sigma U + \frac{1}{\varpi} \partial_\varphi(\Sigma W) = 0, \quad (6.6)$$

$$\partial_t U + U \partial_\varpi U + \frac{W}{\varpi} \partial_\varphi U - \frac{W^2}{\varpi} = -\frac{1}{\Sigma} \partial_\varpi P - \partial_\varpi \Psi, \quad (6.7)$$

$$\partial_t W + U \partial_\varpi W + \frac{W}{\varpi} \partial_\varphi W + \frac{UW}{\varpi} = -\frac{1}{\Sigma} \frac{1}{\varpi} \partial_\varphi P - \frac{1}{\varpi} \partial_\varphi \Psi, \quad (6.8)$$

$$\nabla^2 \Psi = 4\pi S, \quad (6.9)$$

which represent the continuity equation, the Euler equations in the ϖ and φ directions and the Poisson equation, respectively. The quantity Ψ in (6.7)-(6.9) represents the vertically integrated gravitational potential, defined analogously to (6.2)-(6.3), whereas S is the vertically integrated rest mass density of the central source. Stationary and axisymmetric disc models can be built after setting to zero the time derivatives in the system (6.6)-(6.9), and these will serve as the equilibrium solutions of the perturbative analysis.

2.3 Perturbed Equation

The basic equations for the oscillation of the disc are obtained by perturbing the equilibrium configurations constructed as explained above. We confine our attention to the study of

³Note that the dimension of P and Σ is that of the original p and ρ multiplied by a length.

⁴Note that the dimension of U and W is that of a velocity.

infinitesimal pulsations which may be approximated as linear perturbations of the equilibrium fluid states. Furthermore, we will assume a harmonic dependence of the perturbed quantities as

$$\begin{pmatrix} \delta U \\ \delta W \\ q \end{pmatrix} \sim e^{-i\sigma t + ik\varpi}, \quad (6.10)$$

where σ is the frequency (in general complex) of the perturbation, k is a real number and the perturbation in the pressure has been parametrized by introducing the quantity $q \equiv \delta P/\Sigma$. Note that in (6.10) the symbol δ stands for the Eulerian perturbation, and that, according to the Cowling approximation, $\delta\Psi = 0$ everywhere in the equations. It should be stressed that having a radial dependence of the perturbations of the type $\sim e^{ik\varpi}$ is the fundamental property of the local approach, according to which the radial wavelength of the perturbations $2\pi/k$ is smaller than the scale length of the radial variations in the equilibrium properties of the disc. This assumption is usually referred to as the Wentzel-Krammers-Brillouin (WKB) approximation, summarized in the box below.

WKB Approximation: The radial dependence of any complex perturbation quantity can be written in terms of an amplitude and a phase. For instance, the gravitational potential on the equatorial plane can be written as

$$\Psi(\varpi, z=0) = \psi(\varpi)e^{ik(\varpi)}, \quad (6.11)$$

where both ψ and k are taken to be real. The WKB approximation corresponds to the assumption that the phase $k(\varpi)$ varies rapidly as compared to the amplitude $\psi(\varpi)$

$$\frac{dk}{d\varpi} \gg \frac{1}{\psi} \frac{d\psi}{d\varpi}. \quad (6.12)$$

Quite often, the logarithmic derivative of ψ with respect to ϖ turns out to be of order $1/\varpi$, and the WKB approximation can also be written as

$$\frac{dk}{d\varpi} \varpi \gg 1. \quad (6.13)$$

It is often the case that $dk/d\varpi \sim k/\varpi$, which reduces the condition (6.13) to the requirement that k , called the *radial wave number*, is much larger than one.

When perturbing the system (6.6)-(6.8) we assume the perturbations to have small amplitudes and drop quantities that enter the governing equations of any order higher than linear. Subtracting the zeroth-order set given by the equilibrium solution from the set of the perturbed equations, we obtain the linearized perturbation equations as (Shu, 1992)

$$i\sigma\delta U + 2\Omega\delta W = ikq, \quad (6.14)$$

$$-i\sigma\delta W + [2\Omega + \varpi\partial_{\varpi}\Omega]\delta U = 0, \quad (6.15)$$

$$-i\sigma\frac{q}{c_s^2} + ik\delta U = 0, \quad (6.16)$$

where $c_s^2 = \Gamma p/\Sigma$ is the sound speed. We can now cast these equation into a simple real matrix form as

$$\begin{bmatrix} \sigma & 2\Omega & -k \\ \frac{\kappa_r^2}{2\Omega} & \sigma & 0 \\ kc_s^2 & 0 & -\sigma \end{bmatrix} \begin{bmatrix} i\delta U \\ \delta W \\ iq \end{bmatrix} = 0, \quad (6.17)$$

where κ_r is the *epicyclic frequency* defined as

$$\kappa_r^2 = 2\Omega \left[2\Omega + \varpi \frac{d\Omega}{d\varpi} \right]. \quad (6.18)$$

Being an homogeneous linear system, a non-trivial solution to (6.17) exists if the determinant of the coefficients matrix is equal to zero

$$-\sigma^3 + k^2 c_s^2 \sigma + \kappa_r^2 \sigma = 0, \quad (6.19)$$

which then provides the dispersion relation

$$\sigma^2 = \kappa_r^2 + k^2 c_s^2. \quad (6.20)$$

This approximate form of the dispersion relation for disc oscillations was first obtained by Okazaki *et al.* (1987) and was re-derived by several authors in more general situations (see Nowak & Wagoner (1992), Ipser (1994), Silbergleit *et al* (2001)). The two terms in the dispersion relation (6.20) are most easily interpreted when considered separately. To this scope, consider a disc composed of collisionless particles and with specific angular momentum increasing outward. A fluid element displaced perturbed infinitesimally from its equilibrium orbit, while maintaining its angular momentum unchanged, will start oscillating in the radial direction due to the restoring force resulting from rotation. These oscillations are called *inertial oscillations*, and their frequency is the epicyclic frequency $\kappa_r(\varpi)$. In compressible fluids, on the other hand, an additional restoring force due to pressure gradients is present, which produces *acoustic oscillations* with frequency $k^2 c_s^2$. Both these terms contribute to the right hand side of the dispersion relation (6.20) and are collectively referred to as “inertial-acoustic waves”. Novak & Wagoner (1991, 1992) have shown that there are two general classes of solutions to the dispersion relation (6.20), namely “high” and “low” frequency

modes. We will in general identify the high frequency ($\sigma^2 \geq \kappa_r^2$) modes with acoustic p -modes (Kato, 1980) and the low frequency ($\sigma^2 \leq \kappa_r^2$) ones with internal g -modes (Okazaki, 1987), although the dispersion relation for the latter is more complicated than (6.20) [see Kato, 2001].

3 General Relativistic Discs

One of the most important differences between Newtonian and relativistic disc oscillations is that General Relativity can trap normal modes of oscillations near the inner edge of an accretion disc (see the pioneering paper of Kato & Fukue, 1980). The trapping is related to the fact that, in relativistic discs, the radial distribution of the epicyclic frequency has a maximum at a certain radius [cf. Eq. (6.37) below; Okazaki *et al* 1987]. After describing the general physical setup, we will present in Section 3.2 the local approach to the perturbative analysis, as done for Newtonian discs. This will allow us to derive a new relativistic dispersion relation for a relativistic non Keplerian orbital motion. In Section 3.3, on the other hand, we will also consider a global approach and discuss the numerical solution of a system of ODEs in the perturbed quantities.

A comment about the Cowling approximation is also necessary at this point. The extension of the Cowling approximation to the general relativistic case, in fact, is obtained by setting all the metric perturbations to zero. Numerical studies by Lindblom & Splinter (1990) have shown that this can accurately predict the frequencies of the higher order p -modes in the context of non-rotating relativistic stellar models. Remarkably, for a fluid configuration in which the self-gravity is neglected, like the one considered here, the Cowling approximation is an exact description of the pulsations (Ipser & Lindblom, 1992).

3.1 Assumptions and Governing Equations

In order to make the comparison with the results presented in Chapter 5 more direct, we will limit our attention to a Schwarzschild background spacetime. Moreover, since the quantities in the discs considered here are characterized by a small dependence on the spherical angular coordinate θ , it is useful to expand the Kerr metric (with spin of the black hole set equal to zero) around the equatorial plane and retain the resulting form at the zeroth-order in the ratio (z/r) , so as to obtain the Schwarzschild metric in cylindrical coordinates as (Novikov & Thorne, 1973)

$$ds^2 = -e^{2\nu} dt^2 + e^{2\lambda} d\varpi^2 + dz^2 + \varpi^2 d\varphi^2, \quad (6.21)$$

where the potentials ν and λ are related to the gravitational mass M of the black hole by $e^{2\nu} = 1 - 2M/\varpi = e^{-2\lambda}$. The basic equations to be solved in order to construct equilibrium models for perfect fluids are the continuity equation $\nabla_\alpha(\rho u^\alpha) = 0$ and the conservation of energy-momentum, $\nabla_\alpha T^{\alpha\beta} = 0$, where $T^{\alpha\beta}$ are the components of the stress energy tensor, as already defined in Chapter 5 [cf. eq. (5.1)]. Since we are dealing with a curved background

spacetime, it is useful to introduce an orthonormal tetrad carried by the local static observer and defined by the one-form with components

$$\omega^{\hat{t}} = e^\nu dt, \quad \omega^{\hat{\varpi}} = e^\lambda d\varpi, \quad \omega^{\hat{z}} = dz, \quad \omega^{\hat{\varphi}} = \varpi d\varphi. \quad (6.22)$$

In this frame, the components of the four velocity of the fluid are denoted by $u^{\hat{\mu}}$ (with $\mu = t, \varpi, z, \varphi$), and the 3-velocity components are given by

$$v^{\hat{i}} = \frac{u^{\hat{i}}}{u^{\hat{t}}} = \frac{\omega^{\hat{i}}(u)}{\omega^{\hat{t}}(u)}. \quad i = \varpi, z, \varphi \quad (6.23)$$

In analogy to the Newtonian case presented in Section 2, we introduce the 'vertically integrated' quantities, such as pressure and density, in the same way as (6.2) and (6.3) and assume that they obey a polytropic equation of state like (6.1). The equilibrium solution to consider in the perturbative analysis is given by solving equation (5.3) of Chapter 5, whose radial component we rewrite here as

$$\frac{\partial_{\varpi} p}{e + p} = - \frac{\nu_{,\varpi} e^{2\nu} - \varpi \Omega^2}{e^{2\nu} - \varpi^2 \Omega^2}. \quad (6.24)$$

However, since we want to deal with vertically integrated quantities, both the left and the right hand side of equation (6.24) must be integrated in the direction perpendicular to the equatorial plane, obtaining

$$\begin{aligned} \int_{-H}^H \frac{\partial_{\varpi} p}{e + p} dz &= - \int_{-H}^H \frac{\nu_{,\varpi} e^{2\nu} - \varpi \Omega^2}{e^{2\nu} - \varpi^2 \Omega^2} dz \\ \frac{\partial_{\varpi} P}{E + P} &= - \frac{\nu_{,\varpi} e^{2\nu} - \varpi \Omega^2}{e^{2\nu} - \varpi^2 \Omega^2}, \end{aligned} \quad (6.25)$$

where we have used the definition (6.2) and have taken advantage of the fact that the right hand side of (6.24) is a function of the cylindrical radial coordinate only. Note also that the vertically integrated energy density E has been defined analogously to (6.2), namely as

$$E \equiv \int_{-H}^H e dz. \quad (6.26)$$

Equation (6.25) is of course an approximation, but a rather convenient one when dealing with discs confined in small angles around the equatorial plane. Note also that the rest mass density of the disc can be defined as

$$M_d \equiv \int_{r_{\text{in}}}^{r_{\text{out}}} 2\pi \varpi \Sigma u^t \varpi d\varpi, \quad (6.27)$$

with r_{in} and r_{out} being the inner and the outer edge of the disc on the equatorial plane, where the cylindrical and the spherical radial coordinates coincide⁵.

As done in the Newtonian case, the linear perturbation equations are obtained by expanding the variables around their equilibrium values and by substituting them in the hydrodynamics equations, while keeping the first order terms. However, in order to distinguish the local analysis from the global one, we will temporarily assume the perturbation to have just the harmonic time dependence, in the form given by $\delta P, \delta v^i \sim \exp(-i\sigma t)$. The resulting perturbed equations can then be written as

$$0 = -i\sigma \frac{E+P}{\Gamma P} Q + e^{\nu-\lambda} \partial_{\varpi}(\delta V^{\hat{\varpi}}) + \left[2\nu_{,\varpi} + \frac{1}{\varpi} - \frac{A_{,\varpi}}{2A} + \frac{P_{,\varpi}}{\Gamma P} \right] e^{\nu-\lambda} \delta V^{\hat{\varpi}} + i\sigma \frac{\varpi e^{\nu}}{A} \Omega \delta v^{\hat{\varphi}}, \quad (6.28)$$

$$0 = i\sigma e^{\nu-\lambda} \delta V^{\hat{\varpi}} + 2e^{\nu-2\lambda} \Omega \left(1 + \varpi \frac{P_{,\varpi}}{E+P} \right) \delta V^{\hat{\varphi}} + A e^{-2\lambda} \partial_{\varpi} Q, \quad (6.29)$$

$$0 = -i\sigma \delta V^{\hat{\varphi}} + \left(\Omega_{,\varpi} + \frac{2}{\varpi} \Omega - 2\nu_{,\varpi} \Omega \right) \varpi e^{-\lambda} \delta V^{\hat{\varpi}}, \quad (6.30)$$

where $Q \equiv \delta P/(E+P)$ and $A \equiv (u^t)^{-2}$. Note that, according to our approach, we have defined the averaged quantities $\delta V^{\hat{\varphi}}$ and $\delta V^{\hat{\varpi}}$ as

$$\delta V^{\hat{\varpi}} \equiv \frac{1}{2H} \int_{-H}^H \delta v^{\hat{\varpi}} dz, \quad (6.31)$$

and

$$\delta V^{\hat{\varphi}} \equiv \frac{1}{2H} \int_{-H}^H \delta v^{\hat{\varphi}} dz, \quad (6.32)$$

respectively.

3.2 Local Analysis

The local analysis of the system (6.28)-(6.30) can be performed by reintroducing a radial dependence of the perturbed quantities as $\delta P, \delta V^i \sim \exp(ik\varpi)$, where $k(\gg 1)$ is the radial wave number. Although simplified, the number of terms in (6.28)-(6.30) can be further reduced and, in particular, the third and the fourth term can be neglected in the numerical computations. The third term, in fact, is always much smaller than the second one, which contains the radial derivative of the exponential term $\sim \exp(ik\varpi)$, and is therefore $\propto k \gg 1$. Similarly, the fourth term can be discarded according to the following argument. The first term is roughly $\delta P/(\Gamma P) \sim Q/c_s^2$, where c_s is the local sound speed, while the fourth one is

⁵In the following, we will denote the relevant radii of the disc models on the equatorial plane with the usual spherical radial coordinate r .

$\sim (\varpi\Omega)\delta v^{\hat{\phi}}$. The ratio of these two terms is then given by

$$\frac{[4\text{th}]}{[1\text{st}]} \sim \mathcal{O}\left(\frac{\delta V}{Q}\right) \mathcal{O}(|\text{typical velocity}|^3). \quad (6.33)$$

While $(\delta V/Q)$ is the ratio of two perturbed quantities, and is order of unity, the typical velocity of our system can be estimated by considering the orbital velocity at the marginally stable circular orbit, which is $\sim 1/\sqrt{6}$, so that the ratio in (6.33) is much smaller than unity.

After re-defining $\delta U \equiv i\delta V^{\hat{\varpi}}$ and $\delta W \equiv \delta V^{\hat{\phi}}$, the linearized perturbation equations in the unknowns δU , δW and Q can again be written as an homogeneous linear system

$$\mathcal{M}(k, \sigma) \begin{bmatrix} \delta U \\ \delta W \\ Q \end{bmatrix} = 0,$$

where the matrix \mathcal{M} is a function of k and σ . By imposing the determinant of \mathcal{M} to be zero, we can obtain the dispersion relation of the wave as

$$\sigma^3 - \sigma e^{-2\lambda} \left[\left(1 + \varpi \frac{P, \varpi}{E + P} \right) 2\Omega(2\Omega + \varpi\Omega_{, \varpi} - 2\varpi\nu_{, \varpi}\Omega) + e^{2\nu}(1 - e^{-2\nu}\varpi^2\Omega^2)k^2 \frac{\Gamma P}{E + P} \right] = 0, \quad (6.34)$$

whose non-trivial solution is

$$\sigma^2 = k^2 c_s^2 \frac{e^{2(\nu-\lambda)}(1 - e^{-2\nu}\varpi^2\Omega^2)}{1 + c_s^2 \Gamma/(\Gamma - 1)} + \kappa_r^2. \quad (6.35)$$

The dispersion relation (6.35) represents the relativistic generalization of (6.20) in which the epicyclic frequency κ_r is given by

$$\kappa_r^2 \equiv 2\Omega(2\Omega + \varpi\Omega_{, \varpi} - 2\varpi\nu_{, \varpi}\Omega)e^{-2\lambda} \left(1 + \varpi \frac{P, \varpi}{E + P} \right). \quad (6.36)$$

A few comments should now be made about this expression. The first and most obvious one is that it reduces to (6.18) in the Newtonian limit. Secondly, if the term involving pressure gradients is neglected⁶, (6.36) reduces to the expression derived by Okazaki *et al.* (1987) and valid for the keplerian motion in the Schwarzschild spacetime (in spherical coordinates)

$$\kappa_{r, \text{Kep}}^2 = \left(1 - \frac{6M}{r} \right) \frac{1}{r^3}. \quad (6.37)$$

Finally, it predicts a zero epicyclic frequency for a constant angular momentum orbital

⁶Note that this term can be written explicitly as the contribution of the curvature and of the orbital motion only [cf. Eq. 6.25].

motion. This was a trivial statement in the Newtonian framework, where (6.18) vanishes if $\ell \equiv \Omega\varpi^2 = \text{const}$ but not necessarily so in General Relativity. Furthermore, this is the case only with a suitable definition of the specific angular momentum. Recalling the definition given in Chapter 5, $\ell \equiv -u_\phi/u_t$, we have

$$\begin{aligned} \frac{d\ell}{d\varpi} &= \frac{d}{d\varpi}(\varpi^2 e^{-2\nu} \Omega) \\ &= \varpi e^{-2\nu} [2\Omega + \varpi \Omega_{,\varpi} - 2\varpi \nu_{,\varpi} \Omega], \end{aligned} \quad (6.38)$$

which corresponds with the first term in the round bracket of (6.36) and vanishes if $\ell = \text{const}$. This is an important result, since it rules out the possibility that the modes discovered in Chapter 5 could be epicyclic oscillations, and provides evidence (see Section 4) that they should be associated to other restoring forces. It is worth underlying that the property (6.38) provides an additional reason for considering the definition $\ell = -u_\phi/u_t$ as the most natural generalization of the Newtonian angular momentum (see Table 1 of Kozłowski *et al.* (1978) for a summary of the other properties satisfied by ℓ).

3.3 Global Analysis

The global analysis consists in solving the system (6.28)-(6.30) as an eigenvalue problem, treating the perturbed quantities as eigenfunctions and the unknown σ as the eigenfrequency (see Rodriguez *et al.* 2002). This was done numerically in three different situations. The first one focuses on constant angular momentum discs, and will allow us to make a direct comparison with the results obtained in Chapter 5. The second and the third situations refer to non-constant angular momentum distributions. Since the numerical procedure is almost the same in the three case, we will describe it briefly in what follows and devote Sections 4 and Section 5 to the results of the constant and non-constant angular momentum cases.

Boundary conditions

The set of equations (6.28)-(6.30) need to be solved after suitable boundary conditions are imposed at the surface of the disc. In same way as done when considering oscillations in stars, the guiding property to be exploited is that both the unperturbed and the perturbed surface must have zero pressure. This leads us to the zero pressure boundary condition which is widely used in stellar oscillation theory

$$\Delta p = 0, \quad \text{or} \quad \delta p + \xi^j \partial_j p = 0, \quad (6.39)$$

where Δ denotes the Lagrangian perturbation and ξ^i is a displacement vector⁷. Using the relation between the perturbed 4-velocity u^α and the Lagrangian perturbation⁸ of the metric (see Friedman 1978),

$$\Delta u^\alpha = \frac{1}{2} u^\alpha u^\beta u^\gamma \Delta g_{\beta\gamma} \quad (6.40)$$

which in our case reduces to the relation,

$$\xi^\varpi = \frac{ie^{\nu-\lambda}\delta V^{\hat{\varpi}}}{\sigma}, \quad (6.41)$$

we can write the boundary condition as

$$Q + \frac{\delta U}{\sigma} e^{\nu-\lambda} \frac{P_{,\varpi}}{E+P} = 0. \quad (6.42)$$

This condition, which is a simple linear relation between Q and δU , gives us the boundary conditions to be imposed at the inner and outer radii of the disc.

Numerical method

The numerical method used to solve equations (6.28)-(6.30) with the boundary conditions given by (6.42) is the same as adopted by Yoshida & Eriguchi (1995, 1997). The differential equations are discretized on a finite uniform grid and solved as a non-linear set of equations, by a Newton-Raphson procedure. Figure 6.1 shows a schematic representation of the numerical grid used in our computations. The N circles denote the N grid points at which the perturbed variables δU and Q are assigned⁹. The edge filled circle at the left is set at the inner edge of the disc, while the one on the right is placed at the outer edge of the disc. The intermediate points, denoted as crosses in Figure 6.1, are those at which the discretized perturbation equations are assigned. For example, the radial derivative of Q at $r_{i+1/2}$ is expressed as $(Q_{i+1} - Q_i)/\Delta r$, where Δr is the uniform radial stepsize. In that position the value of Q is approximated as $[Q_{i+1} + Q_i]/2$. In total, the number of unknowns are, $(1_{(\text{for } \delta U)} + 1_{(\text{for } Q)}) \times N_{(\text{grid number})} + 1_{(\text{for } \sigma)}$, whereas the number of the equations are $(1_{(\text{baryon})} + 1_{(\text{euler})}) \times (N - 1)_{(\text{grid number})} + 2_{(\text{boundary conditions})} + 1_{(\text{normalization})}$. The number of unknowns is therefore equal to the number of equations, and the problem has a solution¹⁰.

⁷In the case of polytropic stars whose surface density vanishes, this condition is the same as $\delta p = 0$ (Tassoul, 1978).

⁸Note that in the Cowling approximation the Eulerian perturbation of the metric, δg_{ab} , is zero, but the Lagrangian perturbation is generally nonzero. $\Delta g_{ab} = \delta g_{ab} + \mathcal{L}_\xi g_{ab} = \nabla_a \xi_b + \nabla_b \xi_a$.

⁹Most of the computations were performed using a radial grid of $N = 1000$ points.

¹⁰Note that the equation classified as ‘‘normalization’’ arises from the fact that we are dealing with a linear system, and we have therefore the freedom of rescaling quantities by a constant value. For computational purposes, this is done by imposing the initial guess eigenfunction Q to match a certain number (typically unity) at the right edge of the grid.

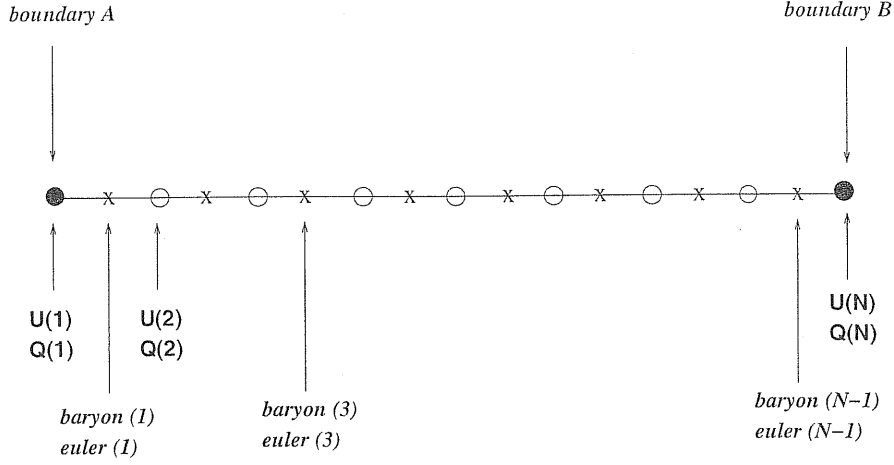


Figure 6.1: Numerical grid for the solution of the system (6.28)-(6.30). The grid covers the range $[r_{\text{in}} - r_{\text{out}}]$ of the disc extension on the equatorial plane. The circles denotes the grid points where the variables δU and Q are given, while the crosses denote the points where the discretized ODEs (denoted as “baryon” and “euler” for the continuity and the Euler equations, respectively) are solved as algebraic equations.

Normalization

Since the spacetime is completely determined by the gravitational mass M of the black hole, we can use M as a scaling factor in the normalization of the relevant quantities involved in the computations. The normalized, dimensionless quantities (indicated as “barred”), are defined as follows

$$r \equiv \bar{r} \left(\frac{M}{M_{\odot}} \right) \cdot \left(\frac{GM_{\odot}}{c^2} \right), \quad (6.43)$$

$$\Sigma \equiv \bar{\Sigma} \left(\frac{M}{M_{\odot}} \right)^{-1} \cdot M_{\odot} \cdot \left(\frac{GM_{\odot}}{c^2} \right)^{-2}, \quad (6.44)$$

$$P \equiv \bar{P} \left(\frac{M}{M_{\odot}} \right)^{-1} \cdot M_{\odot} \cdot \left(\frac{GM_{\odot}}{c^2} \right)^{-2} \cdot c^2, \quad (6.45)$$

$$K \equiv \bar{K} \left(\frac{M}{M_{\odot}} \right)^{\Gamma-1} \cdot M_{\odot}^{1-\Gamma} \cdot \left(\frac{GM_{\odot}}{c^2} \right)^{2(\Gamma-1)} \cdot c^2, \quad (6.46)$$

$$\sigma \equiv \bar{\sigma} \left(\frac{M}{M_{\odot}} \right)^{-1} \cdot \left(\frac{GM_{\odot}}{c^2} \right)^{-1} \cdot c, \quad (6.47)$$

$$\ell \equiv \bar{\ell} \left(\frac{M}{M_{\odot}} \right) \cdot \left(\frac{GM_{\odot}}{c^2} \right) \cdot c. \quad (6.48)$$

4 Constant angular momentum discs

If the specific angular momentum is constant, then, as discussed in Chapter 5, equilibrium disc models can be obtained analytically after fixing five parameters. These are the mass of the black hole M , the equation of state (K and Γ), the potential barrier (ΔW_{in}) and the (constant) angular momentum ℓ . We here just underline that the expression (5.5) giving the rest mass density inside the disc should be interpreted as a relation between integrated quantities, with K and Γ replacing the corresponding constants¹¹ κ and γ .

4.1 Perturbation equations

The assumption of $\ell = \text{const.}$ simplifies the perturbation equations considerably. In fact, according to (6.38), the second term on the right hand side of (6.30) vanishes, thus yielding $\delta V^{\hat{\phi}} = 0$. As a result, the eigenfunctions to compute reduce to Q and δU , which will be calculated through the equations (6.28) and (6.29). These equations can also be rewritten as

$$\sigma Q + e^{\nu-\lambda} \frac{\Gamma P}{E+P} \frac{d\delta U}{dr} + e^{\nu-\lambda} \left[\frac{\Gamma P}{E+P} \left(\nu_{,r} + \frac{2}{r} - \frac{A_{,r}}{A} \right) + \frac{P_{,r}}{E+P} \right] \delta U = 0 \quad (6.49)$$

$$\sigma \delta U + A e^{-\nu-\lambda} \frac{dQ}{dr} = 0. \quad (6.50)$$

4.2 Results

For comparison with the results obtained in Chapter 5, we have solved numerically equations (6.49) and (6.50) considering a disc model very similar to the model (a) reported in Table 5.1 of that Chapter. In particular, we have taken $\ell = 3.8$, $\Gamma = 4/3$, $\bar{K} = 0.01635$. However, since the marginally stable case makes the computation of the eigenfunctions rather difficult at the boundaries of the radial grid, where they tend to diverge, we have chosen an initial configuration slightly below the marginally stable one, namely with $\Delta W_{\text{in}} = -10^{-5}$. The relevant parameters of the resulting disc have been reported in Table 6.1 and should be compared with those of model (a) in Table 5.1.

In Fig 6.2 we have plotted the eigenfunctions Q and δU associated to the fundamental mode and to the first three overtones (o1, o2, o3). The corresponding eigenfrequencies are listed in Table 6.2, where we have included the frequencies up to the fifth overtone. Absolute numbers are not important in the present context, and only the ratios of the overtones to the fundamental frequency are meaningful.

Remarkably, the computed frequencies are accurately in the ratio $2 : 3 : 4 : 5 : \dots$. This is the case for the lowest order modes, but does not hold as the order of the mode¹² (which coincides

¹¹Attention should be paid not to confuse the polytropic constant κ used in Chapter 5 with the epicyclic frequency κ_r .

¹²Note that the number of nodes of the eigenfunction Q is the number of nodes of the eigenfunction δU increased by one.

M_d/M	ℓ	\bar{r}_{in}	\bar{r}_{out}	\bar{r}_{cusp}	\bar{r}_{centre}	ΔW_{in}	$\bar{\Sigma}_{\text{centre}}$ (cgs)
1.0	3.8	4.611	15.880	4.576	8.352	$-1. \times 10^{-5}$	1.16×10^{20}

Table 6.1: Main properties of the constant angular momentum disc model considered. From left to right the columns report: the mass ratio M_d/M , the specific angular momentum (in normalized units), the inner and the outer radii of the disc \bar{r}_{in} and \bar{r}_{out} , the radial position of the cusp, \bar{r}_{cusp} , the radial position of the centre, \bar{r}_{centre} , the potential gap and the surface density at the centre of the disc. This model should be compared with model (a) in Table 5.1 of Chapter 5.

	f	o_1	o_2	o_3	o_4	o_5
$\bar{\sigma}$	0.01777	0.02627	0.03377	0.04061	0.04684	0.05246
nodes of δU	0	1	2	3	4	5

Table 6.2: Eigenfrequencies of the fundamental (f) mode, and of the first five overtones (o_n) of the constant angular momentum disc described in Table 6.1.

with the number of nodes of δU) is increased. As found in the local analysis of Section 3.2, the epicyclic frequency of constant angular momentum discs is zero, making the second term on the right hand side of equation (6.35) vanish. As a result, the modes computed here have pressure as the only restoring force and they are the analogous of p -modes (acoustic modes) in stellar oscillations. This interpretation is also supported by the fact that, according to (6.35) in the absence of inertial oscillations, the fundamental frequency in Table 6.2 is roughly given by the sound crossing frequency of the disc,

$$f \sim \frac{2\pi\bar{c}_s}{(\bar{r}_{\text{out}} - \bar{r}_{\text{in}}) \times 2} \sim 0.0158, \quad (6.51)$$

where we have used the sound velocity \bar{c}_s at the centre of the disc.

In Chapter 5 we showed that the introduction of a particular perturbation in the initial model, namely the introduction of a parametrised radial velocity in addition to the pure orbital motion, was responsible for the appearance of a regular oscillating behaviour in all the fluid variables, with power spectra showing a fundamental mode and a series of overtones in the ratio $1 : 2 : 3 : \dots$

We have also anticipated that the power spectrum of the L_2 norm¹³ of the rest mass density seemed to show peaks in the ratio $2 : 3 : 4 : 5 : \dots$. A possible explanation for these differences in the power spectra could be associated to the fact that the initial perturbation used in Chapter 5 may not be able to excite significantly the oscillations in the fractional frequencies. As a result, the overtones are very hard to detect, and can be revealed only in the power spectrum of particularly sensitive quantities, such as $\|\rho\|_2$.

For this reason, we have performed an additional series of simulations on the model (a) of

¹³This quantity is more suitable than the mass accretion rate for putting into evidence subtle details in the hydrodynamical response of the disc, partly because it is a more fundamental quantity and partly because it is a natural indicator for monitoring the global behaviour of a physical system.

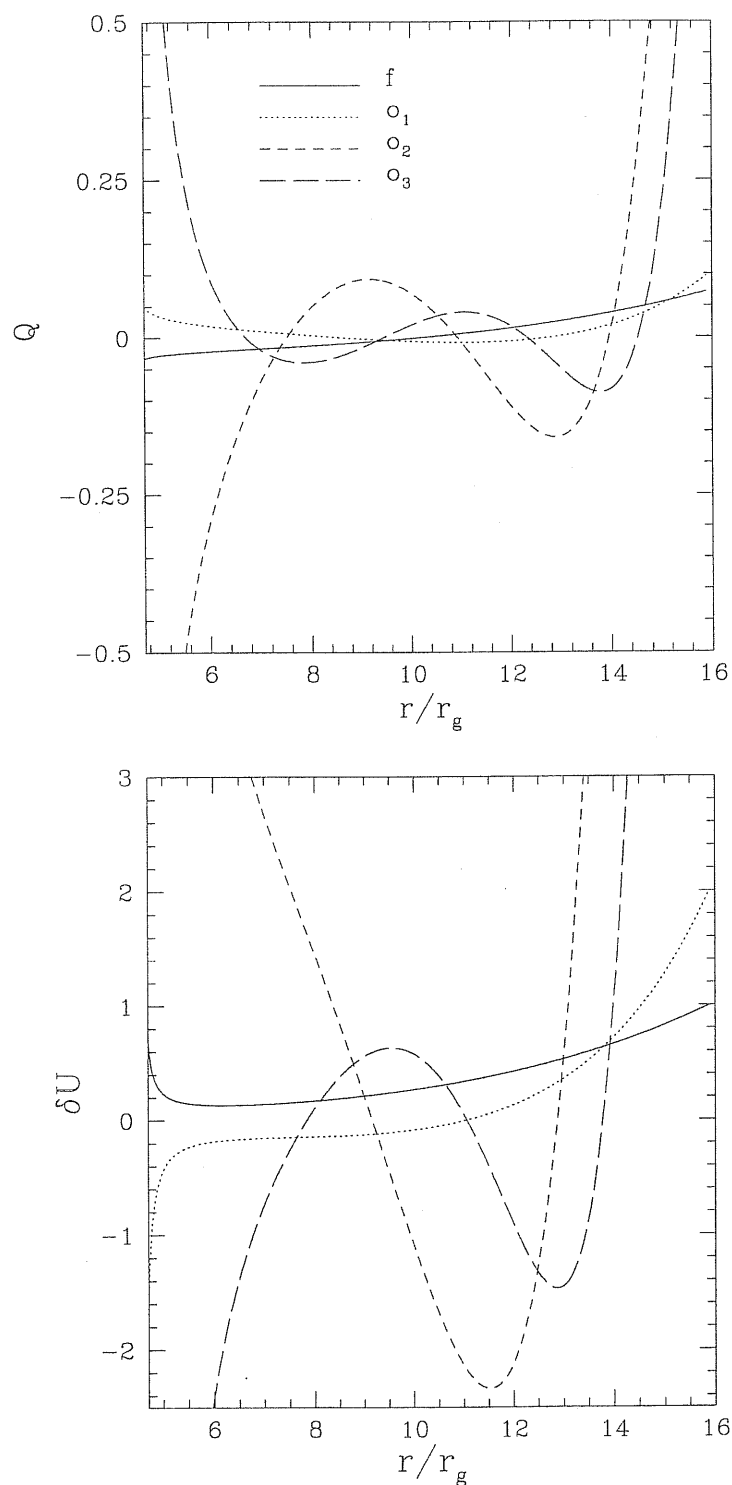


Figure 6.2: Eigenfunctions Q and δU as a function of the radial coordinate for a constant angular momentum disc. Only the fundamental mode (f) and the first three overtones, denoted by o_1 , o_2 and o_3 , have been reported. The order of the mode is given by the number of nodes of δU . The normalization of the eigenfunctions is arbitrary.

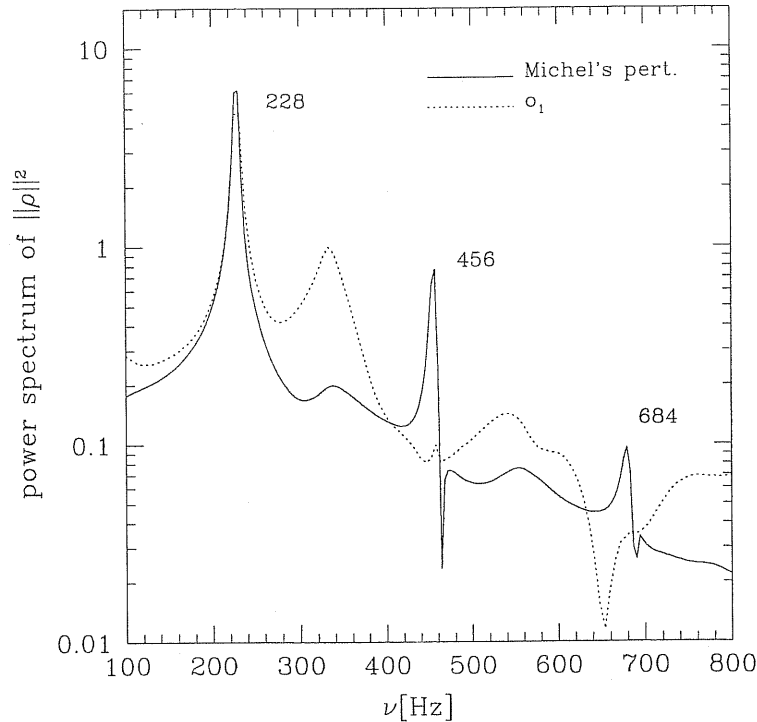


Figure 6.3: Power spectrum of the L_2 norm of the rest mass density for the disc model (a) in Table 1 of Chapter 5. The two spectra differ for the initial perturbations used. Solid line uses the same perturbation in the radial velocity described in Section 4.1 of Chapter 5. The dotted line uses as initial perturbation the computed eigenfunction of o_1 , which excites the first fractional overtone. The spectra have been rescaled in order to match the power of the fundamental frequency.

Chapter 5, by using as initial perturbations in the radial velocity and in the rest mass density the fundamental modes (and its overtones) of the eigenfunctions δU and Q calculated here. Figure 6.3, which reports still preliminary results, shows the power spectrum of $\|\rho\|_2$ for different initial perturbations and suggests that by choosing suitable initial conditions it is possible to excite the overtones of the system.

5 Non-constant angular momentum discs

Constant angular momentum discs are rather poor approximations to realistic discs and some of the properties valid for the first ones may no longer be true for the second ones. For this reason, it is important to extend our mode analysis also to the case of discs with non-constant angular momentum. This will allow us to decide whether the nature of the oscillations described in Chapter 5 are just peculiar of constant angular momentum discs, or the manifestation of a more general behaviour.

5.1 Equilibrium model

To construct an equilibrium model, we need to specify the specific angular momentum distribution ℓ (or, equivalently, the angular frequency Ω). This is, at least to some degree, an arbitrary choice. We just remember that the dynamical stability against axisymmetric

	M_d/M	\bar{r}_{in}	\bar{r}_{out}	\bar{r}_{centre}	\bar{K}	Σ_{centre} (cgs)
linear	1.0	6.5	13.88	9.217	0.004913	1.6×10^{20}
power-law	1.0	6.5	24.75	12.78	0.008479	5.3×10^{19}

Table 6.3: Main properties of the two non constant angular momentum disc models considered. From left to right the columns report: the type of angular momentum distribution, the mass ratio M_d/M , the inner and the outer radii of the disc \bar{r}_{in} and \bar{r}_{out} , the radial position of the centre, \bar{r}_{centre} , the constant \bar{K} in the equation of state and the surface density at the centre of the disc.

perturbation only requires that $d\ell/dr \geq 0$ (*Rayleigh's criterion*¹⁴). Smooth particle hydrodynamics (SPH) simulations of disc formation performed by Davies *et al* (1994) have shown that the final configuration consists of a core surrounded by a disc whose angular momentum distribution is close to that of a power law with index 0.2. In our computations we have therefore adopted two different simple profiles for the specific angular momentum, namely a “linear” one

$$\bar{\ell} = \alpha \bar{r} + \beta, \quad (6.52)$$

and a “power law” one

$$\bar{\ell} = \bar{\ell}_{\text{in}} \left(\frac{\bar{r}}{\bar{r}_{\text{in}}} \right)^a, \quad (6.53)$$

where $\alpha, \beta, \bar{\ell}_{\text{in}}$ and a are free parameters. For the “linear” case, we have chosen $\alpha = 0.03$ and $\beta = 3.6$, whereas in the “power-law” case we have set $\bar{\ell}_{\text{in}} = 1.004\bar{\ell}_K$, where $\bar{\ell}_K$ is the specific angular momentum at the inner edge of a Keplerian disc, and $a = 0.2$. Note that the “linear” case considered is only slightly different from the constant angular momentum case.

In order to obtain the equilibrium models we need to integrate numerically equation (5.3) of Chapter 5 for the given distribution of Ω . The integration is performed along the radial direction only, treating all quantities as vertically integrated ones as explained in Section 3.1. The inner edge of the disc, which is still a free parameter, has been placed at $\bar{r}_{\text{in}} = 6.5$ on the equatorial plane. The relevant parameters of the two disc models considered are reported in Table 6.3.

5.2 Results

Adopting the same numerical technique used for the constant angular momentum disc model, we have solved numerically the full system of equations (6.28)-(6.30), that we re-write here

¹⁴Note that the $\ell = \text{const.}$ case is marginally stable according to this criterion.

in a more compact form as

$$0 = \sigma Q + e^{\nu-\lambda} \frac{\Gamma P}{E+P} \frac{d\delta U}{d\varpi} + e^{\nu-\lambda} \left[\frac{\Gamma P}{E+P} \left(2\nu_{,\varpi} + \frac{1}{\varpi} - \frac{A_{,\varpi}}{A} \right) + \frac{P_{,\varpi}}{E+P} \right] \delta U - \sigma \frac{\varpi e^{\nu}}{A} \Omega \frac{P_{,\varpi}}{E+P} \quad (6.54)$$

$$0 = \sigma \delta U + A e^{-\nu-\lambda} \frac{dQ}{d\varpi} + 2e^{-\lambda} \Omega \left(1 + \varpi \frac{P_{,\varpi}}{E+P} \right) \delta W \quad (6.55)$$

$$0 = \sigma \delta W + \left(\Omega_{,\varpi} + \frac{2}{\varpi} \Omega - 2\nu_{,\varpi} \Omega \right) \varpi e^{-\lambda} \delta U. \quad (6.56)$$

Note that the epicyclic frequency defined by (6.36) does not vanish in this case and a non-zero contribution to the dispersion relation (6.35) is therefore expected. Figures 6.4 shows the surface density distribution (in normalized units) and the radial profile of the epicyclic frequency for the two different disc models.

In Table 6.4 we have reported the eigenfrequencies for both the angular momentum distributions, while the eigenfunctions Q , δU and δW have been plotted in Figures 6.5 - 6.10. Interestingly, the main effect of non-constant angular momentum distributions, namely of having non-zero epicyclic frequencies, appear clearly in the results obtained. Firstly, the fundamental eigenfrequencies of both models are no longer in good agreement with the one estimated by (6.51) as sonic frequencies. In fact, from (6.51) we would obtain a frequency 1.39×10^{-2} for “linear” case and a frequency 6.16×10^{-3} for the “power-law” case. However, if we take into account the existence of epicyclic frequency, the estimation improves. From (6.20) we define an “effective sound speed”, c_e as¹⁵

$$c_e^2 \equiv c_s^2 + \frac{\kappa_r^2}{k^2}. \quad (6.57)$$

If we use c_e , instead of c_s for the estimation of frequency in (6.51), we get 0.0172 for the “linear” and 0.0117 for the “power-law” case, respectively. The numbers obtained are therefore closer to the corresponding fundamental frequencies reported in Table 6.4.

Secondly, by comparing the eigenfunctions for the three different distributions of angular momentum (Figure 6.2 and Figures 6.5 to 6.10), we notice that for the “power-law” case the eigenfunctions go to nearly zero at the inner edge of the disc, while, for two other cases, they do not. This can be understood by comparing the behavior of the epicyclic frequency curves in the different cases. The lower panel of Figure 6.4 shows that in the inner part of the disc the epicyclic frequency for the “power-law” case is higher than the corresponding fundamental frequency (see Table 6.4). Under these circumstances, as seen from (6.20), the wave amplitude goes to zero in the inner part of the disc, which becomes an *evanescent region* of the wave. In another words, the centrifugal barrier produced by rotation makes the

¹⁵We here neglect the correction of General Relativity for a rough estimation.

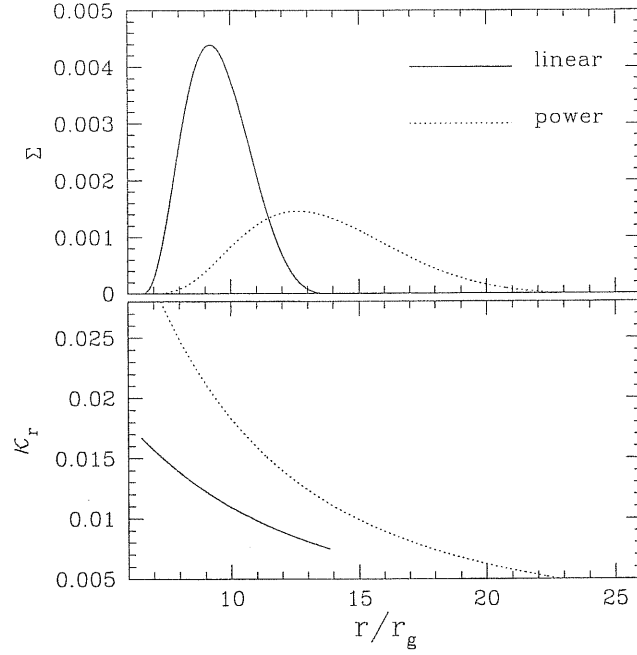


Figure 6.4: Surface density distribution (upper panel) and epicyclic frequency (lower panel), for the disc model with a “linear” distribution of the specific angular momentum (solid line), and with a “power-law” distribution of the angular momentum (dotted line).

epicyclic frequency so high that the wave is reflected back. On the other hand, Figure 6.4 and Table 6.4 show that the fundamental frequency is everywhere higher than the epicyclic frequency for the “linear” distribution of angular momentum. In this case, therefore, there is no evanescent region inside the disc.

Overall, our results confirm what found in the previous Section for the constant angular momentum disc, namely the existence of a series of oscillating modes of the disc. It should be underlined that, for non constant distributions of the angular momentum, the computed frequencies contain the contribution of both the acoustic and the inertial modes, thus producing frequencies ratios deviating from the simple $2 : 3 : 4 : 5 \dots$ relation. The important result, however, is that the oscillations discovered in Chapter 5 belong to the fundamental modes of the disc, and they can be calculated in the correct ratio through a perturbative analysis like the one presented here. Further investigations are needed in order to explore in deeper details these modes for a wide class of initial perturbations. In particular, a fundamental step forward along this direction will be represented by performing a perturbative analysis in the full two dimensional case, by dropping all the approximations related two the simplified “vertically integrated” approach presented in this Chapter.

	f	o_1	o_2	o_3	o_4	o_5
linear	0.01882	0.02686	0.03462	0.04229	0.04995	0.05760
power-law	0.01078	0.01507	0.01912	0.02296	0.02660	0.03005
nodes of δU	0	1	2	3	4	5

Table 6.4: Eigenfrequencies $\bar{\sigma}$ of the fundamental (f) mode, and of the first five overtones (o_n) of the two non constant angular momentum disc models described in Table 6.3. They should be compared with the eigenfrequencies for the constant angular momentum distribution reported in Table 6.2.

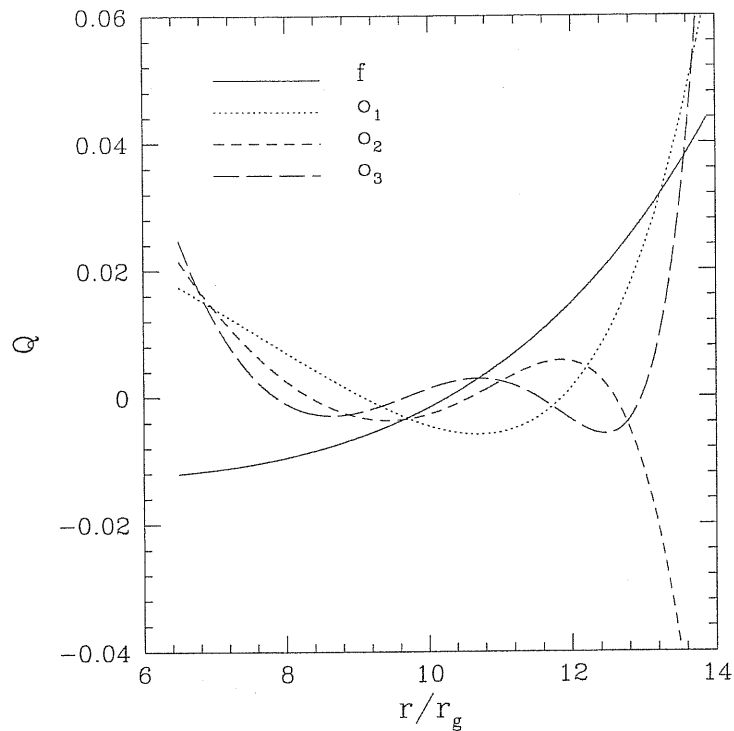


Figure 6.5: Eigenfunctions Q as a function of the radial coordinate for a disc with a linear distribution of the angular momentum. Only the fundamental mode (f) and the first three overtones, denoted by o_1 , o_2 and o_3 , have been reported.

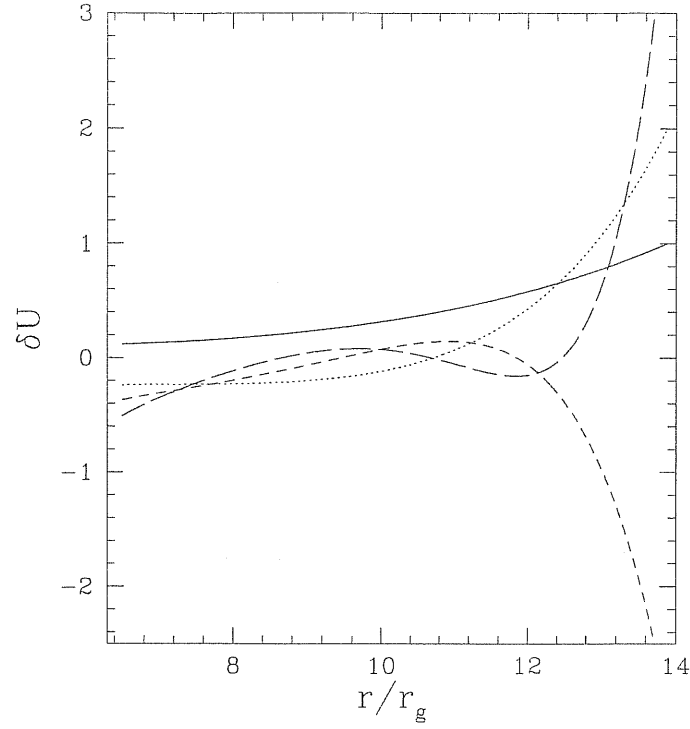


Figure 6.6: Eigenfunctions δU as a function of the radial coordinate for a disc with a linear distribution of the angular momentum. Only the fundamental mode (f) and the first three overtones, denoted by o_1 , o_2 and o_3 , have been reported.

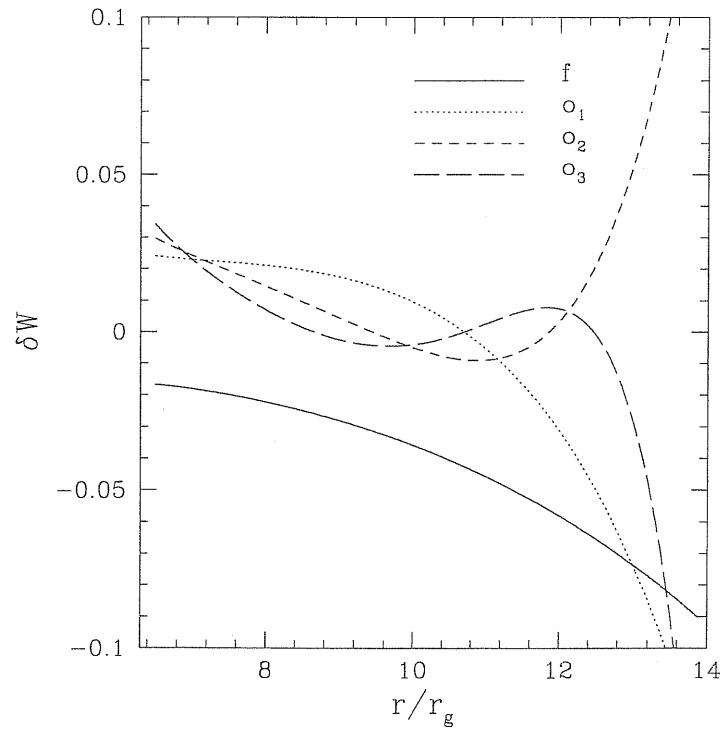


Figure 6.7: Eigenfunctions δW as a function of the radial coordinate for a disc with a linear distribution of the angular momentum. Only the fundamental mode (f) and the first three overtones, denoted by o_1 , o_2 and o_3 , have been reported.

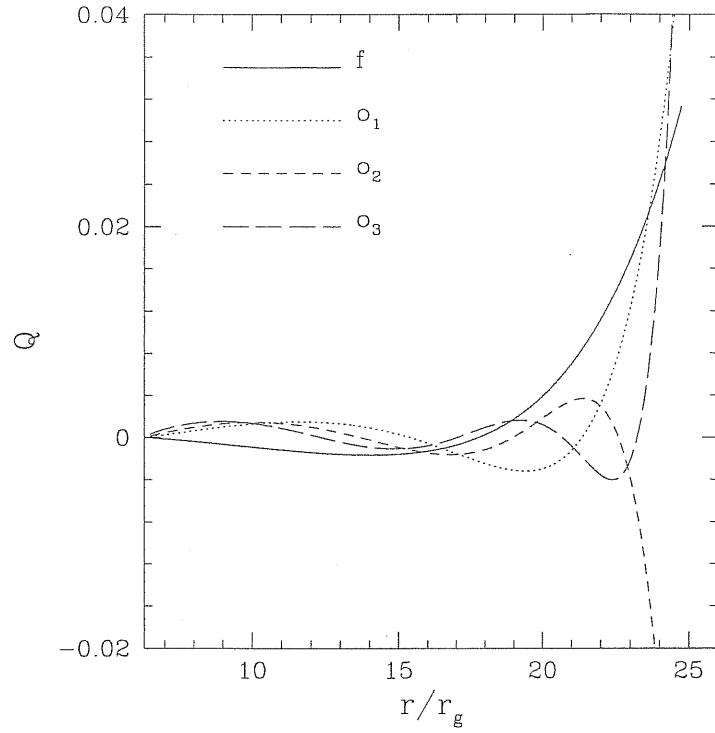


Figure 6.8: Eigenfunctions Q as a function of the radial coordinate for a disc with a “power-law” distribution of the angular momentum. Only the fundamental mode (f) and the first three overtones, denoted by o_1 , o_2 and o_3 , have been reported.

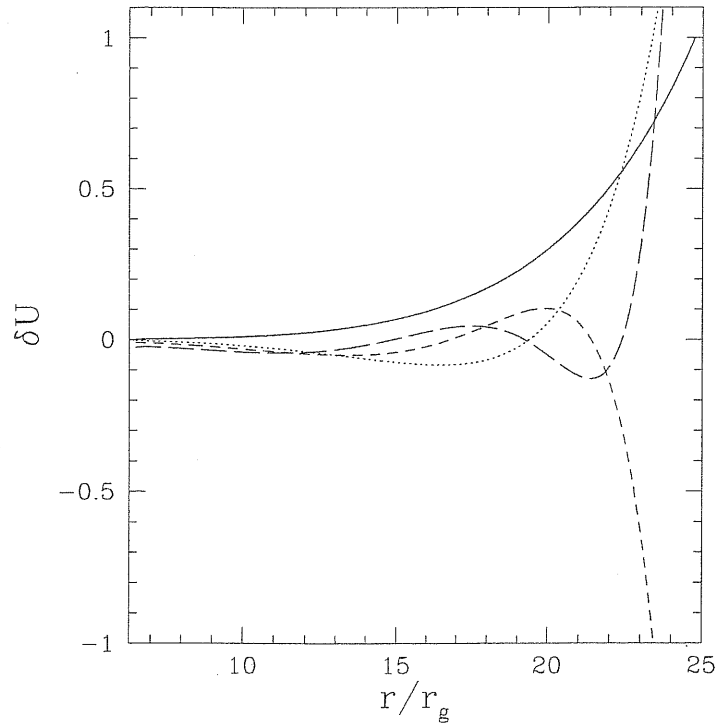


Figure 6.9: Eigenfunctions δU as a function of the radial coordinate for a disc with a “power-law” distribution of the angular momentum. Only the fundamental mode (f) and the first three overtones, denoted by o_1 , o_2 and o_3 , have been reported.

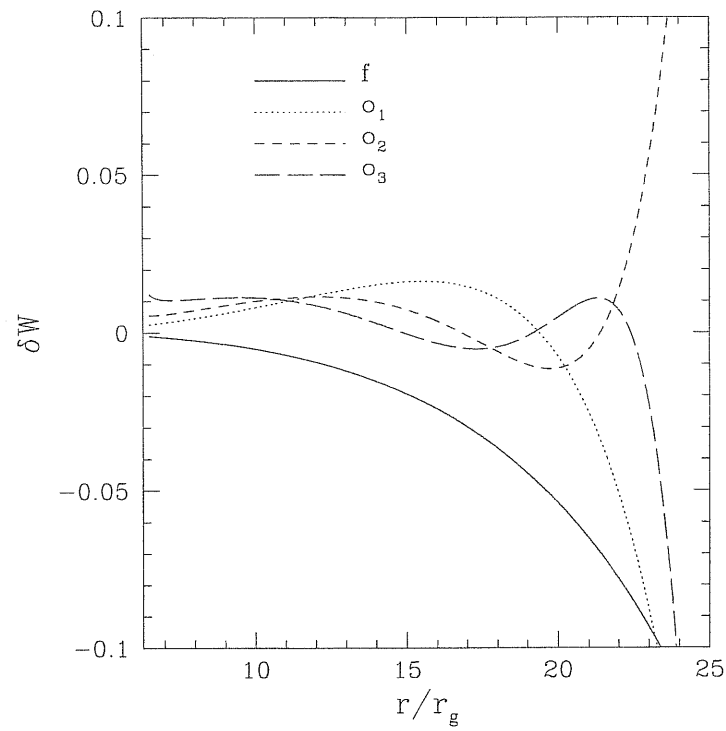


Figure 6.10: Eigenfunctions δW as a function of the radial coordinate for a disc with a “power-law” distribution of the angular momentum. Only the fundamental mode (f) and the first three overtones, denoted by o_1 , o_2 and o_3 , have been reported.

Chapter 7

Dissipative Hydrodynamics

1 Introduction

Dissipative fluid dynamical processes are ubiquitous in astrophysics. They might be due, for instance, to non ideal interaction between gas particles, to turbulent fluid motion in flows with very high Reynolds number, or to collective processes in the collisionless regime.

Modelling dissipative processes like these, with a non-negative rate of entropy production, requires non-equilibrium thermodynamics, and the standard theory for treating them is *Classical Irreversible Thermodynamics*. This theory is based on two fundamental assumptions. The first one is that the local and instantaneous relations between the thermal and mechanical properties of a physical system are the same as for a system in equilibrium¹ (hypothesis of local thermodynamical equilibrium). The second one is that the *constitutive relations* between *thermodynamic fluxes* and *thermodynamic forces* are always linear (see the box below for the definition of these concepts). The physical description resulting from these assumptions has been undoubtedly useful, and has led to a large production of scientific work in many different areas. The Fourier and Navier-Stokes equations, for instance, are derived within this framework and they are currently applied in many fields of astrophysics.

However, Classical Irreversible Thermodynamics contains several undesirable features. First of all, the hypothesis of local thermodynamical equilibrium is too restrictive and, very often, other variables, not found in equilibrium, do influence the thermodynamic equations of irreversible processes. Under these circumstances, as shown by the kinetic theory of gases, the constitutive relations involve evolutionary laws for the fluxes, and the second hypothesis of classical irreversible thermodynamics is also dropped. Moreover, the classical Fourier law of heat conduction leads to a partial differential parabolic equation² for the temperature which implies the propagation of disturbances at an infinite speed.

¹The concepts of thermodynamic equilibrium will be made rigorous in Section 6.1 of this Chapter.

²We recall here that a linear second-order differential equation in two independent variables x and y of the form

$$a \frac{\partial^2 u}{\partial x^2} + b \frac{\partial^2 u}{\partial x \partial y} + c \frac{\partial^2 u}{\partial y^2} + d \frac{\partial u}{\partial x} + e \frac{\partial u}{\partial y} + fu = g, \quad (7.1)$$

is said to be *parabolic* if $b^2 - 4ac = 0$. From a physical point of view parabolic equations describe diffusive phenomena, and a relevant astrophysical example will be discussed in detail in Chapter 8.

Constitutive equations:

In thermodynamics the local production rate of entropy S

$$\frac{dS}{dt} = \sum_i J^i X_i, \quad (7.2)$$

is given by the products of two factors, called the thermodynamic flux J , and the thermodynamic force X , respectively. The fluxes are unknown quantities, unlike the forces which are known functions of the state variables and their gradients. In general, the flux may depend on all of the thermodynamic forces and on the state variables T (temperature) and p (pressure)

$$J^i = J^i(X_1, X_2, \dots, X_j, \dots; T, p). \quad (7.3)$$

Relations like (7.3) are called *constitutive equations* and they express specific properties of the physical system in an irreversible process. Classical Irreversible Thermodynamics always assumes linear relations between fluxes and forces. An example is given by the heat flux \vec{q} , which is connected to its associated thermodynamic force $\vec{\nabla}T^{-1}$ by $\vec{q} = L_{qq} \vec{\nabla}T^{-1}$. The scalar phenomenological coefficient L_{qq} is then related to the transport coefficient of thermal conductivity λ by $L_{qq} = \lambda T^2$, which leads to the Fourier law: $\vec{q} = -\lambda \vec{\nabla}T$.

All of these drawbacks, which could still be acceptable in a Newtonian theory, become even intolerable when the theory is extended to the relativistic regime. In the relativistic theory of non-ideal hydrodynamics first developed by Eckart (1940), for instance, dissipative fluctuations propagate at an infinite speed, there are short wavelength secular instabilities appearing and there is not a well-posed initial value problem for rotating fluid configurations (see Hiscock & Lindblom, 1983). These unattractive circumstances are ultimately due to the assumption that irreversible processes can be described as a sequence of local equilibrium states alone, a fact which is then reflected in the parabolic formulation of the Navier-Stokes equations.

To overcome these difficulties, several *causal type* theories have been introduced, both Newtonian and relativistic. The central idea of these theories is to *extend* the space of variables of conventional theories by incorporating the dissipative quantities (heat flux, shear and bulk stresses, etc.), which are therefore treated as the conserved variables of the ideal fluid, thus restoring causality and stability under a wide range of conditions. The resulting equations, in fact, being hyperbolic in nature, can be interpreted as evolution equations for the dissipative variables as they describe how the “extended” fluxes evolve from an initial arbitrary state to a final steady one. There is, of course, a price to pay in this extension, consisting in a more involved theory from a mathematical point of view, with a large number of variables and parameters. Moreover, no general criteria exists for deriving the evolution equations of the dissipative fluxes, except the restriction imposed by the second law of thermodynamics. A non-relativistic extended theory was first proposed by Müller (1967) and was later generalized to the relativistic case by Israel (1976) and Stewart (1977). The usual name for referring

to these approaches is *Causal Thermodynamics*, or *Rational Extended Thermodynamics*³. We have already shown in Chapter 2 of this Thesis that the basic equations of hydro/thermodynamics can be written as balance laws over a control volume dV

$$\frac{d}{dt} \int \mathbf{U} dV + \int \nabla_i \mathbf{F}^i dV = \int \mathbf{S} dV, \quad (7.4)$$

where \mathbf{U} is the vector of conserved quantities, \mathbf{F} are the fluxes and \mathbf{S} are the source terms. In ordinary thermodynamics the state vector \mathbf{U} has five components, i.e. the densities of rest-mass, momentum and energy. If the source terms \mathbf{S} vanish the balance equations are in fact conservation laws. Even under these circumstances, however, the system of ordinary thermodynamics is not closed, because specific relations must be specified relating the fluxes \mathbf{F} to the state \mathbf{U} . Such relations are often called phenomenological equations, because originally they were empirical laws based on observations. The simplest example of such relations is perhaps the thermal equation of state, which relates the pressure at one point and time to the densities of mass and energy at that point and time. When viscosity and heat conduction are ignored, an hyperbolic system is derived which is given by the Euler equations. In a more realistic description of a fluid the equations connecting \mathbf{U} to \mathbf{S} are given by the equations of Navier-Stokes for the viscous stresses and by the Fourier law for the heat flux. These are *non local* empirical laws, in the sense that the fluxes \mathbf{F}^i at a given point do not depend only on the state \mathbf{U} at that point, but also on the gradients of \mathbf{U} . This additional dependence gives the Navier-Stokes-Fourier system a parabolic structure, which has been satisfactory in a large number of different applications. In the presence of steep gradient or rapid changes, however, this description shows the shortcoming mentioned above and Extended Thermodynamics becomes necessary.

In Rational Extended Thermodynamics, the state \mathbf{U} is extended to include further densities, and the closure of the system is achieved by adopting constitutive equations that are local and instantaneous, so that \mathbf{F}^i and \mathbf{S} at any point and time depend only on the state \mathbf{U} at that point and time. Therefore, the local forms of the balance equations

$$\frac{\partial \mathbf{U}}{\partial t} + \frac{\partial \mathbf{F}^i}{\partial x^i} = \mathbf{S}, \quad \text{with} \quad \mathbf{F}^i = \mathbf{F}^i(\mathbf{U}) \quad \text{and} \quad \mathbf{S} = \mathbf{S}(\mathbf{U}) \quad (7.5)$$

provide a system of hyperbolic partial differential equations. This formulation is particularly attractive both for physicists, since it avoids action at a distance and ensures finite speed of propagation of the signals, and for mathematicians, because it guarantees well-posedness of local Cauchy problem. The initial works on extended thermodynamics (I. Müller, 1967) were motivated by the paradox of thermal waves with infinite speed (see Section 2) which

³Note that the first improvement of Classical Irreversible Thermodynamics was provided by Coleman (1964) with a theory called *Rational Thermodynamics*, which contained the idea of treating entropy and temperature as primitive concepts without a precise physical interpretation. Rational Extended Thermodynamics can be considered as a further improvement of this approach. The name “Causal Thermodynamics”, or “causal type theories” is less specific than Rational Extended Thermodynamics, but is often used as a synonym.

was then solved by allowing the entropy to depend on the heat flux and on the viscous stress (see Section 5). Nowadays, the motivations for pursuing this field of research can be found in the large flexibility of the new theory, which has acquired a strong predictive power in experiments of light scattering, sound dispersion, shock wave structure, non equilibrium radiation, etc.

Even before Extended Thermodynamics received mathematical support from the theory of hyperbolic systems, it benefitted from the contact with the kinetic theory of gases, particularly with the “moment method” of Grad⁴ (Grad, 1949, 1958). Kinetic theory, in fact, played a fundamental role in recognizing that the non-convective entropy flux s is not universally related to the heat flux q by $s = q/T$, but can also depend on the dissipative fluxes⁵. This contact between thermodynamics and kinetic theory became progressively closer as Extended Thermodynamics proceeded to include more and more variables (see Section 6). This Chapter is just a starting point for possible future research and developments. In particular, we will try to motivate the application of the new theory to astrophysics (Section 2); then we will follow the fundamental steps which led to the birth of the extended theory, following more or less the order in which they were historically developed. (Section 3 to 5). Finally we will mention the connection with Kinetic theory in Section 6 and we will investigate the possibility of a numerical counterpart of these new developments in Section 7.

2 Do we need Rational Extended Thermodynamics in Astrophysics?

A question which arises naturally is whether there are astrophysical contexts in which an hyperbolic formulation of the equations for dissipative relativistic fluids is needed. A distinctive feature of Extended Thermodynamics as compared with “Eckart-type theories” (Eckart 1940) is that it naturally recognises the existence of the relaxation time τ of the corresponding dissipative process, namely the time taken by the system to return spontaneously to its steady state. It is precisely before the establishment of the steady regime that hyperbolic and parabolic-type theories differ most significantly. Therefore, if one wishes to study a dissipative process for times shorter than τ , it is fundamental to assume an “hyperbolic viewpoint”, whereas for times larger than τ it may be reasonable to retain a parabolic one. Before referring explicitly to a precise astrophysical example, it is worth mentioning the well known case of the classical Fourier law for the heat flux \vec{q} in the non relativistic regime

$$\vec{q} = -\lambda \vec{\nabla} T, \quad (7.6)$$

⁴In the Grad model, proposed to solve the Boltzmann equation in non-equilibrium situations, the non-equilibrium distribution function f is replaced by its higher order moments.

⁵The first successful application of extended thermodynamics through kinetic theory of gases of photons is due to Struchtrup (1996, 1997).

where T is the temperature and λ is the heat conductivity. This equation leads to a diffusion equation for the temperature of the type

$$\frac{\partial T}{\partial t} = \chi \nabla^2 T, \quad (7.7)$$

where $\chi = \lambda/\rho c_p$ and c_p are the diffusivity and the specific heat at constant pressure, respectively. Equation (7.7) is of parabolic type and it implies that the heat flux vanishes simultaneously with the disappearance of a temperature gradient. On the contrary, we expect that if a thermodynamic force is switched off, a relaxation time will lapse before the corresponding thermodynamic flux dies away. In our example, if $\vec{\nabla}T$ is set to 0 at time $t = 0$ when the heat flux is \vec{q}_0 , we expect a decay law of the type

$$\vec{q} = \vec{q}_0 \exp\left(-\frac{t}{\tau}\right). \quad (7.8)$$

In order to account for this relaxational feature, Cattaneo (1948) modified the Fourier law by using the kinetic theory of gases, obtaining

$$\tau \frac{\partial \vec{q}}{\partial t} + \vec{q} = -\lambda \vec{\nabla} T. \quad (7.9)$$

This expression leads to an hyperbolic equation for the temperature (the “telegraph” equation)

$$\tau \frac{\partial^2 T}{\partial t^2} + \frac{\partial T}{\partial t} - \chi \nabla^2 T = 0, \quad (7.10)$$

which describes the propagation of a thermal wave in the direction \vec{x}

$$T \propto \exp[i(\vec{\sigma} \cdot \vec{x} - \omega t)], \quad (7.11)$$

where $\vec{\sigma}$ is the wave number and ω is the frequency of the signal. The dispersion relation resulting from (7.11) is

$$\sigma^2 = \frac{\tau \omega^2}{\chi} + i\omega, \quad (7.12)$$

so that the phase velocity is

$$v_{ph} = \frac{\omega}{\text{Re}(\sigma)} = \left[\frac{2\chi\omega}{\tau\omega + \sqrt{1 + \tau^2\omega^2}} \right]^{1/2}. \quad (7.13)$$

At low frequencies, $\tau\omega \ll 1$, the phase velocity of the hyperbolic theory (7.13) reduces to $v_{ph} \rightarrow \sqrt{2\chi/\tau}$, which gives the divergent speed of the Fourier law assuming $\tau = 0$. However, outside that regime the two expressions differ significantly from one another, and in the high frequency limit, $\tau\omega \gg 1$, (7.13) reduces to $v_{ph} = \sqrt{\chi/\tau}$, which is the propagation speed of

thermal pulses, also known as the *second sound*. This fact was first discovered experimentally by Peshkov (1944) in Helium II, and later confirmed in solids by a number of experimentalists (see, among the others, Guyer & Krumhansl, 1964). Closely connected with this discussion is the response of a material sample to an instantaneous heat pulse. Also in this case it is possible to show that the introduction of a relaxation term removes the problem of infinite propagation speeds.

Coming back to astrophysics, it is clear that, whenever the thermodynamic time scales become comparable to the dynamical time scales, the assumption of local thermodynamic equilibrium is not justified and parabolic theories are bound to fail. Astrophysical examples where the principles of Extended Thermodynamics has been successfully applied include the gravitational collapse of stars (Di Prisco 1996; Herrera & Martinez, 1998), the processes taking place in the innermost part of accretion discs around black holes (Peitz & Appl 1997), and the analysis of dissipative effects in several cosmological scenarios (Pavon *et al*, 1991; Romano & Pavon, 1993; Maartens & Triginer, 1997; Maartens & Triginer 2000). In the following we will just briefly mention the first of these examples.

2.1 Thermal Relaxation in Gravitational Collapse

The thermal relaxation time in the gravitational collapse of a fluid sphere has usually been ignored, arguing that it is very small compared with the typical timescales of collapse for gravitating systems. The former is in fact of the order of $\tau \sim 10^{-11}$ s for phonon-electron interactions at room temperature (Peirls, 1956), while the latter can be of the order of 10^{-2} s. However, there are situations in which τ cannot be neglected compared with the gravitational collapse time, and this typically happens in the cores of evolved stars, where the quantum cells of phase space are filled-up and the electron mean free path increases thus increasing τ . An order of magnitude estimate for the relaxation time of neutron star matter can be made following the argument presented in the previous Section. If the thermal conductivity is dominated by electrons, then, as reported by Flowers & Itoh (1981), the thermal conductivity λ and the relaxation time τ can be estimated as

$$\lambda \approx 10^{23} \left(\frac{\rho}{10^{14} \text{gcm}^{-3}} \right) \left(\frac{10^8 \text{K}}{T} \right) \text{erg s}^{-1} \text{cm}^{-1} \text{K}^{-1}, \quad (7.14)$$

and

$$\tau \approx \frac{10^{20}}{T^2 v_{ph}^2}, \quad (7.15)$$

respectively, where all quantities are expressed in cgs units. If we now take some standard values for neutron star geometry and physics, namely a radius $R = 10^5$ cm, $\rho = 10^{14}$ g cm $^{-3}$, $v_{ph} = 10^3$ cm s $^{-1}$, corresponding to the velocity of sound in superfluid helium, and a temper-

ature $T = 10^6 K$, we obtain

$$\tau \sim 10^2 s. \quad (7.16)$$

This very rough estimate indicates that the pre-relaxation processes are likely to play a fundamental role in the thermal evolution of very compact objects, making the need for hyperbolic theories of dissipation inescapable. A few years ago, Di Prisco *et al.* (1996) and Herrera & Martinez (1998) showed that the outcome of the stellar collapse depends strongly on the value of τ . In particular, the fluid sphere is seen to bounce if τ is shorter than a critical value. Furthermore, phenomena before complete relaxation may considerably influence the evolution of the system after relaxation. In particular, in spherically symmetric stars with a radial heat flow, the temperature gradient, and hence the luminosity, is highly dependent on the product of the relaxation time and the period of oscillation of the star (Herrera & Santos, 1997).

3 Dissipative Fluids

The general stress-energy tensor for non-ideal fluids takes the form (see Landau & Lifshitz, 1987)

$$T^{\mu\nu} = eu^\mu u^\nu + (p + \Pi)h^{\mu\nu} + q^\mu u^\nu + q^\nu u^\mu + \pi^{\mu\nu}, \quad (7.17)$$

Before commenting on all of the terms in (7.17), it is important to address the issue of the definition of the four-velocity for a dissipative fluid. In relativistic mechanics, in fact, an energy flux involves a mass flux. However, if there is a heat flux, it is no longer possible to define the four velocity of the fluid in terms of the mass flux density. Nevertheless, we can still define the velocity by the condition that, in the rest frame of any fluid element, the momentum is zero and its energy can be expressed by the other thermodynamic quantities as done in the absence of dissipative processes. This corresponds to selecting an average velocity such that the particle flux in the local rest frame of the fluid element vanishes [so called “Eckart-frame description”]. In (7.17) it is implicitly assumed that the state of the fluid is close to a fictitious local thermodynamic equilibrium state, characterized by the local equilibrium scalars n , e , p , s and T , representing the baryon number density, the energy density, the specific entropy and the temperature, respectively. In the rest frame of the fluid element, the four velocity is such that the number and energy densities coincide with the local equilibrium values, and only the pressure in general deviates from it, by the bulk viscous pressure term Π . The other two dissipative terms are the heat flux q^μ and the anisotropic stress tensor $\pi^{\mu\nu}$. Collectively, Π , q^μ and $\pi^{\mu\nu}$ are the thermodynamic fluxes and they account for the deviation of the fluid from an ideal fluid. Overall, these terms are formally defined

as

$$q^\mu \equiv -h_\gamma^\mu T^{\gamma\nu} u_\nu, \quad (7.18)$$

$$p + \Pi \equiv h_{\mu\nu} T^{\mu\nu}, \quad (7.19)$$

$$\pi^{\mu\nu} \equiv h_\gamma^\mu h_\epsilon^\nu T^{\gamma\epsilon} - \frac{1}{3}(p + \Pi)h^{\mu\nu}, \quad (7.20)$$

where $h^{\mu\nu}$ is the usual projection tensor on the three dimensional space orthogonal to u^μ . In irreversible thermodynamics, the entropy is no longer conserved, but grows according to the second law of thermodynamics

$$\nabla_\mu S^\mu \geq 0, \quad (7.21)$$

implying that the entropy flux S^μ has a dissipative vector-value contribution R^μ in addition to the equilibrium values $S^\mu = snu^\mu$, namely

$$S^\mu = snu^\mu + \frac{R^\mu}{T}. \quad (7.22)$$

Note that the specific entropy s remains related to the other thermodynamic scalars by the Gibbs equation

$$Tds = d\left(\frac{e}{n}\right) + p\left(\frac{1}{n}\right), \quad (7.23)$$

which can be adopted as a definition of the temperature T . The dissipative part R^μ in (7.22) is assumed to be a function of the thermodynamic fluxes which vanish in equilibrium. Classical Irreversible Thermodynamics and Rational Extended Thermodynamics differ precisely in the form of the function R^μ , as we will show in Section 4 and Section 5.

As a first step, we need to write down the equations of continuity

$$\nabla_\mu (nu^\mu) = 0, \quad (7.24)$$

and the equation of energy-momentum conservation

$$\nabla_\mu T^{\mu\nu} = 0, \quad (7.25)$$

resulting from the stress energy tensor (7.17). The first one does not pose any particular problem and can be rewritten as

$$\dot{n} + \Theta n = 0, \quad (7.26)$$

where we have denoted the total derivative $u^\mu \nabla_\mu$ of a given quantity f as $\dot{f} \equiv u^\mu \nabla_\mu f$ [see below for the definition of Θ]. On the other hand, (7.25) requires more involved calculations,

leading to the following equations for energy and momentum conservation

$$\dot{e} + \Theta(e + p + \Pi) + 2q_\mu a^\mu + D^\mu q_\mu + \pi^{\mu\nu} \sigma_{\mu\nu} = 0 \quad (7.27)$$

$$(e + p + \Pi)a_\mu + D_\mu(p + \Pi) + D^\nu \pi_{\mu\nu} + a^\nu \pi_{\mu\nu} + h_\mu^\nu q_\nu + \left(\frac{4}{3}\Theta h_{\mu\nu} + \sigma_{\mu\nu} + \omega_{\mu\nu}\right)q^\nu = 0. \quad (7.28)$$

In (7.26), (7.27) and (7.28) we can recognize the fundamental quantities which are usually introduced in hydrodynamics. In particular, a^μ is the four-acceleration, $\Theta = \nabla_\mu u^\mu$ is the volumetric expansion, accounting for shape preserving volume changes, $\sigma_{\mu\nu} = \nabla_{(\mu} u_{\nu)}$ is the symmetric, tracefree shear tensor, $\omega = h_\mu^\gamma h_\nu^\epsilon \nabla_{[\gamma} u_{\epsilon]}$ is the antisymmetric vorticity tensor, and $D_\mu q_\nu = h_\mu^\gamma h_\nu^\epsilon \nabla_\gamma q_\epsilon$ is the covariant spatial derivative.

4 Classical Irreversible Thermodynamics

Classical Irreversible Thermodynamics assumes a linear dependence of R^μ on the thermodynamic fluxes. The only such vector that can be built from $(\Pi, q^\mu, \pi^{\mu\nu})$ and the four velocity u^μ is given by

$$R^\mu = f\Pi u^\mu + gq^\mu, \quad (7.29)$$

where f and g are thermodynamic functions of n and e . However, since the entropy density $(-S^\mu u_\mu)$ must have a maximum in equilibrium, i.e.

$$\left. \frac{\partial}{\partial \Pi} (-S^\mu u_\mu) \right|_{\text{E}} = 0, \quad (7.30)$$

it follows that $f = 0$. Moreover, in the rest frame of the fluid $q^\mu/T \equiv (0, \vec{q}/T)$, which is the entropy flux due to the heat flow only, meaning that we also have $g = 1$. As a result, (7.22) takes the form

$$S^\mu = S n u^\mu + \frac{q^\mu}{T}. \quad (7.31)$$

Using the Gibbs equation (7.23), the continuity equation of particle conservation (7.26) and the energy conservation equation (7.27), the entropy generation rate can be written as

$$T \nabla_\mu S^\mu = -\Theta \Pi - (D_\mu \ln T + a_\mu) q^\mu - \sigma_{\mu\nu} \pi^{\mu\nu}. \quad (7.32)$$

If we require this expression to satisfy the entropy condition (7.21), the simplest relation to impose between the thermodynamic fluxes and the thermodynamic forces Θ , $D_\mu \ln T + a_\mu$

and $\sigma_{\mu\nu}$ is still linear and is given by

$$\Pi = -\zeta\Theta \quad (7.33)$$

$$q_\mu = -\lambda T(D_\mu \ln T + a_\mu) \quad (7.34)$$

$$\pi_{\mu\nu} = -2\eta\sigma_{\mu\nu}, \quad (7.35)$$

where the non-negative *transport coefficients* ζ , λ and η are the bulk viscosity, the thermal conductivity and the shear viscosity, respectively. Equations (7.33)-(7.35) are the constitutive equations in the standard Eckart theory of relativistic irreversible thermodynamics (Eckart, 1940). Once solved with (7.27) and (7.28), these equations provide a complete set for the solution of the relativistic hydrodynamics equations of dissipative fluids. Remarkably, (7.34) implies the existence of a heat flux as a consequence of acceleration, even in the absence of a temperature gradient.

Most of the applications of irreversible thermodynamics in relativity have used this original formulation, but, as can be appreciated from the algebraic nature of the constitutive equations (7.33)-(7.35), the thermodynamic fluxes react instantaneously to the corresponding thermodynamic forces, thus causing the propagation of signals at infinite speed, as shown in Section 2 for the Newtonian Fourier equation (7.34). Motivated by this noncausal propagation of fluctuations in the Eckart theory, Müller (1966) and Israel (1976) sought to generalize the theory in order to overcome this difficulty. Their proposal aimed at changing the expression for the entropy current, as will be explained in the following Section.

5 Extended Thermodynamics

As argued by Müller (1967) and Israel (1976), one might expect the physical density of entropy to differ from sn by terms which go to zero for a fluid in an equilibrium state, i.e. by the terms $\Pi, q^\mu, \pi^{\mu\nu}$. This intuition is supported by kinetic theory, which can motivate R^μ being second order in the thermodynamic fluxes. The truncation at first order, in fact, removes those terms which are necessary for both causality and stability, the two major drawbacks of Classical Irreversible Thermodynamics. The most general algebraic form for R^μ that is at most second order in the fluxes is (Hiscock & Lindblom, 1983)

$$S^\mu = snu^\mu + \frac{q^\mu}{T} - (\beta_0\Pi^2 + \beta_1 q_\nu q^\nu + \beta_2 \pi_{\mu\nu} \pi^{\mu\nu}) \frac{u^\mu}{2T} + \frac{\alpha_0 \Pi q^\mu}{T} + \frac{\alpha_1 \pi^{\mu\nu} q^\nu}{T}. \quad (7.36)$$

The new thermodynamic coefficients β_0 , β_1 and β_2 model the scalar, vector and tensor dissipative contributions to the entropy density, respectively; α_0 and α_1 , on the other hand, model changes in the entropy current due to possible viscous-heat flux coupling. With the new expression (7.36) the entropy density measured in the local rest frame then becomes

$$-S^\alpha u_\alpha = sn - \frac{1}{2T}(\beta_0\Pi^2 + \beta_1 q_\mu q^\mu + \beta_2 \pi_{\mu\nu} \pi^{\mu\nu}), \quad (7.37)$$

which is independent of α_0 and α_1 . In the following we will neglect the coupling between the heat flux and viscosity, corresponding to set $\alpha_0 = \alpha_1 = 0$. Within this approximation, whose validity is strongly dependent on the particular physical conditions examined, the entropy generation rate associated to (7.36) follows from the continuity equation (7.26), the Gibbs equation (7.23) and from (7.27)-(7.28), and is given by

$$\begin{aligned} T\nabla_\alpha S^\alpha = & -\Pi \left[\Theta + \beta_0 \dot{\Pi} + \frac{1}{2} T \nabla_\nu \left(\frac{\beta_0}{T} u^\nu \right) \Pi \right] \\ & -q^\nu \left[D_\nu \ln T + a_\nu + \beta_1 \dot{q}_\nu + \frac{1}{2} T \nabla_\mu \left(\frac{\beta_1}{T} u^\mu \right) q_\nu \right] \\ & -\pi^{\nu\mu} \left[\sigma_{\nu\mu} + \beta_2 \dot{\pi}_{\nu\mu} + \frac{1}{2} T \nabla_\mu \left(\frac{\beta_2}{T} u^\mu \right) \pi_{\nu\mu} \right]. \end{aligned} \quad (7.38)$$

This last expression allows to recognize the new *extended forces* as the terms enclosed in the square brackets of (7.38). The simplest way to satisfy the second law of thermodynamics (7.21) is to impose (as in the classical theory) linear relations between the thermodynamic fluxes and the extended forces. In this case, however, the extended forces contain total derivatives of the corresponding fluxes, and the resulting constitutive equations are given by

$$\tau_0 \dot{\Pi} + \Pi = -\zeta \Theta - \left[\frac{1}{2} \zeta T \nabla_\alpha \left(\frac{\tau_0}{\zeta T} u^\alpha \right) \Pi \right] \quad (7.39)$$

$$\tau_1 h_\alpha^\beta \dot{q}_\beta + q_\alpha = -\lambda (D_\alpha T + T a_\alpha) - \left[\frac{1}{2} \lambda T^2 \nabla_\beta \left(\frac{\tau_1}{\lambda T^2} u^\beta \right) q_\alpha \right] \quad (7.40)$$

$$\tau_2 h_\alpha^\mu h_\beta^\nu \dot{\pi}_{\mu\nu} + \pi_{\alpha\beta} = -2\eta \sigma_{\alpha\beta} - \left[\eta T \nabla_\mu \left(\frac{\tau_2}{2\eta T} u^\mu \right) \pi_{\alpha\beta} \right], \quad (7.41)$$

where the relaxation times have been defined as $\tau_0 \equiv \zeta \beta_0$, $\tau_1 \equiv \lambda T \beta_1$ and $\tau_2 \equiv 2\eta \beta_2$. In many applications the terms in square brackets on the right hand side of equations (7.39)-(7.41) are usually small when compared with the other terms and are often neglected. The resulting equations are then called the Maxwell-Cattaneo equations.

The crucial difference between the Eckart theory and the extended theory of thermodynamics is that in the second one the dissipative fluxes are obtained after the solution of the evolutionary differential equations (7.39)-(7.41), while in the first one the dissipative fluxes are simply given by the algebraic relations (7.33)-(7.35). This evolution feature, also evident in the existence of the relaxation time coefficients, is needed for causality and for modeling all of those phenomena where an accurate description of transition phases is essential. The price paid for this improvement is that new thermodynamic coefficients are introduced. The three relaxation times τ_0 , τ_1 and τ_2 could in principle be calculated from the kinetic theory of gases. More often, however, they are estimated as mean collision times, $1/\tau \sim n \Sigma v$, with Σ being the collision cross section of the process involved and v the mean free particle speed. It should be stressed that the extended theory of thermodynamics cannot be considered

complete unless a link is established with the kinetic theory. After all, the assumption of entropy depending on the heat flux and on the shear stress tensor is rather unconventional from a phenomenological point of view. As shown by Müller & Ruggeri (1998), however, kinetic theory does provide the correct interpretation of the equations presented here and gives the basis for a new version of Extended Thermodynamics. In the following Section we will try to make this connection more apparent

6 Divergence Type Theories

The transport equations for the dissipative fluxes (7.39)-(7.41) have been derived under the assumption that the entropy current vector of Classical Irreversible Thermodynamics can be extended to include terms that are quadratic in the dissipative fluxes⁶[cf. Eq. (7.36)]. However, although all of the disadvantages of the Eckart theory have disappeared, it is apparently not known whether the system (7.39)-(7.41) is always hyperbolic. An alternative formulation of extended thermodynamics has been suggested by Liu *et al.* (1986), and uses as guidelines the principle of relativity, the entropy principle and the requirement of hyperbolicity. This new formulation, which is potentially suitable for numerical applications, is called the *divergence-type* formulation of Extended Thermodynamics and it arises naturally in the kinetic theory of gases.

6.1 The Connection With Kinetic Theory

Statistical thermodynamics defines the particle flux vector n^μ , the stress energy tensor $T^{\mu\nu}$ and the tensor of fluxes $F^{\mu\nu\sigma}$ as the first three moments of the distribution function $f(x^\mu, p^\nu)$, respectively

$$n^\mu = mc \int p^\mu f dp, \quad (7.42)$$

$$T^{\mu\nu} = c \int p^\mu p^\nu f dp, \quad (7.43)$$

$$F^{\mu\nu\sigma} = \frac{1}{m} \int p^\mu p^\nu p^\sigma f dp, \quad (7.44)$$

where m is the rest mass of a particle, p^μ is its four momentum and $dp = \sqrt{-g}/p_0 dp^1 dp^2 dp^3$ is the invariant element of the momentum space. As usual, $f dp$ is the number density of the particles with momentum between p^μ and $p^\mu + dp^\mu$, and the distribution functions f obeys the relativistic version of the Boltzmann equation, namely the Boltzmann-Chernikov equation (see Chernikov 1964). Relativistic kinetic theory implies that dissipative relativistic

⁶For this reason the resulting theory is also called *extended second order thermodynamics*.

fluids are subject to the following conservation laws (Liu *et al.* 1986)

$$\nabla_\mu n^\mu = 0, \quad (7.45)$$

$$\nabla_\mu T^{\mu\nu} = 0, \quad (7.46)$$

$$\nabla_\mu F^{\mu\nu\sigma} = P^{\nu\sigma}, \quad (7.47)$$

where $P^{\mu\nu}$ is called the tensor of *production density of fluxes*. Equations (7.45) and (7.46) are the usual conservation laws of particle number and energy momentum, whereas (7.47) is the balance law of fluxes. Kinetic theory suggests that the tensors $T^{\mu\nu}$, $F^{\mu\nu\sigma}$ and $P^{\nu\sigma}$ are symmetric and shows that the trace of (7.47) reduces to (7.45), implying that $P^{\nu\sigma}$ is tracefree. Equations (7.45)-(7.47) cannot provide field equations for the 14 dynamical fields n^μ and $T^{\mu\nu}$, unless $F^{\mu\nu\sigma}$ and $P^{\nu\sigma}$ are related to one another. These relations are restricted only by the requirement of hyperbolicity, by the relativity principle and by the entropy principle as expressed by (7.21). The production density tensor also allows for a rigorous definition of an equilibrium process as a process in which the production densities $P^{\mu\nu}$ vanish

$$P^{\mu\nu} \Big|_E = 0. \quad (7.48)$$

Since the trace of $P^{\mu\nu}$ is zero (Chernikov, 1963), equation (7.48) amounts to nine independent conditions of equilibrium. Eight of these conditions are trivial since at equilibrium $\pi^{\mu\nu}$ and q^μ must be zero. The remaining condition obviously must give an equilibrium relation between the remaining non-zero quantities P , n and e . We write this relation as

$$P \Big|_E = p(n, e) \quad (7.49)$$

This is the motivation for the introduction of the non-equilibrium part of pressure Π (*the dynamic pressure*) in (7.17), where $P = p + \Pi$. Thus, in equilibrium all the three quantities Π , q^μ and $\pi^{\mu\nu}$ vanish.

Following Liu *et al* (1986), we consider the case where $F^{\mu\nu\sigma}$ and $P^{\nu\sigma}$ are linear in the dissipative fluxes

$$P^{\mu\nu} = B_1^\Pi \Pi (g^{\mu\nu} + 4u^\mu u^\nu) + B_3 (q^\mu u^\nu + q^\nu u^\mu) + B_4 \pi^{\mu\nu}, \quad (7.50)$$

$$\begin{aligned} F^{\mu\nu\beta} = & (C_1^0 + C_1^\Pi \Pi) u^\mu u^\nu u^\beta + \frac{c^2}{6} (\rho m - C_1^0 - C_1^\Pi \Pi) (g^{\mu\nu} u^\beta + g^{\nu\beta} u^\mu + g^{\beta\mu} u^\nu) + \\ & C_3 (g^{\mu\nu} q^\beta + g^{\nu\beta} q^\mu + g^{\beta\mu} q^\nu) - \frac{6}{c^2} C_3 (u^\mu u^\nu q^\beta + u^\nu u^\beta q^\mu + u^\beta u^\mu q^\nu) + \\ & C_5 (\pi^{\mu\nu} u^\beta + \pi^{\nu\beta} u^\mu + \pi^{\beta\mu} u^\nu). \end{aligned} \quad (7.51)$$

Even in a linear theory as characterized by the linear relations (7.50)-(7.51) we shall be able

to calculate the coefficients of linear and quadratic terms of the entropy flux vector as

$$S^\beta = (ns + A_1^\Pi \Pi + A^{\Pi^2} \Pi^2 + A_1^q q^\mu q_\mu + A_1^\pi \pi^{\mu\nu} \pi_{\mu\nu}) u^\beta + (A_2^0 + A_2^\Pi \Pi) q^\beta + A_3^0 \pi^{\beta\mu} q_\mu. \quad (7.52)$$

As required, in equilibrium $P^{\mu\nu} = 0$ and $S^\mu = snu^\mu$. It could be objected that the formulation of extended thermodynamics given by (7.39)-(7.41) contains a smaller number of parameters than the present one, and should therefore be preferred. Liu *et al.* (1986), however, showed that the unknown coefficients in (7.50) and (7.52) can actually be calculated through statistical mechanics, allowing one to make the representations (7.50) and (7.52) very explicit. Also, due to the entropy principle, the coefficients A_1^Π through C_5 are strongly restricted in their dependence on the absolute temperature T and on the fugacity α , defined as

$$\alpha \equiv -\frac{1}{T} \frac{e + Tsn + p}{\rho}, \quad (7.53)$$

providing the equilibrium state functions $\rho(\alpha, T)$, $e(\alpha, T)$, $p(\alpha, T)$, $C_1^0(\alpha, T)$ and $s(\alpha, T)$ are known⁷.

6.2 The Non-degenerate Relativistic gas

The general results reported above can be applied to the limiting case of a non-degenerate relativistic gas. We know that a relativistic gas is described by the Jüttner distribution (Jüttner 1911)

$$f = \frac{y}{\exp[m\alpha/k + u^\mu p_\mu/(kT)] \pm 1}, \quad (7.54)$$

where k is the Boltzmann constant and $y = I/h^3$, h being Planck's constant and I being equal to $2s + 1$ for particles with spin $s\hbar$. The equilibrium distribution function (7.54) takes on different forms according to the degree of degeneracy of the gas and to the different degrees to which relativistic effects become important⁸. Let us just consider a non-degenerate gas, i.e. a gas characterized by large values of the fugacity $m\alpha/k \gg 1$, so that the distribution (7.54) reduces to

$$f = y \exp[-m\alpha/k - u^\mu p_\mu/(kT)]. \quad (7.55)$$

In this case the integrals (7.42)-(7.44) over the distribution function are expressed in terms of the Bessel function of the second kind

$$K_l(\gamma) = \int_0^\infty \cosh(lx) e^{-\gamma \cosh x} dx, \quad (7.56)$$

⁷Fugacity and absolute temperature are the natural variables of statistical thermodynamics. However, one can always switch to the variables (ρ, e) , provided that the thermal equation of state $p = p(\alpha, T)$ is known.

⁸If $\gamma \equiv mc^2/(kT)$ is much larger than 1, we have a non-relativistic gas; if instead γ is much smaller than 1 the gas is ultra-relativistic.

and, after very lengthy calculations, the fundamental thermodynamic quantities can be written as (Müller & Ruggeri, 1998)

$$n = e^{-\frac{m}{k}\alpha} 4\pi y m^3 c^3 \frac{K_2}{\gamma}, \quad (7.57)$$

$$e = \rho c^2 \left(G - \frac{1}{\gamma} \right), \quad (7.58)$$

$$p = \rho c^2 \frac{1}{\gamma} = nkT, \quad (7.59)$$

$$s = k \left[\ln 4\pi y m^3 c^3 + \ln \frac{K_2}{n\gamma} + \gamma G \right], \quad (7.60)$$

where $G(\gamma) = \frac{K_3}{K_2}$ is a function of $\gamma = \frac{mc^2}{kT}$. Note that from (7.58) and (7.59) it follows that $G = (e+p)c^2$ is nothing but the specific enthalpy, expressed as a function of the temperature through γ . Moreover, the pressure is related to the particle density in the same way as in a classical ideal gas,⁹ a fact which was first noted by Jüttner (1911). The remarkable fact is that, within this approximation, the coefficients entering (7.51) and (7.52) can be written explicitly as (see Müller & Ruggeri, 1998)

$$C_1^0 = \rho \left(1 + \frac{6}{\gamma} G \right), \quad (7.61)$$

$$C_1^\pi = -\frac{6}{c^2}. \quad (7.62)$$

$$\frac{(2 - \frac{5}{\gamma^2}) + (\frac{19}{\gamma} - \frac{30}{\gamma^3})G - (2 - \frac{45}{\gamma^2})G^2 - \frac{9}{\gamma}G^3 + (1 - \frac{1}{\gamma^2} + \frac{5}{\gamma}G - G^2)\frac{1}{48}m^3c^3\frac{A(\alpha)}{n\gamma^5}}{\frac{3}{\gamma} - (2 - \frac{20}{\gamma^2})G - \frac{13}{\gamma}G^2 + 2G^3}$$

$$C_3 = -\frac{1}{\gamma} \frac{1 + \frac{6}{\gamma}G - G^2 + \frac{1}{240}m^3c^3\frac{A(\alpha)}{n\gamma^5}}{1 + \frac{5}{\gamma}G - G^2}, \quad (7.63)$$

$$C_5 = \left(\frac{6}{\gamma} + \frac{1}{G} \right) + \frac{1}{G} \frac{1}{240}m^3c^3\frac{A(\alpha)}{n\gamma^5}, \quad (7.64)$$

$$A_1^{\Pi^2} = \frac{1}{4} \frac{k}{m^3c^2} \frac{\gamma^2}{n} \frac{1 - \frac{1}{\gamma^2} + \frac{5}{\gamma}G - G^2}{\frac{3}{\gamma} - (2 - \frac{20}{\gamma^2})G - \frac{13}{\gamma}G^2 + 2G^2} C_1^\Pi, \quad (7.65)$$

$$A_1^q = \frac{1}{2} \frac{k}{m^2c^6} \frac{\gamma}{n} \frac{\frac{5}{\gamma} + (\frac{30}{\gamma^2} - 1)G - \frac{10}{\gamma}G^2 + G^3 + \frac{1}{48}m^3c^2\frac{A}{n\gamma^6}}{(1 + \frac{5}{\gamma}G - G^2)^2}, \quad (7.66)$$

$$A_1^\pi = -\frac{1}{4} \frac{k}{m^2c^4} \frac{\gamma^2}{n} \frac{1}{G^2} \left(1 + \frac{6}{\gamma}G + \frac{1}{240}m^3c^3\frac{A}{n\gamma^5} \right), \quad (7.67)$$

⁹In general, it is not possible to invert $G(\gamma)$. In the low temperature limit, however, when $\gamma \gg 1$, the function G is well approximated by $G \simeq 1 + 5/2\gamma$ (Synge, 1957). If we wish to make this expression compatible with a standard polytropic equation of state $p = \kappa \rho^\Gamma$, where Γ is the adiabatic index, it turns out that it must be $\Gamma = 5c^2/(2\gamma\epsilon)$, ϵ being the usual specific internal energy.

$$A_2^0 = \frac{1}{T}, \quad (7.68)$$

$$A_2^\Pi = \frac{k}{m^2 c^4} \frac{\gamma}{n} \cdot \frac{-2 + \frac{5}{\gamma^2} - (\frac{22}{\gamma} - \frac{30}{\gamma^3} G + (4 - \frac{65}{\gamma^2}) G^2 + \frac{22}{\gamma} G^3 - 2G^4 + (1 - \frac{1}{\gamma^2} + \frac{5}{\gamma} G - G^2) \frac{1}{48} m^3 c^3 \mathcal{A}}{(1 + \frac{5}{\gamma} G - G^2)(-\frac{3}{\gamma} + (2 - \frac{20}{\gamma^2} + \frac{13}{\gamma} G^2 - 2G^3))} \quad (7.69)$$

$$A_3^0 = \frac{k}{m^2 c^4} \frac{\gamma}{n} \frac{1 + \frac{6}{\gamma} G - G^2 + \frac{1}{240} m^3 c^3 \frac{\mathcal{A}}{n \gamma^5}}{G(1 + \frac{5}{\gamma} G - G^2)} \quad (7.70)$$

Overall, the balance equations (7.45)-(7.47), with the representation (7.17), (7.50), (7.51) and the expression (7.61)-(7.64) provide a set of field equations for the variables n , e , u^μ , Π , $\pi^{\mu\nu}$ and q^μ , which contains only one unknown function of one variable, i.e. \mathcal{A} , and three negative valued functions of n and e , i.e. B_1^π , B_3 and B_4 . Liu *et al.* (1986) have also proved that extended thermodynamics contains Eckart's theory as an approximation.

6.3 Extended Thermodynamics of moments

The extension of the number of fields does not stop at 14 (the independent terms out of n , u^μ , $\pi^{\mu\nu}$, p , q^μ and e), but proceeds to include the higher order moments of the distribution function. However, the extension to a large number of fields raises the question of their interpretation and of their controll, especially when planning to make numerical computations. Furthermore, there is an important drawback connected with this procedure. Namely, the introduction of spurious characteristic speeds, i.e., characteristic waves that arise only from the truncation procedure (connected with the number of moments retained in the theory) and which have no counterpart in the underlying kinetic description. Since these characteristics represent a fan which broadens as the number of moments increases, there could be serious difficulties due to the appearance of nonphysical discontinuities in the solution of the equations. Fortunately, it has been shown by direct numerical integration (Weiss 1995) that the discontinuities can occur only at the highest characteristic speed, and the latter increases with the number of retained moments.

7 Discussion

After this brief review of the different formulations of Rational Extended Thermodynamics, it is worth turning to astrophysics in order to provide at least an idea of what are the possibilities for an application of these new theories in modeling specific astrophysical processes. It should be said that the equations of a causal divergence-type theory will often require modifications when applied to specific contexts. One fundamental objection that is usually made is related to the physical content of the causal fluid theories. The transport coefficients, for example, as derived in this framework by Liu *et al.* (1986) describe transport by the gas particles, but it is a very well known fact that microscopic transport is too inefficient to

account for the observed properties of many astrophysical systems. This is for instance the case for the angular momentum transport in accretion discs, and for the heat transport in stars. The correct approach in these cases would require a turbulence model on top of a causal fluid theory. In the absence of such a description, a first order approximation consists of assuming that the turbulence does indeed behave like a microscopic phenomenon¹⁰.

Following a very pragmatic approach, for example, the problem of non causality in the context of transonic accretion has been addressed in two different ways. For steady flow Narayan (1992) has recovered causality by calculating the coefficient of kinematic viscosity within an extended version of the flux-limited diffusion theory (Levermore & Pomraning, 1981). The influence of this modified viscosity coefficient was studied in stationary accretion discs by Popham & Narayan (1992) and Syer & Narayan (1993). A relativistic generalization of the modified viscosity has been proposed in models of stationary accretion discs by Peitz & Appl (1997). A different approach was proposed by Papaloizou & Szuszkiewicz (1994), which is directly related to a causal description of thermodynamics allowing for an application to time-dependent models of accretion disc boundary layers.

Finally, it is worth discussing the work done in the formulation of the relativistic hydrodynamics equations for dissipative fluids that would be suitable for numerical calculations. The application of causal type theories to relativistic non ideal hydrodynamics has mainly been prevented by the absence of an appropriate formulation of the equations, either in the form given by (7.33)-(7.35co), or in the divergence type formulation (7.45)-(7.47). Recently, however, Peitz & Appl (1999) recast both sets of equations in the $3 + 1$ formalism of Arnowitt, Deser & Misner, (1962), thus providing an appealing tool for numerical applications. It should be stressed, however, that the most convenient formulation could come from divergence type theories, which, in principle, could allow for the implementation of HRSC methods to the hydrodynamics of dissipative fluids.

¹⁰Magnetic turbulent viscosity has been simulated by Brandenburg *et al.*, 1995.

Chapter 8

Magnetic Field Decay in Neutron Stars

1 Introduction

This last Chapter of the thesis is about the influence of strongly curved space-times on the properties of electromagnetic fields in slowly rotating neutron stars.

It is well known that the coupling between general relativistic effects and electromagnetic fields is particularly important in the vicinity of neutron stars which are among the most relativistic astrophysical objects and are characterized by very intense magnetic fields (Lamb 1991, Glendenning 1996). Many observations indicate that in young neutron stars the surface magnetic field strengths are of the order of $10^{11} - 10^{13}$ G. In some exceptional cases, as those of magnetars, magnetic field strengths $\geq 5 \times 10^{14}$ G are considered responsible for the phenomenology observed in soft gamma-ray repeaters (Duncan & Thompson 1992, Thompson & Duncan 1995). Older neutron stars, observed as recycled pulsars and low mass X-ray binaries, show instead surface magnetic fields that are much weaker $\leq 10^{10}$ G suggesting that these are subject to a decay, even if it is still difficult to establish whether the decay is due to accretion (Geppert & Urpin, 1994; Konar & Battacharya, 1997) or to other processes. In the case of isolated neutron stars, the possibility of magnetic field decay as a result of accretion does not arise, but there are still a number of different ways in which the energy stored in the magnetic field can be lost. This can happen either through the emission of electromagnetic (dipole) radiation, through Ohmic decay, through ambipolar diffusion, or through more complicated effects such as “Hall cascades” (see Goldreich and Reisenegger 1992 for a review). The investigation of these scenarios requires combined efforts. On one hand, there is the search for a more precise description of the microphysics of the processes involved, some of which are still not well quantified. On the other hand, attention is paid to a more realistic description of the gravitational effects on the properties of the electromagnetic fields in highly curved spacetimes. The investigation of the general relativistic corrections to the solution of Maxwell equations in the spacetime of a relativistic star has a long history. The initial works of Ginzburg & Ozernoy (1964), Anderson & Cohen (1970) and of Petterson

(1974) on the stationary electromagnetic fields in a Schwarzschild spacetime have revealed that the spacetime curvature produces magnetic fields which are generally stronger than their Newtonian counterparts (see also Wasserman & Shapiro 1983 for a subsequent derivation). More recently, Sengupta has also considered the problem of the Ohmic decay rate in a Schwarzschild spacetime (Sengupta, 1997). His approach is strictly valid only for the region of spacetime external to the star as it does not provide a correct general relativistic description of the electromagnetic fields internal to the star. Within these approximations, however, Sengupta (1997) has pointed out that the effects of intense gravitational field seem to decrease the overall decay rate by a couple of orders of magnitude. The same problem has also been considered in more detail by Geppert, Page and Zannias (2000). Their analysis was aimed at a mathematically consistent solution of Maxwell equations also in the spacetime region internal to the star and makes therefore use of a generic metric for a non-rotating relativistic star. Their results, while confirming a decrease in the typical decay time for the magnetic field, also show that the decay time is smaller but comparable with the one found in flat spacetime.

The general relativistic effects induced by the rotation of the star were first investigated by Muslimov & Tsygan (1992) in the slow rotation approximation. A similar approach was also used by Muslimov and Harding (1997) for the electromagnetic fields external to a rotating magnetized star. Their analysis refers to a charge filled magnetosphere and represents the relativistic extension of the Goldreich-Julian model. Using a different derivation, Prasanna and Gupta (1997) have also investigated the properties of the electromagnetic fields in the magnetosphere of a relativistic rotating neutron star, with special attention being paid to the dynamics of charged test particles. Finally, Rezzolla *et al* (2001) have extended all of the above investigations by considering the solution of Maxwell equations in the internal and external background spacetime of a slowly rotating magnetized relativistic star. The star is there considered isolated and in vacuum, with a dipolar magnetic field which is not assumed aligned with the axis of rotation. As a result of this analysis, it was possible to show that in the case of finite electrical conductivity, general relativistic corrections due both to the spacetime curvature and to the dragging of reference frames are present in the induction equations. Moreover, when the stellar rotation is taken into account, each component of the magnetic field is governed by its own evolutionary law, thus removing the degeneracy encountered in the case of nonrotating spacetimes. In the present Chapter, through a number of calculations, we will present the numerical solution of those equations focusing on the evolution of the magnetic field when different rates of stellar rotation, different inclination angles between the magnetic moment and the rotation axis, as well as different values of the electrical conductivity are considered. All of these calculations have been performed for a constant temperature relativistic polytropic star and make use of a consistent solution of the initial value problem which avoids the use of artificial analytic functions.

Overall, we will show that the rotation of the star and of the background spacetime introduce a *decrease* in the decay rate of the magnetic field. In general, however, the rotation-induced

corrections are hidden by the high electrical conductivity of the neutron star matter and are effectively negligible even for the fastest known pulsar. Also in the absence of rotation, the spacetime curvature introduces modifications to the evolution of the magnetic field when compared with the corresponding evolution in a flat spacetime. These modifications depend sensitively on both the metric functions of the interior spacetime and on the radial profile of the electrical conductivity. In the case the star is modeled as a polytrope and the electrical conductivity is assumed to be uniform in space and time, the spacetime curvature generally increases the decay rate of the magnetic field as compared to the flat spacetime case, with this increase being dependent on the compactness of the star.

The system of units chosen in this Chapter is given by setting $G = c = M_\odot = 1$. (However, for those expressions of astrophysical interest, we have written the speed of light explicitly.).

2 The Structure of the Star

We assume that the background metric is that of a stationary, axially symmetric system truncated at the first order in the angular velocity Ω . In a coordinate system (ct, r, θ, ϕ) , the “slow rotation metric” for a rotating relativistic star (see, for example, Hartle 1967, Hartle & Thorne 1968, Landau & Lifshitz 1971) is

$$ds^2 = -e^{2\Phi(r)} dt^2 + e^{2\Lambda(r)} dr^2 - 2\omega(r)r^2 \sin^2 \theta dt d\phi + r^2 d\theta^2 + r^2 \sin^2 \theta d\phi^2, \quad (8.1)$$

where $\omega(r)$ is the angular velocity of a free-falling inertial frame, also known as the Lense-Thirring angular velocity. Note that using the slow-rotation approximation gives rather accurate results for all pulsar periods so far observed. The metric (8.1) has coefficients each of which is the lowest-order term of a series expansion in ascending powers of Ω . Comparing the magnitude of the neglected higher order terms with that of the one retained in each case, gives ratios of the order $R^3 \Omega^2 / GM$ which is smaller than 10% even for the fastest-known millisecond pulsar PSR 1937+214. On the other hand, for realistic values of the stellar magnetic field (i.e. $B = 10^{11} - 10^{13}$ G) we can also neglect the contribution of the electromagnetic fields to the background spacetime geometry and determine the internal structure of the star and its interior spacetime after solving the following system of ordinary differential equations (henceforth TOV system, from Tolmann, 1939; Oppenheimer & Volkoff, 1939)

$$\begin{aligned} \frac{dp}{dr} &= -\frac{(p+e)(m+4\pi r^3 p)}{r^2(1-2m/r)}, \\ \frac{dm}{dr} &= 4\pi r^2 e, \\ \frac{d\Phi}{dr} &= \frac{m+4\pi r^3 p}{r^2(1-2m/r)} = -\frac{1}{e} \frac{dp}{dr} \left(1 + \frac{p}{e}\right)^{-1}, \end{aligned} \quad (8.2)$$

where $p(r)$ is the pressure, $e(r)$ is the energy density and $m(r)$ is the mass enclosed within r . Once an equation of state has been chosen, the TOV system can be solved numerically together with the differential equation for the Lense-Thirring angular velocity $\omega(r)$ in the internal region of the star

$$\frac{1}{r^3} \frac{d}{dr} \left[r^4 e^{-(\Phi+\Lambda)} \frac{d\bar{\omega}}{dr} \right] + 4 \frac{d(e^{-(\Phi+\Lambda)})}{dr} \bar{\omega} = 0, \quad (8.3)$$

where $\bar{\omega} \equiv \Omega - \omega$ is the angular velocity of the fluid as measured from the local free falling (inertial) frame. After selecting a value for the central rest-mass density, the set of differential equations (8.2) – (8.3) is solved from the centre of the star until the pressure vanishes, thus determining the radius R . For the integration of eq. (8.3), the solution near the centre of the star is simplified if we use the analytic power series expansion $\bar{\omega}/\bar{\omega}_c \simeq 1 + 8\pi(e_c + p_c)r^2/5$, valid for $r \rightarrow 0$ and where the label “c” refers to a quantity at the centre of the star (Miller, 1977). Since in the vacuum region of spacetime external to the star $\omega(r) = 2J/r^3$, with J being the total angular momentum, we can determine the two unknown quantities J and ω_c by imposing continuity of the angular velocity and of its first derivative at the surface.

The interior of the star influences the magnetic evolution either macroscopically, by affecting the metric quantities which enter the induction equations, or microscopically, through the electrical conductivity σ which, in turn, depends on the star’s temperature and chemical composition (see Urpin & Konenkov, 1997; Page *et al* 2000). Our attention is here mainly focussed on assessing the contribution coming from rotational effects in general relativity on the decay of the magnetic field ¹. As a consequence, we will neglect the thermal and rotational evolution of the neutron star and simply consider a constant in time and uniform in space electrical conductivity. This is an approximation, but a necessary one to disentangle the many different effects that intervene in the general relativistic evolution of the magnetic field. Furthermore, as will be discussed in Section 4, the assumption of a uniform electrical conductivity does not affect the role of a rotating background spacetime in the evolution of the magnetic field.

The relativistic star is modelled as a polytrope with equation of state

$$p = K\rho^{1+1/N}, \quad (8.4)$$

where ρ , K , N are the rest-mass density, the polytropic constant and the polytropic index, respectively. As “fiducial” model of neutron star we consider a polytrope with index $N = 1$, polytropic constant $K = 100$, and central rest-mass density $\rho_c = 1.28 \times 10^{-3}$. In this case, the radius R and the total mass M obtained through the solution of the TOV system are respectively $R = 14.15$ Km and $M = 1.40 M_\odot$, yielding a compactness ratio $\eta = 0.29$. The

¹It should be mentioned that general relativistic corrections can appear also in the constitutive relations of the Maxwell equations, such as in the general relativistic form of Ohm’s law (Ahmedov 1999). These corrections are usually negligible in the electrodynamics of relativistic stars and will be neglected here.

rotation period usually chosen for this model is $P = 10^{-3}$ s.

3 Evolution of the Internal Magnetic Field

As mentioned in Section 1, the presence of the stellar rotation lifts the degeneracy found in the case of a nonrotating star (Geppert *et al* 2000) and three distinct induction equations regulate the general relativistic evolution of the magnetic field. In this Section we discuss the solution of the induction equations for each of the magnetic field components. The main difficulties encountered in the numerical solution are related to the definition of a consistent initial value problem and to the complex nature of the partial differential equations when a misalignment between the rotation axis and the magnetic dipole moment is present. A strategy is therefore needed to handle these difficulties.

3.1 The Relativistic Induction Equations

The induction equations for the magnetic field of a slowly rotating relativistic star with finite electrical conductivity have been derived by Rezzolla *et al* (2001) and we will briefly recall them here for completeness. All the measurements are performed in the orthonormal tetrad frame of a “zero angular momentum observer” (ZAMO) and we assume that the spatial components of the magnetic field four-vector in this frame are solutions of the Maxwell equations in the separable form

$$B^{\hat{r}}(r, \theta, \phi, \chi, t) = F(r, t) \Psi_1(\theta, \phi, \chi, t) , \quad (8.5)$$

$$B^{\hat{\theta}}(r, \theta, \phi, \chi, t) = G(r, t) \Psi_2(\theta, \phi, \chi, t) , \quad (8.6)$$

$$B^{\hat{\phi}}(r, \theta, \phi, \chi, t) = H(r, t) \Psi_3(\phi, \chi, t) , \quad (8.7)$$

where F, G, H and Ψ_1, Ψ_2, Ψ_3 account for the radial and angular dependences, respectively. Here, χ is the inclination angle of the stellar magnetic dipole moment relative to the rotation axis and the time dependence in F, G, H is here due to the fact that we are not considering an infinite electrical conductivity but are allowing the magnetic dipole moment to vary in time.

At first order in Ω , the angular eigenfunctions Ψ_i are not affected by general relativistic corrections and assume the flat spacetime expressions

$$\Psi_1 = \cos \chi \cos \theta + \sin \chi \sin \theta \cos \lambda(t) , \quad (8.8)$$

$$\Psi_2 = \cos \chi \sin \theta - \sin \chi \cos \theta \cos \lambda(t) , \quad (8.9)$$

$$\Psi_3 = \sin \chi \sin \lambda(t) , \quad (8.10)$$

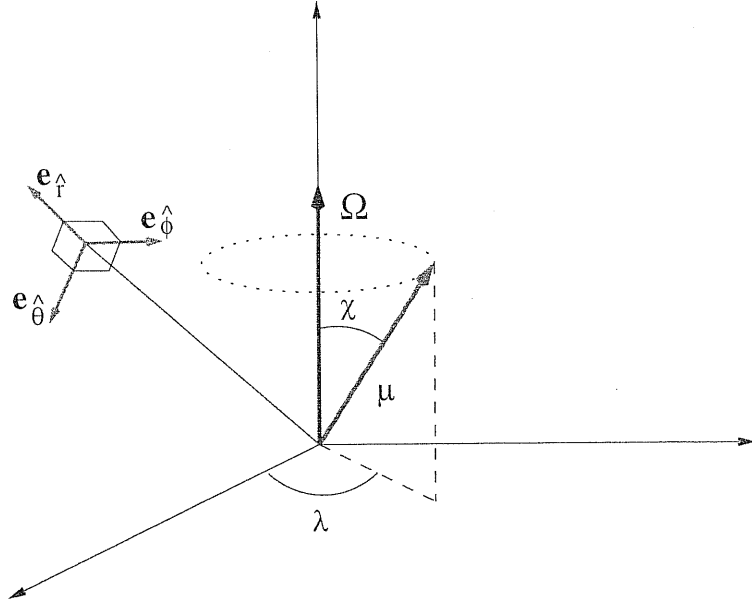


Figure 8.1: Schematic representation of a misaligned rotator. Here $(e_{\hat{\theta}}, e_{\hat{r}}, e_{\hat{\phi}}, e_{\hat{\phi}})$ is a local orthonormal frame, μ is the magnetic dipole moment of the star, χ is the inclination angle relative to the rotation axis, and λ the instantaneous azimuthal position.

where $\lambda(t) \equiv \phi - \Omega t$ is the instantaneous azimuthal position (see Fig. 8.1). Assuming that the contribution of electric currents are negligible² the general relativistic evolution equations for the radial eigenfunctions $F(r, t)$, $G(r, t)$, $H(r, t)$ are

$$\begin{aligned} \frac{\partial F}{\partial t} \Psi_1 \sin \theta = & \frac{c^2 e^{-\Lambda}}{4\pi\sigma r^2} \left\{ [e^{\Phi} r (G - H)]_{,r} \sin \chi \cos \lambda - 2 \left[(e^{\Phi} r G)_{,r} + e^{\Phi+\Lambda} F \right] \Psi_1 \sin \theta \right. \\ & - \frac{1}{4\pi\sigma} \sin \chi \sin \lambda \left\{ [\omega r (H - G)]_{,r} (1 - 2 \sin^2 \theta) \right. \\ & + 2\omega e^{-\Phi} \left[(e^{\Phi} r H)_{,r} + e^{\Phi+\Lambda} F \right] \sin^2 \theta \\ & \left. \left. - \Omega r (G - H) \Phi_{,r} (1 - 2 \sin^2 \theta) \right\} \right\}, \end{aligned} \quad (8.11)$$

$$(8.12)$$

²Because the magnetic field decay is studied on timescales that are much longer than the electromagnetic wave crossing time, this is a very good approximation.

$$\begin{aligned}
\frac{\partial G}{\partial t} \Psi_2 = & \frac{c^2}{4\pi\sigma r} \left\{ \frac{e^\Phi (G - H)}{r \sin^2 \theta} \cos \theta \sin \chi \left[\cos \lambda + \frac{\omega e^{-\Phi}}{4\pi\sigma} \sin \lambda \right] \right. \\
& + e^{-\Lambda} \left[e^{-\Lambda} (e^\Phi r G)_{,r} + e^\Phi F \right]_{,r} \Psi_2 \\
& - \frac{e^{-\Lambda}}{4\pi\sigma} \cos \theta \sin \chi \sin \lambda \left\{ e^{-\Lambda} [\omega r (G - H)]_{,r} + \omega \left[F + e^{-(\Lambda+\Phi)} (r e^\Phi H)_{,r} \right] \right. \\
& \left. \left. + \Omega [\Phi_{,r} e^{-\Lambda} r (G - H)] \right\} \right\}, \tag{8.13}
\end{aligned}$$

$$\begin{aligned}
\frac{\partial H}{\partial t} \sin \lambda = & \frac{c^2 e^{-\Lambda}}{4\pi\sigma r} \left\{ \left[e^{-\Lambda} (e^\Phi r H)_{,r} + e^\Phi F \right] \left[\sin \lambda - \frac{\omega e^{-\Phi}}{4\pi\sigma} \cos \lambda \right] \right\}_{,r} \\
& + \frac{c^2 e^\Phi (G - H)}{4\pi\sigma r^2 \sin^2 \theta} \left[\sin \lambda - \frac{\omega e^{-\Phi}}{4\pi\sigma} \cos \lambda \right]. \tag{8.14}
\end{aligned}$$

Together with the evolution equations (8.11)–(8.14), the scalar functions F , G , and H also satisfy the constraint condition of zero-divergence for the magnetic field

$$\left[(r^2 F)_{,r} + 2e^\Lambda r G \right] \sin \theta (\cos \chi \cos \theta + \sin \chi \sin \theta \cos \lambda) + e^\Lambda r (H - G) \sin \chi \cos \lambda = 0. \tag{8.15}$$

A rapid look at equations (8.11)–(8.14) shows that in a rotating spacetime the evolution of the poloidal and toroidal components are correlated and that an initially purely poloidal magnetic field can gain a toroidal component during its evolution and vice-versa. Moreover, since the second term in equation (8.15) does not depend on θ , the only way to satisfy (8.15) is to have $G = H$, which makes the integration of (8.14) unnecessary.

In the case of a nonrotating star, on the other hand, the three induction equations (8.11)–(8.14) are not independent and the magnetic field evolution is described by a single scalar function F governed by the following evolution equation:

$$\frac{\partial F}{\partial t} = \frac{c^2 e^{-\Lambda}}{4\pi\sigma r^2} \left\{ \left[e^{\Phi-\Lambda} (r^2 F)_{,r} \right]_{,r} - 2e^{\Phi+\Lambda} F \right\}, \tag{8.16}$$

corresponding to the solution found by Geppert et al. (2000). When the metric functions Φ and Λ refer only to the vacuum region of spacetime external to the star, equation (8.16) further simplifies to

$$\frac{\partial F}{\partial t} = \frac{c^2}{4\pi\sigma r^2} \sqrt{\frac{r-2M}{r}} \left\{ \left[\left(1 - \frac{2M}{r} \right) (r^2 F)_{,r} \right]_{,r} - 2F \right\}, \tag{8.17}$$

and which now corresponds to the solution found by Sengupta (1997). However, one should

underline that using a Schwarzschild metric is intrinsically inadequate to describe physical systems such as pulsars in which the coupling of electromagnetic fields and rotation is a key feature.

3.2 Strategy of the Numerical Solution

The numerical solution of equations (8.11)–(8.14) is simplified if done in terms of the new quantities

$$\tilde{F} \equiv r^2 F , \quad (8.18)$$

$$\tilde{G} \equiv e^\Phi r G , \quad (8.19)$$

$$\tilde{H} \equiv e^\Phi r H , \quad (8.20)$$

which, when the inclination angle χ is nonzero and the electrical conductivity is uniform, allow us to rewrite eqs. (8.11)–(8.14) schematically as

$$\frac{\partial \tilde{F}}{\partial t} = f_1 \tilde{F}_{,rr} + f_2 \tilde{F}_{,r} + f_3 \tilde{F} + f_4 \tilde{H}_{,r} + f_5 \tilde{G} + f_6 \tilde{G}_{,r} , \quad (8.21)$$

$$\frac{\partial \tilde{G}}{\partial t} = g_1 \tilde{G}_{,rr} + g_2 \tilde{G}_{,r} + g_3 \tilde{G} + g_4 \tilde{F}_{,r} + g_5 \tilde{F} + g_6 \tilde{H}_{,r} + g_7 \tilde{H} , \quad (8.22)$$

$$\frac{\partial \tilde{H}}{\partial t} = h_1 \tilde{H}_{,rr} + h_2 \tilde{H}_{,r} + h_3 \tilde{H} + h_4 \tilde{F}_{,r} + h_5 \tilde{F} + h_6 \tilde{G} . \quad (8.23)$$

Explicit expressions for the set of coefficients f_i, g_i, h_i can be found in Appendix D. For $\chi \neq 0$, the coefficients f_i, g_i, h_i have terms which are time-dependent trigonometric functions of Ωt and, as a result, each of the eqs. (8.21)–(8.23) is not a simple parabolic equation describing a pure diffusive phenomenon. In addition to a secular Ohmic decay, in fact, there will be a periodic modulation produced by the rotation of the star. This is evident if we look, for instance, at the coefficient f_1 in Appendix D and which is given by the sum of two terms. The first one is the constant “diffusion” coefficient responsible for the decay on a secular timescale. The second term, on the other hand, represents the correction due to the stellar rotation. The periodic modulation is produced by the trigonometric function $\tan \lambda$ and varies therefore on the dynamical timescale set by the rotation period of the star, P . The presence of these periodic terms spoils the parabolic character and makes the set of eqs. (8.21)–(8.23) a mixed hyperbolic-parabolic one.

Although the integration of eqs. (8.21)–(8.23) is complicated in the general case, we are here favoured by the fact that all of the terms proportional to Ω or to ω (i.e. all of the terms directly related to the stellar rotation) scale like σ^{-2} and that the electrical conductivity in

realistic neutron stars is very high, ranging in the interval $10^{21} - 10^{28} \text{s}^{-1}$. As a result, the star's rotation period is about twenty orders of magnitude smaller than the secular timescale and can be ignored in the numerical solution of the equations. In practice then, we set all of the periodic time-varying terms to be constant coefficients and solve the set of eqs. (8.21) – (8.23) as a purely parabolic system. In this way we can capture the secular decay without having to pay attention to the high frequency modulation. In Section 4, where we discuss the results of the numerical integration of the induction equations (8.21) – (8.23), we will also comment on the validation of this procedure.

Another important aspect of the numerical solution is the use of the zero-divergence constrain equation (8.15). We do not need, in fact, to integrate in time all of the eqs. (8.21) – (8.23) but can restrict the evolution to two of them and obtain, at each timestep, the remaining unknown radial eigenfunction from the solution of the constraint equation (8.15). Adopting this strategy in the numerical solution reduces the computational costs and, most importantly, enforces a constrained solution at each timestep.

Having three induction equations, we can follow the decay of each component of the magnetic field separately. The physically relevant quantity is however the modulus of the magnetic field which, in the locally flat spacetime of the ZAMO observer, is simply given by $|B| = [(B^{\hat{r}})^2 + (B^{\hat{\theta}})^2 + (B^{\hat{\phi}})^2]^{1/2}$. The evolution of this quantity, evaluated at the surface of the star, is the one that will be discussed in the remainder of the chapter.

3.3 The Initial Value Problem

The consistent solution of the initial value problem for the general relativistic decay of the magnetic field in a rotating neutron star suffers from two difficult aspects. The first one is that at present the initial topology and location of the magnetic field in neutron stars can be only argued on the basis of some assumptions, so that the magnetic field can either permeate the entire star, or be confined in a layer close to the stellar surface. The first configuration is more plausible if the magnetic field is the final product of a dynamo action amplification (see Thompson & Duncan, 1993), while the second field configuration is more realistic in a scenario in which the magnetic field is originated by thermoelectric effects (Urpin *et al*, 1986; Wiebicke & Geppert, 1996). We here focus our attention mostly on the case of a magnetic field permeating the entire star, but in Section 4 we also show how the decay of the magnetic field depends on the depth of penetration inside the star, when simplified assumptions on the microphysics at the crust-core boundary are made.

The second difficult aspect of the initial value problem concerns the definition of an initial configuration which is also solution of the general relativistic Maxwell equations. A possible approach to this problem is the one proposed by Geppert *et al* (2000) (but see also Sang and Chanmugan, 1987), who have considered the initial magnetic field to be described by Stoke functions that represent, in flat spacetime, a class of exact solutions of the induction

equation. In this case, the radial eigenfunction $\tilde{F}(r)$ at the initial time can be obtained from

$$\tilde{F}(r, t) = B_0 \left[\frac{\sin(\pi r/R)}{\pi^2 r/R} - \frac{\cos(\pi r/R)}{\pi} \right] e^{-\pi^2 t/4\sigma R^2}, \quad 0 \leq r \leq R, \quad (8.24)$$

for $t = 0$, where B_0 is the initial surface magnetic field at the magnetic pole. Because eq. (8.24) is not a solution of the general relativistic Maxwell equations, one expects an initial error being introduced in the solution of the induction equations, but also that this error should disappear rapidly as the solution tends to the one satisfying the Maxwell equations. To circumvent the problem of an inaccurate solution during the initial stages of the evolution and in order to calculate an initial magnetic field which is solution of the relativistic Maxwell equations, we here treat the initial magnetic field as the one permeating a perfectly conducting medium. In this case, Rezzolla et al. (2001a, 2001b) have shown that consistent radial eigenfunctions can be obtained after solving the following set of equations [see (71) – (73) of Rezzolla *et al* 2001].

$$\tilde{F}_{,r} + 2e^{\Lambda-\Phi}\tilde{G} = 0, \quad (8.25)$$

$$\tilde{H}_{,r} + \frac{e^{\Phi+\Lambda}}{r^2}\tilde{F} = 0, \quad (8.26)$$

$$\tilde{H} - \tilde{G} = 0. \quad (8.27)$$

In particular, combining eqs. (8.25) and (8.26), we obtain a second-order differential equation for the unknown radial eigenfunction \tilde{F}

$$\frac{d^2\tilde{F}}{dr^2} + \frac{d}{dr}(\Phi - \Lambda)\frac{d\tilde{F}}{dr} - 2e^{2\Lambda}\frac{\tilde{F}}{r^2} = 0. \quad (8.28)$$

Equation (8.28) can be solved as a two-point boundary value problem after specifying values for the magnetic field at the edges of the numerical grid. More specifically, the initial magnetic field at the inner edge of the grid is chosen to be zero both when the magnetic field permeates the whole star and when it is confined to a crustal layer. On the other hand, the initial magnetic field at the outer edge of the grid is chosen to match a typical surface magnetic field for a neutron star and is therefore set to be $B_0 = 10^{12}$ G. Once the initial profile for \tilde{F} has been calculated through eq. (8.28), the corresponding initial values for \tilde{G} and \tilde{H} follow immediately from eqs. (8.25) and (8.27). As a comparison, we have also solved the induction eqs. (8.21) – (8.23) using as initial condition eq. (8.24) and the corresponding eigenfunctions \tilde{G} and \tilde{H} again as computed from the conditions (8.25) and (8.27).

Fig. 8.2 shows the initial values for the two different prescriptions and, in particular, with a solid line the initial profile as obtained through the solution of the Maxwell eqs. (8.28) and

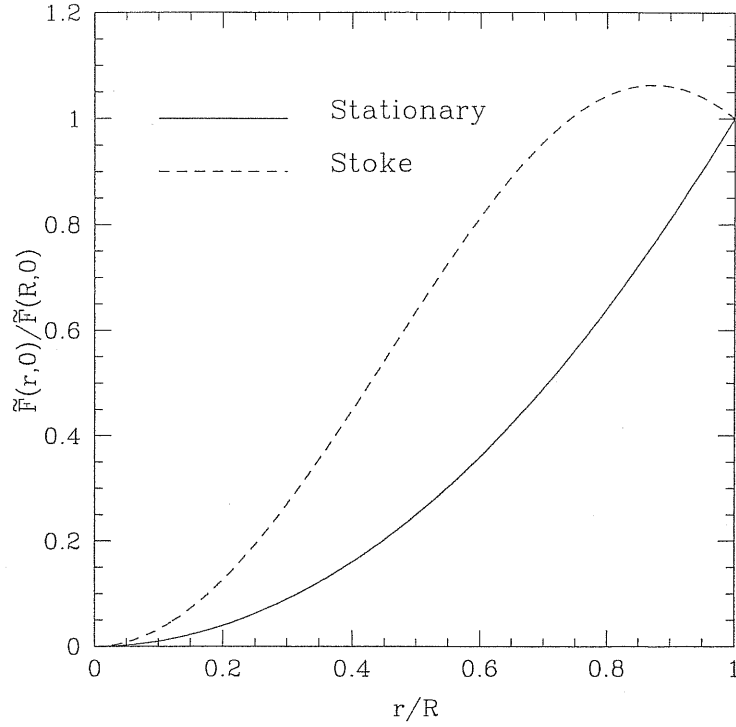


Figure 8.2: Possible initial values for the radial eigenfunction \tilde{F} of the radial component of the magnetic field normalized to the value at the surface, shown as a function of the radial position in the star. The solid line represents the radial eigenfunction \tilde{F} as obtained from the integration of the Maxwell eqs. (8.28), while the dashed line represents the Stoke profile (8.24).

with a dashed line the Stoke profile given by expression (8.24). The noticeable differences between the two initial profiles provide a simple explanation of why the use of Stoke's function produces an initially inaccurate evolution (cf. Fig. 8.3).

The use of the strategy discussed above for the calculation of the initial value problem clearly requires the solution of an additional set of equations but it has the advantage of removing the adjustment of the solution during the initial stages of the decay and provides a more accurate estimate of the magnetic field decay. A discussion of this as well as a comparison with evolutions performed with the Stoke function will be discussed in Section 4. Finally, another aspect worth stressing is that by using eq. (8.28) we also automatically satisfy appropriate boundary conditions at the surface of the star.

3.4 Boundary Conditions

In order to correctly solve the induction equations (8.21) – (8.23), it is essential that appropriate boundary conditions are specified both at the inner edge of the computational domain as well as at the stellar surface.

As for the initial value problem, the inner boundary condition imposed during the evolution is that of a zero magnetic field and is applied both when the magnetic field permeates the whole star and when it is confined to the crust. In the first case, this choice guarantees a regular behaviour of the radial eigenfunctions at the origin, while it reflects the absence of

magnetic field below the crust in the second case. The evolution of the magnetic field has shown to be quite sensitive to the boundary conditions imposed at the stellar surface, but proper boundary conditions can be derived if we assume that there are no electrical currents on the surface and impose a matching between the external and the internal solutions of the magnetic field. The radial eigenfunctions $F(r)$, $G(r)$, and $H(r)$ outside the slowly rotating relativistic star have been derived Rezzolla *et al* (2001) [see eqs. (90)–(92) therein] and are given by

$$\tilde{F}(r) = -\frac{3r^2}{4M^3} \left[\ln N^2 + \frac{2M}{r} \left(1 + \frac{M}{r} \right) \right] \mu , \quad (8.29)$$

$$\tilde{G}(r) = \frac{3N^2}{4M^2} \left[\frac{r}{M} \ln N^2 + \frac{1}{N^2} + 1 \right] \mu , \quad (8.30)$$

$$\tilde{H}(r) = \tilde{G}(r) , \quad (8.31)$$

where $N(r) \equiv (1 - 2M/r)^{1/2} = e^\Phi$ and μ is the magnetic dipole moment. Since the constraint expressed by eq. (8.25) holds also on the stellar surface, we then have

$$\tilde{F}_{,r} \Big|_R + 2e^{\Lambda-\Phi} \tilde{G}(R) = 0 . \quad (8.32)$$

Moreover, when electrical surface currents are not present, we can use eq. (8.29) and (8.30) to express $\tilde{G}(R)$ as

$$\tilde{G}(R) = - \left(\frac{\tilde{N}^2 M}{R^2} \right) \frac{R \ln \tilde{N}^2 / M + 1 / \tilde{N}^2 + 1}{\ln \tilde{N}^2 + 2M(1 + M/R)/R} \tilde{F}(R) , \quad (8.33)$$

where $\tilde{N} \equiv N(r = R)$. Straightforward calculations allow to conclude that

$$R \tilde{F}_{,r} \Big|_R = \Pi(\eta) \tilde{F}(t, R) , \quad (8.34)$$

where $\Pi(\eta)$ is a constant given by

$$\Pi(\eta) \equiv \frac{4n(1 - \eta) + 2\eta(2 - \eta)/(1 - \eta)}{2 \ln(1 - \eta) + 2\eta + \eta^2} , \quad (8.35)$$

with $\eta \equiv 2M/R$ being the compactness of the star. The corresponding boundary conditions for \tilde{G} and \tilde{H} are then easily obtained by means of (8.31) and (8.33).

Note that eq. (8.34) coincides with the boundary condition used by Geppert *et al* (2000) in the case of a static, spherically symmetric background geometry. This is due to the fact that,

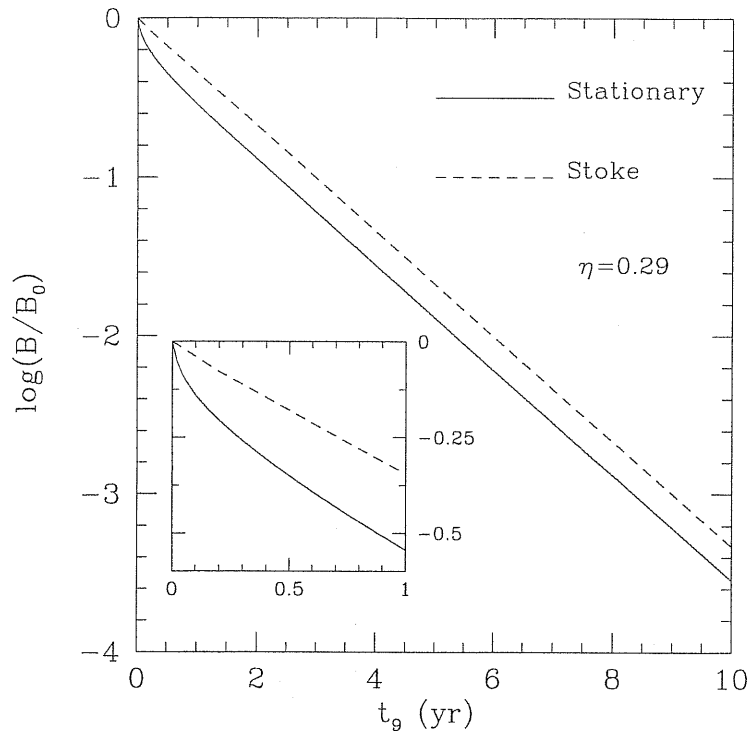


Figure 8.3: Difference in the decay of the magnetic field when a consistent initial magnetic field is used (solid line) or when a Stoke function is used as initial condition (dashed line). The inset shows a magnification of the evolution during the first 10^9 yr. Here $\sigma = 10^{25} \text{ s}^{-1}$ and $P = 10^{-3} \text{ s}$. See the main text for a complete discussion.

as discussed by Rezzolla *et al* (2001), the corrections to the components of the magnetic field enter at orders higher than the first one in Ω . Details on the numerical implementation of the surface boundary conditions are presented in Appendix E.

4 Numerical Results

In order to integrate the set of induction eqs. (8.21)–(8.23), we have built a numerical code which implements the Crank-Nicholson implicit evolution scheme and which provides second order accuracy both in space and in time (see Morton & Mayers, 1994). The accuracy of the code has been checked by computing the time evolution of eq. (8.24) which provides, in a flat spacetime, an exact solution of the induction equation. The results obtained indicate that the relative error between the numerical and the analytic solutions over a timescale of three Newtonian Ohmic times $\tau_{\text{ohm}} \equiv 4\pi R^2 \sigma / c^2$, is always below 0.5% for the level of grid resolution usually implemented in our calculations.

Established the consistency and accuracy of the code, we have proceeded to solve the general relativistic induction equations for our relativistic rotating star. As mentioned in Section 3.2, if the inclination angle between the rotation axis and the dipolar magnetic moment is nonzero, the secular decay has a periodic modulation due to the stellar rotation. We have also discussed that because the decay timescale and the rotation period timescale differ for about

twenty orders of magnitude, we can neglect the time dependence (which is $\propto \sin \lambda$) contained in each of the coefficients f_i , g_i , h_i and set the periodic terms equal to an arbitrary constant value. To validate this procedure and verify that the periodic modulation does not affect the secular evolution, we have solved the induction equations using different constant coefficients and found that the secular results are indeed insensitive to the value chosen for the constant coefficients. We have also followed the solution of the complete set of eqs. (8.21) – (8.23) (i.e. not considering the time-periodic terms as constant) on a timescale which is longer than the dynamical timescale but still much smaller than the secular one. Also in this case we have verified that the modulated evolution, which is superimposed on the secular one, shows the small decrease corresponding to the secular decay.

Our discussion of the results starts by comparing the evolution of eqs. (8.21) – (8.23) for the two different prescriptions of the initial value problem discussed in Sect. 3.3 (cf. Fig. 8.2) for our fiducial neutron star. Before presenting the results of the comparison, it is useful to discuss briefly the subtleties related to the measure of the magnetic field time decay; as will become apparent later, this is an important issue which might lead to seemingly conflicting results. The gauge freedom inherent in the theory of General Relativity allows for the choice of arbitrary observers with respect to which the measure of physically relevant quantities is made. The choice of a certain class of observers might rely on the mathematical advantages that this class may have, but not all observers are physically suitable observers. Locally inertial observers are certainly preferable and in a rotating spacetime, as the one considered here, ZAMO observers represent a natural choice. Of course, there is an infinite number of such observers, each one performing his own measure of the magnetic field decay, so that one should then select a specific set of inertial observers on the basis of physical considerations. The results presented will be referred to a ZAMO observer on the surface of the star and at a latitude $\theta = \pi/2$. The values of the magnetic field measured by this observer and its time evolution can then be converted to the equivalent ones measured by other ZAMOs at different radial and polar positions through simple transformations involving the difference in the red-shifts and latitudes. Once the choice of a suitable class of inertial observers is made, it is also important that the results of the general relativistic magnetic field decay are expressed using appropriate units. In their work, Geppert *et al* (2000) have quantified the decay of magnetic field in a relativistic constant density, nonrotating star in terms of the Newtonian Ohmic time. As we shall show below, while this choice is acceptable for a constant density star, it could be misleading in general.

The two solutions of eqs. (8.21) – (8.23) are presented in Fig. 8.3 and show the decay of the magnetic field, rescaled on a timescale $t_9 \equiv 10^9$ yr. It is interesting to note that while the asymptotic decay rates of the magnetic field are almost the same for the two approaches, a final difference emerges. This is because when using Stoke's function as initial data, the evolution does not satisfy Maxwell's equations during the initial stages (see the small inset in Fig. 8.3), but settles onto a constrained solution only after that time. Moreover, the outer boundary conditions expressed by eqs. (8.33) and (8.34) cannot be satisfied exactly by

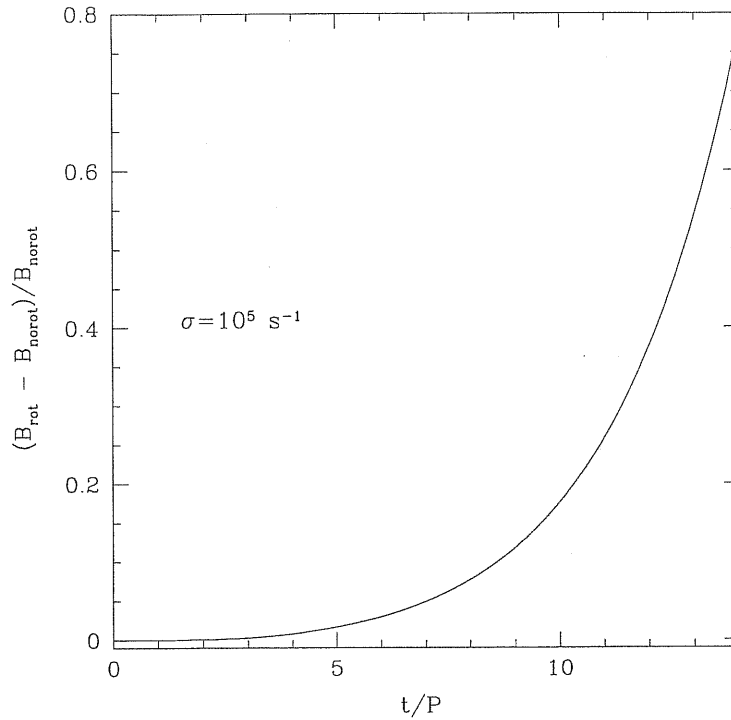


Figure 8.4: Relative difference in the evolution of a magnetic field in a nonrotating star B_{nonrot} and in a rapidly rotating one B_{rot} . The electrical conductivity is here set to be $\sigma = 10^5 \text{ s}^{-1}$, while the star been set to have a period $P = 10^{-3} \text{ s}$.

Stoke's function and this introduces an additional error. As a result, after a time $t \sim t_9 \text{ yr}$, the two solutions differ of about 45%, but this difference does not grow further in time. Next, we discuss the effects introduced by the rotation of the star and of the spacetime. In this case it is worth distinguishing the interest in finding a general relativistic correction, from the impact that these corrections actually have on the magnetic field decay in a realistic rotating neutron star. As discussed in Section 3.2, in fact, the high value of the electrical conductivity in realistic neutron stars tends to make the general relativistic corrections due to rotation rather minute. In particular, we have found that when considering an electrical conductivity $\sigma = 10^{25} \text{ s}^{-1}$ in a rapidly rotating neutron star with one millisecond rotation period, the relative difference in the magnetic field after $15 t_9 \text{ yr}$ is only one part in 10^{12} . Nevertheless, general relativistic, rotation-induced corrections have an interest of their own and these corrections can be more easily appreciated if smaller (and therefore less realistic) values of the electrical conductivity are considered. In Fig. 8.4 we show the relative difference in the evolution of a magnetic field in a nonrotating star, B_{nonrot} , and in a rapidly rotating one with a millisecond period, B_{rot} . In this case and just for illustrative purposes, an electrical conductivity $\sigma = 10^5 \text{ s}^{-1}$ has been considered. As can be appreciated from the figure, the corrections due to the rotation *decrease* the rate of decay of the magnetic field and after a few rotation periods, the fastly rotating star will maintain a magnetic field which is about a factor of two larger than the one calculated for the nonrotating star. Overall, the results obtained indicate that General Relativity does introduce, through the rotation of the spacetime, new

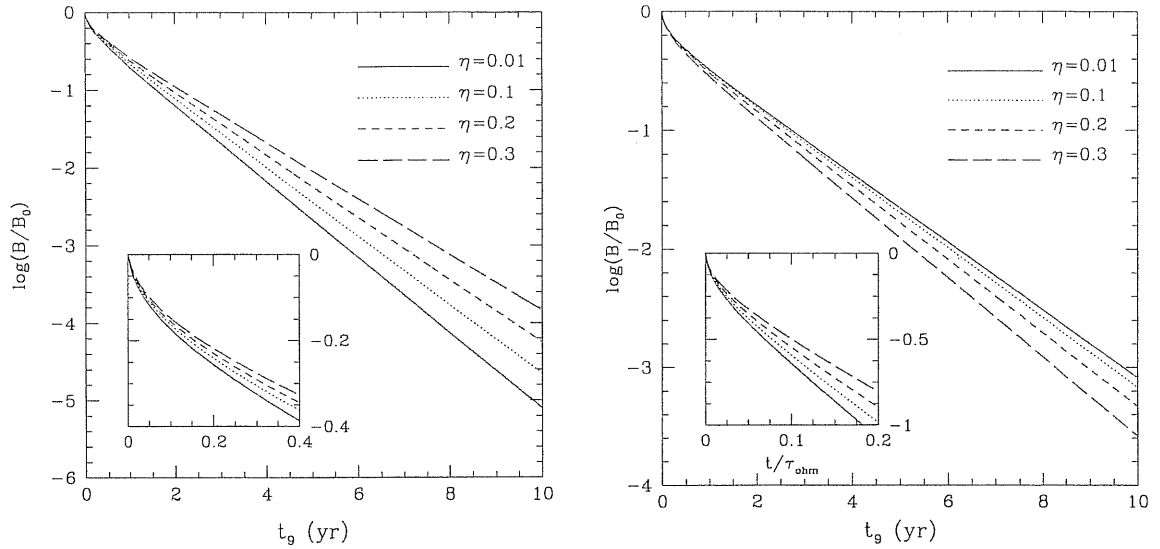


Figure 8.5: Decay of the surface magnetic field as measured by a ZAMO observer on the surface of the star at a latitude $\theta = \pi/2$, expressed on a timescale $t_9 \equiv 10^9$ yr. The left panel refers to a constant density stellar model and shows an asymptotic decay rate of the magnetic field which is *decreasing* for increasing values of the stellar compactness. The inset in the left panel focuses on the initial stages of the evolution when the decay is larger. The right panel, on the other hand, refers to an $N = 1$ polytropic stellar model and shows an asymptotic decay rate which is *increasing* for increasing values of the stellar compactness. Here the central density is the free parameter determining the stellar compactness. The small inset in the right panel of the figure shows how the use of an Ohmic timescale as normalizing unit can lead to erroneous interpretations.

corrections to the evolution of the magnetic field, slightly *decreasing* its decay rate. This effect, however, is usually hidden by the high electrical conductivity of the stellar medium and can be neglected in general. The results discussed above depend also on the inclination between the rotation axis and the magnetic dipole moment, with the decrease rate being larger for larger inclination angles. In particular, for $\chi = \pi/2$, the residual magnetic field after $10 t_9$ yr is smaller of a factor two as compared to the corresponding magnetic field for an inclination $\chi = 0$.

Next, we compare the results of our calculations for a polytropic relativistic star with those for a constant density star. This will provide a first qualitative estimate of the importance of the metric functions in the actual evolution of the magnetic field. The results are presented in Fig. 8.5 with the left panel referring to a constant density model and the right one to our fiducial polytropic model.

In the case of a constant-density star, we confirm the results obtained by Geppert *et al* (2000) and find that the evolution of the magnetic field approaches an exponentially decaying behaviour, with an asymptotic decay rate which is generally *decreasing* with increasing stellar compactness. The inset in the left panel of Fig. 8.5 shows in more detail the initial stages of the magnetic field decay and allows to appreciate that the magnetic field evolution is initially following an exponential decay with decay rates which are quite large but that then reach an asymptotic value after about 10^8 yr (Geppert *et al* 2000).

In the case of a polytropic star, on the other hand, the results in the right panel of Fig. 8.5

show a behaviour which is the opposite to the one encountered for a constant density model and that the asymptotic decay rate of the magnetic field is *increasing* with increasing stellar compactness. When a uniform electrical conductivity is used, the explanation behind the two distinct behaviours has to be found in the deviations that emerge in the internal spacetime for the two stellar models and in particular in the first radial derivatives of the metric functions Φ and Λ [cf. eqs. (8.2)–(8.3)]. These deviations produce sensible quantitative differences in the coefficients of eqs. (8.21)–(8.23) (see the Appendix D for the explicit form of the coefficients) which are then responsible for the increase in the decay rate. It should also be remarked that the behaviour shown in the left panel could be easily reproduced, also in the case of a polytropic model, by means of a suitably defined electrical conductivity. In other words, the results presented in Fig. 8.5 underline that a definitive conclusion on the general relativistic evolution of the magnetic field cannot be drawn until a more realistic treatment of the electrical conductivity and of the equation of state is made.

The inset in the left panel of Fig. 8.5 can be used to explain the comment made above on the use of relevant normalization units. In the inset, in fact, we have plotted the same evolution shown in the main panel but with the time being normalized in terms of the Newtonian Ohmic time. Note that when we do so, the overall behaviour is inverted and the decay rate of the magnetic field is now decreasing for increasing stellar compactness. This is clearly incorrect and the misleading behaviour is due to the fact that the concept of an Ohmic time is a purely Newtonian one and is therefore justified only in a Newtonian context. A more suitable normalizing unit for a nonrotating relativistic star would be the general relativistic analogue of the Newtonian Ohmic time: $\tilde{\tau}_{\text{ohm}} \equiv 4\pi R^2 e^{2\Lambda - \Phi} \sigma / c^2$ as can be derived from eqs. (8.21)–(8.23) in the limit $\Omega = 0$. Using this normalization, we would recover the correct behaviour, with a magnetic field asymptotic decay rate generally *increasing* with stellar compactness. Unfortunately the validity of $\tilde{\tau}_{\text{ohm}}$ is limited to nonrotating stellar models only. Because of the difficulties of defining an Ohmic timescale for the induction equations of a relativistic rotating star, we measure the magnetic field evolution simply in terms of the time measured by our ZAMO observer.

Finally, we discuss the differences introduced in the decay of the magnetic field when the latter is confined to a spherical shell between an inner radius R_{IN} and the surface of the star. In this case, the initial values for the radial eigenfunctions are calculated self-consistently along the procedure discussed in Section 3.3. In Fig. 8.6 we show the evolution of the magnetic field in our fiducial neutron star for different values of the parameter $q \equiv R_{\text{IN}}/R$. Note that decreasing the volume in which the magnetic field is confined has the effect of *increasing* the decay rate of the magnetic field so that if the initial magnetic field permeates about 90% of the stellar volume ($q = 0.5$), the residual surface magnetic field after $10 t_9$ yr is about a factor thirty smaller than in the case the magnetic field permeates the whole star ($q = 0$). Although our analysis does not take into account the microphysics of the stellar interior and in particular the role played by the chemical composition and by the temperature, it confirms the Newtonian results of Urpin and Koenkov (1997) and those

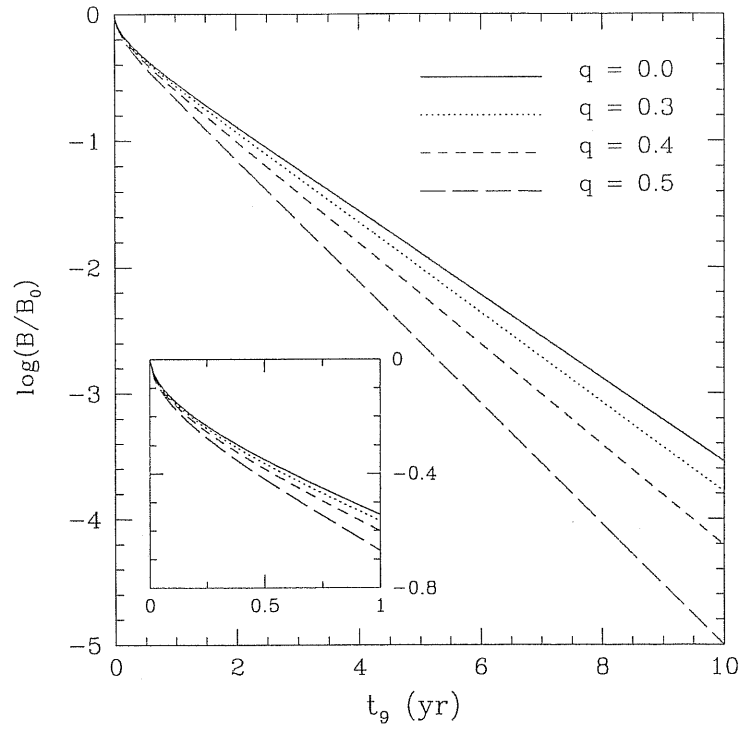


Figure 8.6: Decay of the surface magnetic field when the magnetic field does not penetrate the whole star. The different curves refer to different values of the parameter $q \equiv R_{\text{IN}}/R$, with R_{IN} being the inner radius of the stellar shell where the magnetic field is confined.

of Page *et al* (2000), who have shown that the magnetic field decay is slower for deeper magnetic field penetration (see also Konenkov & Geppert, 2001). Because this behaviour mimics the increase in the decay rate produced by an increasing compactness of the stellar model, it is essential to be able to determine, prior to observations, the geometry and location of the magnetic field within the neutron star and to distinguish the different contributions to the overall magnetic field decay.

More extended comments will be presented in the concluding Chapter of the thesis.

Chapter 9

Conclusions

The conclusions of our work can be summarized in three main points, corresponding to the three main fields of research which we have investigated:

- We have presented a new procedure for the numerical solution of the exact Riemann problem in relativistic hydrodynamics for both one-dimensional and multi dimensional flows (Rezzolla & Zanotti, 2001; Rezzolla, Zanotti, Pons, 2002). In this approach special attention is paid to the relativistic invariant expression for the relative velocity v_{12} between the unperturbed left and right states. This has been shown to be a monotonic function of the pressure p_* in the region formed between the wave fronts.

The use of the relative velocity has a number of advantages over alternative exact Riemann solvers discussed in the literature. In particular, it extracts the information implicitly contained in the data for the two initial states in order to deduce the wave pattern that will be produced by the decay of the discontinuity between these two states. This, in turn, allows an “a priori” determination to be made of the interval in pressure bracketing p_* and the correct functional form for the nonlinear equation whose root will solve the exact Riemann problem. All of these advantages translate, in practice, into a simpler algorithm to implement and an improved efficiency in the numerical solution of the Riemann problem.

Because of all of these advantages, its intrinsic simplicity of implementation and the numerical efficiency gain which it produces, this new exact Riemann solver should be considered as an interesting alternative to the traditional exact Riemann solver presently discussed in the literature.

Evaluating the invariant jump in the velocities normal to the discontinuity surface is also very useful in the case of multi dimensional flows. Under these circumstances, in fact, the presence of tangential velocities is imprinted in the expression of the relative velocity and this feature has allowed us to reveal a new special relativistic effect (Rezzolla & Zanotti, 2002). Unless the relative velocity between the two unperturbed portions of the fluid along the normal to the discontinuity surface is zero (as in the classical “shock tube problem”) it is always possible to produce a change in the wave pattern by varying the tangential velocities in the initial states, while keeping the rest

of the thermodynamic quantities of the Riemann problem unmodified. This represents a new effect which has no analog in Newtonian hydrodynamics and provides an example where considerations of numerics leads to the discovery of new physical effects.

- We have performed general relativistic hydrodynamics simulations of axisymmetric massive and compact tori orbiting a Schwarzschild black hole with a constant specific angular momentum. These objects have hydrostatic and hydrodynamical properties (i.e. large masses in small volumes with central rest-mass densities reaching almost nuclear matter density) that make them behave effectively as neutron stars, while possessing a toroidal topology. Our attention has been concentrated on two different aspects of the dynamics of these tori.

The first one was focussed on the suggestion that the toroidal neutron stars might be dynamically unstable to the runaway instability only if suitably chosen initial data were prescribed. To investigate this we have used a time-dependent numerical code that integrates the general relativistic hydrodynamics equations on a curved background using HRSC methods. The evolution of the spacetime is an essential feature for the development of the instability and has been modelled through a sequence of stationary Schwarzschild spacetimes differing only in the total mass content, which is computed in terms of the total rest-mass accreted onto the black hole at each instant. The conclusion reached is that, at least for constant specific angular momentum tori whose self-gravity is neglected, the initial Roche lobe overflow is not a necessary condition for the development of the instability, which represents a natural feature of the dynamics of these objects. Very recent numerical work shows that this conclusion does not necessarily hold when the specific angular momentum is not constant.

The second aspect was focussed on the dynamical response of these relativistic tori to the perturbations that are expected to be present after the catastrophic events that lead to their formation. Upon the introduction of suitably parametrized perturbations, the toroidal neutron stars have shown a regular oscillatory behaviour resulting both in a quasi-periodic variation of the mass accretion rate as well as of the rest-mass distribution. This response has been interpreted in terms of the excitation of oscillations modes which could be associated with the p -modes of toroidal neutron stars. These modes, which have been detected both in their fundamental frequencies as well as in their overtones, depend systematically on the average density of the tori, and a disco-seismologic analysis could provide important information on the physical properties of these toroidal neutron stars.

High rest-mass densities together with a toroidal topology are the basic properties that yield large mass quadrupoles for these toroidal neutron stars. As a consequence of the excitation of oscillations, the mass quadrupoles are induced to change rapidly and intense gravitational radiation is thus produced. Estimates made within the Newtonian quadrupole approximation have shown that strong gravitational waves can be produced during the short lifetime of these tori. In particular, the gravitational radiation emitted

by these source is comparable or larger than the one that is expected during the gravitational collapse of a stellar iron core, with a rate of detectable events which could also be larger given the variety of physical scenarios leading to the formation of a massive torus orbiting a black hole. Overall, the strength of the gravitational waves emitted and their periodicity are such that signal-to-noise ratios $\sim \mathcal{O}(1) - \mathcal{O}(10)$ can be reached for sources at 20000 or 10 Kpc respectively, making these new sources of gravitational waves detectable and potentially important.

The results reported here are a first step towards the understanding of the dynamics of toroidal neutron stars and call for a number of natural extensions and improvements. In particular, we plan to extend the simulations to the more realistic scenario of non-constant angular momentum tori, in order to find out if our conclusions regarding both the oscillation properties of toroidal neutron stars and the large amplitude of the associated gravitational wave emission still hold. In addition, it is interesting to improve, using more accurate approaches, the calculation of the gravitational radiation from the oscillations as well as from the runaway instability in the region of the parameter space where the instability could exist. Equally interesting is to include the effects introduced by self-gravity of the torus and determine the quantitative differences that will be encountered in this case. Last but not least, it is worth analyzing how the presence of a Kerr black hole would modify the present results, determining, in particular, the dependence of this phenomenology on the spin of the central black hole.

The results obtained here also provide promising suggestions for further work in a number of research areas different from the ones considered here. Firstly, they indicate that more needs to be investigated about the oscillation properties of relativistic tori and geometrically thick discs. Secondly, they suggest the possibility that the phenomenology observed in the quasi-periodic X-ray luminosity existing in LMXB's might be related, in some form, to the quasi-periodic accretion resulting from oscillation modes of the discs. Thirdly, and perhaps most importantly, these results show that new and unexpected sources of gravitational radiation could exist and might be observed when the new detectors of gravitational radiation become fully operative in the near future.

- A complete general relativistic description of the electromagnetic field of a slowly rotating star, with misaligned magnetic field, is a challenging task. If the stellar medium has a finite electrical conductivity it is possible to show that the stellar rotation removes the degeneracy in the evolution equations for the magnetic field and that three distinct induction equations need to be solved to account for the magnetic field decay. In this Thesis we have solved numerically the general relativistic induction equations (Zanotti & Rezzolla, 2002), investigating the effects of different rotation rates, different inclination angles between the magnetic moment and the rotation axis, and different values of the electrical conductivity. The aim of these numerical calculations is that of quantifying the corrections induced by general relativistic effects (both due to space-time curvature and to the stellar rotation) on the evolution of the magnetic field of a

slowly rotating neutron star.

In order to single out purely general relativistic effects from those due to the microphysics of the Ohmic dissipation, we have considered a simplified physical description of the neutron star. In particular, the star has been modeled as a polytrope rotating with a fiducial period of one millisecond, the electrical conductivity has been considered to be uniform inside the star and we have not included a treatment to consider the evolution of the stellar rotation and temperature. On the other hand, special attention has been paid to obtaining a consistent solution of the initial value problem and for the initial magnetic field we have taken a stationary solution of the general relativistic Maxwell equations. In this way we have avoided the use of initial magnetic field configurations that are only approximate solutions of the Maxwell equations (e.g. solutions of the Maxwell equations only in the limit of flat spacetime). Besides eliminating the error entering during the initial stages of the magnetic field decay, our prescription for the initial value problem also provides a more accurate solution of the Maxwell equations.

The results of these computations have shown that there exist general relativistic, rotation-induced corrections to the evolution of the magnetic field. These effects generally produce a *decrease* in the rate of magnetic field decay. However, their contribution is masked by the high value of the electrical conductivity in realistic neutron stars and can be neglected in general. Our calculations also indicate that general relativistic effects not induced by the stellar rotation can modify the time evolution of the magnetic field in a magnetized star. Such effects are closely related to the properties of the spacetime internal to the star and for a polytropic stellar model with uniform electrical conductivity these effects generally *increase* the decay rate of the field. The validity of this conclusion is however limited. Density gradients are in fact expected in a realistic star and these will affect the behavior of the electrical conductivity which, in turn, will influence the decay of the magnetic field.

Our conclusions are that the general relativistic evolution of the magnetic field in rotating neutron stars can be studied with confidence already in a nonrotating background spacetime. However, the role of a curved background spacetime on the decay of the magnetic field can be fully assessed only when the details of both a realistic equation of state and a realistic electrical conductivity are carefully taken into account.

As a concluding remark we would like to underline that the results presented in this Thesis reflect much of our personal view on a profitable approach to modern relativistic hydrodynamics. In this view, the investigation of aspects of "fundamental hydrodynamics" in the search of new and more efficient techniques for the solution of the Euler equations is continuously married to the application of the above techniques to precise physical problems. We have found this sinergetic exchange of experience between basic and applied hydrodynamics extremely useful and fascinating.

Appendix A

Monotonicity of the relative velocity as function of p_*

This Appendix is devoted to the proof that v_{12}^x is a monotonic function of p_* . As mentioned in the main text, this is an important property and the basis of our approach. In particular, because of our choice of considering the initial left state as the one with highest pressure, the proof of monotonicity will be obtained if we show that v_{12}^x is a monotonically *increasing* function of p_* . To simplify our notation we will drop the superscript “ x ” denoting the normal component of velocity.

1 One-dimensional Flows

Denoting by a' the first derivative of the quantity a with respect to $p_* = p_3 = p_3'$, it is straightforward to obtain that the first derivative of (3.12) is

$$v'_{12} = \frac{v'_{1,C}(1 - v_{2,C}^2) - v'_{2,C}(1 - v_{1,C}^2)}{(1 - v_{1,C} v_{2,C})^2}. \quad (\text{A.1})$$

Since $v_{1,C} \leq 1$, $v_{2,C} \leq 1$, the two terms in the parentheses of (A.1) are always positive, and the proof that v_{12} is monotonically increasing will follow if it can be shown that $v'_{1,C}$ and $-v'_{2,C}$ are both positive. We will do so for each of the three possible wave patterns.

Two Shock Fronts

Taking the derivative of the fluid velocity ahead of the left propagating shock front (measured from the contact discontinuity) [cf. equation (3.18)] we obtain

$$v'_{1,C} = \frac{(e_1 + p_1) [(e_3 - e_1)(e_3 + p_1) + (p_3 - p_1)(e_1 + p_3)e'_3]}{2v_{1,C}(e_1 + p_3)^2(e_3 + p_1)^2}. \quad (\text{A.2})$$

Since the energy density is an increasing function of pressure, $e'_3 > 0$; furthermore, $p_3 \geq p_1$ and $e_3 \geq e_1$ for the wave pattern considered and $v'_{1,C} > 0$ as a result. The equivalent

expression for the derivative of the fluid velocity ahead of the right propagating shock front (measured from the contact discontinuity) [cf. eq (3.19)] can be obtained by replacing in equation (A.2) the indices 1 and 3 by 2 and 3' respectively, i.e.

$$v'_{2,C} = \frac{(e_2 + p_2) [(e_{3'} - e_2)(e_{3'} + p_2) + (p_{3'} - p_2)(e_2 + p_{3'})e'_{3'}]}{2v_{2,C}(e_2 + p_{3'})^2(e_{3'} + p_2)^2}. \quad (\text{A.3})$$

Since now for the wave pattern considered: $v_{2,C} < 0$, $p_{3'} \geq p_2$ and $e_{3'} \geq e_2$, we are led to conclude that $-v'_{2,C} > 0$, thus making the overall v'_{12} positive for any value of p_3 .

One Shock and One Rarefaction Wave

In this case we only need to show that $v'_{1,C} > 0$ since for the velocity ahead of the right propagating shock front we can use the results derived in (A.3). Taking the derivative of expression (3.23) then yields

$$v'_{1,C} = -\frac{2A'_+(p_3)}{[1 + A_+(p_3)]^2}, \quad (\text{A.4})$$

where

$$\begin{aligned} A'_+(p_3) &= -4 \left| \frac{(\gamma - 1)^{1/2} + c_s(p_1)}{(\gamma - 1)^{1/2} - c_s(p_1)} \right| \frac{A_+(p_3)^{(2-\sqrt{\gamma-1})/2}}{[(\gamma - 1)^{1/2} + c_s(p_3)]^2} c'_s(p_3) \\ &\equiv -C_1 c'_s(p_3), \end{aligned} \quad (\text{A.5})$$

where $C_1 > 0$. When the sound speed $c_s(p_3)$ is an increasing function of pressure, as is the case for a polytropic equation of state [cf. eq (3.2)], $v'_{1,C} > 0$ and therefore $v'_{12} > 0$.

Two Rarefaction Waves

What we need to show in this case is that $v'_{2,C} < 0$ since we can exploit the previous result that $v'_{1,C} > 0$. In this case, taking the derivative of expression (3.27) one obtains

$$v'_{2,C} = -\frac{2A'_-(p_{3'})}{[1 + A_-(p_{3'})]^2}, \quad (\text{A.6})$$

where now

$$\begin{aligned} A'_-(p_{3'}) &= 4 \left| \frac{(\gamma - 1)^{1/2} + c_s(p_2)}{(\gamma - 1)^{1/2} - c_s(p_2)} \right| \frac{A_-(p_{3'})^{(2+\sqrt{\gamma-1})/2}}{[(\gamma - 1)^{1/2} + c_s(p_{3'})]^2} c'_s(p_{3'}) \\ &\equiv C_2 c'_s(p_{3'}) \end{aligned} \quad (\text{A.7})$$

with $C_2 > 0$ and therefore $v'_{2,C} < 0$.

We have therefore shown that for all of the wave patterns considered $v'_{1,c} > 0$ and $-v'_{2,c} > 0$, thus proving that v_{12} is always a monotonically increasing function of p_* .

2 Multi-dimensional flows

In the case of multidimensional flows, a rapid look at expression (A.1) suggests that the proof of the monotonicity will follow from showing that $(v_3^x)' < 0$ and $(v_3^x)' > 0$ in equations (3.10) and (3.11),

In the case when a rarefaction wave is present, the proof is indeed straightforward. According to (3.47) and (3.50), in fact, $(v^x)'$ across the rarefaction wave is negative when the rarefaction wave propagates towards the left [implying that $(v_3^x)'$ is negative] and it is positive when the rarefaction wave propagates towards the right [implying that $(v_3^x)'$ is positive].

If a shock wave is present, on the other hand, a proof for the most general case and in terms of simple algebraic relations cannot be given. On the other hand, a rather simple analytic proof can be found in the simpler case in which $v_1^x = v_2^x = 0$; while this is certainly not the most general case, numerical calculations have shown that the result holds in general. Consider therefore a shock wave propagating towards the left¹; after lengthy but straightforward calculations it is possible to show that

$$(v_3^x)' = \frac{H_1(V_s - v_1^x)(1 - V_s v_1^x) - H_1 \Delta p (1 - (v_1^x)^2) V_s' - V_s' (\Delta p)^2}{[H_1(V_s - v_1^x) + \Delta p V_s]^2}, \quad (\text{A.8})$$

where we have set $H_1 \equiv h_1 \rho_1 W_1^2$ and $\Delta p \equiv p - p_1 > 0$, and where p is the pressure behind the shock. If we now impose that $v_1^x = 0$, we can write the derivative of (3.40) as

$$\frac{V_s'}{V_s} = \frac{J'}{J} \frac{\rho_1^2 W_1^2}{J^2 + \rho_1^2 W_1^2}. \quad (\text{A.9})$$

Inserting (A.9) in (A.8) we can conclude that $(v_3^x)'$ is negative if and only if

$$J(\rho_1^2 W_1^2 + J^2) h_1 - \rho_1 \Delta p J' (\rho_1 h_1 W_1^2 + \Delta p) < 0. \quad (\text{A.10})$$

Using (3.44) to calculate J' , one finds that (A.10) can be written as

$$-\frac{\rho_1(H_1 - \Delta p)}{J^2} - 2h_1 < \frac{1}{\gamma(\gamma - 1)} \frac{\rho_1(H_1 + \Delta p)}{\rho^2} \left[\frac{1}{\epsilon} - \gamma(\gamma - 2) \right], \quad (\text{A.11})$$

where ρ and ϵ are the rest-mass density and the specific internal energy behind the shock front. Because the right hand side of (A.11) is always positive for any $\gamma \leq 2$, the condition

¹A similar analysis can be repeated for the right-propagating shock wave.

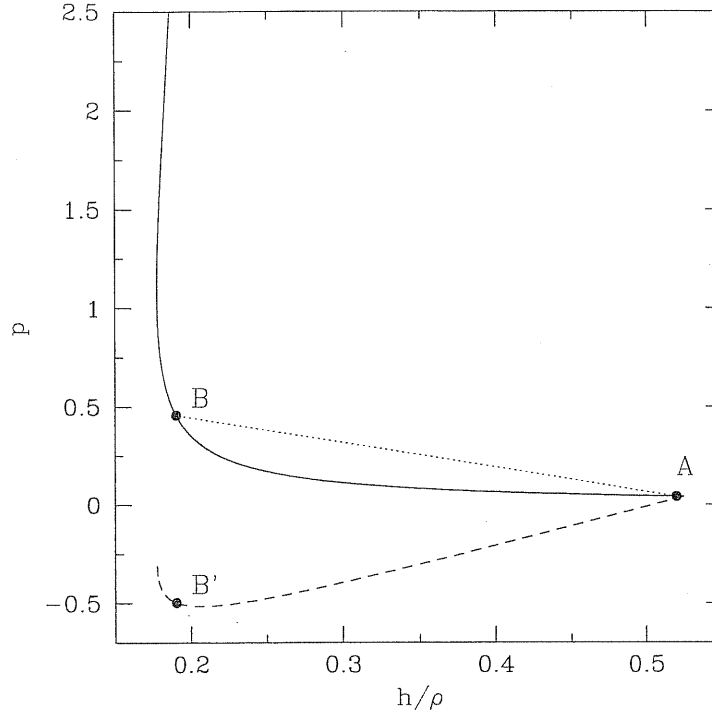


Figure A.1: The solid curve represents the Taub adiabat and the points A and B on it the states ahead and behind a left-propagating shock wave. See the main text for a discussion.

for monotonicity (A.11) will be satisfied if its left hand side is negative, i.e. if

$$-J^2 < -\rho_1 \frac{\Delta p - H_1}{2h_1} \equiv -\alpha . \quad (\text{A.12})$$

At this point the proof can be continued graphically and making use of the Taub adiabat. In the plane $(h/\rho, p)$, in fact, the Taub adiabat (3.45) selects the points solutions of the hydrodynamical equations across a shock wave, therefore connecting the state ahead of the shock front with the one behind it. In Fig. A.1, this curve is indicated with a solid line and we have indicated with the points A and B the states ahead (region 1) and behind (region 3) the shock front. Once an initial state A has been chosen, the mass flux will determine the point B of the Taub adiabat solution of the Rankine-Hugoniot relations. Because of this, the slope of the chord connecting the point A with B (shown as a dotted line in Fig. A.1) is equal to $-J^2$. Indicated with a dashed line, Fig. A.1 also shows the equivalent of the Taub adiabat passing through the state A but having mass flux equal to $\alpha^{1/2}$, i.e.

$$p = -\alpha \left(\frac{h}{\rho} - \frac{h_1}{\rho_1} \right) + p_1 . \quad (\text{A.13})$$

The point B' on such a curve represents the state behind the shock wave and, as it is clearly shown in Fig. A.1, the slope of the chord AB' is always larger than the corresponding slope

for the chord AB, thus stating that the condition (A.11) is indeed verified and that $(v_{3'}^x)'$ is therefore positive.

Appendix B

Newtonian limits of $(\tilde{v}_{12})_{2S}$, $(\tilde{v}_{12})_{SR}$, $(\tilde{v}_{12})_{2R}$

We here show that the three limiting values of $(\tilde{v}_{12})_{2S}$, $(\tilde{v}_{12})_{SR}$ and $(\tilde{v}_{12})_{2R}$ reduce to their Newtonian counterparts in the limit of $v, c_s \rightarrow 0$, and $h \rightarrow 1$. In particular, we will restrict ourselves to considering the case of a polytropic equation of state (3.2) and of a onedimensional flow.

We start by considering the Newtonian limit of $(\tilde{v}_{12})_{2S}$ [cf. Eq. (3.20)] which is obtained when $p/e \ll 1$ and $e \rightarrow 1/V$, with $V = 1/\rho$ being the specific volume. In this case, then

$$\begin{aligned} (\tilde{v}_{12})_{2S} \Big|_{\text{Newt}} &= \sqrt{\frac{(p_1 - p_2)(\hat{e} - e_2)}{\hat{e}e_2}} \\ &= \sqrt{(p_1 - p_2)(1/e_2 - 1/\hat{e})} . \end{aligned} \quad (\text{B.1})$$

which coincides with the corresponding expression derived by Landau and Lifshitz (1987) but with inverted indices.

We next consider the Newtonian limit of $(\tilde{v}_{12})_{SR}$ [cf. Eq (3.25)] which is obtained when both $c_s(p_3) \ll 1$ and $c_s(p_1) \ll 1$. In this case,

$$\begin{aligned} A_+(p_3) &\simeq \left(1 - \frac{c_s(p_3)}{\sqrt{\gamma-1}}\right)^{4/\sqrt{\gamma-1}} \left(1 + \frac{c_s(p_1)}{\sqrt{\gamma-1}}\right)^{4/\sqrt{\gamma-1}} \\ &\simeq \left(1 - \frac{4c_s(p_3)}{\gamma-1}\right) \left(1 + \frac{4c_s(p_1)}{\gamma-1}\right) \\ &\simeq 1 - \frac{4}{\gamma-1}(c_s(p_3) - c_s(p_1)) . \end{aligned} \quad (\text{B.2})$$

so that the Newtonian limit of $(\tilde{v}_{12})_{SR}$ is given by

$$\begin{aligned} (\tilde{v}_{12})_{SR} \Big|_{\text{Newt}} &= \frac{1 - A_+(p_3)}{2} \Big|_{p_3=p_2} \\ &\simeq -\frac{2}{\gamma-1} c_s(p_1) \left[1 - \frac{c_s(p_3)}{c_s(p_1)} \right] \Big|_{p_3=p_2}. \end{aligned} \quad (\text{B.3})$$

Bearing in mind that

$$\frac{c_s(p_3)}{c_s(p_1)} \Big|_{p_3=p_2} = \left(\frac{p_2}{p_1} \right)^{(\gamma-1)/2\gamma}, \quad (\text{B.4})$$

we obtain

$$(\tilde{v}_{12})_{SR} \Big|_{\text{Newt}} = -\frac{2}{\gamma-1} c_s(p_1) \left[1 - \left(\frac{p_2}{p_1} \right)^{(\gamma-1)/2\gamma} \right], \quad (\text{B.5})$$

which again coincides with the corresponding expression derived by Landau and Lifshitz (1987) but with inverted indices.

Finally, we consider the Newtonian limit of $(\tilde{v}_{12})_{2R}$ [cf. Eq (3.29)] for $c_s(p_1), c_s(p_2) \ll 1$. In this case S_1 and S_2 in (3.32) and (3.33) can be approximated as

$$\begin{aligned} S_1 &\simeq 1 + \frac{4c_s(p_1)}{\gamma-1}, \\ S_2 &\simeq 1 - \frac{4c_s(p_2)}{\gamma-1}. \end{aligned} \quad (\text{B.6})$$

so that the Newtonian limit is given by

$$\begin{aligned} (\tilde{v}_{12})_{2R} \Big|_{\text{Newt}} &= \frac{S_2 - S_1}{S_1 + S_2} = \left[-\frac{4c_s(p_1)}{\gamma-1} - \frac{4c_s(p_2)}{\gamma-1} \right] \left[2 + \frac{4}{\gamma-1} [c_s(p_1) - c_s(p_2)] \right]^{-1} \\ &= \left[-\frac{2c_s(p_1)}{\gamma-1} - \frac{2c_s(p_2)}{\gamma-1} \right] \left[1 - \frac{2}{\gamma-1} [c_s(p_1) - c_s(p_2)] \right] \\ &= -\frac{2c_s(p_1)}{\gamma-1} - \frac{2c_s(p_2)}{\gamma-1}. \end{aligned} \quad (\text{B.7})$$

Once more, expression (B.7) coincides with the corresponding expression derived by Landau and Lifshitz (1987) but with inverted indices.

Appendix C

A closed form solution in the case of Two Rarefaction Waves

As discussed in Sections 3.3 of Chapter 3 for the onedimensional Riemann problem, when $(\tilde{v}_{12})_{2R} < (v_{12})_0 < (\tilde{v}_{12})_{SR}$, the initial conditions give rise to two rarefaction waves and it is possible to derive a closed form solution for the unknown pressure p_* . In this way we can, at least in principle, avoid any numerical root finding procedure and determine the solution exactly. In this Appendix we first derive this analytic solution in the context of relativistic hydrodynamics and then calculate its Newtonian limit. We will restrict ourselves to considering the particular case of a polytropic equation of state (3.2).

Using expression (3.16) we can write the pressures p_3 and $p_{3'}$ as functions of the sound speeds $c_s(p_3)$ and $c_s(p_{3'})$ which, for convenience, we will hereafter refer to as x and x' respectively

$$p_3 = k_1^{-1/(\gamma-1)} \left[\frac{x^2(\gamma-1)}{\gamma(\gamma-1) - \gamma x^2} \right]^{\gamma/(\gamma-1)}, \quad (\text{C.1})$$

$$p_{3'} = k_2^{-1/(\gamma-1)} \left[\frac{(x')^2(\gamma-1)}{\gamma(\gamma-1) - \gamma(x')^2} \right]^{\gamma/(\gamma-1)}, \quad (\text{C.2})$$

where $k_1 = p_1/\rho_1^\gamma$ and $k_2 = p_2/\rho_2^\gamma$ are the two constants entering the polytropic equation. Since $p_3 = p_{3'} = p_*$, we can obtain the following relation between x' and x :

$$(x')^2 \equiv \frac{\gamma(\gamma-1)x^2}{\gamma x^2(1-\alpha) + \alpha\gamma(\gamma-1)}, \quad (\text{C.3})$$

where $\alpha \equiv (k_1/k_2)^{1/\gamma}$. The expression for the relative velocity (3.29) can also be written as

$$\frac{A_+(p_3)}{A_-(p_{3'})} = \frac{1 - (v_{12})_0}{1 + (v_{12})_0}. \quad (\text{C.4})$$

and we then use expressions (3.24) and (3.28) to expand the left hand side of (C.4). After

some algebra we are then left with

$$\left(\frac{\Gamma - x}{\Gamma + x}\right) \left(\frac{\Gamma - x'}{\Gamma + x'}\right) = \left[\frac{\Gamma - c_s(p_2)}{\Gamma + c_s(p_2)}\right] \left[\frac{\Gamma - c_s(p_1)}{\Gamma + c_s(p_1)}\right] \left[\frac{1 - (v_{12})_0}{1 + (v_{12})_0}\right]^{\Gamma/2}, \quad (\text{C.5})$$

where $\Gamma^2 \equiv \gamma - 1$ and the right hand side of (C.5) is a constant which we rename as

$$\Pi \equiv \left[\frac{\Gamma - c_s(p_2)}{\Gamma + c_s(p_2)}\right] \left[\frac{\Gamma - c_s(p_1)}{\Gamma + c_s(p_1)}\right] \left[\frac{1 - (v_{12})_0}{1 + (v_{12})_0}\right]^{\Gamma/2}. \quad (\text{C.6})$$

Introducing now the auxiliary quantity

$$\beta \equiv \frac{1 + \Pi}{1 - \Pi}, \quad (\text{C.7})$$

expression (C.5) can be written as

$$(x')^2 = \left[\frac{\Gamma(x\beta - \Gamma)}{x - \Gamma\beta}\right]^2. \quad (\text{C.8})$$

Comparing now (C.3) and (C.8) gives a 4-th order equation in the unknown sound velocity x

$$a_0 x^4 + a_1 x^3 + a_2 x^2 + a_3 x + a_4 = 0, \quad (\text{C.9})$$

where

$$a_0 \equiv 1 - \beta^2(1 - \alpha), \quad (\text{C.10})$$

$$a_1 \equiv -2\Gamma\alpha\beta, \quad (\text{C.11})$$

$$a_2 \equiv \Gamma^2(1 - \alpha)(\beta^2 - 1), \quad (\text{C.12})$$

$$a_3 \equiv 2\Gamma^3\alpha\beta, \quad (\text{C.13})$$

$$a_4 \equiv -\alpha\Gamma^4. \quad (\text{C.14})$$

The analytic solution of equation (C.9) will yield at least two real roots, one of which will be the physically acceptable one: i.e. positive, less than one, and such that the pressure p_* falls in the relevant bracketing interval.

In its Newtonian limit, equation (C.9) reduces to a second order equation in the unknown sound velocity

$$\left(\frac{1}{\alpha} - 1\right) x^2 + 2\Sigma x - \Sigma^2 = 0, \quad (\text{C.15})$$

where

$$\Sigma \equiv c_s(p_1) + c_s(p_2) + \frac{(\gamma - 1)}{2} v_{12}, \quad (\text{C.16})$$

and $v_{12} = v_1 - v_2$. The fact that the Newtonian Riemann problem in the case of two rarefaction waves can be solved analytically is well known and is at the basis of the so called “Two Rarefaction Approximate Riemann Solver” (Toro 1997) described in Section 7.3 of Chapter 2.

Appendix D

The numerical solution of the induction equations

In this Appendix we provide the explicit expressions for the coefficients f_i , g_i , h_i appearing in the new form of the induction equations (8.21) – (8.23)

$$\begin{aligned} f_1 &= \frac{c^2 e^{\Phi-2\Lambda}}{4\pi\sigma} - \frac{c^2 e^{-2\Lambda}}{(4\pi\sigma)^2} \omega \tan \lambda (1 - 2 \sin^2 \theta) , \\ f_2 &= \frac{c^2 e^{\Phi-2\Lambda}}{4\pi\sigma} (\Phi_{,r} - \Lambda_{,r}) + \frac{c^2 e^{-2\Lambda}}{(4\pi\sigma)^2} \tan \lambda (1 - 2 \sin^2 \theta) (\Omega \Phi_{,r} + \omega \Lambda_{,r} - \omega_{,r}) , \\ f_3 &= \frac{-2c^2 e^{\Phi}}{4\pi\sigma r^2} - \frac{2\omega c^2}{(4\pi\sigma r)^2} \sin \theta \frac{\Psi_3}{\Psi_1} , \\ f_4 &= \frac{-2c^2 e^{-\Phi-\Lambda}}{(4\pi\sigma)^2} \omega \sin \theta \frac{\Psi_3}{\Psi_1} , \\ f_5 &= \frac{2c^2 e^{-\Phi-\Lambda}}{(4\pi\sigma)^2} \tan \lambda (1 - 2 \sin^2 \theta) (\Phi_{,r} (\Omega + \omega) - \omega_{,r}) , \\ f_6 &= \frac{-2c^2 e^{-\Phi-\Lambda}}{(4\pi\sigma)^2} \omega \tan \lambda (1 - 2 \sin^2 \theta) ; \end{aligned}$$

$$\begin{aligned}
g_1 &= \frac{c^2 e^{\Phi-2\Lambda}}{4\pi\sigma} - \frac{c^2 e^{-2\Lambda}}{(4\pi\sigma)^2} \omega \cos \theta \frac{\Psi_3}{\Psi_2} , \\
g_2 &= -\frac{c^2 e^{\Phi-2\Lambda}}{4\pi\sigma} \Lambda_{,r} + \frac{c^2 e^{-2\Lambda}}{(4\pi\sigma)^2} \cos \theta \frac{\Psi_3}{\Psi_2} [\Phi_{,r}(2\omega - \Omega) + \omega \Lambda_{,r} - 2\omega_{,r}] , \\
g_3 &= \frac{c^2 e^{\Phi}}{(4\pi\sigma)r^2} \frac{\cos \theta \sin \chi}{\sin^2 \theta \Psi_2} (\cos \lambda + \frac{\omega e^{-\Phi}}{4\pi\sigma} \sin \lambda) , \\
&\quad - \frac{c^2 e^{-2\Lambda}}{(4\pi\sigma)^2} \cos \theta \frac{\Psi_3}{\Psi_2} [\omega_{,rr} - \omega_{,r}(\Lambda_{,r} + 2\Phi_{,r}) + \Phi_{,rr}(\Omega - \omega) + (\omega - \Omega)(\Phi_{,r}^2 + \Phi_{,r}\Lambda_{,r})] , \\
g_4 &= \frac{c^2 e^{\Phi-\Lambda}}{(4\pi\sigma)r^2} \left[e^{\Phi} - \frac{\omega}{4\pi\sigma} \cos \theta \frac{\Psi_3}{\Psi_2} \right] , \\
g_5 &= \frac{c^2 e^{2\Phi-\Lambda}}{(4\pi\sigma)r^2} (\Phi_{,r} - \frac{2}{r}) - \frac{c^2 e^{\Phi-\Lambda}}{(4\pi\sigma r)^2} \cos \theta \frac{\Psi_3}{\Psi_2} (\omega_{,r} - \frac{2\omega}{r}) , \\
g_6 &= -\frac{c^2 e^{-2\Lambda}}{(4\pi\sigma)^2} \cos \theta \frac{\Psi_3}{\Psi_2} [\Phi_{,r}(\omega - \Omega) - \omega_{,r}] , \\
g_7 &= -\frac{c^2 e^{-2\Lambda}}{(4\pi\sigma)^2} \cos \theta \frac{\Psi_3}{\Psi_2} [\Phi_{,rr}(\omega - \Omega) - \omega_{,rr} + \Phi_{,r}^2(\Omega - \omega) + \Phi_{,r}\Lambda_{,r}(\Omega - \omega) + \omega_{,r}(2\Phi_{,r} + \Lambda_{,r})] ; \\
h_1 &= \frac{c^2 e^{\Phi-2\Lambda}}{4\pi\sigma} (1 - \frac{\omega e^{-\Phi}}{4\pi\sigma} \cot \lambda) , \\
h_2 &= \frac{c^2 e^{\Phi-2\Lambda}}{4\pi\sigma} \left[\frac{e^{-\Phi}}{4\pi\sigma} \cot \lambda (\omega \Phi_{,r} + \omega \Lambda_{,r} - \omega_{,r}) - \Lambda_{,r} \right] , \\
h_3 &= -\frac{c^2 e^{\Phi}}{(4\pi\sigma)r^2 \sin^2 \theta} \left(1 - \frac{\omega e^{-\Phi}}{4\pi\sigma} \cot \lambda \right) \\
h_4 &= \frac{c^2 e^{2\Phi-\Lambda}}{(4\pi\sigma)r^2} \left[1 - \frac{\omega e^{-\Phi}}{4\pi\sigma} \cot \lambda \right] , \\
h_5 &= \frac{c^2 e^{2\Phi-\Lambda}}{(4\pi\sigma)} \left[(\Phi_{,r} - \frac{2}{r}) (1 - \frac{\omega e^{-\Phi}}{4\pi\sigma} \cot \lambda) + \frac{e^{-\Phi} \cot \lambda}{4\pi\sigma} (\omega \Phi_{,r} - \omega_{,r}) \right] , \\
h_6 &= \frac{c^2 e^{\Phi}}{(4\pi\sigma)r^2 \sin^2 \theta} \left(1 - \frac{\omega e^{-\Phi}}{4\pi\sigma} \cot \lambda \right) .
\end{aligned}$$

Appendix E

Implementing surface boundary conditions

This Appendix shows how the surface boundary conditions expressed by equations (8.30) and (8.34) can be implemented in a numerical code. By adopting the standard finite-difference notation in which $u_j^n \equiv u(x_j, t^n)$ and assuming a uniform radial grid with J gridpoints, the finite difference form of eq. (8.34) is given by

$$\tilde{F}_{J+1}^n - \tilde{F}_{J-1}^n = 2\Pi(\eta)\Delta x \tilde{F}_J^n / R, \quad (\text{E.1})$$

where $\Delta x = x_j - x_{j-1}$, $\Delta t = t^{n+1} - t^n$, The unknown value of \tilde{F}_J^{n+1} , comes after introduction of (E.1) into the Crank-Nicholson scheme, centered at J ; lengthy but straightforward calculation give

$$\begin{aligned} \tilde{F}_J^{n+1} = & \frac{\alpha(f_1^n \tilde{F}_{J-1}^n + f_1^{n+1} \tilde{F}_{J-1}^{n+1}) + \tilde{F}_J^n [1 + f_3^n \Delta t / 2 - f_1^n \alpha + \Pi(\eta) \alpha \Delta x (f_2^n \Delta x / 2 + f_1^n) / R]}{1 - f_3^{n+1} \Delta t / 2 + f_1^{n+1} \alpha - \Pi(\eta) \alpha \Delta x (f_2^{n+1} / 2 \Delta x + f_1^{n+1}) / R}, \end{aligned} \quad (\text{E.2})$$

where $\alpha = \Delta t / \Delta x^2$. There are still two unknowns entering (E.2), i.e. \tilde{G}_{J+1}^n and \tilde{H}_{J+1}^n . However, they represent the external solution and by using eqs. (8.31) and (8.33), they can be written as

$$\tilde{G}_{J+1}^n = \tilde{H}_{J+1}^n = -\frac{\tilde{N}^2 M}{(R + \Delta x)^2} \frac{(R + \Delta x) \ln \tilde{N}^2 / M + 1 / \tilde{N}^2 + 1}{\ln \tilde{N}^2 + 2M(1 + M / (R + \Delta x)) / (R + \Delta x)} \tilde{F}_{J+1}^n, \quad (\text{E.3})$$

where \tilde{N} is the value of N at $R + \Delta x$

$$\tilde{N} \equiv N \Big|_{R+\Delta x} = \left(1 - \frac{2M}{R + \Delta x}\right)^{1/2}. \quad (\text{E.4})$$

The updated values of \tilde{G} and \tilde{H} now follow immediately from (8.33) with time evolved value of F_J^{n+1} given by (E.2).

Appendix F

The stress formula

In this Appendix we derive equation (5.29) showing that the wave amplitude can be calculated avoiding any time derivatives. We recall that A_{20}^{E2} is defined as the second time derivative of the mass quadrupole moment of the source

$$A_{20}^{E2} \equiv k \frac{d^2}{dt^2} \left[\int \rho \left(\frac{3}{2} z^2 - \frac{1}{2} \right) r^4 dr dz \right], \quad (\text{F.1})$$

where $z = \cos \theta$ and $k = 16\pi^{3/2}/\sqrt{15}$. However, this definition would pose serious problems from a computational point of view, because the discretization of the time derivative causes high frequencies noise in the gravitational wave signal, with noise amplitudes that are often larger than the signal itself. Therefore, as explained in Chapter 5, the standard practice is to use the Euler equations to replace time derivatives with spatial derivatives. Let us first rewrite (F.1) as

$$A_{20}^{E2} = k \frac{d^2}{dt^2} \int \rho \Psi r^2 dr dz, \quad (\text{F.2})$$

where $\Psi = \frac{1}{2}(3z^2 - 1)r^2$. The total time derivative of Ψ , assuming axisymmetry and stationarity ($\partial_t = \partial_\phi = 0$), is given by $\dot{\Psi} = v^i \partial_i \Psi$, which, after straightforward calculations, leads to

$$\frac{d}{dt} \Psi = r \left[v^r (3z^2 - 1) - 3z \sin \theta v^\theta \right]. \quad (\text{F.3})$$

Now, (F.3) can be further derived as $\frac{d^2}{dt^2} \Psi = \partial_t \dot{\Psi} + v^i \partial_i \dot{\Psi}$, where

$$\partial_t \dot{\Psi} = r \left[(3z^2 - 1) \partial_t v^r - 3z \sin \theta \partial_t v^\theta \right]. \quad (\text{F.4})$$

It is at this stage that Euler equations are used, in order to express $\partial_t v^r$ and $\partial_t v^\theta$ as

$$\partial_t v^r = \frac{(v^\theta)^2 + (v^\phi)^2}{r} - v^r \partial_r v^r - \frac{v^\theta}{r} \partial_\theta v^r - \partial_r \Phi - \frac{1}{\rho} \partial_r p \quad (\text{F.5})$$

$$\partial_t v^\theta = \frac{(v^\phi)^2}{r} \cot \theta - \frac{v^r v^\theta}{r} - v^r \partial_r v^\theta - \frac{v^\theta}{r} \partial_\theta v^\theta - \frac{1}{r} \partial_\theta \Phi - \frac{1}{r\rho} \partial_\theta p, \quad (\text{F.6})$$

respectively, where Φ is the Newtonian gravitational potential. Very lengthy calculations allow to write (F.4) explicitly, which in turn leads to the following expression for the wave amplitude (F.1)

$$\begin{aligned} A_{20}^{\text{E2}} = & k \int \rho \left[(3z^2 - 1)v_r^2 + v_\theta^2(2 - 3z^2) - v_\phi^2 - 6z\sqrt{1 - z^2}v_\theta v_r \right. \\ & \left. - (3z^2 - 1)r \left(\partial_r \Phi + \frac{1}{\rho} \partial_r p \right) + 3z\sqrt{1 - z^2} \left(\partial_\theta \Phi + \frac{1}{\rho} \partial_\theta p \right) \right] r^r dr dz. \end{aligned} \quad (\text{F.7})$$

The last step in our analysis consists in showing the pressure gradient terms do not actually contribute to the intergral (F.7), and that it actually reduces to the stress formula (5.29) given in Chapter 5. To this extent, let us isolate the term

$$C = \int \rho \left[-(3z^2 - 1)r \frac{1}{\rho} \partial_r p + 3z\sqrt{1 - z^2} \frac{1}{\rho} \partial_\theta p \right] r^2 dr dz, \quad (\text{F.8})$$

which appears in (F.7). We now recall that $\partial_\theta p = -\sqrt{1 - z^2} \partial_z p$, and define the function $f = (z^3 - z)r^3$. This allows a direct integration by parts of (F.8), where the domain of integration is $[0, +\infty]$ in the coordinate r and $[0, \pi]$ in the coordinate θ

$$\begin{aligned} C &= \int_{-1}^1 \int_0^\infty \rho \left[-(3z^2 - 1)r^3 \partial_r p + 3(z^3 - z)r^2 \partial_z p \right] dr dz \\ &= \int_{-1}^1 \int_0^\infty \rho (-\partial_z f \partial_r p + \partial_r f \partial_z p) dr dz \\ &= - \int_0^\infty \rho f \partial_r p \, dr \Big|_{-1}^1 + \int_{-1}^1 \rho f \partial_z p \, dz \Big|_0^\infty. \end{aligned} \quad (\text{F.9})$$

However, the first of these two last integrals is trivially zero, and the second one also vanishes if the physical system is confined within a certain radius, i.e. pressure is a function with compact support. As a result, the term C in (F.8) vanishes and the stress formula is obtained.

Bibliography

- [1] Abramowicz, M. A., 1974, *Acta Astron.*, 24, 45.
- [2] Abramowicz, M. A. Jariszyński, M. & Sikora, M., 1978, *A&A*, 63, 221.
- [3] Abramowicz, M. A., Calvani, M., Nobili, L., 1983, *Nature*, 302, 597.
- [4] Abramowicz, M. A., Karas V., Lanza, A., 1998, *A&A*, 331, 1143.
- [5] Ahmedov, B. J., 1999. *Phys. Lett. A*, 256, 9.
- [6] Aloy, A. M., Ibañez, J. M., Martí, J. M., 1999, *ApJ Suppl.*, 122, 151
- [7] Anile, A. M. 1989, *Relativistic Fluids and Magneto-Fluids: with Applications in astrophysics and plasma physics*, Cambridge University Press
- [8] Anile, A. M. and Russo, G., 1987a, *Phys. Fluids*, **29**, 2847
- [9] Anile, A. M. and Russo, G., 1987b, *Phys. Fluids*, **30**, 1045
- [10] Anderson, J. L., Cohen, J. M., 1970. *Astrophys. Space Science*, 9, 146.
- [11] Ansorg, M., Kleinwächter, A., Meinel, R., 2002, [astro-ph/0208267](#).
- [12] Arnowitt, R., Deser, S., Misner, C. W., 1962 *The dynamics of general relativity*, in Witten, L. ed, *Gravitation: An introduction to current research*. Wiley, New York
- [13] Banyuls, F., Font, J. A., Ibañez, J. M., Martí, J.M., Miralles, J. A., 1997, *ApJ*, 476, 221
- [14] Bicknell, G. V., Wagner, S. J., [astro-ph/0204439](#)
- [15] Blanchet, L. Damour, T., Schafer, G., 1990, *MNRAS*, 242, 289.
- [16] Blandford, R. D. 2002, *Prog. of Theor. Phys. Suppl.*, 143, in press, [astro-ph/0110394](#)
- [17] Boyer, R. H., 1965, *Proc. Cambridge Phil. Soc.* 61, 527.
- [18] Brandenburg, A., Nordlund, A., Stein, R. F., Torkelsson, U., 1995, *ApJ*, 446, 741.

- [19] Brandt, S., Font J. A., Ibáñez J. M., Massó J., Seidel, E., 2000, *Comput. Phys. Comm.*, 124, 169.
- [20] Cattaneo, C., 1948, *Atti Semin. Mat. Fis. Univ. Modena*, 3, 3
- [21] Centrella, J., Wilson, J. R., 1984, *ApJ*, 54, 229.
- [22] Chandrasekhar, S. 1961, *Hydrodynamic and Hydromagnetic Stability*, Dover Pub. Inc., NY
- [23] Chernikov, N. A., 1964, *Acta Phys. Polonica*, 23.
- [24] Colella, P., 1982, *SIAM J. Sci. Stat. Comput.*, 3, 76.
- [25] Colella, P., Woodward, P. R., 1984, *J. Comput. Phys.*, 54, 174
- [26] Coleman, B. D., 1964, *Arch. Rat. Mech. Anal.*, 17, 1.
- [27] Cowling, T. G., 1941, *MNRAS*, 101, 367.
- [28] Courant, R., Friedrichs, K. O., Lewy, H., 1928, *Math. Ann.*, 100, 32
- [29] Courant, R., Friedrichs, K. O., 1948, in *Supersonic Flows and Shock Waves.*, Interscience.
- [30] Courant, R., Isaacson, E., Rees, M., 1952, *Comm. Pure Appl. Math.*, 5, 243.
- [31] Daigne, F., Mochkovitch, R., 1997, *MNRAS*, 285, L15.
- [32] Damour, T., Iyer, B., Sathyaprakash, B. S., 2001, *Phys. Rev. D*, 63, 044023.
- [33] Davies, M. B., Benz, W., Piran, T., Thielemann, F. K., 1994, *ApJ*, 431, 742.
- [34] Dimmelmeier H., Font J. A., Müller E., 2002, *A&A*, 393, 523.
- [35] Di Prisco, A., Herrera, L., Esculpi, M., 1996, *Class. Quantum Grav.*, 13, 1053
- [36] Donat, R., Marquina, A., 1996, *J. Comput. Phys.*, 125, 42.
- [37] Duncan, R. C., Thompson, C., 1992. *ApJ*, 392, L9.
- [38] Ebisawa, K., Mitsuda, K., Inoue, H., 1989, *PASJ*, 41, 519.
- [39] Eckart, C., 1940, *Phys. Rev.*, 58, 919
- [40] Einfeldt, B., 1988, *SIAM J. Num. Anal.*, 25, 294.
- [41] Eulerink, F., Mellema, G., 1994, *A&A*, 284, 654
- [42] MacFayden, A. I., Woosley, S. E., 1999, *ApJ*, 524, 262.

- [43] Finn L. S. in *Frontiers in Numerical Relativity*, ed. C.R. Evans, S. L. Finn., & D.W. Hobill (Cambridge University Press, Cambridge, England, 1989).
- [44] Fishbone, L. G., Moncrief, V., 1976, ApJ, 207, 962.
- [45] Flowers, N., Itoh, N., 1981, ApJ, 250, 750.
- [46] Font, J. A., Ibáñez, J. M., Martí, J. M, Marquina, A., 1994, A&A, 282, 304.
- [47] Font, J. A., Ibáñez, J. M., 1998, ApJ, 494, 297.
- [48] Font, J. A., 2000, Living Reviews in Relativity, 3, 2.
- [49] Font, J. A., Miller, M., Suen, W., Tobias, M., 2000, Phys. Rev. D, 61, 044011
- [50] Font, J. A. 2000 *Living Reviews in Relativity*, Vol 3, 2.
- [51] Font, J. A., Goodale T., Iyer S., Miller M., Rezzolla L., Seidel E., Stergioulas N., Suen W., Tobias M., 2002, Phys. Rev. D 65, 084024.
- [52] Font, J. A., Daigne, F., 2002a, MNRAS, 334, 383.
- [53] Font, J. A., Daigne, F., 2002b, ApJL, *submitted*.
- [54] Friedman, J. L., 1978, Comm. Math. Phys., 62, 247.
- [55] Geppert, U., Urpin V., 1994, MNRAS , 271, 490.
- [56] Geppert, U., Page, D., Zannias, T., 2000. Phys. Rev. D, 61, 123004
- [57] Ginzburg, V. L., Ozernoy, L. M., 1964. Zh. Eksp. Teor. Fiz., 47, 1030.
- [58] Glendenning, N. K., 1996 Compact Stars, Springer-Verlag, New York.
- [59] Godunov, S. K. 1959, *Mat. Sb.*, **47**, 271.
- [60] Goldreich, P., Reiseneger, A., 1992. ApJ, 395, 250.
- [61] Grad, H., 1949, Comm. Appl. Math., 2.
- [62] Grad, H., 1958, in *Handbuck der Physic XII*, Springer Heidelberg.
- [63] Gupta, A., Mishra, A., Mishra, H., Prasanna, A. R., 1998, Class. Quantum Grav. 15, 3131.
- [64] Guyer, R. A., Krumhansl, J. A., 1964, Phys. Rev., 133, 1411.
- [65] Harten, A., Lax, P. D., van Leer, B., 1983, SIAM Reviews, 25, 35.
- [66] Hawley, J. F., Wilson, J. R., Smarr, L. L., 1984a, ApJ, 277, 296.

- [67] Herrera, L., Santos, N. O., 1997, MNRAS, 287, 161
- [68] Herrera, L., Martinez, J., 1998, Gen. Rel. Gravit., 30, 445.
- [69] Hiscock, W. A., Lindblom, L., 1983, Ann. Phys., 151, 466.
- [70] Hou, T. Y., LeFloch, P., 1994, Math. of Comput., 62, 497.
- [71] Igumenshchev, I. V., Beloborodov, A. M., 1997, MNRAS, 284, 767.
- [72] Ipser, J. R., Lindblom, L., 1992, ApJ, 389, 392.
- [73] Ipser, J. R., 1994, ApJ, 435, 767.
- [74] Israel, W., 1976, Ann. Phys., 100, 310
- [75] Ibañez, J. M., Martí, J. M. 1999, *J. Comp. Appl. Math.* **109**, 173.
- [76] Jüttner, F., 1911, Annalen der Physik, 34.
- [77] Kato, S., Fukue, J., 1980, PASJ, 32, 377.
- [78] Kato, S., Fukue, J., Mineshige, S., 1998, in *Black Hole Accretion Disks*, Kyoto University Press, Japan.
- [79] Kato S., 2001, PASJ, 53, 1.
- [80] Khanna, R., Chakrabarti, S. K., 1992, MNRAS, 259, 1.
- [81] Kochanek, C., Shapiro, S. L., Teukolsky, S. A., Chernoff, D. F., 1990, ApJ, 358, 81.
- [82] Koenigl, A., 1980, *Phys. Fluids* **23**, 1083.
- [83] Konar, S., Bhattacharya, D., 1997, MNRAS , 284, 311.
- [84] Konenkov, D., Geppert, U., 2001, MNRAS, 325, 426.
- [85] Konno K., Kojima Y., 2000, Prog. of Theor. Phys. 104, 1117.
- [86] Kozłowski, M., Jaroszynski, M., Abramowicz, M. A., 1978, A&A, 63, 209.
- [87] Lamb, F. K., 1991. In: *Frontiers of Stellar Evolution*, p.299, ed. Lambert, D. L., Astron. Soc. Pacific.
- [88] Landau, L. D. and Lifshitz, E. M. 1987, *Fluid Mechanics (Second Edition)*, Pergamon.
- [89] Lax, P. D., Wendroff, B., 1960, Comm. Pure Appl. Math., XVII, 381.
- [90] Lee, W. H., Kluzniak, W., 1999a, MNRAS, 308, 780.
- [91] Lee, W. H., Kluzniak, W., 1999b, ApJ, 526, 178.

- [92] Lee, W. H., MNRAS, 318, 606.
- [93] Levermore, C. D., Pomraning, G. C., 1981, ApJ, 248, 321.
- [94] Leveque, R. J. 1992, *Numerical Methods for Conservation Laws*, Birkhauser
- [95] Leveque, R. J., Mihalas, D., Dorfi, E. A., Müller, E., 1998, *Computational Methods for Astrophysical Fluid Flows* Saas-Fee Advanced Course 27, Springer
- [96] Lewin, W. H. G., Paradijs, J., van den Heuvel, 1995, in *X-ray Binaries*, Cambridge University Press.
- [97] Lindblom, L., Splinter, R. J., 1990, ApJ, 348, 198.
- [98] Liu, I., Müller, I., Ruggeri, T., 1986, Ann. Phys., 169, 191.
- [99] Lubow, S. H., Ogilvie, G. I., 1998, ApJ, 504, 983.
- [100] Markovic, D., Lamb, F. K., 1998, ApJ, 507, 316.
- [101] Maartens, R., Triginer, J., 1997, Phys. Rev D., 56, 8.
- [102] Maartens, R., Triginer, J., 2000, Gen. Rel. Grav., Vol. 32, No. 9.
- [103] Marquina, A., 1994, SIAM J. Scient. Comp., 15, 892
- [104] Marquina, A., Martí, J. M., Ibañez, J. M., Miralles, J. A., Donat, R., 1992, A&A, 258, 566.
- [105] Martí, J.M., Ibañez, J. M., Miralles, J. A. 1991, Phys. Rev. D 43, 3794.
- [106] Martí, J.M. & Müller, E. 1994, J. Fluid Mech., 258, 317.
- [107] Martí, J.M. & Müller, E., Font J. A., Ibañez, J. M., 1995, ApJ, 448, L105.
- [108] Martí, J.M. & Müller, E. 1996, J. Comp. Phys., 123, 1.
- [109] Martí, J.M. & Müller, E., Font J. A., Ibañez, J. M., Marquina, A., 1997, ApJ, 479, 151.
- [110] Martí, J.M. & Müller, E. 1999, *Living Reviews in Relativity*, Vol 2, 3
- [111] Masuda, N., Eriguchi, Y., 1997, ApJ, 489, 804.
- [112] Masuda, N., Nishida, S., Eriguchi, Y., 1998, MNRAS, 297, 1139.
- [113] May, M. M., White, R. H., 1966, Phys. Rev., 141, 1232.
- [114] Meszaros, P. 2002 *Annu. Rev. Astron. Astrophys.*, 40 in press, astro-ph/0111170
- [115] Michel, F., 1972, Astrophys. Spa. Sci., 15, 153.

- [116] Miller, J. C., 1977. MNRAS 179, 483.
- [117] Mineshige, S., Hosokawa, T., Machida, M., Matsumoto, R., 2002, astro-ph/0208406.
- [118] Morton, K. W., Mayers, D. F., 1994, *Numerical Solution of Partial Differential Equations*, Cambridge University Press
- [119] Müller, I., 1967, Z. Physik, 198, 329
- [120] Müller, I., Ruggeri, T., 1998, in *Rational Extended Thermodynamics*, Springer.
- [121] Muslimov, A., Harding, A. K., 1997. ApJ, 485, 735.
- [122] Muslimov, A., Tsygan, A. I., 1992. MNRAS, 255, 61.
- [123] Narayan, R., 1992, ApJ, 394, 261.
- [124] Norman, M. L., Winkler, K. A., in *Astrophysical Radiation Hydrodynamics*, edited by M. L. Norman and K. H. A. Winkler (Reidel, Dordrecht, Holland, 1986).
- [125] Novak, M. A., Wagoner, R. V., 1991, ApJ, 378, 656.
- [126] Novak, M. A., Wagoner, R. V., 1992, ApJ, 393, 697.
- [127] Novak, M. A., 1995, P.A.S.P., 718, 1207.
- [128] Novikov, I., Thorne, K. S., 1973, in *Black Holes*, eds. B. de Witt and C. de Witt, Gordon and Breach, NY 491, 663.
- [129] Oppenheimer, J. R., Volkoff, G.M., 1939. Phys. Rev., 55, 374.
- [130] Okazaki, A. T., Kato, S., Fukue, J., 1987, PASJ, 39, 457.
- [131] Osher, S., Chakravarthy, S., SIAM J. Numer. Anal., 1984, 21, 995.
- [132] Papaloizou, J., Szuszkiewicz, E., 1994, MNRAS, 268, 29.
- [133] Peirls, R., in *Quantum Theory of Solids*, Oxford University Press, 1956, London.
- [134] Peitz, J., Appl, S., 1997, MNRAS, 286, 681.
- [135] Peitz, J., Appl, S., 1999, Class. Quantum Grav., 16, 979.
- [136] Peshkov, V., 1944, J. Phys., 8, 381.
- [137] Psaltis, D., *et al.*, 1999, ApJ, 520, 763.
- [138] Nowak, M. A., Wagoner, R. V., 1992, ApJ, 393, 697.
- [139] Page, D., Geppert, U., Zannias, T., 2000, Astron. Astrophys., 360, 1052.

- [140] Pavon, D., Bafaluy, J., Jou, D., 1991, *Class. Quantum Grav.*, 8, 347.
- [141] Petterson, J. A., 1974. *Phys. Rev.*, D10, 3166.
- [142] Peitz, J. Appl, S., 1997, *MNRAS*, 286, 681
- [143] Pons, J.A., Font, J.A., Martí, J.M., Ibañez, J.M. & Miralles, J.A. 1998, *Astron. Astroph.* 339, 638.
- [144] Pons, J.A., Font, J.A., Ibañez, J.M., Martí, J.M., Miralles, J.A., 1998, *A&A*, 339, 638.
- [145] Pons, J.A., Martí, J.M., Müller, E. 2000, *J. Fluid Mech.* 422, 125.
- [146] Phopam, R., Narayan, R., 1992, *ApJ*, 394, 255.
- [147] Prasanna, A. R., Gupta, A., 1997, *Il Nuovo Cimento B*, 112, 1089.
- [148] Press, W. H., Teukolsky, S. A. Vetterling, W. T., Flannery, B. P., 1992, *Numerical Recipes in Fortran 77*, Cambridge University Press, Second Ed.
- [149] Psaltis, D., Norman, C., astro-ph/0001391.
- [150] Rezzolla L., Shibata M., Asada H., Baumgarte T. W. Shapiro S. L., 1999 *ApJ*, 525, 935.
- [151] Rezzolla, L., Lamb, F. K., Shapiro, S. L., 2000 *ApJL*, 531, L141.
- [152] Rezzolla, L., Ahmedov, B. J., Miller, J. C., 2001a, *MNRAS*, 322, 123
- [153] Rezzolla, L., Ahmedov, B. J., Miller, J. C., 2001b, *Found. of Phys.*, 31, 1051.
- [154] Rezzolla, L. & Zanotti, O. 2001, *J. Fluid Mech.* 449, 395.
- [155] Rezzolla, L., Zanotti, O., Pons, J. A., 2002, *submitted*
- [156] Rezzolla, L. & Zanotti, O. 2002, *Phys. Rev. Letter*, 89, 11.
- [157] Rezzolla L., Yoshida S'i, Zanotti O., 2002 *in preparation*
- [158] Richtmyer, R. D. and Morton, K. W. *Difference Methods for Initial Value Problems* Interscience-Wiley, New York (1967)
- [159] Rindler, W. *Introduction to Special Relativity*, Clarendon Press, New York (1982)]
- [160] Rodriguez M. O., Silbergleit A. S., Wagoner R. V., 2002, *ApJ*, 567, 1043.
- [161] Roe, P. L., 1981, *J. Comput. Phys.*, 43, 357.
- [162] Romano, V., Pavon, D., 1993, *Phys. Rev. D*, 46, 1396.

- [163] Ruffert M., Janka, H.-T., 1999, A&A, 344, 573.
- [164] Ruffert, M., Janka, H.-T., 2001, A&A, 380, 544.
- [165] Sang Y. and Chanmugam G., 1987, ApJ, 323, L61.
- [166] Sengupta, S., 1995. ApJ, 449, 224.
- [167] Sengupta, S., 1997. ApJ, 479, L133.
- [168] Syer, D., Narayan, R., 1993, MNRAS, 198, 339.
- [169] Shakura, N. I., Sunyaev, R. A., 1973, A&A, 24, 337.
- [170] Shibata, M., Baumgarte, T. W., Shapiro, S. L., 2000, Phys. Rev. D, 61, 4012.
- [171] Shibata, M., Uryū, K., 2000, Phys. Rev. D, 61, 4001.
- [172] Shu, F., 1992, in *The physics of Astrophysics, Vol 2, Gas dynamics*, University Science Books.
- [173] Silbergleit, A. S., Wagoner, R. V., Rodriguez, M., 2001, ApJ, 548, 335.
- [174] Synge, J. L., 1957, in *The relativistic gas*, Holland.
- [175] Smoller, J. and Temple, B., 1993, Commun. Math. Phys., 156, 67.
- [176] Sod, G. A. 1978, *J. Comp. Phys.*, 27, 1.
- [177] Spada, M., Ghisellini, G., Lazzati, D., Celotti, A., 2001, MNRAS, 325, 1559
- [178] Spruit, H. C., 1999, A&A, 341, L1.
- [179] Stergioulas, N., Living Reviews in Relativity, 1, 8.
- [180] Stewart, J. M., 1977, Proc. R. Soc. London A, 365, 43.
- [181] Struchtrup, H., 1996, in *Zur Irreversiblen Thermodynamik der Strahlung*, Dissertation, Berlin.
- [182] Struchtrup, H., 1997, Ann. of Phys., 257.
- [183] Tanaka, Y., Lewin, W. H. G., 1995, in *X-ray binaries* (eds. W. H. Lewin, J. van Paradijs, E. P. J. van den Heuvel) Cambridge University Press.
- [184] Tassoul, J. L., 1978, in *Theory of Rotating Stars*, Princeton University Press.
- [185] Taub, A. H., 1948, *Phys. Rev.*, 74, 328.
- [186] Thompson, C., Duncan, R., 1993., ApJ, 408, 194.

- [187] Thompson, C., Duncan, R. C., 1995. MNRAS, 275, 255.
- [188] Thompson, K. W., 1986, J. Fluid Mech., 171, 365
- [189] Thorne, K. S., in *300 Years of Gravitation*, edited by S. Hawking and W. Israel, Cambridge University Press, Cambridge, 1987.
- [190] Tolmann, R.C., 1939. Phys. Rev., 55, 364.
- [191] Toro, E. 1997, *Riemann Solvers and Numerical Methods for Fluid Dynamics*, Springer.
- [192] Urpin, V., Konenkov, D., 1997. MNRAS, 292, 167.
- [193] Urpin, V., Levshakov, S., Yakovlev, D., 1986. MNRAS, 219, 703.
- [194] van der Klis, M. *et al.*, 1996, IAU Circ 6319.
- [195] van der Klis, M., Wijnands, R., Chen, W., Horne, K., 1997, ApJ, 481, L97.
- [196] van der Klis, M., 2000, ARA&A, 38, 717.
- [197] Van Leer, B., 1979, J. Comput. Phys., 32, 101
- [198] van Putten, M. H. P. M., 2001a, Phys. Rev. Lett., 87, 091101.
- [199] van Putten, M. H. P. M., 2001b, ApJ, 575, L71.
- [200] Vietri, M., Stella, L. 1998, ApJ. 507, L45.
- [201] Wagoner, R., Silbergleit, A. S., Rofriguez, M. O., 2001, ApJ, 559, L25.
- [202] Wasserman, I., Shapiro, S. L., 1983. ApJ, 265, 1036.
- [203] Weiss, W., Müller, I., 1995, Continuum Mech. Thermodyn., 7, 123.
- [204] Whitham, G. B. *Linear and non-linear waves*, John Wiley & Sons, 1974
- [205] Wiebicke, H. J., Geppert, U., 1996. Astron. Astrophys. , 309, 203.
- [206] Wilson, D. B., 1972, ApJ, 173, 431.
- [207] Wilson, D. B., 1984, Nature, 312, 620.
- [208] Winkler, W., "The VIRGO/GEO Collaboration", Vision document
www.astro.cf.ac.uk/geo/euro/
- [209] Hawley, J. F., Smarr, L. L., Wilson, D. B., 1984, ApJ Suppl., 55, 211.
- [210] Yoshida, S., Eriguchi, Y., 1995, ApJ, 438, 830.
- [211] Yoshida, S., Eriguchi, Y., 1997, ApJ, 490, 779.

- [212] Zanotti, O., Rezzolla, L., 2002, MNRAS, 331, 376.
- [213] Zanotti, O., Rezzolla, L., Font, J. A., 2002, MNRAS, *submitted*.